Spectroscopie optique de boîtes quantiques de graphène

Thomas Liu

université
PARIS-SACLAY

Spectroscopie optique de boîtes quantiques de graphène

Optical spectroscopy of graphene quantum dots

Thèse de doctorat de l'université Paris-Saclay

École doctorale n° 572, ondes et matière (EDOM)
Spécialité de doctorat: Physique
Graduate School : Physique, Référent : ENS Paris-Saclay

Thèse préparée dans l'unité de recherche **LuMIn**
(Université Paris-Saclay, ENS Paris-Saclay, CentraleSupélec, CNRS),
sous la direction de **Jean-Sébastien LAURET**, professeur des universités,
et le co-encadrement de **Loïc RONDIN**, maître de conférences

Thèse soutenue à Paris-Saclay, le 3 mars 2023, par

Thomas LIU

Composition du jury

Membres du jury avec voix délibérative

Michel Orrit Professeur des universités, University of Leiden	Président
Nedjma Bendiab Professeure des universités, Université Grenoble Alpes	Rapporteur & Examinatrice
Guillaume Schull Professeur des universités, Université de Strasbourg	Rapporteur & Examinateur
Elizabeth Boer-Duchemin Maîtresse de conférences, Université Paris-Saclay	Examinatrice

THESE DE DOCTORAT
NNT : 2023UPASP027

université PARIS-SACLAY | ÉCOLE DOCTORALE Ondes et matière (EDOM)

Titre: Spectroscopie optique de boîtes quantiques de graphène
Mots clés: Spectroscopie, boîte quantique, graphenoïde

Résumé: Les boîtes quantiques de graphène (abrégé GQD en anglais) sont des nano-objets composés d'une centaine d'atomes de carbone. Ces atomes peuvent être disposés selon diverses géométries conduisant à un large éventail de propriétés. Leur taille intermédiaire entre petites molécules et solides en fait une plateforme idéale pour tester les prédictions théoriques, à la fois de la chimie quantique et de la physique de la matière condensée. Cependant, bénéficier pleinement des potentialités offertes par l'accordabilité des propriétés des GQDs nécessite de pouvoir rigoureusement relier leur géométrie aux propriétés électroniques qui en découlent. Dans cette optique, une étude approfondie des propriétés intrinsèques de ces objets a été réalisée dans le cadre de cette thèse. Ce travail a été mené en couplant des études spectroscopiques, en solution et à l'échelle de l'objet individuel, à des simulations théoriques.

L'étude d'une boîte quantique de graphène à symétrie triangulaire (C96C12) a permis de mettre en avant l'effet d'agrégation en solution, et de comparer les observations aux prédictions théoriques. Les résultats à l'échelle de l'objet unique ont également pu être confrontés à la théorie avec succès, menant par ailleurs à une caractérisation des impuretés fluorescentes observables dans les expériences de spectroscopie d'objets uniques, des résultats non directement liés aux GQDs, mais qui représentent un apport nécessaire à leur utilisation à l'échelle de l'objet unique. Enfin, l'étude d'une classe de GQD présentant une forme allongée a permis de sonder l'effet de la symétrie et de la taille sur les propriétés optiques de ces objets et, notamment grâce à l'homogénéité remarquable de leurs propriétés en échantillon, de proposer une nouvelle classe de GQD prometteuse pour les applications.

Cette thèse a ainsi permis d'approfondir l'étude de ces objets, là où leur caractérisation se limite trop souvent à une étude sommaire en solution. Grâce à une compréhension accrue des propriétés de boîtes quantiques, elle ouvre ainsi la porte à l'utilisation des GQDs dans différentes applications, de l'optoélectronique au développement de capteurs, et à leur couplage avec différents matériaux, permettant encore d'étendre leur domaine d'applications.

Title: Optical spectroscopy of graphene quantum dots
Keywords: Spectroscopy, quantum dots, nanographene

Abstract: Graphene quantum dots (GQDs) are nano-objects made of hundreds of carbon atoms. These atoms can be arranged in various geometries leading to a wide range of properties. Their intermediate size between small molecules and solids makes them a perfect platform to test theoretical predictions both of quantum chemistry and condensed matter physics. However, accessing these potentialities offered by the tunability of the GQDs' properties requires a precise understanding of the dependence between geometry and electronic properties. To that extent, a thorough investigation of the intrinsic properties of these objects is developed in this thesis. This study coupled spectroscopic measurements, both in solution and at the single-object level, and theoretical calculations.

The investigation of a GQD with triangular symmetry (C96C12) exhibited the formation of aggregates in solution, and lead to an extensive understanding of the experimental observations using theoretical calculations. Single-object results are also successfully verified with theory, and, additionally, lead to a thorough characterization of fluorescent impurities observable in single-object experiments, which represents an essential step to enable the manipulation of GQDs at the single-object level. Finally, the study of a new class of rod-shaped GQDs enabled the investigation of the effect of symmetry and size on the optical properties, and demonstrated, thanks to the high homogeneity of their property, the potential of these new GQDs for applications.

The results presented in this thesis provide an extensive view of the characterization of the properties of graphene quantum dots, which are usually only briefly characterized in solution. The deepened understanding gained by these studies represents a necessary and promising step towards the use of these objects for applications in optoelectronics or quantum sensing, for instance by coupling them with other materials.

Remerciements

On vit pour toujours dans le souvenir de l'amour que l'on a donné.

Yogi

Il me faut commencer ce court prélude par remercier chaleureusement Jean-Sébastien Lauret, qui m'a accueilli au sein de l'équipe pour cette thèse sur les GQDs. Durant ces années, c'est toujours avec des mots encourageants qu'il a dirigé mes travaux et m'a fait découvrir le monde de la recherche, tout en m'accordant une confiance qui, dès le début, m'a responsabilisé dans la rigueur de ma démarche scientifique. Il m'a notamment montré qu'il reste toujours une chose à explorer ou à valoriser, malgré le chaos apparent des résultats décourageants obtenus par moments. Ces leçons de persévérance de d'optimisme, je les garde précieusement et je tâcherai de les appliquer, et ce même au-delà du cadre de la recherche. Évidemment, toujours par deux ils vont, je souhaite remercier Loïc Rondin, dont l'enthousiasme et le dynamisme sont contagieux, et qui ne manquait pas, lui non plus, de partager des mots d'encouragement, une grosse chope de thé à la main. Il a toujours été présent pour m'apporter son aide et son conseil sur l'expérience, pour partager son avis critique (toujours pertinent) sur les résultats que j'obtenais ou pour partager ses préparations culinaires, dont nous dévorions avec plaisir toutes les parts (à l'exception de la dernière).

Je remercie également chaleureusement Michel Orrit d'avoir accepté de participer à mon jury et d'en être le président. Cela est d'autant plus symbolique à mes yeux car je lui dois mes premiers pas dans le milieu de la spectroscopie de molécules uniques, que j'ai eu la chance de découvrir lors d'un stage au sein de son équipe à Leiden. Je remercie Nedjma Bendiab et Guillaume Schull d'avoir accepté de rapporter ma thèse, ainsi qu'Elisabeth Boer-Duchemin pour l'avoir examinée.

Je remercie Fabien Bretenaker, directeur du Laboratoire LuMIn, de m'avoir accueilli au sein du laboratoire, et d'avoir toujours eu ce regard malicieux de bienveillance à l'égard des doctorants.

Je remercie aussi Djamel Benredjem, qui m'avait au tout début de ma thèse accueilli au Laboratoire Aimé Cotton (car j'ai tout de même fait partie de ce laboratoire pour les tous premiers mois de ma thèse), ainsi que Thomas Pino, directeur de l'ISMO, pour l'hébergement de nos expériences à l'ISMO lors des travaux du 505, et Rachel Méallet-Renault, Farah Savina, les services mécaniques et autres acteurs de l'ISMO, qui ont permis

la continuation du travail lors de notre hébergements dans leurs locaux.

Je souhaite remercier tous les collaborateurs avec qui j'ai pu travailler durant ma thèse, notamment les théoriciens de l'Université de Mons (David Beljonne, Claire Tonnelé, Silvio Osella), les chimistes de Mainz (Akimitsu Narita), et les spectroscopistes du LPENS (Christophe Voisin, Yannick Chassagneux). Je remercie tout particulièrement Stéphane Campidelli, qui, en plus de diriger la partie synthèses des GQDs que j'ai étudié, m'a accueilli à plusieurs reprises au CEA pour réaliser diverses mesures, et également Daniel Medina-Lopez, que je n'ai connu que souriant et enthousiaste. Il a toujours été aisé et agréable d'échanger avec Stéphane et Daniel, et c'était un plaisir de pouvoir travailler avec eux.

Mon travail de thèse s'est fait dans une équipe formidable où chaque membre a contribué à créer un environnement de travail dans lequel j'étais à l'aise et ravi de travailler. Les membres permanents (Emmanuelle, Cédric, Elsa, Gaëlle) ont toujours été à l'écoute et prêts à m'apporter des conseils et à échanger avec moi.

Il y a eu tous les doctorants et post-doctorants qui m'ont accueilli dans l'équipe, dont Timothée (*Allooo c'est pour les pizzas...*), Paul, François et Gabriel. J'ai eu le privilège dès mon arrivée d'être le spectateur de la création de la discipline du Basket-boulettes, dans laquelle mes ainés avaient un talent indéniable.

Je n'oublie pas Thomas, frère de prénom et de thèse, qui s'est vu affubler le dénominatif *2* même si son arrivée au sein de l'équipe a précédé la mienne.

À la suite du confinement et lors de ma deuxième année (c'est la meilleure après tout), j'ai eu la chance de rencontrer Hugo (représentant appliqué et memeur masqué fasciné par tout ce qui brille), Damien (ami de la nature et prêcheur du MCU), et Christine (grande défenseure du taboulé libanais et des dettes non payées), avec qui ce sont de réelles aventures que j'ai pu partager (dont la plus notable devrait être l'observation assidue du terrain vague bordant le CESFO lors des pauses thé méridiennes), sans mentionner tous les *culinary night out*. Je n'oublie évident pas Trang, Maxime, Joanna, qui ont également pris part à ces découvertes, ainsi que les stagiaires avec qui j'ai pu travailler durant ma thèse (Baptiste, Juliette, Simon, Pranav, Sudhan).

Enfin, sur la fin de ma thèse, j'ai pu faire la connaissance des nouveaux thésards, dont Inès (Inette) ou Trung, à qui je souhaite plein de bonnes choses pour la suite.

Que serait le travail sans la pause déjeuner, j'en profite pour faire un petit clin d'œil à l'équipe du CESFO, qui a toujours su m'accueillir chaleureusement, notamment Luis et Abdel. Je n'ai à ce jour toujours pas compris l'origine de cet enthousiasme qu'ils avaient pour moi...

J'ai eu la chance que mon équipe fasse partie d'un jeune laboratoire rempli de membres bienveillants, et je ne pourrais faire la liste de tous les membres permanents et membres de l'administration avec qui j'ai pris plaisir à interagir. Il y a évidemment tous les thésards et post-docs (notamment Florian, Gautier, Alan, Isis, Marie-Charlotte, Cassandra et Joseph) avec qui, malgré la distance entre les différents sites du laboratoire, je me réjouissais d'aller partager une boisson, afin de partager anecdotes et histoires sur notre vie au labo.

Je ne saurais non plus oublier de remercier tous les membres du département de physique de l'ENS Paris-Saclay, que j'ai connus d'abord en tant qu'enseignants à Cachan, et que j'ai pris plaisir à déranger par la suite, mais qui ont su me le rendre en temps voulu. Je pense notamment à Christian et Zina, Jean-Baptiste et Arnaud, Simon et Colin, tous d'une extrême bienveillance à mon égard. Je n'oublie pas également les membres du département de chimie, notamment Cécile, et Laure-Lise. Dans le cadre de mes enseignements, c'était un plaisir d'interagir avec Frédéric M., Nathan L., Lucien C., Antoine H, Céline J., Jean-Xavier B.

Dans un cadre plus personnel, j'ai vécu mes années de thèse en parallèle de celles de mes camarades d'école, ces lurons physiciens (dont je suis le Sixième docteur) dont l'amitié m'est chère. Je dois évidemment remercier Jennifer, qui n'a cessé d'être une interlocutrice privilégiée lors de notre hébergement à l'ISMO, ainsi qu'après notre déménagement vers le 505. D'une simple collègue d'étage à qui j'essayais d'emprunter de l'azote liquide au début de la thèse, elle est devenue cette confidente que l'on aime déranger avec ses plaintes et ses doléances intempestives (et ô combien de fois suis-je passé l'embêter dans son bureau). Et, également aux côtés de Paul et Benou, mes compères enchanteurs, j'ai passé une troisième année mouvementée et riche en émotions et en décadence, à la découverte de nouvelles amitiés (notamment des jeunes camarades matheux).

Je pense également à tous mes amis de prépa, de lycée (tout particulièrement Jeanne, avec qui nous ne cessons de nous suivre depuis tant d'années), et même d'avant, qui m'ont soutenu et encouragé durant ces années de thèse, et ce jusqu'au jour de ma soutenance. Je n'oublie évidemment pas Laurent Le, ce cher compère qui m'a suivi aux Pays-Bas et que j'ai ensuite retrouvé à l'ISMO, et dont j'admire sans cesse les talents de commère.

Je dois également remercier mes colocs botuleux Théo, Clément H. et Arthur, ainsi que Clément P., le coloc de la dernière heure, que je retrouvais avec plaisir chaque soir en rentrant de Saclay, et sans qui ces années de thèse ne se seraient pas déroulées de la même manière. Je pense à Sarah, qui s'est essayée coloc également, ainsi que secrétaire à domicile. Ainsi que Rémy, camarade de cœur, avec qui j'ai passé un nombre indécent d'heures à apprécier les arts vivants.

Vu que ce diplôme marque la fin de mes études, c'est une occasion de remercier tous les enseignants et enseignantes que j'ai eus durant ma scolarité, pour qui j'ai un grand respect et une sincère gratitude. Enfin, je conclus cette longue liste de remerciements avec ma famille, qui m'a apporté tant d'amour et que j'aspire à rendre fier, et qui s'est encore agrandie durant ma thèse avec l'arrivée de la petite Chloé.

Encore une fois, humblement et avec gratitude, merci.

Contents

Preface

Ever since the experimental isolation of graphene by Geim and Novoselov in 2004 [1] using mechanical exfoliation of graphite, a large range of experiments have explored the properties of this novel material. Unique electronic properties have been demonstrated, such as room-temperature quantum Hall effect [2] or Klein tunneling [3, 4], direct consequences of its specific honeycomb lattice. Other transport properties, including high electrical and thermal conductivity, have also been observed, which makes it a material of choice for technological applications [5]. Concerning optical properties, given the absence of gap in the electronic band structure, transitions are possible for all photon energies. It has been experimentally demonstrated that the absorption rate is independent of the energy for optical frequencies [6].

The inherent absence of energy bandgap is a drawback for the use of graphene for field-effect transistor applications and logic devices [7, 5]. Early research paths to open a gap included electrically-gated bilayer graphene [8] or lithographically-patterned graphene nanoribbons [9], which, however, failed to open a gap wider than a few hundreds of meV. Nanometer-sized structures of graphene, called *graphene quantum dots* (GQD), have demonstrated the possibility to open a gap in graphene on a larger range of frequencies. Using this approach should theoretically enable a wide tunability of the electronic properties, due to a high sensitivity of the properties to the topology of the GQD (edges, size, symmetries). GQDs have first been studied theoretically, and various reports have tried predicting the influence of the structure of the GQD on its electronic and optical properties. However, these studies remained speculative since the studied GQDs could not be precisely synthesized, due to a lack of control on the structure during synthesis. The interest for this class of objects has soared alongside the development of precise synthesis methods, namely *bottom-up* methods, which enable a controlled and reproducible fabrication of GQDs with a rigorous tailoring of their topology. The efforts made in the field of chemical synthesis now open the way to the synthesis of a large collection of GQDs and to the design of arbitrary GQD structures, with possible sidechains or heteroatoms added to it.

Prior to my thesis, the research group of Jean-Sébastien Lauret had focused on the study of a triangular-shaped GQD composed of 96 carbon atoms [10], with the observation of stable single-photon emission at room temperature. They rigorously characterized the photophysics of this object using single-molecule spectroscopy and also explored the effect of functionalization on the energy levels of the GQD. This demonstration of the possibility to study GQDs at the single-object level (when GQD characterizations

are usually limited to ensemble measurements) has given a new level of precision in the study of the properties of GQDs, and has since caught the interest of several research teams who see in GQDs the possibility to enrich the list of candidates for organic-molecule-based technologies [11].

Thanks to bottom-up synthesis, the scope of accessible GQD structures seems endless. The possibility to change at will the properties of GQDs paves the way for the reverse-engineering of GQDs, where, according to a desired application, the corresponding GQD can be tailored and synthesized. Nonetheless, a thorough understanding of the property-geometry relationship in GQDs is necessary in order to achieve this objective, and this necessarily requires a deeper focus on the characterization of their optical properties, a subject which still remains timidly explored. Moreover, the usability of a GQD and its integrability in devices is conditioned by the possibility to effectively isolate and observe it experimentally. The tendency of large graphene flakes to aggregate and the contamination of samples by organic impurities complexify the isolation of single GQDs and prevent a straightforward exploitation of their intrinsic properties. Understanding the composition of samples and the origin of their contamination are thus unavoidable tasks to address this issue, and represent essential steps towards the processability of these objects.

In this context, I focused during my thesis on the study of GQDs using optical spectroscopy. Combining both ensemble and single-object measurements, I investigated the photoluminescence properties of GQDs by first pursuing the work previously started on the 96-carbon-atom GQD, in order to provide a broader understanding of their optical properties, with the objective to fully understand the experimental observations made on this system. Alongside this work, I sought to unravel the origin of fluorescent impurities when studying GQDs, in order to provide tools to unambiguously isolate single GQDs in prepared samples. These steps were indispensable before moving on to a broader range of GQDs. I eventually pursued the study of the property-geometry relationship by exploring GQDs with different geometries, bringing additional insight on this promising class of fluorescent systems.

In this manuscript, I condensed the results obtained during my stay in the group of Jean-Sébastien Lauret, and organized them as follows:

In Chapter 1, I present a brief overview of GQD physics, from its theoretical description to its fabrication. In particular, I emphasize the large tunability of the properties of GQDs enabled by the controlled bottom-up synthesis of these objects. The description of single-object spectroscopy, a tool to study the properties of single GQDs, and of basic concepts of fluorescence physics is detailed, along with possible applications accessible with this method. The recent research paths and applications envisionned for GQDs are also reviewed.

Chapter 2 focuses on the experimental methods used during my thesis to study the optical properties of GQDs. I rapidly describe the chemical synthesis followed to obtain the GQDs studied during my thesis and the MALDI-TOF method used to evaluate the purity of the synthesis batches. The protocole used to prepare the samples are then detailed, followed by the description of the various spectroscopic measurements in so-

lution (absorption, photoluminescence in steady-state and time-resolved, polarization-dependent measurements) along with the technical details of the single-molecule experimental setup.

Chapter 3 is focused on the investigation of the origin of impurities observed in single-molecule experiments. Contamination of samples may complicate the identification of single GQDs, thus motivating a thorough characterization of these emitters in order to differentiate them from GQDs. I present in this chapter the spectral characterization of the impurities and discuss, given the experimental observations, their possible origin. A comparison with previously reported impurities is also given in order to enrich the discussion.

Chapter 4 presents the results obtained of the $C_{96}C_{12}$ triangular GQD, which had been previously studied in the group. The study of the GQD in solution is discussed and experimental results and theoretical predictions are compared. I also examine the role of symmetry-breaking on the optical properties of this GQD. Results at the single-object level are also presented, both at room and low temperature. Characteristic spectral features, resolved at low temperature, are highlighted and attributed to vibrational modes of the GQD. I show how these results bring insight on the manipulation of GQDs at the single-object level, and may hint at effects of perturbations due to a GQD's environment. I also describe the selection method used to discriminate GQDs from impurities when looking at single objects.

In Chapter 5, I describe the results obtained for a new class of rod-shaped GQDs, which exhibit astonishingly narrow emission lines at room temperature. By combining theoretical calculations and photoluminescence spectroscopy in solution, the spectral observations can be fully explained. The effect of symmetry on the energy levels is discussed by comparing with the triangular $C_{96}C_{12}$ GQD. Single-molecule results are also described, and confirm the homogeneity of samples expected from results in solution. Finally, the effect of size on the electronic properties is discussed, along with the role of the *t*Bu sidechains in the solution-processability of GQDs.

Chapter 1

Introduction to the optical investigation of graphene quantum dots

Contents

Introduction

The objective of this chapter is to give an overview of the study of graphene quantum dots both theoretically and experimentally, and to show how the development of these 0D nano-objects relies on the coordinated work of chemistry, theoretical calculations and experimental measurements, and may give rise to a large range of applications.

In a first section, I will briefly describe the physical objects we call graphene quantum dots and how these systems can be theoretically described and experimentally synthesized. Then in a second section, I succinctly present the framework of fluorescence spectroscopy and of single-molecule spectroscopy, which represents an essential tool to precisely study the photophysics of graphene quantum dots and bring insight into the property-structure relationship. Finally, in a concluding section, I will provide a short overview of the promising results recently observed for graphene quantum dots and the first concrete applications envisioned for these objects.

1.1 Description of graphene quantum dots

1.1.1 Necessity of gap opening in graphene

Graphene is a 2D material constituted of carbon atoms arranged in a honeycomb lattice, as shown in Figure 1.1(a). The structure can be described by a hexagonal lattice with a basis of two atoms per unit cell, with lattice unit vectors:

$$\mathbf{a}_1 = a\left(\frac{3}{2}\mathbf{e}_x + \frac{\sqrt{3}}{2}\mathbf{e}_y\right) \quad \text{and} \quad \mathbf{a}_2 = a\left(\frac{3}{2}\mathbf{e}_x - \frac{\sqrt{3}}{2}\mathbf{e}_y\right), \tag{1.1}$$

with $a \approx 1.42\,\text{Å}$ the distance between two neighboring carbon atoms. The associated Brillouin zone corresponds to a hexagon, and is represented in Figure 1.1(b). It can be described using the reciprocal-lattice vectors:

$$\mathbf{b}_1 = \frac{2\pi}{a}\left(\frac{1}{3}\mathbf{e}_x + \frac{\sqrt{3}}{3}\mathbf{e}_y\right) \quad \text{and} \quad \mathbf{b}_2 = \frac{2\pi}{a}\left(\frac{1}{3}\mathbf{e}_x - \frac{\sqrt{3}}{3}\mathbf{e}_y\right). \tag{1.2}$$

Considering valence bond theory, the σ bonds between neighboring atoms result from hybridized sp^2 orbitals. In addition to the σ bond, each carbon atom provides one p electron, which contributes to the formation of delocalized π bonds, and which determine the electronic properties of the material.

The general band structure of graphene can be determined using tight-binding calculations considering only the π-bands (*i.e.* the π electrons). Considering only nearest-neighbor interaction, the energy bands are described by [12]:

$$E(\mathbf{k}) = \pm t\sqrt{1 + 4\cos\left(\frac{\sqrt{3}}{2}k_x a\right)\cos\left(\frac{1}{2}k_y a\right) + 4\cos^2\left(\frac{1}{2}k_y a\right)}, \tag{1.3}$$

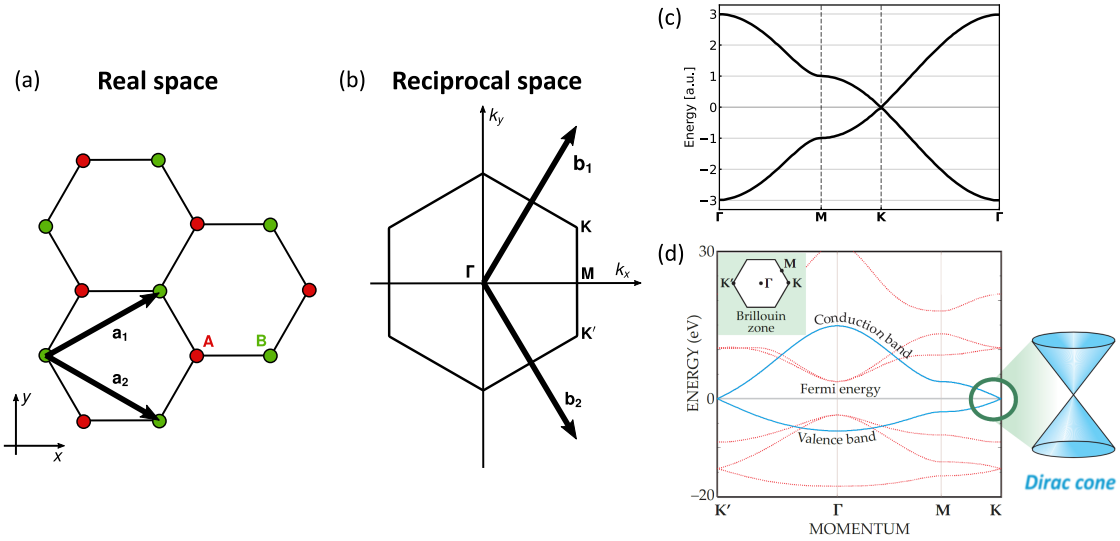

Figure 1.1: (a) Honeycomb lattice of graphene, described by a hexagonal lattice with lattice unit vectors $\mathbf{a}_1$ and $\mathbf{a}_2$, with two carbons atoms (**A** and **B**) in a unit cell. (b) Corresponding Brillouin zone. (c) Dispersion relation of the π-bands obtained using tight-binding calculation with only nearest-neighbor hopping (using Eq.1.3). (d) More detailed band structure of graphene (without restraining to nearest neighbors). The band gap vanishes at the K and K' points, forming Dirac cones (linear dispersion relation) as highlighted on the right. From [7].

where t is the nearest-neighbor hopping energy. This dispersion relation is represented in the Brillouin zone in Figure 1.1(c). One particularity of the band structure is the absence of electronic band gap: the conduction (upper π-band) and valence (lower π-band) bands meet at the K (and K') points of the Brillouin zone. A more precise description is given in Figure 1.1(d), obtained in the case where we do not limit the tight-binding calculation to nearest neighbors (by also taking into account second-nearest neighbors). Interestingly, when focusing on low-energy excitations, we can place ourselves around the K or K' points. The dispersion relation can be developed to:

$$E(\mathbf{q}) = \pm v_F \hbar |\mathbf{q}| \tag{1.4}$$

where $\mathbf{q} = \mathbf{k} - \mathbf{K}$, with $\mathbf{K}$ the position of the K point, and v_F the Fermi velocity (of the order of 10^6 m/s). The band structure takes the shape of Dirac cones, which meet at the Dirac points K and K', as highlighted in Figure 1.1(d). The linear dispersion relation announces that the behavior close to K points can be understood using massless Dirac fermion physics.

The physical properties of graphene have attracted much attention, notably after the first isolation of graphene sheets in 2004 [1]. A large variety of experiments explored these unique properties, yielding both fundamental results [13, 14] and concrete applications [15, 16, 17]. Nonetheless, while it became a unique advantage for applications such

as nanoelectronics, the absence of band gap is an obstacle for the community more interested in the study of its optical properties [18], and prevents the use of graphene in other fields such as for logic applications [19]. To this end, finding ways of opening a gap in the electronic band structure of graphene is necessary.

1.1.2 From graphene to graphene quantum dots

Confining down to zero dimension

Various examples of gap engineering have been demonstrated using graphene. Early results of gap opening were obtained for example for bilayer graphene, used as a field-effect transistor [8], yielding a gap at the K point up to mid-infrared. However, if we consider only a monolayer of graphene, a straight-forward way of inducing a gap is spatial confinement.

By reducing the dimensionality of graphene, and thus inducing spatial confinement, one may open a gap in its band diagram. Given the linear dispersion near the K point shown ealier in Eq.1.4, the gap resulting from confinement scales as $\Delta E \propto 1/d$, with d the characteristic size of the confined structure [20]. Graphene being a 2D material (charge carriers are already confined in the plane of the material), confining along one direction of the material plane yields a 1D confinement. The resulting objects are referred to as *graphene nanoribbons*. Carbon nanotubes may also be classified as 1D graphene given their structure. Confining along the second direction of space results in small pieces of graphene and to a 0D confinement, thus the qualification as **graphene quantum dot (GQD)**.

Clarifying denomination

In the literature, according to the community, the denomination of similar objects may vary. Considering the solid-state physics approach adopted up until now, the denomination *quantum dot* refers to the increased confinement of the electrons along the three directions of space as the size of the material decreases. However, if we now adopt the point of view of chemical physicists, they will recognize in these same objects a class of *polycyclic aromatic hydrocarbons* (PAHs). This denomination describes any organic compounds composed of multiple aromatic cycles, and may even include objects which do not exhibit only aromatic rings. The denomination PAH is thus seemingly more general than graphene quantum dots and may therefore be used to describe the same objects. Nonetheless, this denomination has historically been used for relatively small compounds (with up to 10-20 aromatic cycles). It would seem unfit to refer to a flake of graphene with an average size of tens of nanometers (more than thousands of aromatic cycles) as a PAH, although it can already be referred to as a graphene quantum dot, which can for instance demonstrate Coulomb blockade [21]. We thus choose to use the denomination of graphene quantum dot given the relatively large size of the objects manipulated in this thesis.

One can usually encounter the denomination *nanographene*, which refers to objects sharing the honeycomb structure of graphene, but are spatially limited on the

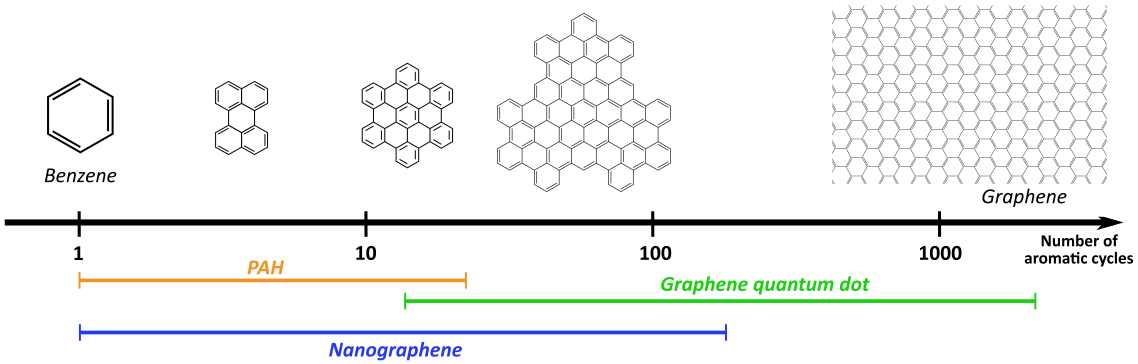

Figure 1.2: General denominations used for graphene-based aromatic compounds found in the literature according to their size.

scale of nanometers. This denomination thus includes both graphene quantum dots and graphene nanoribbons.

Graphene quantum dots must be distinguished from *carbon dots* (or carbon nanodots, carbon quantum dots), which can be seen as the carbon-based counterpart of usual semiconductor quantum dots. They thus refer to nanopieces of graphite, and are consequently not composed of an unique layer of carbon atoms.

Theoretical description of graphene quantum dots

Confining the graphene lattice to a finite-size object induces a quantification due to the boundary conditions imposed by the edges. Similarly to a particle in a box, the confinement induces a quantization of the wave vector $\mathbf{k}$, which should evolve following $2n\pi/d$ (in order of magnitude), with d the lateral size of the GQD and n an integer. A simple description of the electronic wavefunctions of the GQD can thus be done using standing wave states. For example, a calculation of the wavefunctions was performed for triangular graphene quantum dots and reported in [22], as represented by its Clar structure[1] in Figure 1.3(a). The authors showed that the quantization of the wave vector can be illustrated by its decomposition in a basis composed of vectors $\mathbf{K}_1$ and $\mathbf{K}_2$ (which have a magnitude scaling as $1/L$, L being the length of one edge of the triangular GQD):

$$\mathbf{k}_{n,m} = n\mathbf{K}_1 + m\mathbf{K}_2, \tag{1.5}$$

with n and m integers. Given the symmetry of the system, the study of the Brillouin zone of graphene can be limited to the white area represented in Figure 1.3(b). The quantization of the wave vector is illustrated in Figure 1.3(c), where each point corresponds to a possible value of the wave vector given the boundary conditions. Using tight-binding

[1] Aromatic compounds can be represented by replacing 6 π electrons in a single aromatic cycle by a π sextet (a circle is usually drawn in the cycle to represent the sextet). The Clar structure corresponds to representation maximizing the number of sextets [23].

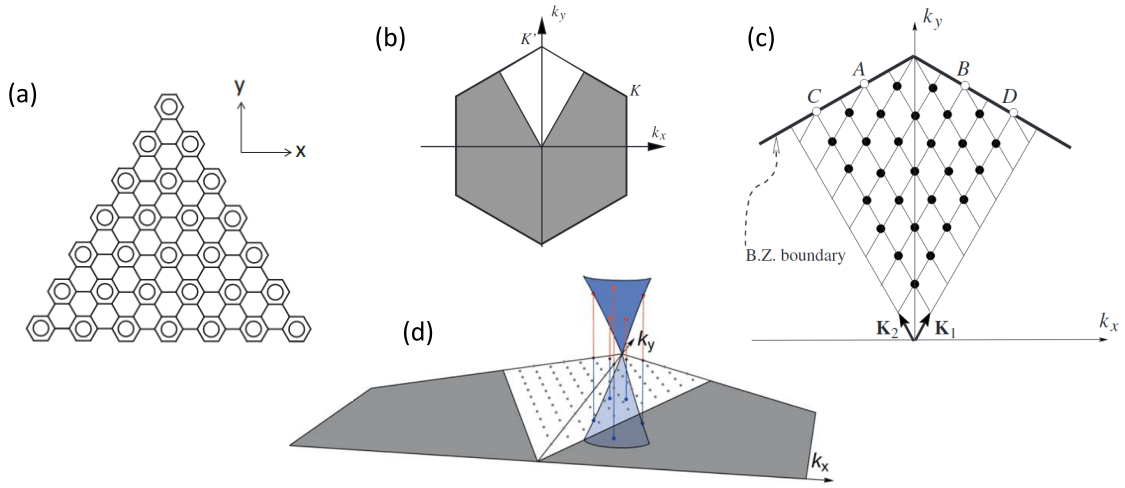

Figure 1.3: (a) Structure of a triangular fully-benzenoid GQD, with $N = 8$ (*i.e.* $N - 1$ correspondig to the number of C=C dimer along one side of the GQD). (b) The white polygon shows the area of the Brillouin zone of graphene (the whole hexagon) where the allowed wave vectors are located (result of the triangular symmetry). (c) Allowed values of $\mathbf{k}_{n,m}$, for the case where $N = 5$. (d) Schematic representation of the low-lying electron and hole states, corresponding to the projection of the allowed $\mathbf{k}_{n,m}$ values onto the Dirac cones. Figures adapted from [22] and [27].

calculations, the energy spectrum can be calculated:

$$E_{n,m} = \pm t\sqrt{3 + 2\cos\left(\frac{2\pi n}{3N}\right) + 2\cos\left(\frac{2\pi m}{3N}\right) + 2\cos\left(\frac{2\pi(n+m)}{3N}\right)} \tag{1.6}$$

with $N - 1$ the number of carbon dimers along one side of the triangular GQD, and t the nearest-neighbor hopping energy. The low-energy states are illustrated in Figure 1.3(d), which correspond to the projection of the allowed $k_{n,m}$ values onto the Dirac cones. The quantization of the wave vector highlights the dependence of the band gap as $1/d$ mentioned in the previous subsection.

Theoreticians predict this description to be valid for armchair edge GQDs [24], which is the case for the GQDs studied during my thesis. Differences can be observed in the case of zig-zag edge GQDs [2].

Alternatively to the standing wave states' model, that relies on a continuous description of the system, one can use the slightly more refined tight-binding model. Both descriptions provide similar results for GQDs made up from more than around 100 carbon atoms [28].

[2] Zig-zag edge GQDs cannot be described using an unique Clar structure, and are thus not fully benzenoid (*i.e.* all the double bonds cannot be all accounted for by representing only sextets in aromatic cycles [23]), with double bonds or unpaired electrons at the edges of the GQD. As a result, zero-energy states are predicted to appear, which result from edge states of the GQD [25, 24, 26].

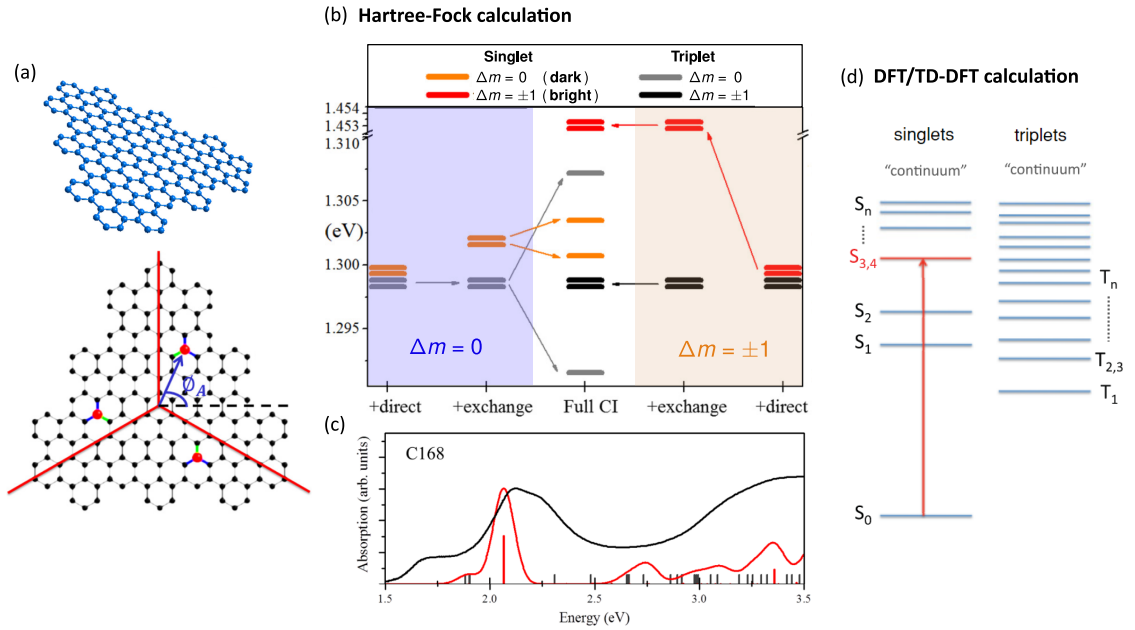

Figure 1.4: Theoretical calculations for a $C_{168}H_{42}$ GQD represented in (a). (b) Hartree-Fock calculations considering direct (electron-hole interaction), exchange (electron-electron interaction) or the full description. The left side (blue) focuses on $\Delta m = 0$ excitons, while the right side (orange) focuses on $\Delta m = \pm 1$ excitons. The middle column depicts all the levels. (c) Comparison of the absorption spectrum calculated (red) with the experimental data (black). Adapted from [35]. (d) Schematic representation of the singlet and triplet states calculated using TD-DFT. The red arrow indicates bright transitions. From [36].

However, both these models (tight-binding model and standing wave states) simplify the system to a single-particle description. Although they account well for the gap opening and is satisfactory for large GQDs (above 1000 carbon atoms) [29, 30], they lack in precision for the study of smaller GQDs [31]. This is due to the absence of many-body effects in the modelization. Indeed, the electron-electron or electron-hole interactions are for instance not negligible for small GQDs (which are subject to stronger confinement) [32, 33]. These interactions can be computed using Hartree-Fock methods or configuration interaction methods [34, 31], and have managed to describe several experimental results. For instance, Ozfidan *et al.* reported the study of a $C_{168}H_{42}$ GQD represented in Figure 1.4(a) [35]. They underlined the effect of the various interactions on the splitting between the various states, in particular the direct Coulomb interaction, describing the electron-hole interaction, and the exchange interaction, describing the electron-electron interaction, as shown in Figure 1.4(b). The selection rule on the total angular momentum m results from the symmetry of the GQD (the symmetry axes are shown in Figure 1.4(a)). In the end, they showed, as plotted in the center column of Figure 1.4(b), that there exists two low-lying dark singlet states (in orange) and two higher bright singlet states which are degenerated (in red) when considering a full description of the system. A good agreement with the experimental absorption curve can be appreciated in Figure 1.4(c).

Density functional theory (DFT) calculations come as an alternative to the Hartree-Fock method. The DFT method naturally takes into account many-body effects (such as the electron-hole interaction) as the various transitions are computed [37, 36, 38]. DFT and TD-DFT (time-dependent DFT) calculations have satisfyingly reproduced experimental observations[3] [39, 40]. For instance, the schematic energy levels calculated for the same $C_{168}H_{42}$ GQD using DFT are depicted in Figure 1.4(d), as reported in [36][4]. The results are consistent with the calculations performed using Hartree-Fock methods, with for instance two low-lying dark singlet states (S_0 and S_1) and two higher degenerated bright singlet states (S_3 and S_4).

A few reports have used many-body perturbation theory and the Bethe-Salpeter equation to compute the photo-excited states of GQDs [32], as it was already performed for graphene nanoribbons [41, 42]. Usually used for semiconductors, this method is less frequently used for GQDs (*i.e.* finite-sized objects), for which TD-DFT proves to be more convenient to use [36]. However, using TD-DFT to compute large GQDs comes with a computational cost, scaling as a power-law with the size of the GQD.

1.1.3 Influence of the geometry on the electronic properties of GQDs

As it was already mentioned in a previous paragraph, the theoretical description revealed the strong effect of the geometry on the electronic properties of the GQD. As the size of the GQD decreases, the confinement of the delocalized charge carriers increases, yielding a consequent increase of energy gap, as shown for the case of hexagonal GQDs in Figure 1.5(a). However, various geometric characteristics other than the size of the GQD may also influence the electronic properties. As predicted theoretically [26] and observed experimentally [43], one may encounter difficulties in describing the properties of the GQD without a precise knowledge of its edges. As shown in Figure 1.5(b) for the case of triangular GQDs of 168 carbon atoms, the edges directly impact the energy of the eigenstates of the GQD calculated using tight-binding, in particular with the appearance of zero-energy levels in the spectrum. Moreover, we can envision changing the hydrogen terminating the edges of the GQD with other atoms (referred as *functionalization*). Functionalizing the edges of GQDs may also be a way of tuning the properties of GQDs. As demonstrated for example by Cocchi *et al.* [34], the energy levels are predicted to globally shift with the addition of halogen atoms at the edges of GQDs, as shown in Figure 1.5(c) for a particular GQD.

More fundamentally, modifying the symmetry has also been predicted to strongly influence the properties of GQDs, in particular in terms of selection rules for the various transitions [44]. This aspect will be detailed later in this manuscript as it was a subject of discussion during my thesis.

Since one may envision infinite ways of confining the electrons for graphene quantum dots, there results in equally-infinite associated electronic properties. Considering

[3] A concrete example will be developed in Chapter 5.

[4] To be more precise, the DFT results from Schumacher were published before the Hartree-Fock from Ozfidan and co-workers.

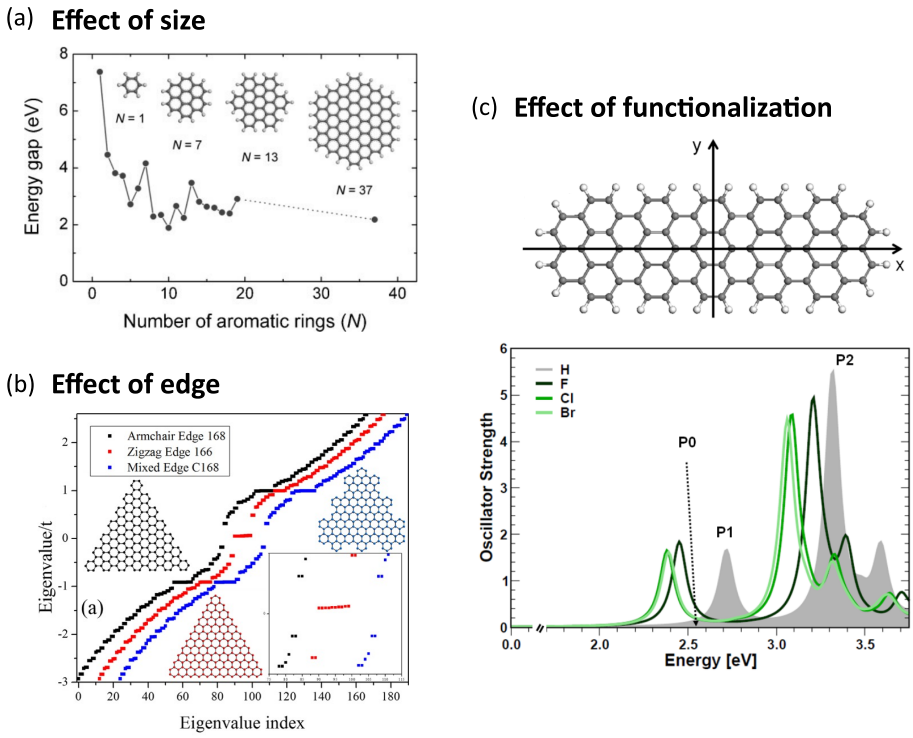

Figure 1.5: (a) Effect of size: evolution of the energy band gap with the number of aromatic cycles, calculated using DFT [46]. (b) Effect of edges: energy levels of triangular C_{168} for different edges, using tight-binding calculations [31]. Inset: zoom on the zero-energy levels, which appear only for the zig-zag edge GQD. (c) Effect of edge functionalization: absorption spectrum for various edge functionalization of the GQD depicted on top, calculated using TD-DFT [34]. P_0, P_1 and P_2 identify the three lowest singlet transitions.

that the studies mentioned up until now remain for a large part purely theoretical, an objective for physicists is to verify the precision of the predicted dependence of the electronic properties of a GQD on its geometry. Investigating synthesis routes to produce GQDs with rigorous geometry-control seems therefore essential to enable such a study. Moreover, this geometry-control has proven to be also essential for the use of GQDs for reproducible devices. Indeed, although general behaviors seem unaffected, specific characteristics may need a careful attention to the geometry of the GQD used. For example, in the case of Coulomb blockade devices, the observation of Coulomb diamonds in the conductance diagram is not conditioned by the geometry of the GQD. However, the position and size of the diamonds depend strongly on the edges of the GQD [45].

1.1.4 Synthesizing graphene quantum dots

Two main synthesis routes exist for nanographene systems, namely the top-down and bottom-up approaches [47, 48]. I succinctly describe these two methods in the case of the synthesis of graphene quantum dots in this section.

The first widely-used route to produce GQDs is the top-down approach. Schemati-

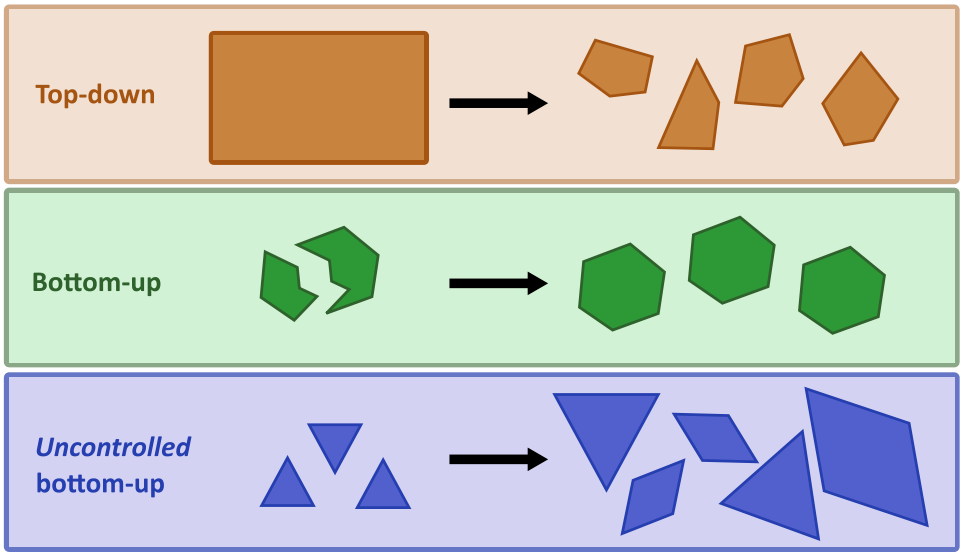

Figure 1.6: Schematic illustration comparing the general principle of the synthesis methods for GQDs. Top-down methods start from large graphene-based objects and cut them down to produce GQDs, with different shapes and sizes. Bottom-up synthesis starts from carefully-chosen precursors to control the geometry of the yielding GQD. In *uncontrolled* bottom-up, the synthesis yields different GQDs which can be selected *a posteriori*.

cally, this method consists in cutting down a graphene sheet (or other graphene-based object) into nanoscale pieces. These methods rely on few-step protocols, with a high yield for the synthesis. While first top-down approaches used lithography on graphene flakes to produce the desired object [9, 21], more recent methods prefer synthesis in solution using solvothermal or acid treatments. A seminal example of these top-down approaches was given by Pan and collaborators, who demonstrated the production of GQDs with an average size of 9.6 nm *via* the oxydation of graphene sheets followed by a hydrothermal treatment [49], as schematized in Figure 1.7(a). Other comparable methods followed [50, 51]. The major drawback of top-down approach is the low control of the geometry of the resulting objects, even after separation and purification steps. Since the electronic properties of a GQD is closely linked to its geometry, the top-down approach prevents any clear interpretation of the emission properties of the GQDs obtained *via* top-down synthesis. In fact, the emission properties are often dominated by defects states [52], and the dispersion in size induces a significant inohomogeneous broadening [50]. An example is given for the GQDs reported in [49], which exhibit a large size distribution (Fig. 1.7(b)), resulting in the broad structureless photoluminescence spectrum, which varies with the excitation wavelength (Fig.1.7(c)).

In contrast to top-down approaches, bottom-up methods, using protocols from organic synthesis, rely on the selection of procursors, which, after multiple steps of controlled reactions, yield the desired compound. Using a naive schematic picture, where the top-down approach starts from large graphenoid compounds and cuts them down into smaller objects, the bottom-up approach starts from smaller compounds which re-

act with each other to form the final object, as shown in Figure 1.6. In this approach, the choice of the precursors determines the structure of the final product *via* a specific synthesis route (a concrete example is described in Chapter 2). The geometry of the final product is therefore precisely controlled. This synthetic approach was first used by Klaus Müllen for the synthesis of large graphene quantum dots [53, 54, 55], and has since been perfected and extended to the synthesis of a large range of GQDs by his collaborators and students [56, 57, 58, 59] (examples are given in Figure 1.7(d)). This approach has enabled the controlled synthesis of a large variety of objects [60], both in geometry and in size. Given the large range of different specificities for each synthesis protocol developed, I can only redirect the reader to a more exhaustive description of the various synthesis protocols and technical details, in Ref. [57] for instance. The precise control of the structure of the final product enables the design of specific graphenoid systems, for example by creating non-planar structures [59, 40], or by changing the side-groups attached to the aromatic structure, essential for the solubility of the GQD [61, 62]. Moreover, precise functionalization of GQDs has also been demonstrated, for instance with the chlorination of the edges of GQDs [63] (the control over these various parameters is illustrated in Figures 1.7(e)-(h)). Overall, bottom-up synthesis plays a key role in the use of GQDs in nano-physics, as it delivers the precisely-designed building blocks for various possible applications [64].

We can note that a few teams proposed synthesis routes which we can categorize as *uncontrolled bottom-up* approaches, in which the synthesis relies on the combination of precursors to form larger structures, but with a large variety of possible resulting products (*e.g.* often a large range of possible sizes). For example, Wang and collaborators [65] reported on the synthesis of water-soluble GQDs *via* the fusion of pyrene molecules. Although this approach proposed new methods to functionalize the edges of GQDs, it only managed to produce a relatively broad distribution in size. More recently, new methods to synthesize nitrogen-doped GQDs using cheap and safe chemicals also managed to produce rapidly a large quantity of GQDs but with a lacking control on the size distribution of the synthesis batch [66]. We can still highlight a notable exception with the method proposed by Yuan and collaborators to produce triangular-shaped GQDs using solvothermal treatment [67]. They managed to obtain a high level of purity in terms of geometry in the final batch by relying on an efficient purification process.

The large variety of methods to produce GQDs reflects the range of possible applications for GQDs and their demand in terms of precision of the synthesis route. The top-down approach, although efficient for large scale production, produces non-uniform ensembles of GQDs. Concurrently, the constant proposition of new uncontrolled bottom-up synthesis routes testifies to the on-going interest to find ways to efficiently produce GQDs with roughly-controlled emission properties using cheap methods and soft experimental conditions. Nonetheless, in the case where specific properties are needed, one must rely on controlled synthesis routes using controlled bottom-up methods. The complexity of this approach comes with a cost of time and a comparably-lower overall product yield, but the precise control of the geometry of the produced GQD is a condition *sine qua non* to accurately understand its electronic properties and to ensure the reproducibility of the synthesis.

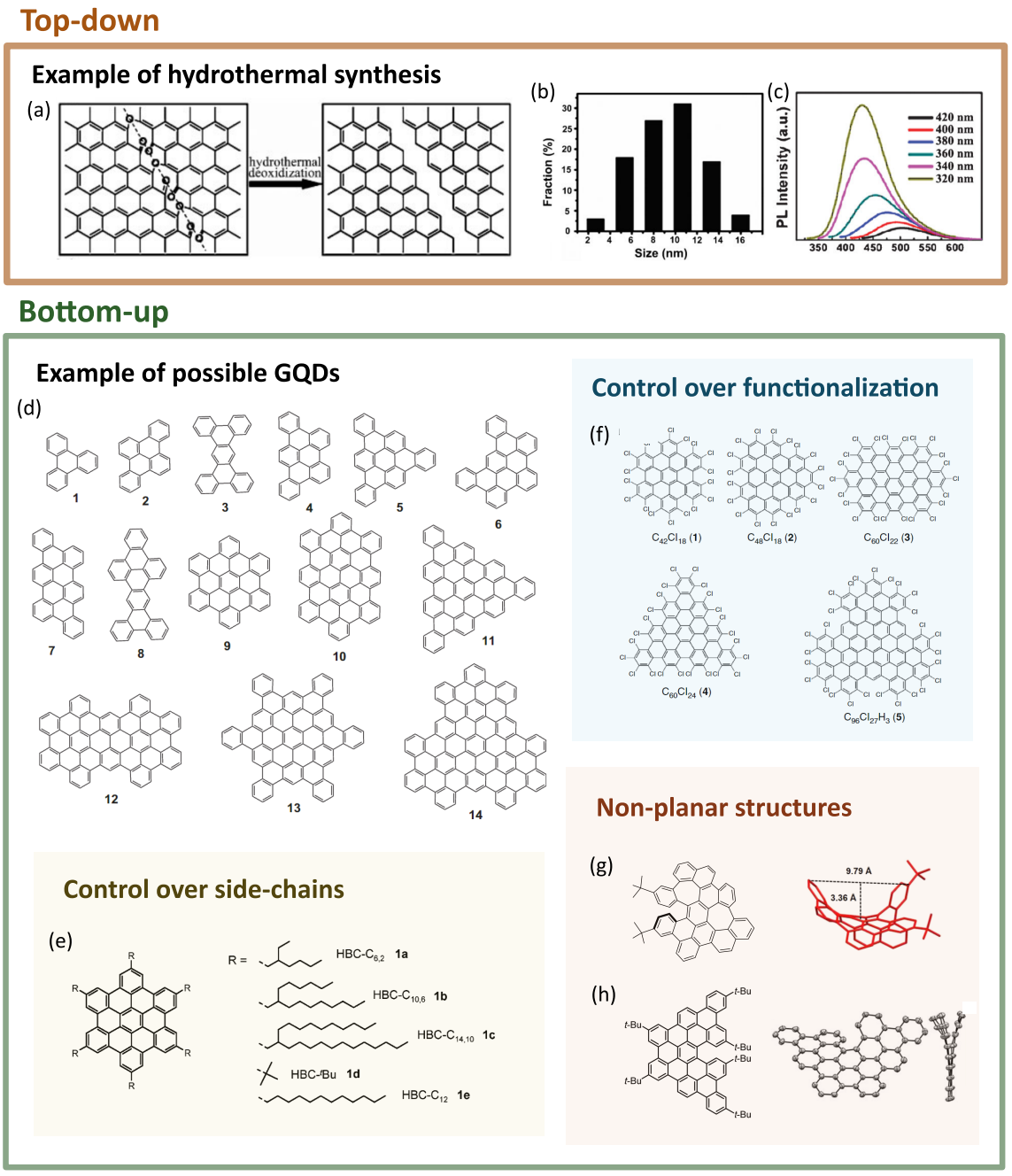

Figure 1.7: (a) Schematic representation of top-down synthesis of GQDs using hydrothermal cleaving of graphene sheets, along with (b) the resulting size distribution of the GQDs and (c) the photoluminescence spectra for different excitation wavelengths. Adapted from [49]. (d) Example of possible GQDs synthesized *via* bottom-up synthesis, taken from [60]. (e) Example of different possible side-chains on hexa-*peri*-hexabenzocoronenes (adapted from [62]). (f) Demonstration of precise edge-chlorination on a large range of GQDs, from [63]. (g)-(h) Example of non-planar GQDs, with (left) their chemical structure and (right) their 3D representation: (g) negatively-curved GQDs, from [59] and (h) fjord-edge GQDs, from [40].

1.2 Spectroscopy of single nano-objects

In order to study GQDs and, more specifically, the effect of geometry on the electronic properties, single-object spectroscopy comes as the method of choice. Before presenting the modern investigation routes and applications unlocked by this experimental method (which could benefit from GQDs), I briefly summarize basic concepts of molecular fluorescence.

1.2.1 Basics of fluorescence

Describing the energy levels

The energy levels of a molecular quantum emitters such as GQDs can be schematically represented by a Jablonski diagram. An example is shown in Figure 1.8. The bold horizontal lines correspond to the purely-electronic states of the GQD. Given the spin multiplicity of the energy levels, singlet and triplets are usually encountered in polycyclic aromatic hydrocarbons, with the ground electronic state corresponding to a singlet state (labelled S_0), followed by singlet (S_1,..., S_i) and triplet (T_1,..., T_i) excited states.

Additional levels arise from the coupling between the electronic states and the vibrations of the molecule. The wavefunction of the system will therefore depend on both the electronic and nuclear coordinates. Using the Born-Oppenheimer approximation, the electronic and nuclear coordinates can be decoupled. As a result, the wavefunctions can be factorized as the product of the electronic and vibrational wavefunction:

$$|S_0, n\rangle \simeq |S_0\rangle|n\rangle, \tag{1.7}$$

with n the quanta of vibrational excitation in the ground state for a given vibrational mode. This description yields the diagram given in Figure 1.8 (in the case where we consider coupling to only one mechanical mode of the system), with the equally-spaced horizontal lines above the purely-electronic levels corresponding to states where the electronic wavefunction remains the same, but with quanta of vibrational excitation in the system ($n \neq 0$). The energy split between the successive states is $\hbar\omega_{\text{vib}}$, the energy of a quantum of vibrational excitation.

Transitions between the levels

The system can be excited from its ground state to any higher excited state, for instance after the absorption of a photon (in the case of a photo-excitation), as represented by the blue vertical ascending arrow in Figure 1.8. The excited system can relax back to its ground state *via* various competing relaxation channels, either radiative or non-radiative.

The transition rate Γ between two states can be given by the Fermi golden rule, and is thus predicted to depend on the transition dipole moment. Let us consider ground and excited states $|S_0, n\rangle$ and $|S_1, n'\rangle$, with $|n\rangle$ and $|n'\rangle$ the vibrational component of the wavefunction in the electronic ground state S_0 and excited state S_1 respectively (n

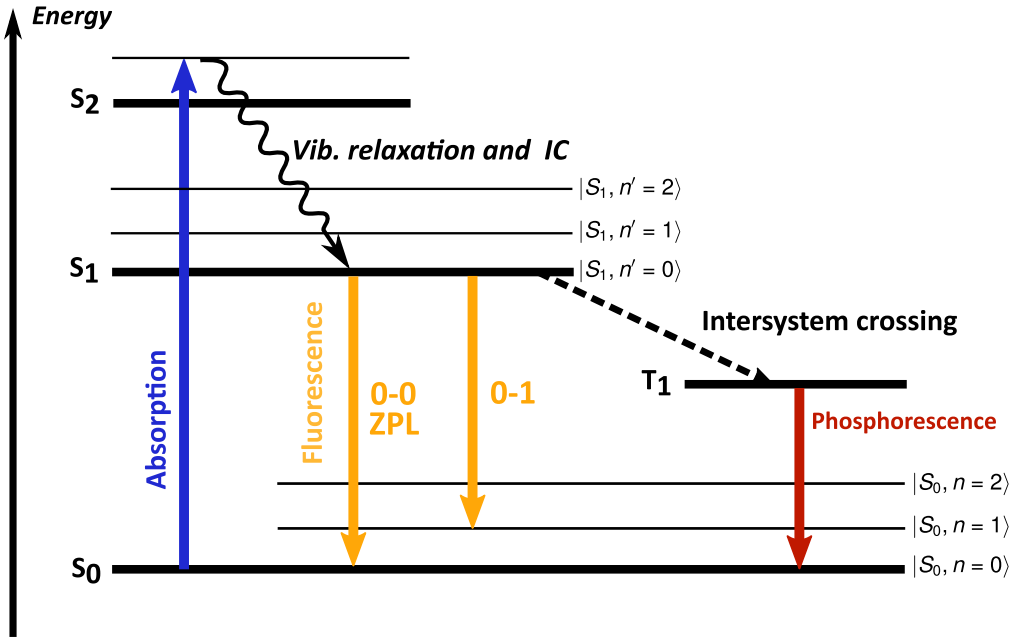

Figure 1.8: Schematic Jablonski diagram of the energy levels of a molecule. Bold horizontal lines correspond to purely-electronic states, additional horizontal lines correspond to vibrational states associated with the electronic state (considering only one mechanical mode. Vib. relaxation: vibrational relaxation. IC: internal conversion. n and n' are the quanta of vibrational excitation in the ground and excited states respectively.

and n' the quanta of vibrational excitation in the ground and excited states). In the Condon approximation (or Franck-Condon principle), the dipole operator $\hat{\mu}$ can be limited to the electronic component. In other words, the dependence of Γ can be separated as the product between an electronic and vibrational component [68]. The electronic component is the usual transition dipole moment, defined as $\mu = \langle S_1|\hat{\mu}|S_0\rangle$. Another physical quantity often introduced is the oscillator strength f which is proportional to μ^2 [69], and is thus also a measure of the transition probability. A vanishing oscillator strength indicates a dark transition (which is negligibly allowed).

The strength of the contribution of the vibrational levels is given by the Franck-Condon factor F, defined as:

$$F = |\langle n|n'\rangle|^2 \tag{1.8}$$

This factor corresponds to the overlap of the wavefunctions of the two vibrational states of the transition considered. In most cases, this overlap amplitude decreases drastically as the numbers n and n' increase. Using a harmonic well to model the potential along the vibration coordinate considered, it can be shown that F decreases exponentially relatively to n or n' [70]. Because of that, only the transitions between the first excited vibrational states (*i.e.* with low values of n and n') are generally considered and observed.

Not considered in this presentation is the transition passing by a triplet. Although forbidden in a dipolar approach, coupling between singlet and triplet states is weakly allowed through spin-orbit coupling. Transitions to triplet states (referred to as *intersystem crossing*, represented by a dashed arrow in Figure 1.8) result in interruptions of the

fluorescence emission, generally referred to as blinking (although radiative decay may be apreciated from the triplet state, commonly referred to as phosphorescence).

Given the existence of both radiative and non-radiative decay channels, the effectiveness of the fluorescence emission of a molecule is characterized by the fluorescence quantum yield:

$$\gamma = \frac{k_r}{k_r + k_{nr}}, \tag{1.9}$$

where k_r and k_{nr} are the radiative and non-radiative decay rates. Therefore, a value close to unity indicates that the system relaxes mainly through radiative decays, which is ideal for spectroscopic measurements. Blinking may also arise from a reversible photochemical transformation of the molecular structure [70]. An irreversible transformation results in bleaching, when the new molecular structure obtained after the permanent transformation is non-fluorescent. A known mechanism for photo-blinking and photo-bleaching is the photo-degradation of a dye molecule in the presence of molecular oxygen [71]. Molecular oxygen is inactive in its triplet ground state but may become reactive in its lowest excited singlet state and react with neighboring organic dyes. The excitation of the molecular oxygen from its triplet ground state to its singlet state is possible by energy transfer from the photo-excited triplet state of a neighboring organic molecule.

Spectroscopic measurements

The absorption spectrum is obtained by considering the transitions from the ground vibrational state of the ground electronic state (*i.e.* state $|S_0, n = 0\rangle$) to any higher excited state. Each transition leads to a peak in the absorption spectrum, with an intensity proportional to the Franck-Condon factor and to the dipole moment associated with the transition. Symmetrically, the emission spectrum is obtained considering the transitions from the ground vibrational state of the excited electronic state (*i.e.* state $|S_1, n' = 0\rangle$) to any vibrational states of the ground state[5]. For a majority of molecules, the vibrations in the ground state are comparable to those in the excited state, resulting in the emission and absorption spectra being symmetrical relatively to the $0-0$ line (*i.e.* a transition $|S_0, n = 0\rangle \longrightarrow |S_1, n' = 0\rangle$), referred to as mirror symmetry. The transitions are represented in Figure 1.8. An example of mirror symmetry between the absorption and fluorescence spectra is given in Figure 1.9(a), in the case of anthracene molecules in tetrahydrofuran. Generally, a small shift between the two spectra is observed, corresponding to the Stokes shift.

In fluorescence spectroscopy, we usually distinguish the purely-electronic transition from the other transitions. The $0-0$ transition occurs without the creation or annihilation of phonons. The line associated with the transition is thus usually referred to as the *zero-phonon line* (ZPL). The transitions $0-n'$ are accompanied with the creation or annihilation

[5]This is usually referred to as the Kasha rule, which predicts that, given the efficiency of vibrational relaxation (the time scale of non-radiative relaxation from excited vibrational states to the ground vibrational state is about 10^3 times shorter than the fluorescence lifetime), fluorescence is observed as radiative relaxation from the ground vibrational state of the excited electronic state.

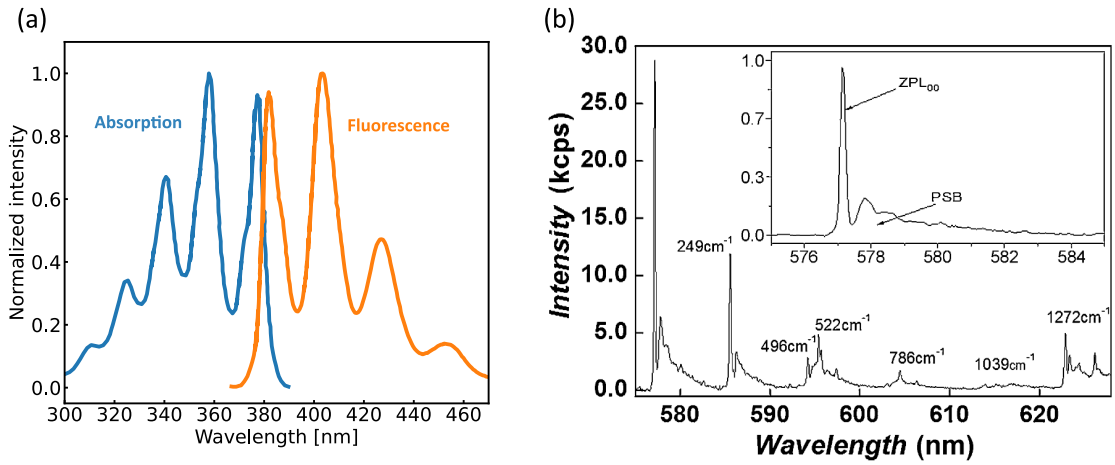

Figure 1.9: (a) Example of mirror symmetry between absorption and fluorescence spectra, here for anthracene in tetrahydrofuran. Adapted from [73]. (b) Example of fluorescence spectrum from single terrylene studied in *para*-dichlorobenzene, measured at 1.5 K. The inset gives a zoom on the ZPL and its red-shifted phonon side-band (PSB). From [72].

of one or more quanta of vibrational energy in intramolecular vibration modes. In addition to these transitions, if we consider the possible low-frequency vibrational modes of the environment (*e.g.* phonon modes of the matrix) coupled to the system, there results a broad continuous band which is red-shifted relatively to ZPL in the emission spectrum, referred to as *phonon sidebands* (PSB) or phonon wings. In Figure 1.9(b) an example of the fluorescence spectrum of a single terrylene molecule in *para*-dichlorobenzene is given, as reported in [72]. For this system, coupling to phonon modes of the matrix gives rise to the phonon sideband close to the ZPL, while the intramolecular vibrations result in the $0-1$ transitions responsible to the redshifted emission lines. The energies in wavenumber given above the vibronic lines correspond to the different vibrations of the terrylene molecule.

The optical absorption of the molecule can also be probed indirectly using fluorescence excitation, which consists in collecting the emission of photons at a certain wavelength while scanning the excitation wavelength. In contrast to the absorption spectrum, the fluorescence excitation spectrum is obtained as a result of three consecutive processes: absorption, vibrational relaxation[6], and fluorescence emission.

1.2.2 Emergence of single-molecule spectroscopy

A convenient way of studying the properties of fluorescent systems is to perform ensemble spectroscopic measurements, in solution for instance. Nonetheless, this approach prevents the measurement of properties specific to a given molecule and to its direct

[6]One may be more precise and identify two non-radiative processes: internal conversion, which is a transformation of electronic energy to vibrational energy through nuclear tunneling (the global energy is left unchanged by this process), and vibrational relaxation, which corresponds to a relaxation of the system without any change of electronic state.

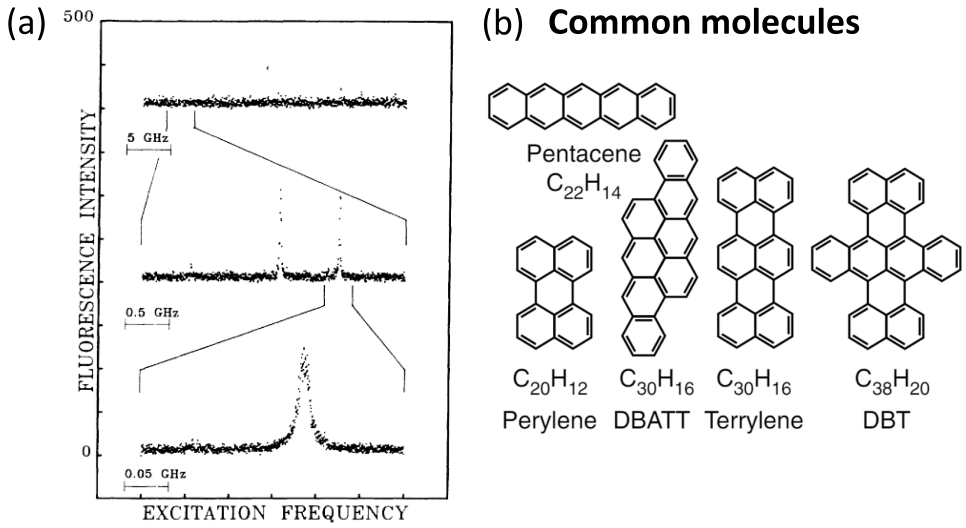

Figure 1.10: (a) Fluorescence spectra of pentacene in *p*-terphenyl at 1.8 K. The measured linewidth is 12 MHz. From [76]. (b) Example of fluorescent molecules commonly used for single-molecule devices. Adapted from [11].

environment, since all the physical quantities measured are averaged over a great number of objects. From the dispersion of properties, inherent to ensemble measurements, arises an inhomogeneous broadening for each measurement [74].

Studying a specific sub-population of molecules can be achieved using hole-burning techniques, where a spectral hole is induced upon irradiation of an ensemble of molecules with an intense narrow-band excitation. Another approach would be to collect signals from an isolated single molecule. Around the 1990s, the first experiments measuring the optical signal of single molecules were performed by Moerner and Kador using absorption [75], and Orrit and Bernard using excitation fluorescence [76]. In fact, the latter group reported a significant increase of signal-to-noise ratio relatively to the former group using fluorescence instead of absorption when studying the same system, namely pentacene molecules embedded in a *p*-terphenyl crystal. The reported spectroscopy was performed on cold systems (below 5 K), reaching high resolution and enabling the measurement of ultra-narrow emission lines, almost reaching the fundamental lifetime-limited width of transitions, as shown in Figure 1.10(a). The success of these experiments relied on both spatial and detection selectivity.

Since then, the experimental method for such measurements has been optimized, in particular when confocal microscopy proved to also enable single-molecule measurements [77], and has since become accessible to many research groups.

For single-molecule experiments, samples consist in a host-guest solid structure, where the molecules of interest (guests) are embedded in a selected matrix (host). Since the coupling of molecules may impact the electronic properties of the guest molecule (in particular *via* the coupling to phonon modes of the matrix), careful matrix selection is necessary, in particular for low-temperature measurements. Organic single crystals such as naphthalene and anthracene are common hosts for organic dye molecules. Shpol'skii

matrices (long linear alkane chains) have also proved to efficiently isolate molecules in an inert solid environment [78].

If the concentration is low enough, spatial selection is enough to isolate a single fluorescent molecule. Otherwise, individual molecules can be addressed spectrally by resonantly exciting the ZPL. Given the inhomogeneous broadening, even if a relatively large number of molecules is located in the scanned volume, only a few will respond resonantly to the excitation.

Single-molecule experiments can be performed at both room and low temperature. The advantage of cooling the system down to liquid-helium temperatures (around 4 K) resides mainly in the line-narrowing and increased intensity of the ZPL, which enables precise measurements of the energy of the ZPL and thus of any physical effects which may affect the ZPL.

In the end, the main requirements to achieve high resolution fluorescence spectroscopy are a system with a high fluorescence quantum yield (a few examples are given in Figure 1.10(b)), a rigid stable matrix to trap the molecules of interest in stable environments and an intense and narrow ZPL. Moreover, additional precautions have to be taken into account to suppress photo-blinking and photo-bleaching processes [71].

1.2.3 Modern explorations of single-object spectroscopy

Ever since the 1990s, the field of single-molecule microscopy has significantly expanded. Apart from applications in biophotonics, where tracking single fluorophores with high precision is the starting block of a large range of applications [79, 80], the precision of the measurement of fluorescent lines in low-temperature spectroscopy paved the way for the use of single molecules for applications which awaited such precision to be unlocked. In particular, once the electronic and optical properties of a fluorophore are understood, exploring the influence of the system to any external stimuli (*i.e.* any perturbations in its environment) provides plenty of possible levers to take advantage of the single-molecule precision.

By taking advantage of the high sensitivity of the electronic properties of molecules to perturbations in their direct environment, various research teams explored the possibility of using single molecules as sensors. Since perturbations will impact the fluorescence of the molecule, in particular its ZPL, one can use single-molecule spectroscopy to optically and without contact measure local characteristics, an asset to minimize system perturbations. For instance, the large Stark effect of specific systems has shown the possibility of locally measuring weak variations of electric fields [81]. In Figure 1.11(a), the effect of an external electric field on the ZPL frequency of multiple single dibenzoterrylene molecules embedded in 2,3-dibromonaphthalene is represented. The slope of the ZPL trace takes two possible values, corresponding to two orientations of the transition dipole moment in the crystalline structure relatively to the electric field orientation. Other examples, such as the optical measurement of local strain variation in the host matrix, have also been demonstrated [82].

A thorough understanding of the effect of local perturbations becomes an asset when one decides to control the transition frequency of the emitters. The most straightforward

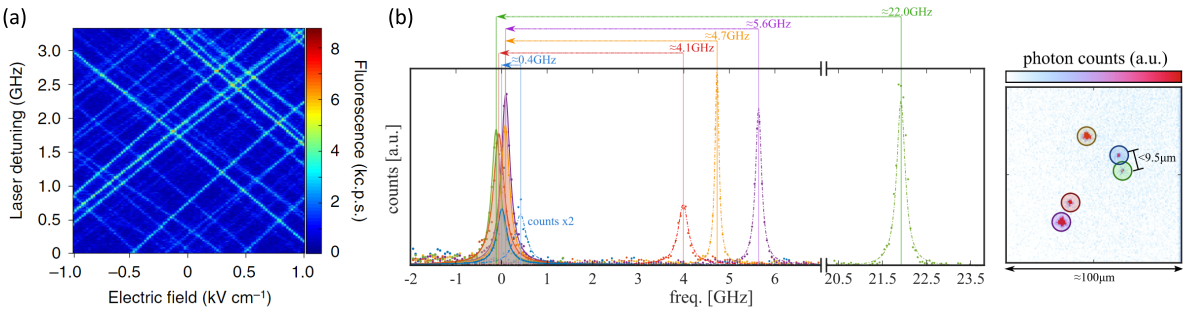

Figure 1.11: (a) Linear Stark shift measured for dibenzoterrylene single molecules in 2,3-dibromonaphthalene. The electric field is applied using gold electrodes on the sbustrate. From [81]. (b) Example of ZPL frequency tuning of five distinct dibenzoterrylene molecules using focused laser beam exposure. Dotted lines correspond to the ZPL before shifting, area-shaded solid lines correspond to the ZPL after shifting. Right: Fluorescence map with the excitation of all five molecules. From [85].

option is to use electric fields to tune the electronic levels of a molecule *via* Stark effect [83]. Recent advances on this topic include using 2D materials to modulate and tune ZPL on a wide range of frequency (400 GHz) [84]. The possibility of using light to tune the frequency of the ZPL has recently been demonstrated, which enables a spatial control of the electric field used to tune the ZPL [85]. As shown in Figure 1.11(b), by controlling the radiation dose of a focused laser beam, the ZPL of distinct neighboring molecules can be tuned to a same frequency.

Finally, placing the molecule inside a cavity may shape its emission spectrum. If the cavity mode is tuned to resonance with the ZPL frequency of the molecule, the system is converted into a two-level system, with the overall emission from the excited level concentrated into the ZPL with no emission *via* vibronic transitions [86]. This represents an essential step in the preparation of single molecules for various quantum applications.

The demonstration of controlled single-photon generation [90, 91] has revealed the potential of single molecules for applications needing the manipulation of single quantum objects. Various experiments have since explored the possiblity of manipulating photons generated by single molecules, in particular by characterizing and controlling the properties of the photon emission. Single-photon purity may be assessed using second-order correlation measurement (described in the next chapter), with an anti-bunching signature expected for single-photon sources, as shown for example in Figure 1.12(a). Interference between photons following a Hong-Ou-Mandel (HOM) configuration, a hallmark experiment of quantum optics, provides a measure of the indistinguishability of photons emitted from a molecule, and has been demonstrated for various systems [92, 93]. Single-photon interference has also been demonstrated in the case of two remote molecules by Lettow *et al.* [88]. Using the setup represented in Figure 1.12(b), they followed the interference visibility as they changed the frequency detuning between two remote molecules using Stark shifts. In the case of two molecules in resonance, they observed a clear signature of HOM effect. More recently, indistinguishability has been demonstrated in the case of a triggered source, indispensable for logic applications [94].

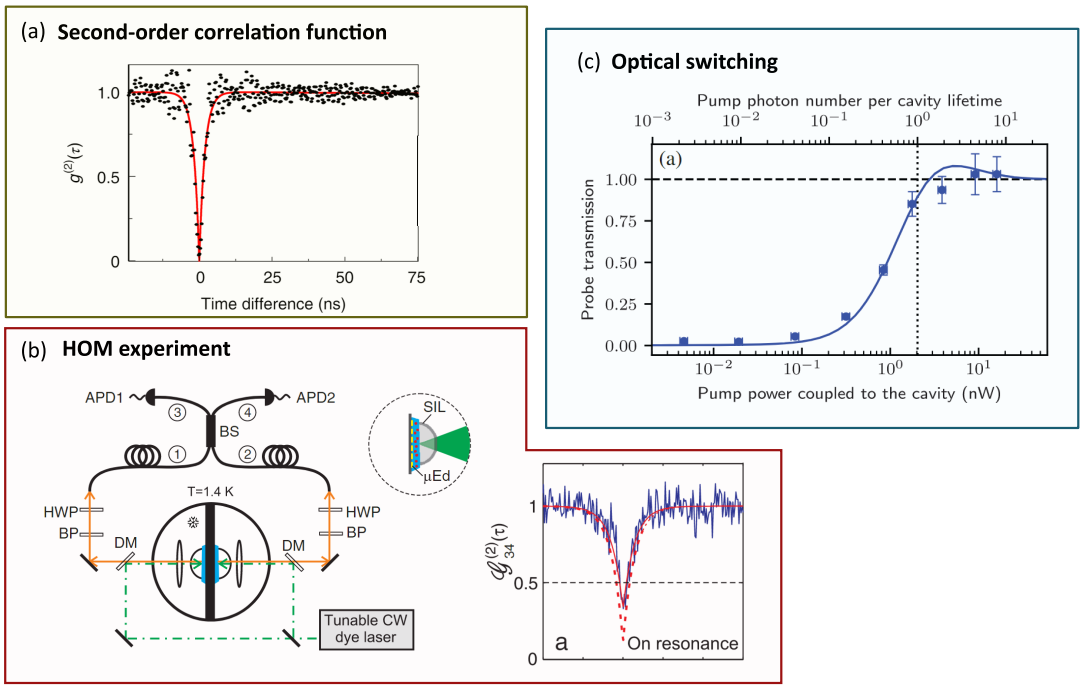

Figure 1.12: (a) Example of second-order correlation function measurement for a dibenzoterrylene molecule in anthracene. Adapted from [87] (b) Left: Schematic of the setup used to perform HOM experiments, with sample of dibenzanthanthrene (DBATT) embedded in *n*-tetradecane. HWP: half-wave plate; BP: bandpass filter; BS: beam splitter; DM: dichroic mirror; APD: avalanche photodiode; SIL: solid-immersion lens; μEd: gold microelectrodes. Right: Intensity cross correlation function of the output of the BS when the two emitters are tuned in resonance. Red lines are fitting curves. From [88]. (c) Transmission of the probe beam as a function of the pump beam power. Both beams are focused on a dibenzoterrylene molecule embedded in anthracene and placed in a Fabry-Pérot cavity. Adapted from [89].

Bell's inequality violation experiments have also been demonstrated with photons generated by single molecules [95], confirming the relevance of single molecules as potential building blocks for quantum technologies.

In the same context, nonlinear manipulation of photons has also emerged as a field of exploration [96]. Recent reports aim at using single molecules as optical transistors or for optical switching, in which a single molecule may act on an optical signal, controlled by a gating beam [97, 98]. Recently, it was reported that strong coupling between a single molecule and a microcavity leads to a high-efficiency of nonlinear processes [89]. In Figure 1.12(c), the intensity of the probe beam transmission is plotted for different pump beam powers (both beams are focused on dibenzoterrylene molecule embedded in anthracene in a Fabry-Pérot resonator). With only one photon per cavity lifetime, the probe beam transmission is turned on, while it is otherwise blocked by the molecule.

The possible applications envisioned for single molecules mentioned in the previous paragraph require the integration of the molecules in nanostructures. The possibility to interface single molecules and photonic structures or circuits has thus attracted the attention of various researchers. As a first approach, shaping the environment of a single molecule may enable a control of its emission properties, enhancing or directing the emission for example. By using metallic antennas such as gold nanoparticles [99], nanorods [101] or other shaped antennas, such as bowtie structures [102], the emission of a single molecule can be significantly enhanced (due to an increased excitation efficiency and an advantageous modification of the radiative and non-radiative decay rates [101]), and may lead for example to low-noise generation of single photons as demonstrated in [103]. As shown in Figure 1.13(a), as a gold nanoparticle is moved closer to a single molecule, the intensity of the fluorescence signal significantly increases, which can be linked to the simultaneous decrease of the fluorescence lifetime of the emitter.

Interaction between light and matter can also be enhanced by integrating molecules in nanofabricated structures. By using electron-beam lithography on polymers, Ciancico *et al.* proposed a controlled method to pattern the environment of a single molecular emitter [87], demonstrating for instance an increase of the fluorescence signal in the case of a polymer bullseye nanoantenna [100]. In Figure 1.13(b), room-temperature results show an enhancement of the emission by a factor 2, resulting from an increase of the collection efficiency. With the aim of integrating single molecules in circuits, an essential step towards applications in quantum technologies, coupling to waveguides has long been investigated [104]. Recently, various groups reported efficient coupling of photons generated by single molecules to waveguides [105, 106]. A schematic representation of a silicon nitride (SiN) waveguide is given in Figure 1.13(c). Single molecules placed at the center of the waveguide can be excited *via* the grating couplers on either side of the waveguide. Fluorescence from the single molecules is observed from their initial position, but also from the grating couplers, as observed in a camera shot given at the bottom of the figure. Improving the coupling between photonic structures and molecules has led to the exploration of ring resonators [107] and plasmonic-dielectric waveguides [108]. Next steps now consist in integrating these waveguides into circuits with low-loss propagation, with the objective of complexifying the existing structures and proposing quantum nanocircuits or other exploitable nanophotonic platforms [109].

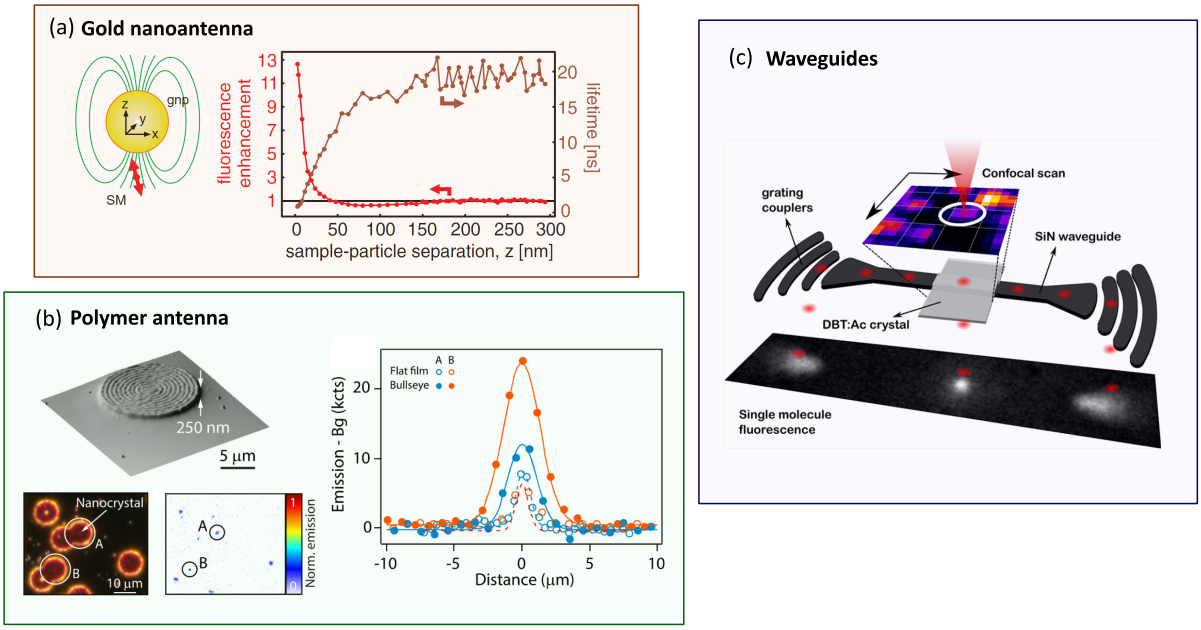

Figure 1.13: (a) (Left) Schematic representation of the gold nanoparticle (gnp) with an adjacent single molecule (SM). (Right) Evolution of the fluorescence enhancement (ratio between signal detected with and without the gold nanoparticle) and of the fluroescence lifetime with the distance between the gold nanoparticle and the molecule. Adapted from [99] (b) Example of polymer bullseye antenna with a dibenzoterrylene molecule in anthracene nanocrystal at its center. (Top left) Atomic force microscopy (AFM) image. (Bottom left) Dark-field reflection image and fluorescence map. (Right) Comparison of room-temperature fluorescence for two molecules before and after the integration within a bullseye antenna. From [100]. (c) Schematic representation of a silicon nitride (SiN) waveguide with a grating coupler at each end of the waveguide. Dibenzoterrylene molecules in anthracene (DBT:Ac) are localized at the center of the waveguide, and can be monitored using confocal raster scans (top). (Bottom) Camera image of the fluorescence signal emitted when excited: fluorescence is observed from the molecule and from the grating couplers. Adapted from [89].

An exhaustive review has recently been published by Toninelli *et al.* [11] which summarizes the advances in the field of applications of single-object spectroscopy towards quantum applications. Other reviews, such as [110], propose a more global overview of the field of single-molecule spectroscopy, including non-fluorescent methods which are not discussed here since not linked to the study of this thesis. Moreover, I have not here mentioned the large range of works which are focused not on device fabrication but on more fundamental characterization of the photophysics of single molecules [111, 112, 71, 113], or on the exploration of new guest-host systems [72, 114]. Indeed, although a plethora of applications can be envisioned, the studies mentioned up until now are often limited to the same systems, as highlighted in [11], namely the organic molecules given in Figure 1.10(b). While giving a succinct guideline for choosing adequate fluorophores, Toninelli *et al.* underline the necessity of exploring new possible systems, which may broaden the scope of possible candidates for the applications mentioned in this section.

1.3 The promises of graphene quantum dots

This section focuses on the description of the potential of graphene quantum dots and tries to unravel why the study of these objects have recently attracted increasing attention.

1.3.1 Tunability of the properties of GQDs

We saw that the properties of a graphene quantum dot are closely linked to its topology (size, edges, symmetry). An uncontrolled manipulation of these objects may thus result in a large dispersion of properties due to the high sensitivity to any dispersion in topology. However, put another way, if we manage to precisely understand the link between electronic properties and the geometry of the GQD, we may envision using this high tunablity to our advantage. Indeed, given the precise control over the symmetry of the object conferred by bottom-up synthesis, physicists contemplate a new playground for controlled engineering of electronic properties according to desired applications.

1.3.2 Simplifying the manipulation of GQDs

Common GQDs (*i.e.* fully-benzenoid, not functionalized) are stable and present low toxicity compared to other not fully carbon-based fluorophores (such as heavy-metal based quantum dots). Although a few applications or production methods rely on surface synthesis, GQDs are primarily processed using solutions. However, one major drawback is the intermolecular π-π interaction which forms insoluble GQD aggregates, especially for large GQDs. This leads to a modification of the optical properties of the solution and prevents the manipulation of single GQDs.

Adding bulky side-chains to the GQD is a common solution to prevent the interaction between GQDs [62, 115, 116]. Chemists thrive on this hurdle and have managed to constantly propose new synthesis routes to produce GQDs with varying side-chains in

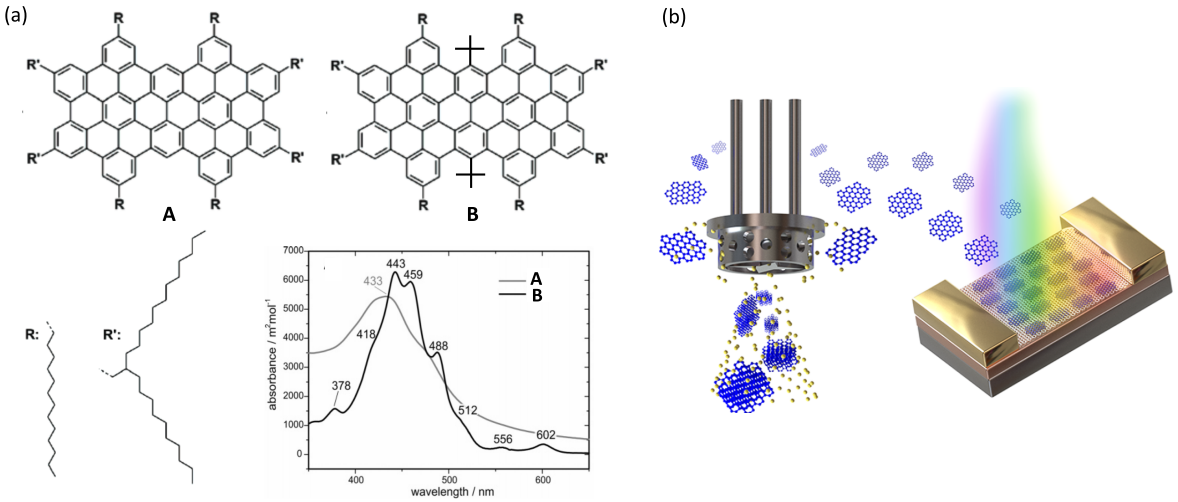

Figure 1.14: (a) (Top) Chemical structure of two GQDs with (**A**) or without (**B**) *tert*-butyl groups (highlighted in red). (Bottom) Comparison between the absorption spectrum of **A** and **B** in THF. Adapted from [117]. (b) Schematic representation of the high-shear mixing exfoliation of GQD aggregates into monomers, which can be deposited on graphene to form a graphene-GQD van der Waals heterostructure. From [118].

order to reach the objective of single-GQD dispersion in solution. The elaboration of non-planar GQDs has also demonstrated a net decrease in the tendency of forming aggregates [59, 40]. As an example, in Figure 1.14(a) I show the effect of the addition of two *tert*-butyl groups on GQD **A**, yielding GQD **B**. A clear difference can be observed in the absorption spectrum and can be explained by the slight distortion of the GQD plane as the additional bulky groups are added. The aggregation is suppressed for GQD **B**, and we recover more-resolved transitions in the absorption spectrum [117].

Recently, Z. Liu *et al.* reported on a method to obtain solution-processable graphene quantum dots [118]. Instead of relying on aliphatic side-chains to enhance the solubility of the GQD, which may induce small perturbations in the electronic properties of the GQD, they used high-shear mixing exfoliation to break up GQD aggregates into GQD monomers in solution, as schematized in Figure 1.14(b). By choosing N-Methyl-2-pyrrolidone (NMP) as solvent, the isolated GQD monomers are stabilized in suspension. The protocol reported in their article thus uses this method to propose simple fabrication of van der Waals heterostructures, depositing GQDs on graphene monolayer.

The progress made in GQD processability represents a great asset for both the use of GQDs in solution and its integration in devices. However, further efforts still need to be done, in particular for the manipulation of GQDs at the single-object level, which is a subject I have tackled during my thesis.

1.3.3 Ensemble applications of GQDs

Although single-object manipulation seems like the intuitive way of studying and exploiting the potential of graphene quantum dots, certain applications are not conditioned by

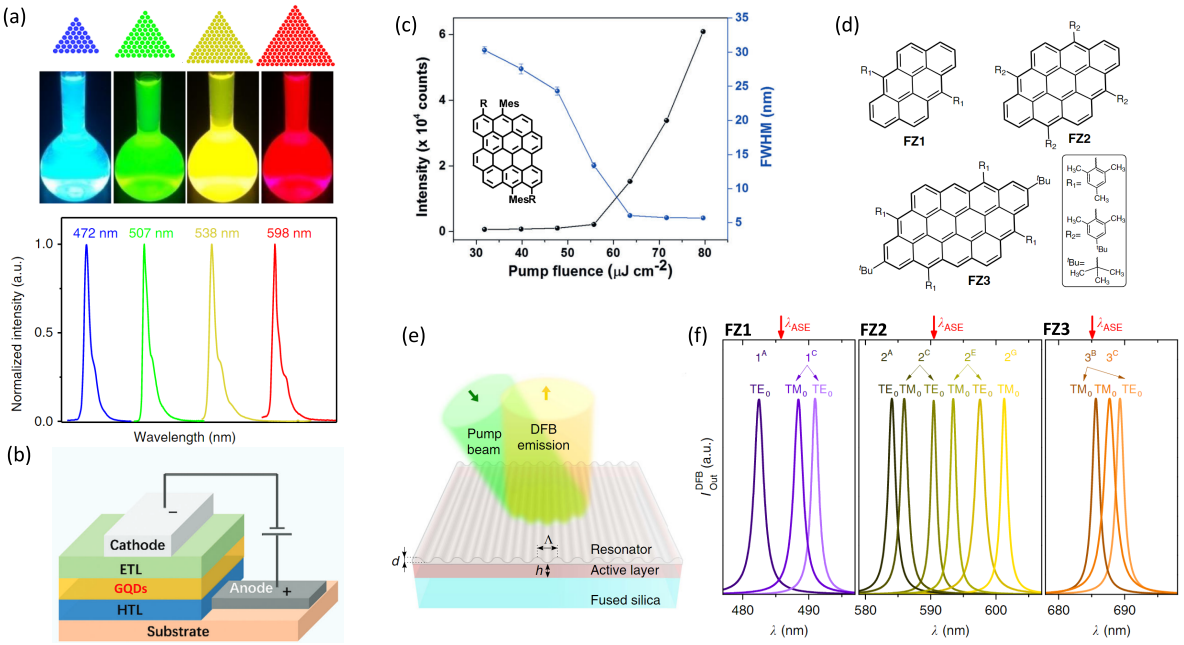

Figure 1.15: (a) (Top) Schematic representation of the GQD structure, and (middle) GQD in ethanol under UV light (415 nm), with (bottom) the corresponding photoluminescence spectra. From [67] (b) Simplified device structure of electroluminescent LEDs. Adapted from [119]. (c) Amplified spontaneous emission (ASE) signature of DBOV (represented in inset, R=$C_{12}H_{25}$) in polystyrene excited with 435 m laser, with the evolution of photoluminescence intensity (black curve) and full width at half-maximum (FWHM) (blue curve) for different excitation fluences. From [58]. (d) Chemical structure of zigzag-edged GQDs used for lasing applications. (e) Architecture of the distributed feedback laser (DFB) used with GQDs. (f) Spectra of DFB lasers based on GQD-doped polystyrene active layers. Each panel corresponds to a different GQD respresented in (d). Spectra in a same panel correspond to devices with different geometrical parameters (h thickness of active layer, Λ spatial period of the resonator). The red arrow indicates the maximum of the ASE for each GQD. Adapted from [116].

a precise control of their geometry. The applications in bio-imaging and bio-sensing are for the most part unaffected by the absence of precise control over the geometry of the GQDs [120]. Nonetheless, a precise control of the geometry may lead to narrower spectral features in solution, as shown for instance with the triangular GQDs presented in Figure 1.15(a). The color of the fluorescence can be tuned according to the size of the GQD. Using these GQDs, Yuan *et al.* demonstrated the fabrication of efficient electroluminescent LEDs, by embedding GQDs in poly(*N*-vinyl carbazole) (PVK) deposited in the middle of a device as schematized in Figure 1.15(b) [67]. They measured state-of-the-art current efficiency for a GQD-based LED. Many different research teams have proposed GQDs for LED applications, as summarized in [119]

Various investigations have also been carried out for photovoltaic and photodetection applications [115, 121]. For instance, recent reports have demonstrated that coupling GQDs with a graphene layer can result in a high responsivity photodetector [118]. The efficient coupling between the GQD and the graphene layer, acting as the charge transporting channel, has been made possible thanks to efficient dispersion of GQDs in solution, as previously shown in Figure 1.14(b). Moreover, by changing the absorption wavelength of the GQD deposited, one may tune the color sensitivity of the detector [122].

Finally, GQDs have recently gained attention as a possible optical gain medium for lasing applications. Paternò *et al.* have reported, in the case of dibenzo[*hi,st*]ovalene (DBOV), the observation of amplified stimulated emission (ASE) with a relatively low power threshold [58]. Indeed, when embedded in polystyrene and excited using a 415 nm laser, the photoluminescence intensity drastically increases above a threshold, accompanied with line narrowing, as shown in Figure 1.15(c). Following these results, other GQDs have been tested, in particular zigzag-edged GQDs (as shown in Figure 1.15(d)), and have been implemented in a series of simple devices, such as the one represented in Figure 1.15(e), consisting of an active layer (GQDs embedded in polystyrene) and a top-layer polymer distributed-feedback resonator (a periodically-structured resonator). By changing the GQD and the geometrical parameters of the device (the height of the active layer h and the periodicity of the resonator Λ), Bonal and collaborators demonstrated the possibility to tune the lasing wavelength of the device [116], as shown in Figure 1.15(f), where each panel corresponds to a different GQD (and the different curves to different geometrical parameters). Other reports have since explored the possibility to target near-infrared wavelength by changing the topology or adding functional groups to GQDs [123, 124].

The full extent of GQD systems and possible applications cannot be exhaustively described here, but are documented in a large range of review articles [125, 48, 126, 127, 128, 129], which highlight the vitality of this research field.

1.3.4 Manipulating single GQDs and applications of nanographenes towards quantum devices

Using top-down methods, the possibility to directly etch circuits on a sheet of graphene has demonstrated various single GQD application such as single-electron transistors [130]. However, in these cases, the size and edges of the GQD are coarsely defined. The po-

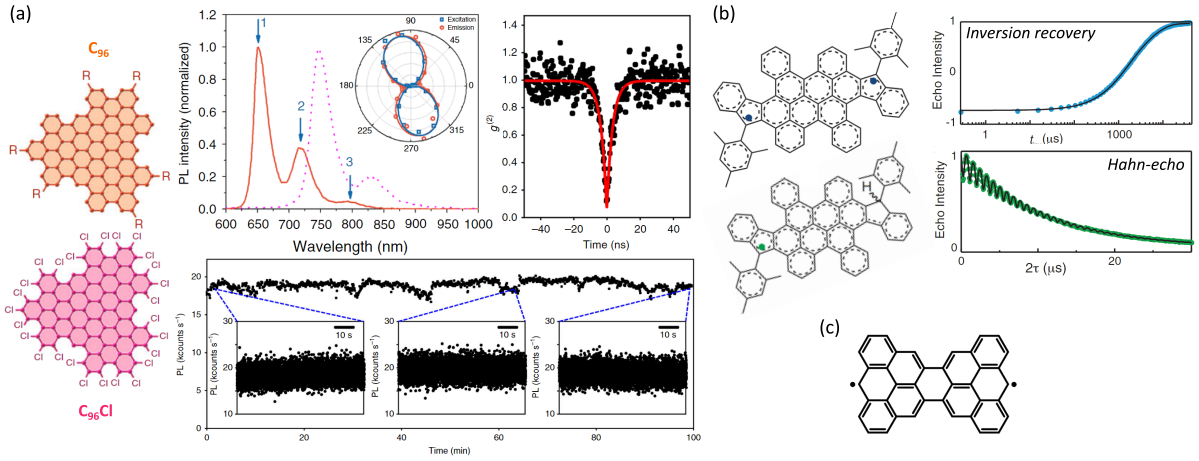

Figure 1.16: (a) (Left) Chemical structure of triangular C_{96} GQD with linear alkyl side-chains (R=$C_{12}H_{24}$) (in orange) or fully chlorinated $C_{96}Cl$ (in pink). (Center) Fluorescence spectrum for C_{96} GQD (solid line) and $C_{96}Cl$ (dotted line) in 1,2,4-trichlorobenzene, with in inset the polarization diagram in excitation (blue) and emission (red). (Right) Second-order correlation function from a single GQD. (Bottom) Photoluminescence time trace of a single GQD, with fluctuations due to setup instabilities. From [10]. (b) (Left) Chemical structure of GQDs with two (top) or one (bottom) unpaired electrons, studied by Lombardi *et al.* and (right) lifetime measurement of T_1 the spin-lattice time (using inversion recovery, in blue) and T_2 the spin coherence time (using Hahn-echo sequence, in green). Adapted from [132]. (c) Chemical structure of Clar's goblet, composed of 38 carbon atoms, which due to topological frustration leaves two unpaired electrons (represented by single dots). From [133].

tential of the geometry-control of graphene quantum dots (which becomes crucial when looking at single GQDs, where the effect of ponctual defects cannot be averaged out) has first been exhibited by theoreticians, who described the possibility to engineer curious properties by controlling the topology of the GQD [131].

A significant demonstration of this potential was given when Zhao *et al.* successfully demonstrated that GQDs may work as bright and stable single-photon sources at room temperature [10]. As shown in Figure 1.16(a), for a triangular C_{96} GQD, the fluorescence is characterized by a spectrum centered around 640 nm and shows a strong anti-bunching signature. The time trace of the photoluminescence signal indicates a stable photon emission, essential for applications. These results bring us a step closer to using GQDs for all the possible applications mentioned in Section 1.2.3. The tunability of the emission properties is also demonstrated by comparing the effect of edge-chlorination on the C_{96} GQD, which redshifts the transitions. GQDs could then not only offer a wider range of possible single-molecule systems (as awaited by the community) but also open the way to other unexplored applications by engineering the GQD's topology.

For instance, Lombardi and co-workers have demonstrated that by engineering defects in GQDs (by introducing pentagonal rings), one can obtain open-shell radical GQDs (*i.e.* with unpaired π electrons) [132]. In ensemble measurements, they managed to con-

trol the spin population and performed coherence-time measurements using common spin resonance protocols, as shown in Figure 1.16(b), demonstrating a competitive coherence time for these GQDs. One can also use topologically-frustrated GQDs (without defects in the sp^2 structure) to form radicals [134, 135]. A recent example is the observation of an antiferromagnetic ground state for a GQD referred to as Clar's goblet, represented in Figure 1.16(c) [133]. These approaches reflect the growing interest for the study of open-shell radicals which have become candidates for optoelectronic [136, 137, 138] or for spintronic applications [139].

Conclusion

This chapter provides the general context in which I developed the experiments presented in this thesis. Starting from the definition of graphene quantum dots, we have seen that they can be considered as a 0D confinement of 2D graphene. The theoretical description of these objects in the case of precise geometries have revealed the great potential of GQDs in terms of property tunability. However, in order to experimentally benefit from these advantages, one must rely on a precise control of their fabrication. The advances in organic chemistry, in particular in the field of bottom-up methods, have enabled the required control over geometry and given access to a large range of different GQDs.

The study of fluorophores is generally limited to ensemble measurements, where the properties are averaged over a large number of objects. Single-molecule spectroscopy arose as a method of choice to study GQDs. Indeed, by studying them at the single-object level, one can easily distinguish the intrinsic properties of GQDs from extrinsic effects (*e.g.* perturbations from the environment). Single-molecule spectroscopy has given rise to a large field of applications, which exploit the precision enabled by the manipulation of single quantum objects, as shown with several examples given in this chapter. Limited to the same few molecular systems for most applications, this field may benefit from the high tunability of GQDs.

GQDs have indeed already led to a wide range of applications, some of which have been overviewed in this chapter. Among them, it has been shown that they can efficiently be used as stable single-photon sources at room temperature, which makes them potential candidates to be used for applications developed for single organic molecules. Other applications of GQDs include integrating them in optoelectronic devices [140], for which chemists continuously elaborate new synthesis routes to obtain GQDs with optimized properties.

The possibility to engineer specific electronic properties is an asset which explains the current growing interest for GQDs. The tunability of geometry enabled by bottom-synthesis opens the way towards reverse-engineering: how to promptly engineer a desired property onto a GQD by acting on its topology. However, reaching this ideal requires a better understanding of the property-geometry relationship in GQDs.

Although several teams have started to link geometrical effects to electronic properties [33], studies going in depth into the photophysics of GQDs and the influence of geometrical factors remain scarce [126]. Such studies must necessarily harness the skills of chemists, theoreticians and experimentalists in order to efficiently provide a comprehensive study of specific GQDs. To that end, I have focused in my thesis on the study of several systems and explored their properties and behaviors in different environments, working in close collaboration with chemists and theoreticians.

Chapter 2

Experimental methods and associated technical details

Contents

Introduction

In order to analyze the optical properties of GQDs, our group primarily employs spectroscopy methods using optical excitation. During my thesis, I mainly focused on two types of characterization methods: ensemble spectroscopy characterization in solution (for a simultaneous study of a large number of GQDs) and characterization at the single-object level (to probe each GQD individually in order to strip results from ensemble effects). I describe in this chapter the experimental methods used during my thesis.

After succinctly describing the bottom-up synthesis method of GQDs and their characterization methods in a first part, I develop the sample preparation protocol for both solution measurements and single-molecule experiments. I then present an overview of the spectroscopy methods used for ensemble measurements in solution in the third section of this chapter. Finally, in the fourth section, I present the single-molecular photoluminescence setup and the measurements that can be performed on it, at both room and low temperature.

2.1 Bottom-up synthesis of GQDs

The GQDs studied during my thesis were synthesized using bottom-up method in order to precisely control their geometry. The synthesis of the object and characterization of the synthesis batch were performed by Daniel Medina-Lopez, Dr. Julien Lavie and Dr. Stéphane Campidelli at CEA Saclay. I mention succinctly in this section the protocol and the characterization methods. Since I did not perform these experiments, I will not detail here the experimental conditions.

2.1.1 Chemical synthesis

Synthesis of triangular $C_{96}C_{12}$ GQD

The synthesis of triangular $C_{96}C_{12}$ GQD has previously been reported in Refs. [141, 10]. The synthesis route is given in Figure 2.1(a). We recall here the main steps of the synthesis. Precursors 1,3,4-triethynylbenzene (compound **1'**) and 3,4-bis(4-dodecylphenyl)-2,5-diphenylcyclopentadienone (**2'**) are introduced in a reactor and react in the presence of o-xylene following a Diels-Alder cycloaddition. After filtration and washing, dendrimer **3'** is obtained. The dendrimer (dispersed in dichloromethane, under Argon) is put in contact with $FeCl_3$ dissolved in nitromethane ($MeNO_2$) for oxidative cyclodehydrogenation. After a controlled reaction time, the solution is quenched with methanol and filtered, yielding the desired pure product. I redirect readers to reference [10] for more technical details on the protocol.

Synthesis of rod-shaped GQDs

The synthesis of rod-shaped GQDs is described with more details in reference [142]. I describe first the synthesis of C_{96}-tBu_8, with the corresponding synthesis route shown in

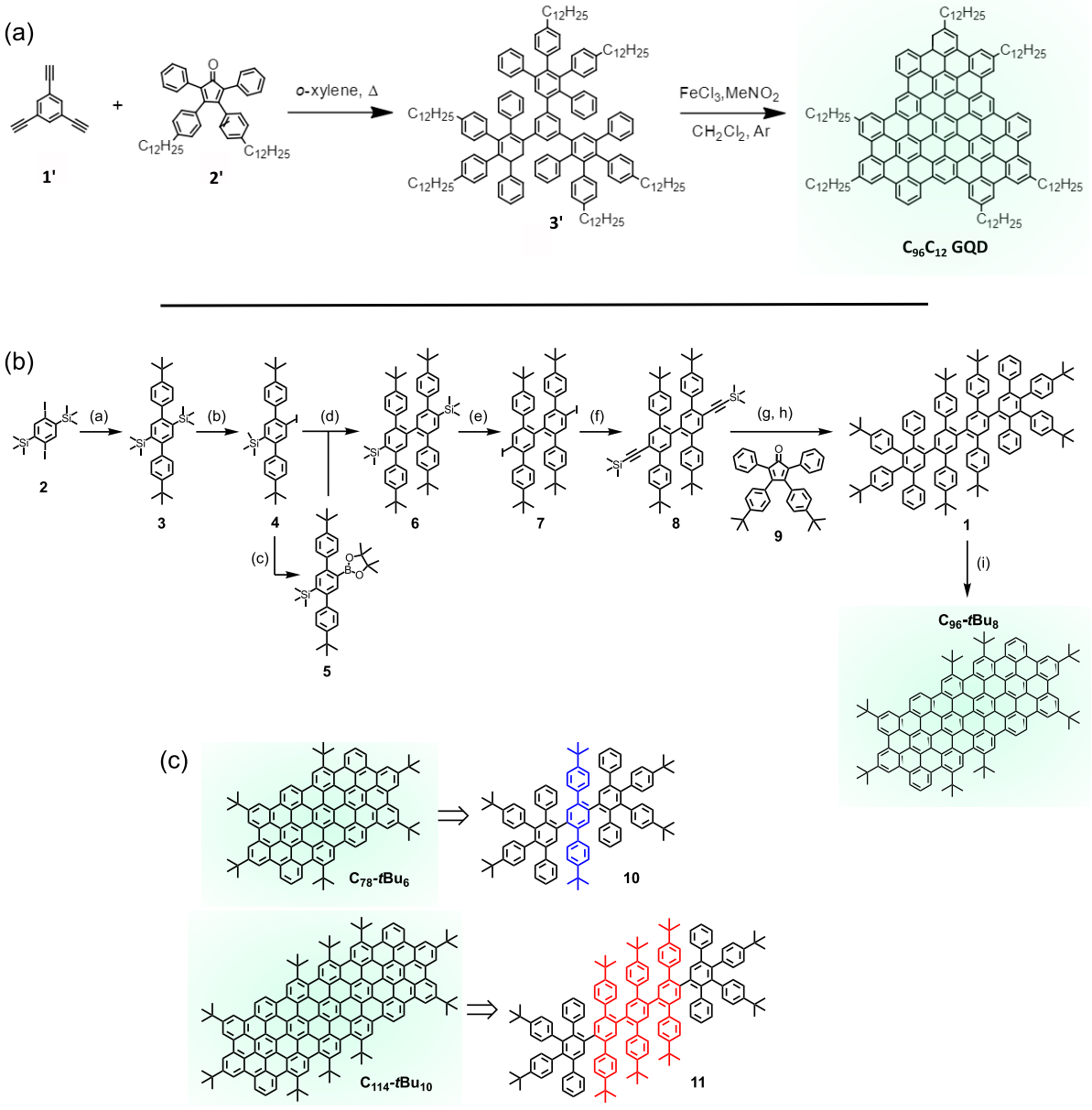

Figure 2.1: (a) Synthesis route of $C_{96}C_{12}$. Adapted from [10]. (b) Synthesis route of C_{96}-tBu_8. (c) C_{78}-tBu_6 and C_{114}-tBu_{10} and their respective dendrimers. Adapted from [142].

Figure 2.1(b).

Starting from 1,4-diiodo-2,5-bis(trimethylsilyl)benzene **2**, a Suzuki-Miyaura reaction with 4-*tert*-butylphenylboronic acid in the presence of $Pd(OAc)_2$ and SPhos leads to intermediate **3** (step *a*). One equivalent of iodine monochloride ICl is added in order to mono-iodinate **3**, yielding **4** (step *b*). **4** is then borylated leadig to **5** (step *c*). The Suzuki-Miyaura coupling between **4** and **5** leads to compound **6** (step *d*). In order to recover the alkyne precursor for the Diels-Alder reaction (similarly to compound **1'**), **6** is first iodinated with ICl (yielding **7**, step *e*), and coupled with ethynyltrimethylsilane to obtain **8** (step *f*). Deprotection (step *g*) with tetra-*n*-butylammonium fluoride (TBAF) yields the desired alkyne derivative (*i.e.* where the trimethylseline is replaced by a H), and reaction with **9** *via* Diels-Alder reaction, similarly to the first step in the previous synthesis route, leads to the desired dendrimer **1** (step *h*). Finally, the dendrimer is oxidized in the presence of $FeCl_3$ (step *i*) and yields the rod-shaped GQD.

Using retrosynthetic analysis, the dendrimers leading to the rod-shaped GQDs composed of 78 and 114 carbon atoms can be determined (dendrimers **10** and **11** respectively), as shown in Figure 2.1(c). **10** and **11** differ from **1** by the number of terphenyl units in their core. While **1** had a diterphenyl core, **10** contains only one unit (highlighted in blue in Fig.2.1(c)) and **11** containd three (highlighted in red). Therefore, in order to obtain **10**, compound **3** must be doubly-iodinated, leading to a compound similar to **7** in reactivity, but with only one terphenyl unit. The steps *f*, *g* and *h* lead then to **10**.

In order to obtain **11**, a compound similar to **7**, this time with three terphenyl unit, must be synthesized. This is possible by performing a Suzuki-Miyaura coupling similar to step *d*, between two equivalents of **5** with one equivalent of a doubly-iodinated **3** (the aforementioned molecule needed for **10**). Reactions analogous to steps *e* to *h* lead then to dendrimer **11**.

Additional experimental details for the synthesis of rod-shaped GQDs can be found in [142].

Purification of rod-shaped GQDs

Purification of rod-shaped GQDs is performed by ultra-centrifugation and by size-exclusion chromatography on Bio-beads S-X1 or S-X3 with tetrahydrofurane (THF) as eluent. The latter method relies on the size of each the components of a mixture in order to separate them: performed in a column filled with specific beads, the molecules of the mixture may interact with the beads as the eluent (the solvent carrying the mixture of molecules) flows in the column due to gravity. Since smaller molecules will interact more with the small pores of the beads, they will take more time to reach the bottom of the column than the larger molecules. The beads are thus carefully chosen in order to efficiently separate the GQDs from by-products.

2.1.2 Characterization of the synthesis batch: MALDI-TOF

In order to characterize the composition of the synthesis batch, multiple usual methods are used, such as NMR, thin-layer chromatography, Atmospheric Pressure Photo-

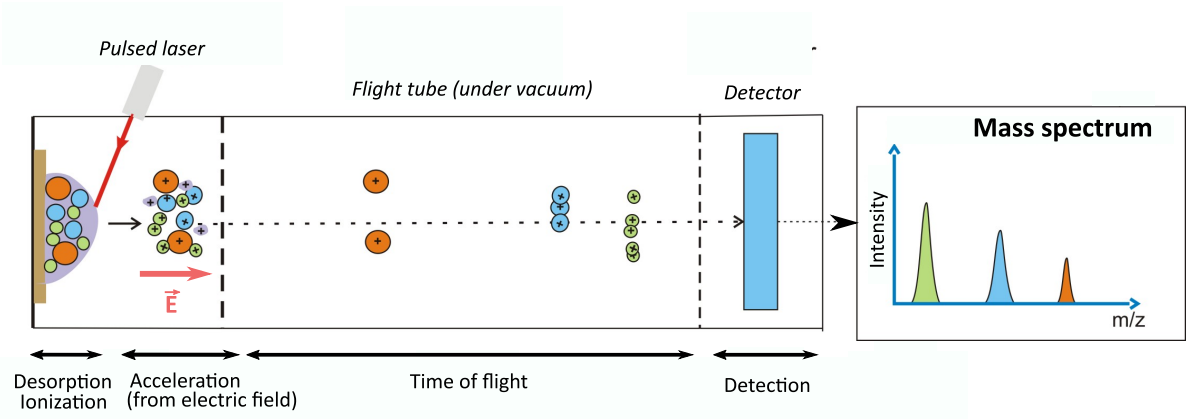

Figure 2.2: Principle of MALDI-TOF mass spectroscopy (adapted from https://pedagogie.ac-montpellier.fr).

Ionization mass spectroscopy. In this section, I will only describe rapidly the principle of MALDI-TOF measurements, since spectra resulting from this method will be exploited in the following chapters.

Mass spectroscopy is a category of characterization method used to map the mass of all the compounds in a mixture. It can therefore be used to determine the constituents of a synthesis batch, and in particular detect the presence of by-products.

Matrix-assisted laser desorption/ionization (MALDI) is a method used in mass spectrometry in order to ionize the analyzed compounds. As indicated by the name of the method, the analyzed mixture is embedded in a chosen matrix which will then be excited using a laser beam pulse. Desorption of excited matrix molecules then follows, and induces analyzed molecules to be carried in the gas phase. By charge transfer, the analyzed molecules are themselves ionized and accelerated by a fixed electric potential towards the mass spectrometer. We used Time Of Flight detection (MALDI-TOF), which uses the time taken for each ion to reach the detector to determine its mass. The time of flight is more specifically linked to the m/z ratio (mass over charge) of the ion, with the time of flight increasing with the m/z ratio, as depicted in Figure 2.2 (where larger spheres correspond to ions with greater m/z ratio). This method is now commonly-used in mass spectroscopy, and is convenient to analyze large chemical structures, for instance in microbiology for compound identification [143].

It is important to note that the relative intensity of the peaks in MALDI-TOF does not exactly reproduce the ratio between the different constituents of the analyzed mixture, since the efficiency of the ionization process, which is directly linked to the number of ions produced and thus to the intensity of the peaks, will vary for each constituent present in the mixture. Moreover, instead of observing only one peak (as naively indicated in Fig.2.2), the presence of one molecular species will result in a family of peaks in the experimental mass spectrum measured. These peaks result from the existence of different stable isotopes in nature for each element composing the molecular structure,

inducing a small dispersion of the mass. Since the relative abundance of stable isotopes for common elements is tabulated, it is possible to simulate the relative ratios of the isotopic peaks for each species given its chemical formula, and thus analyze the chemical composition of the sample.

In our case, MALDI-TOF measurements were performed on a Bruker Autoflex Speed or on a Bruker UltrafleXtreme, using DCTB matrix. Simulations of mass spectra are performed using Prot pi Mass spectrum simulator[1].

2.2 Sample preparation

2.2.1 Dispersion of GQDs/ solution preparation

The first step of analyzing GQDs is to disperse them in an adequate solvent. We mainly use 1,2,4-trichlorobenzene (TCB), due to its high efficiency for dispersing aromatic compounds [144].

Triangular $C_{96}C_{12}$ GQDs prove to be difficult to disperse. Simply adding TCB to grains of $C_{96}C_{12}$ yields a suspension of black microscopic grains. Additional dispersion methods are required. We first perform ultra-sonication (Elma, Elmasonic P) during 30 s (pulsed mode, 37 kHz frequency, power 100). We restrain ourselves from extending the ultra-sonication time since degradation of the solvent has been observed on longer timescales [145]. In certain cases, magnetic agitation of the solution was performed during 12 hours (with 400 rpm). The obtained solution shows a brown hue. Resulting stock solutions reach a target GQD concentration of 3×10^{-5} mol/L, by dispersing 0.5 mg of triangular $C_{96}C_{12}$ powder in 11.1 g of TCB, or 0.5 mg of rod-shaped $C_{96}t\mathrm{Bu}_8$ in 14.9 g of TCB[2].

Stock solutions are diluted for photoluminescence measurements and for single-object samples. Dilution ranges 10^1 to 10^5, and dilution by 10^2 is often chosen for photoluminescence in solution[3]. Solutions are prepared (except for the ultra-sonication step[4]) and stored under inert atmosphere (Ar) in glovebox between measurements. During storage, a precaution concerning light exposition has been taken by wrapping stored samples in aluminium foil[5].

Rod-shaped GQDs are on the other hand easily soluble in TCB. No ultra-sonication is required to disperse the powder.

2.2.2 Single-molecule samples

Single-molecule experiments require emitters to be fixed in a solid matrix. In our experiments, we use a polystyrene matrix (PS), purchased from Sigma-Aldrich (Ref. 331651).

[1] https://www.protpi.ch/calculator/MassSpecSimulator

[2] Given $d_{TCB} = 1.46\,\mathrm{g/mL}$, $M_{C_{96}C_{12}} = 2191.3\,\mathrm{g/mol}$ and $M_{C_{96}t\mathrm{Bu}_8} = 1630\,\mathrm{g/mol}$.

[3] The concentration is often estimated by performing optical absorption spectroscopy and comparing the absorbance value of the peaks associated with the GQD of interest.

[4] Solutions are sealed using parafilm before taken out of the glovebox.

[5] Effect of light exposition on the degradation of triangular $C_{96}C_{12}$ samples has been observed. This issue has not been thoroughly investigated during my thesis.

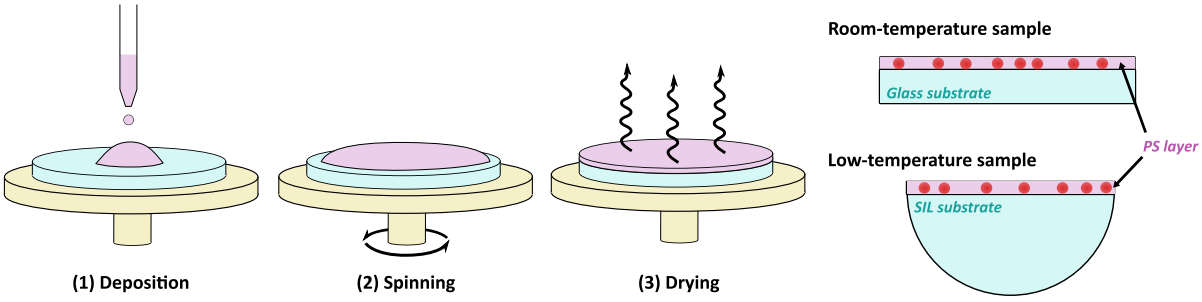

Figure 2.3: (Left) Illustration of the spin-coating procedure. (Right) Structure of the resulting single-molecule samples for room-temperature (top) and low-temperature (bottom) experiments.

The solid matrix is deposited on a glass coverslip substrate (Schott Nexterion) for room-temperature measurements, or on a half-ball solid-immersion lens (SIL) of lanthanum-doped glass (S-LAH79) with a diameter of 4 mm (Edmund Optics) for low-temperature measurements. I describe in this section the protocol followed for the preparation of a sample.

The solution deposited on the substrate results from the mixture of a solution containing GQDs in TCB (in a concentration low enough to observe single objects in the experiments) and a solution of PS in TCB. The solution of PS in TCB is prepared by adding beads of PS (as purchased from manufacturer) in TCB, yielding a concentration of 10 wt% (*i.e.* the mass of PS added in TCB represents 10% of the final weight of the solution). The solution is heated on a hot plate during 30 min at 75°C to favor the dissolution of PS beads. The GQD solution and the PS solution are added in equal proportion for the final solution, which has therefore a concentration of PS of 5 wt%.

Before deposition, each substrate is cleaned by oxygen-plasma treatment during 5 min, which eliminates any contamination on its surface. The substrate is then placed on the rotational platform of a spin-coater (Spin150, APT GmbH). The spin-coating process is schematized in Figure 2.3. After deposition of a drop of the final solution, the sample is spinned at 1000 rpm during 180 s, with 500 rpm/s acceleration, in order to obtain an homogeneous layer of solution on the surface of the substrate. The sample is then dried on a hot plate at 90°C during 1 h. During the drying step, the solvent evaporates and there remains only a layer of solid PS matrix, with GQDs embedded in it, as shown on the right of Figure 2.3.

For low-temperature experiments, the same procedure is performed, but with a SIL substrate. The rotational speed of the spin-coater is set at 2000 rpm. Inhomogeneities in the deposition layer could be observed in a few SIL samples after the preparation protocol described here. Further tests should be performed in order to optimize the deposition method on SIL (maybe extend the rotation time in order for the drying process to occur during the spinning of the platform).

Measurements of the thickness of the deposited layer have been performed. The results are described in Chapter 3.

2.3 Ensemble spectroscopy methods in solution

2.3.1 Absorption spectroscopy

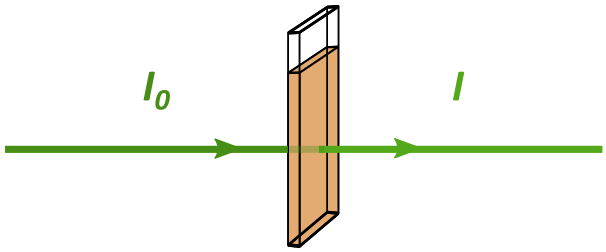

Figure 2.4: General definition of the absorbance.

Absorption spectroscopy gives a direct access to the energy levels of a system of interest. As mentioned in the previous chapter, a system (molecule, material) may absorb incident photons with energies corresponding to allowed transitions in its energy diagram. For a given sample, the absorption is quantified by comparing the intensity I_0 of an incident monochromatic light beam with the intensity I of the transmitted beam (*i.e.* after passing through the sample), as defined in Figure 2.4. We thus define the *absorbance*, or optical density, at a given wavelength as:

$$\mathcal{A} = -\log\left(\frac{I}{I_0}\right). \tag{2.1}$$

Theoretically, in the linear regime, for a solution with a single absorbing species, the absorbance can be directly linked to c the concentration of absorbing molecules, ℓ the length of the optical path in the solution and ϵ the molar absorption coefficient (or molar extinction coefficient), following the Beer-Lambert law:

$$\mathcal{A} = \epsilon \times \ell \times c \tag{2.2}$$

The molar absorption coefficient ϵ is a wavelength-dependent factor which describes the capacity of an absorbing species to absorb at a given wavelength. It can be linked to the oscillator strength of the energy transitions of the species [146]. If multiple absorbing species are present in solution, $\mathcal{A}$ can be expressed as the sum of the absorbance due to each species present. We generally refer to the measurement of $\mathcal{A}$ for a set of wavelengths as the absorption spectrum of a sample.

During my thesis, absorption spectrocopy in solution was performed using a commercial spectrometer (PerkinElmer Lambda 950). Cuvettes with 2 mm optical beam path are used (Hellma Analytics, Quartz Glass High performance cuvette). A schematic representation of the spectrometer is given in Figure 2.5. Two excitation sources are available, with two lamps covering a large range of wavelength (from near-UV to near IR). The selection in wavelength is then performed by an integrated monochromator. In this

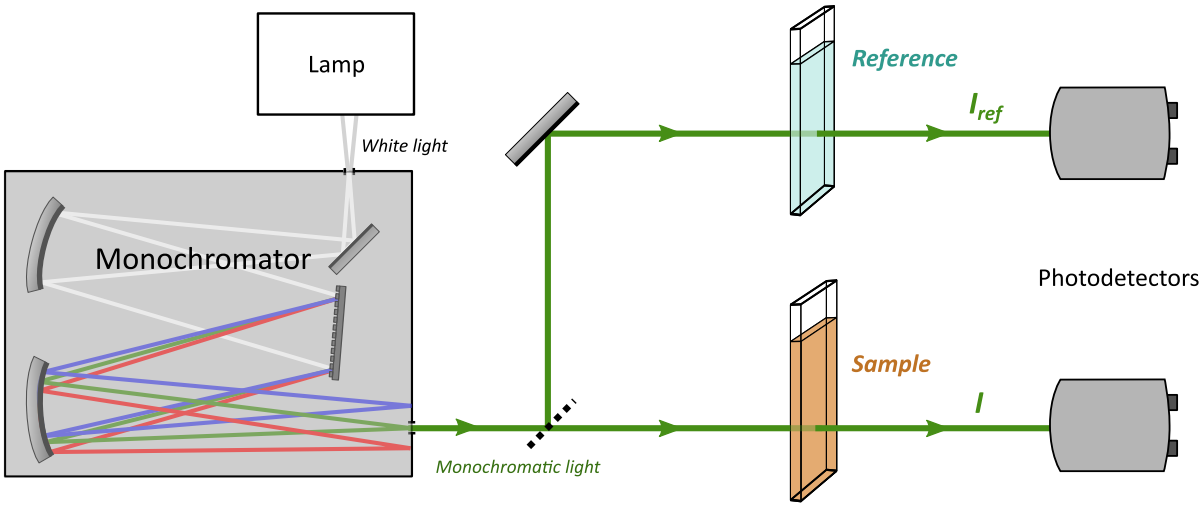

Figure 2.5: Principle of a double-beam optical absorption spectrometer.

spectrometer, the excitation beam is separated into two paths, which allows a simultaneous measurement of the transmitted intensity from the sample of interest I and from a reference sample I_{ref}. In our case, the reference sample is an indentical cuvette filled with solvent. Calculating direcly $-\log(I/I_{\text{ref}})$ eliminates the contribution of the cuvette and the solvent in the absorbance measured. We therefore have access directly to the absorbance only due to the composition of the sample solution.

2.3.2 Photoluminescence spectroscopy

Photoluminescence (PL) spectroscopy is a method focused on the spectral analysis of the luminescence of a system following a photo-excitation (light stimulation). After an off-resonance excitation (excitation at high energy relatively to the probed transitions), the system relaxes to lower-lying excited states via fast non-radiative transitions. The energy of the photons emitted by the system results from radiative transitions from states populated by the excitation process. Given Kasha's rule, the populated state is usually the lowest-lying excited singlet state. In constrast to absorption spectroscopy which probes the allowed transitions from the ground state of the system, PL spectroscopy probes the photons resulting from allowed transitions of the system as it relaxes from excited states *via* radiative channels, themselves in competition with non-radiative channels. These two methods do not therefore deliver the same informations on the studied system.

Photoluminescence measurements in solution were performed using a commercial spectrofluorometer (Horiba, FluoroMax+), with solution placed in cuvettes with 1 cm beam path. The general operation of the instrument is given in Figure 2.6. A xenon lamp is used for excitation, and the excitation wavelength λ_{exc} can be selected using a monochromator. The emission is collected in a path perpendicular to the excitation beam path and sent to a monochromator coupled with a photodetector. By scanning the emission wavelength λ_{em} at the output of the second monochromator, the PL spectrum of the solution can be constructed. The slit width of each monochromator can be chosen in order to

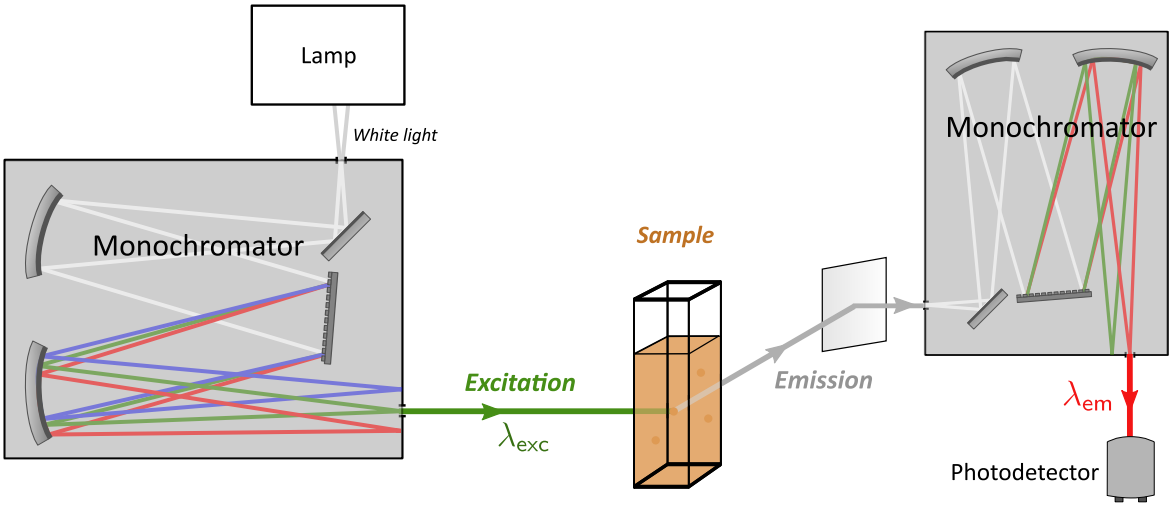

Figure 2.6: General principle of PL measurements in solution.

tune the spectral resolution, as well as the exposure time for each wavelength position during measurements. Corrections relative to the intensity fluctuations of the lamp and to the spectral response of the detector are automatically performed by the instrument.

Photoluminescence excitation spectroscopy (PLE)

As described in the previous paragraph, in photoluminescence spectroscopy, the excitation wavelength is usually fixed and the emission wavelength is scanned in order to measure the spectrum of the luminescence of the object. Complementarily, one can fix the emission wavelength and scan the excitation wavelength. This method is referred to as *photoluminescence excitation spectroscopy* (PLE). The PLE spectra are obtained by plotting the emission intensity collected at λ_{em} against the excitation wavelength λ_{exc}. Similarly to absorption spectroscopy, PLE spectroscopy investigates the response for various excitation wavelengths. However, while absorption spectroscopy simply probes the existence and the intensity of transitions at given energies, PLE spectroscopy investigates the succession of three mechanisms: the efficiency of the absorption at λ_{exc}, non-radiative relaxation to an excited state, from which follows an emission at λ_{em} (see Figure 2.7). In the case where the system relaxes efficiently (*i.e.* without any significant competition from transitions towards other excited states) *via* non-radiative relaxation towards the excited state from which the emission is probed, the resulting PLE spectrum would reproduce the absorption spectrum. On the other hand, PLE spectra can strongly differ from absorption spectra if absorbing species in a solution do not result in any fluorescence.

PLE spectroscopy is performed with the same instrument as PL spectra, as schematized in Figure 2.6. This time, the first monochromator scans the excitation wavelength while the second one is fixed at a chosen λ_{em}.

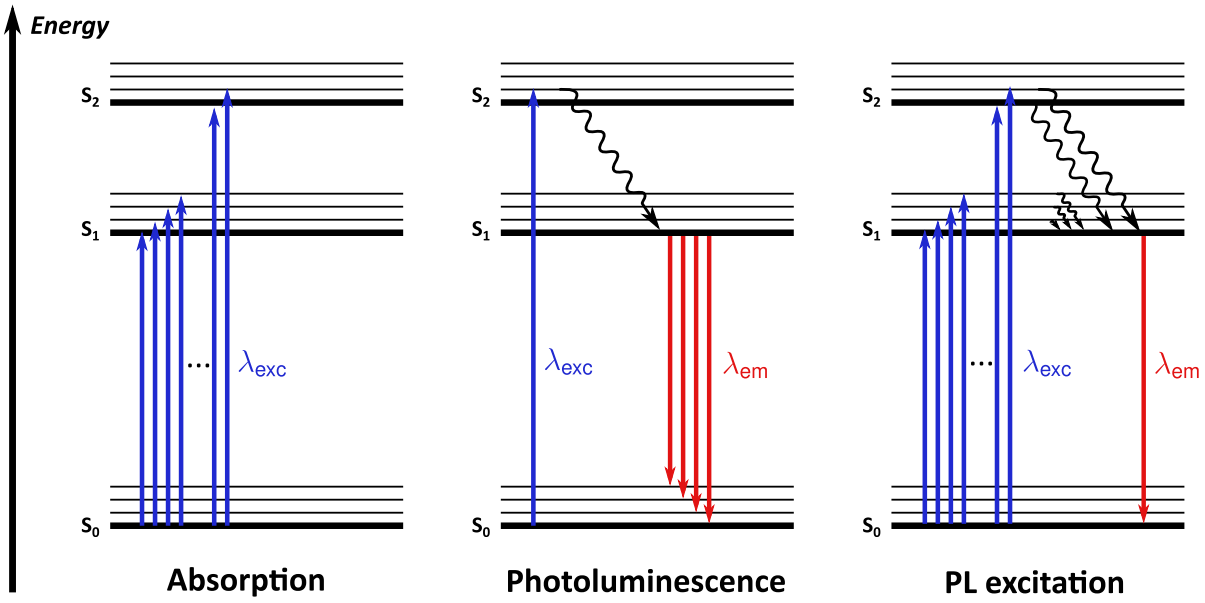

Figure 2.7: Transitions probed in absorption (left), PL (center) and PLE (right) spectroscopy.

By scanning both the excitation and emission wavelength (*i.e.* by measuring PL spectra for successive excitation wavelengths), it is possible to constuct a 2D PL-PLE map, with λ_{em} as x-axis and λ_{exc} as y-axis.

2.3.3 Time-resolved photoluminescence spectroscopy

When a system is in an excited state, the lifetime of the state depends on the rate of possible decay channels (radiative and non-radiative) from this state. Let us describe the most common behavior by considering a population $n(t)$ of emitters in an excited state. Considering only decay channels with a probability depending on the population of the excited state, the rate equation describing the evolution of $n(t)$ can be written:

$$\frac{\mathrm{d}n}{\mathrm{d}t} = -k_r n(t) - k_{nr} n(t) \tag{2.3}$$

with k_r and k_{nr} the radiative and non-radiative decay rates. The evolution of $n(t)$ follows therefore an exponential decay law:

$$n(t) = n(t=0)\mathrm{e}^{-t/\tau} \quad \text{with} \quad \tau = \frac{1}{k_r + k_{nr}}. \tag{2.4}$$

The quantity τ is the lifetime of the excited state. Since the emitted intensity resulting from this excited state is proportional to $n(t)$, it will follow the same exponential decay. In terms of single-photon emission, this means that the probability of an emitter to emit a photon is governed by an exponential law with lifetime τ. However, the decay can follow more complex laws in certain cases (*e.g.* multi-exponential or non-exponential), which

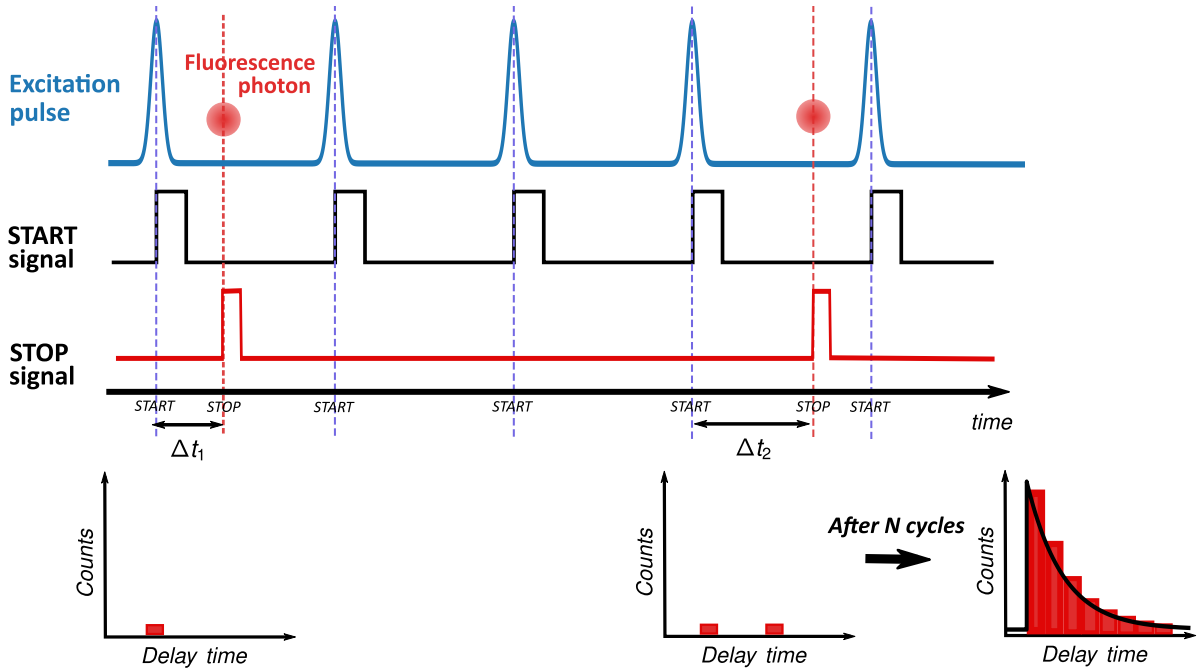

Figure 2.8: General principle of TCSPC measurements. A START signal starts a timer for each excitation pulse generated. When the detector detects a fluorescence photon, the STOP signal sends a pulse to stop the timer. The measured delay (labelled Δt_1 and Δt_2 in this example) is added to a histogram. After a large number N of excitation cycles, the fluorescence decay curve is obtained.

can result, for example, from the inhomogeneity in the environment of the emitters, or the existence of quenching processes.

The decay dynamics can be probed using time-resolved photoluminescence (TRPL), which monitors the time-evolution of the luminescence intensity following an optical stimulus. Experimentally, TRPL curves (*i.e.* the time-evolution of the intensity at a particular emission wavelength) are measured using the Time-Correlated Single-Photon Counting (TCSPC) method. Using a pulsed source, the sample is periodically excited. The photons emitted after each excitation follow a time distribution corresponding to the studied decay dynamics of the excited state population. The measurement of this distribution is done by Start-Stop acquisition (schematized in Figure 2.8): a signal from the pulsed source starts a timer which is stopped when a signal from the detector indicates the detection of a photon. A counter adds each measurement from the timer to a histogram of the time delays. By accumulating the signal over a large number of periods, the counter can build the desired distribution of time delays between excitation pulse and photon emission. The minimum bin width is set by the resolution of the timer. However, this method does not allow for the detection of a second photon after the first one (this design originates from the existence of a dead time after the detection of a photon during which the detector cannot detect another photon). In order to prevent an over-representation of early photons (*i.e.* with short time delays) in the histogram due to

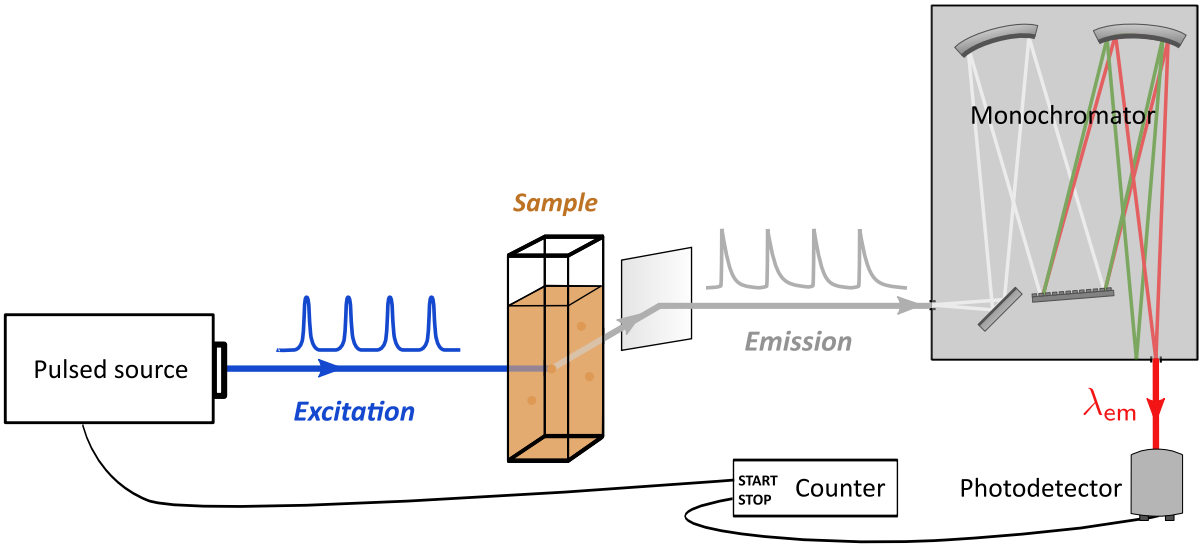

Figure 2.9: General principle of the setup used for TRPL measurements.

the neglect of photons (called *pile-up effect*), the probability of observing two photons during one pulse must be minimized so that only single photons (or none) are observed per excitation cycle. To do so, the intensity (in counts/s) should be set much lower than the repetition rate of the pulsed source. In our experiments, we limit ourselved to a fluorescence collection rate below 2% of the repetition rate of the excitation source.

However, the decay dynamics would only be measured in an ideal case where the instrument (source, detection, electronics) has an instantaneous and infinitely resolved sensibility. In reality, the internal deviations from the ideal case (*e.g.* the excitation pulse is never rigurously a Dirac pulse but has finite width) impose a non-ideal response of the intrument at short timescales. The contribution of all the broadening factors due to the instrument is measured in the Instrument Response Function (IRF), which is the curve measured by the instrument to an ideal instantaneous emission (*i.e.* to a decay with an infinitely-short lifetime). Usually, the IRF can be measured using scattered light, for example from a solution of colloidal silica (LUDOX for instance). In the end, the experimental TRPL curve results from the convolution between the IRF and the theoretical fluorescence decay curve. Therefore, when analyzing the data, we make sure to fit the decay data using convolution with the previously-measured IRF.

During my thesis, I measured TRPL curves using the same spectrophotometer as for PL spectroscopy. The white lamp and the monochromator in the excitation part are replaced by a pulsed source for these measurements, as shown in Figure 2.9. We mainly use solid-state pulsed diodes (NanoLED), at 483 nm with a pulse width below 200 ps and a repetition rate of 1 MHz. The maximum resolution of the device is 25 ps/channel, the bin width was usually set to 53.7 ps during experiments. The IRF of the instrument, given in Figure 2.10, was measured using a diluted LUDOX solution.

Finally, I would like to mention that we also used a home-built setup for a few TPRL measurements. The source used was a supercontinuum pulsed laser (Fianium), for which the emission wavelength can be tuned using acousto-optic filters. The pulses produced

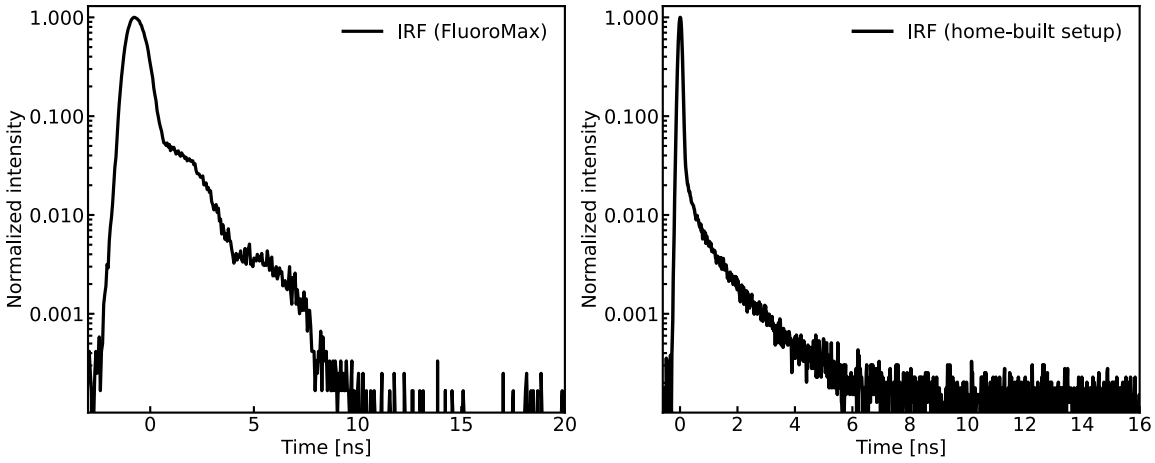

Figure 2.10: IRF for (left) the commercial spectrophotometer (FluoroMax) and (right) for the home-built photoluminescence setup.

have a 6 ps pulse width, and a 60 MHz repetition rate. The detection was performed using a SP-2358 monochromator from Princeton Instruments (the same one used for single-object experiments) coupled with an avalanche photo-diode (APD), ID100 from ID Quantique. A glass coverslip reflected a fraction of the excitation beam into a photodiode to generate START pulses. The TCSPC module used is a PicoHarp300 card from PicoQuant (minimum bin width of 25 ps).

2.3.4 Fluorescence anisotropy

Definition of the anisotropy factor

In order to investigate the polarization-dependence of fluorescence emission, polarization-resolved measurements can be performed on samples. To quantify this phenomenon, we usually introduce a dimensionless quantity, namely the *fluorescence anisotropy factor* r. Given a linearly-polarized excitation, the factor is defined as:

$$r = \frac{I_{\parallel} - I_{\perp}}{I_{\parallel} + 2I_{\perp}}, \tag{2.5}$$

with $I_{\parallel}$ and $I_{\perp}$ the intensity of fluorescence detected in a given direction with polarization parallel and perpendicular to the excitation polarization (see Figure 2.11(b)). The factor can be seen as the ratio between the polarized fraction of fluorescence and the total fluorescence intensity. For instance, $r = 0$ for a non-polarized (or depolarized) fluorescence emission. The numerical value of the factor can be computed in the case of dipolar emission. Classical electromagnetism predicts that the magnitude of the field emitted with polarization along an axis is proportional to the projection of the transition dipole moment into this axis [147]. Therefore, if we consider a dipole forming an

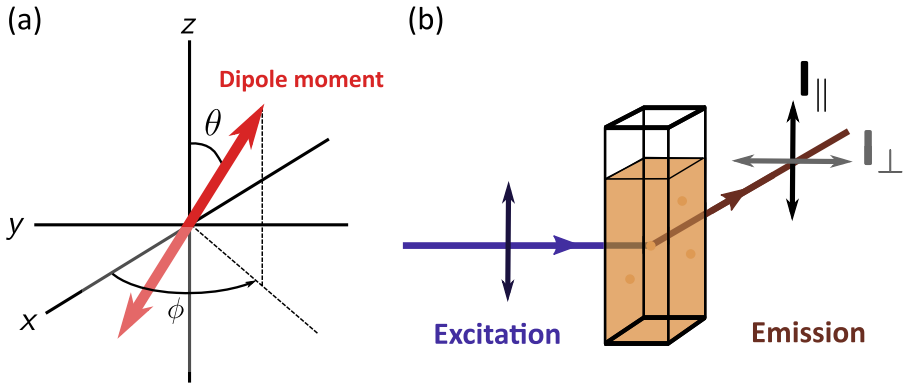

Figure 2.11: (a) Spherical coordinate system to describe the dipole moment orientation. Excitation polarization is along the z-axis. (b) Definition of $I_{\parallel}$ and $I_{\perp}$ for a linearly-polarized excitation (represented by black double-headed arrow).

angle θ with the z-axis, chosen as the excitation polarization axis, and adopt a spherical coordinate system as shown in Figure 2.11(a), we obtain that:

$$I_{\parallel} \propto \cos^2(\theta) \quad \text{and} \quad I_{\perp} \propto \sin^2(\theta)\sin^2(\phi). \tag{2.6}$$

Since we consider the signal from an ensemble of emitters, the intensities are averaged based on the excitation photoselection (*i.e.* the preferential excitation of certain fluorophores given the excitation polarization) and the distribution of emitter orientation in the sample. Given the invariance of the system by rotation around the z-axis[6] in a solution, the average of $\sin^2(\phi)$ yields a factor $1/2$. The factor can therefore be expressed as:

$$r = \frac{3\langle\cos^2(\theta)\rangle - 1}{2} \quad \text{with} \quad \langle\cos^2(\theta)\rangle = \int_0^{\pi/2} f(\theta)\cos^2(\theta)\mathrm{d}\theta. \tag{2.7}$$

where $f(\theta)\mathrm{d}\theta$ represents the probability of finding an *excited* emitter[7] oriented in $[\theta, \theta + \mathrm{d}\theta]$. Since we consider random distribution of emitters in θ, the probability of finding dipoles with orientation between θ and $\mathrm{d}\theta$ is proportional to $\sin(\theta)\mathrm{d}\theta$. Moreover, the probability of absorption for an emitter with a absorption transition dipole oriented at an angle θ relatively to the excitation axis evolves as $\propto \cos^2(\theta)$ [148]. In this case, the normalized probability can be expressed as:

$$f(\theta)\mathrm{d}\theta = \frac{3}{2}\cos^2(\theta)\sin(\theta)\mathrm{d}\theta, \tag{2.8}$$

where the factor $3/2$ is a normalization factor. Therefore, Equation 2.7 gives $\langle\cos^2(\theta)\rangle = 3/5$ and, more importantly, $r = 0.4$.

We have only considered up until now the case where the absorption and emission dipoles are collinear. We can generalize the result for the case when the absorption and

[6] Dipoles with different ϕ angles are excited with the same probability, and the population of emitters is homogeneously distributed around the z-axis.

[7] The distribution of *excited* emitters is different from the distribution of emitters due to excitation photoselection.

β (in °)	0	45	54.7	90
r	0.4	0.1	0	−0.2

Table 2.1: Value of the anisotropy factor for various angular displacement between absorption and emission dipole moments.

emission dipoles are diplaced by an angle β:

$$r = \frac{2}{5}\left(\frac{3\cos^2(\beta) - 1}{2}\right). \tag{2.9}$$

The values observed for the anisotropy factor are given in Table 2.1, which varies in solution between 0.4 (parallel dipole moments) and −0.2 (orthogonal dipole moments).

Excitation anisotropy spectra can be measured and are usually plotted as $r = f(\lambda_{exc})$, *i.e.* by plotting the fluorescence anisotropy emission at a given wavelength λ_{em} for successive value of the excitation wavelength λ_{exc}[8]. This is done experimentally by measuring polarization-resolved PLE spectra and calculating r for each excitation wavelength. r will vary with the relative orientation between the transition dipole of the successively excited absorption transitions and the dipole of the emission transition (between ground state and lowest excited singlet state). Usually, since absorption and emission involving the same electronic transitions have nearly collinear transition dipoles, r will tend towards 0.4 for higher λ_{exc} values (as λ_{exc} tends towards λ_{em}).

If, at a given excitation wavelength, various absorption transitions are possible (either from the species or from different emitting species in the sample), the total anisotropy is given by a weighted sum of the anisotropy for each transition. Considering the simplest case of two transitions a and b, the fractional contribution f_a and f_b of each transition to the absorption spectrum can be defined as:

$$\mathcal{A}_a(\lambda) = f_a(\lambda)\mathcal{A}(\lambda) \quad \mathcal{A}_b(\lambda) = f_b(\lambda)\mathcal{A}(\lambda) \tag{2.10}$$

with $\mathcal{A}(\lambda)$ the total absorption spectrum, and $\mathcal{A}_{a/b}(\lambda)$ the absorption spectrum for state a/b. For any wavelength, the sum of the fractional contributions is unity $f_a(\lambda)+f_b(\lambda) = 1$. If we note r_a and r_b the anisotropy of states a and b, the total anisotropy is then given by:

$$r(\lambda_{exc}) = f_a(\lambda_{exc})r_a + f_b(\lambda_{exc})r_b. \tag{2.11}$$

Finally, it is important to note that, due to rotational diffusion and other depolarization effects, the measured value is often lower than the theoretical value. In the extreme case where the rotational diffusion process occurs on very short timescales relatively to

[8] Since the emission is usually observed from the lowest singlet state, we rarely see any effect in emission anisotropy spectra.

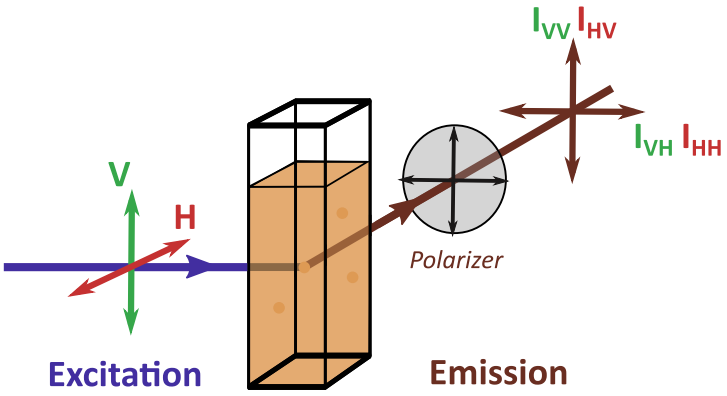

Figure 2.12: Experimental method to measure the anisotropy factor. The intensities in green and red correspond respectively to cases when the excitation is vertical (V) or horizontal (H).

the fluorescence lifetime, we lose all correlation between excitation and emission polarization and the anisotropy factor drops to 0. In order to prevent this effect, the rotational characteristic time should be longer than the lifetime of the excited state, which can be possible by choosing a viscous solvent.

Steady-state fluorescence anisotropy measurements

Experimentally, fluorescence anisotropy measurements are often performed using a "L-format" configuration (with perpendicular excitation and emission paths). The solution is excited using a linearly-polarized excitation, and $I_{\parallel}$ and $I_{\perp}$ are measured by detecting the intensity transmitted by a polarizer placed in the detection path. We can easily see that in order to have access to both $I_{\parallel}$ and $I_{\perp}$, the cuvette must be excited using a vertical (V) polarization. By orienting the detection polarizer vertically (V) and horizontally (H), we thus have access to $I_{\parallel}$ and $I_{\perp}$. More precisely, let I_{VV} and I_{VH} the intensity measured when detecting with vertically- and horizontally-oriented emission polarizer, after exciting with vertically-oriented polarization, as shown in Figure 2.12. We have:

$$I_{VV} = k S_V I_{\parallel} \qquad I_{VH} = k S_H I_{\perp} \tag{2.12}$$

with S_V and S_H the sensitivities of the detection to vertically- and horizontally-polarized light, and k a numerical factor taking into account various non-polarization-dependent factors. As we can see, the measurement of I_{VV} and I_{VH} is not sufficient to compute r since an instrument-dependent factor $G = S_V/S_H$ must be determined (usually termed *G-factor*). This can be resolved by noticing that, when exciting with horizontally-polarized light,

$$I_{HV} = k S_V I_{\perp} \qquad I_{HH} = k S_H I_{\perp} \tag{2.13}$$

with I_{HV} and I_{HH} the intensity detected with vertically- and horizontally oriented polarizer. The G-factor can therefore directly be determined as $G = I_{HV}/I_{HH}$, and finally we

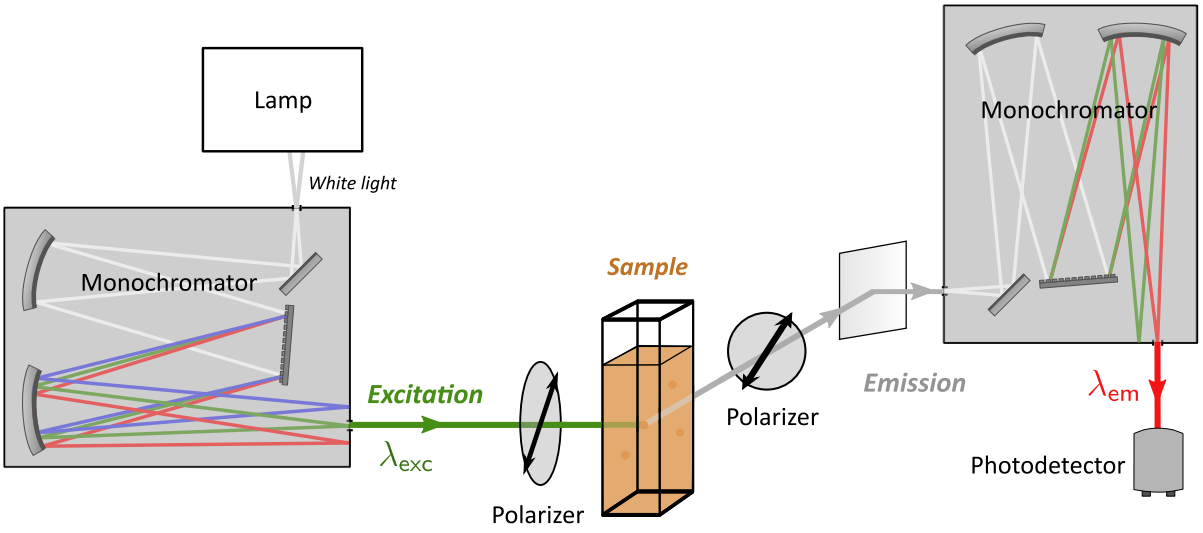

Figure 2.13: Schematic representation of the device used for fluorescence anisotropy measurements.

recover the anisotropy factor:

$$r = \frac{I_{VV} - GI_{VH}}{I_{VV} + 2GI_{VH}}. \tag{2.14}$$

During my thesis, the anisotropy measurements were performed using the spectrophotometer FluoroMax, the same as for other photoluminescence measurements in solution. A simplified schematic of the device is given in Figure 2.13: polarizers have been added in the excitation and emission paths, in order to measure the four signals I_{VV}, I_{VH}, I_{HV} and I_{HH}. During acquisition, for each λ_{exc} position, the four signals are measured by rotations of the polarizers. At the end, after the four PLE spectra have been measured, the anisotropy spectrum is computed using Equation 2.14.

In order to minimize the effect of rotational diffusion, we chose to perform experiments by mixing sample solutions with a viscous solvent, in our case castor oil (Ref. 259853, from Sigma Aldrich). Indeed, we can express the rotational correlation time τ_{rot}, *i.e.* the characteristic timescale of rotational diffusion, by [146]:

$$\tau_{rot} = \frac{4/3\pi R^3 \eta}{k_B T}, \tag{2.15}$$

with η the dynamical viscosity of the solvent, R the radius of an equivalent sphere for the emitter, T the temperature and k_B the Boltzmann constant. The equation shows that the decay time of the anisotropy increases with the viscosity of the solvent. TCB has a viscosity of around 3.29×10^{-2} Pa.s, while the viscosity of castor oil reaches 0.65 Pa.s. If we estimate $R \sim 1$ nm for a $C_{96}C_{12}$ GQD, τ_{rot} is of the order of 10 ns for TCB, and 1 µs in castor oil at room-temperature. Solutions for steady-state measurements are prepared with a ratio 90/10 castor oil/TCB ratio (in weight). Given the difficulty of cleaning the cuvettes

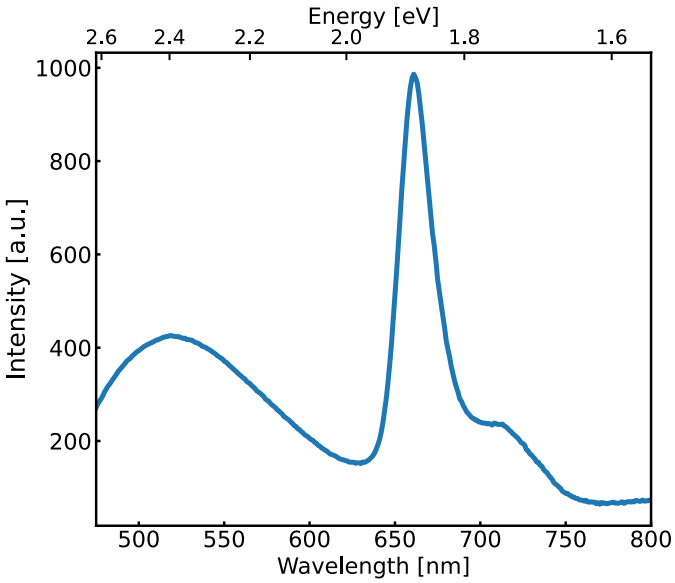

Figure 2.14: PL spectrum of castor oil and TCB (90/10), excited at 450 nm.

after being filled with castor oil, disposable cuvettes were used (BRAND®macro-cuvettes, in polystyrene) for measurements with this solvent.

A drawback of castor oil is that the solvent itself exhibits fluorescence, as shown in Figure 2.14. This method was efficient only on emitters which do not emit in the same wavelength range as the fluorescence peak of castor oil.

Time-resolved fluorescence anisotropy measurements

Since rotational diffusion causes the loss of correlation in polarization, a possibility to recover the anisotropy factor is to perform time-resolved measurements. For a spherical emitter, the time-dependence of the anisotropy factor can be given by:

$$r(t) = r_0 \mathrm{e}^{-t/\tau_{\mathrm{rot}}}, \tag{2.16}$$

with r_0 the fundamental anistropy, *i.e.* the anisotropy if the emitters were frozen and no rotational diffusion occured. For more complex geometries, additional characteristic times can be introduced and result in more complex time-dependences. The time-evolution of $r(t)$ is obtained by measuring the TRPL curves of all four intensities (I_{VV}, I_{VH}, I_{HV} and I_{HH}), and by using the same Equation 2.14. The resulting curve $r(t)$ decreases from a value r_0 (at $t = 0$, upon excitation) to 0 with a timescale τ_{rot}.

Experimentally, this is performed once again on the same setup as for TRPL measurements. Since the pulsed diode is already polarized, the polarizer on the excitation beam path is replaced by a half-wave plate. The same method as for TRPL measurements is used for the collection of TRPL curves for each polarization configuration.

2.4 Single-molecule spectroscopy

2.4.1 Confocal microscopy setup

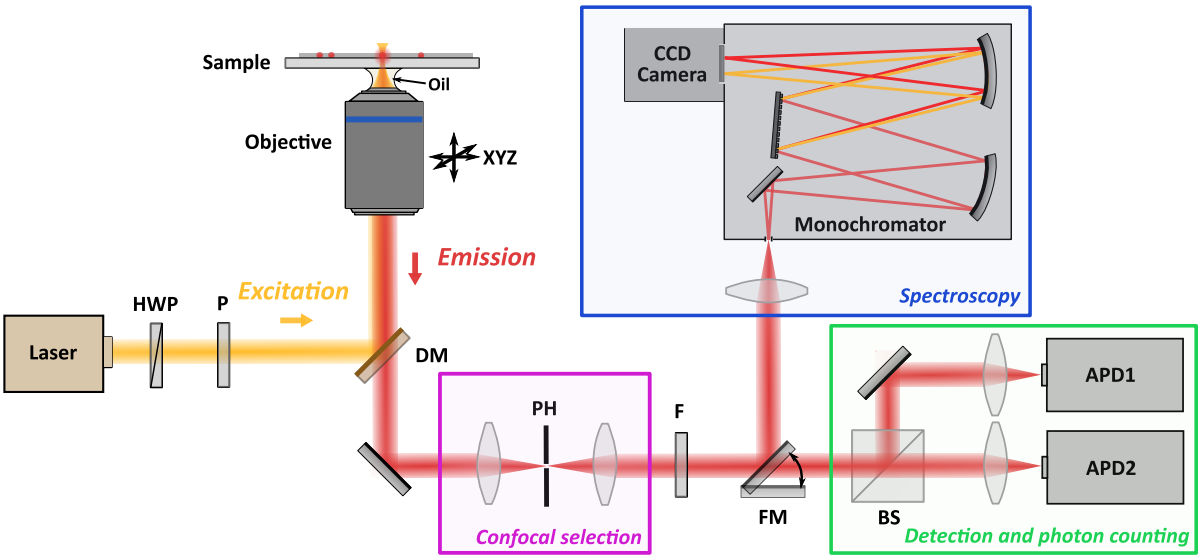

Figure 2.15: Simplified schematic representation of the microphotoluminescence setup. HWP: half-wave plate, P: Polarizer, DM: dichroic mirror, PH: pinhole, F: filter, FM: flipping mirror, APD: avalanche photodiode.

The single-molecule study is achieved by using confocal microscopy. The principle of this method resides in the confocality between the excitation focalization point in the sample and a confocal pinhole in the detection path which spatially filters the emission collected. Given this configuration, we ensure that the emission is collected favorably from the emitter in the excitation spot and we minimize the contribution of neighboring or out-of-focus emitters, reducing background and noise. In our case, since the emission from the sample uses the same microscope objective, the separation between excitation and emission is then performed using a dichroic mirror. A general scheme of the setup is given in Figure 2.15, with the excitation path drawn in yellow, and the emission path in red.

Focalization on the sample

In order to selectively excite the sample, a microscope objective is used to focus light onto the sample. The objective used is an oil-immersion microscope objective (Olympus UPlanSApo 60x), with a numerical aperture NA = 1.35 greater than unity to achieve a higher collection efficiency. For an infinity-corrected objective, the effective focal length can be estimated from its magnification, defined as the magnification of the object into an image formed at the focus of a tube lens. For Olympus objectives, the focal length

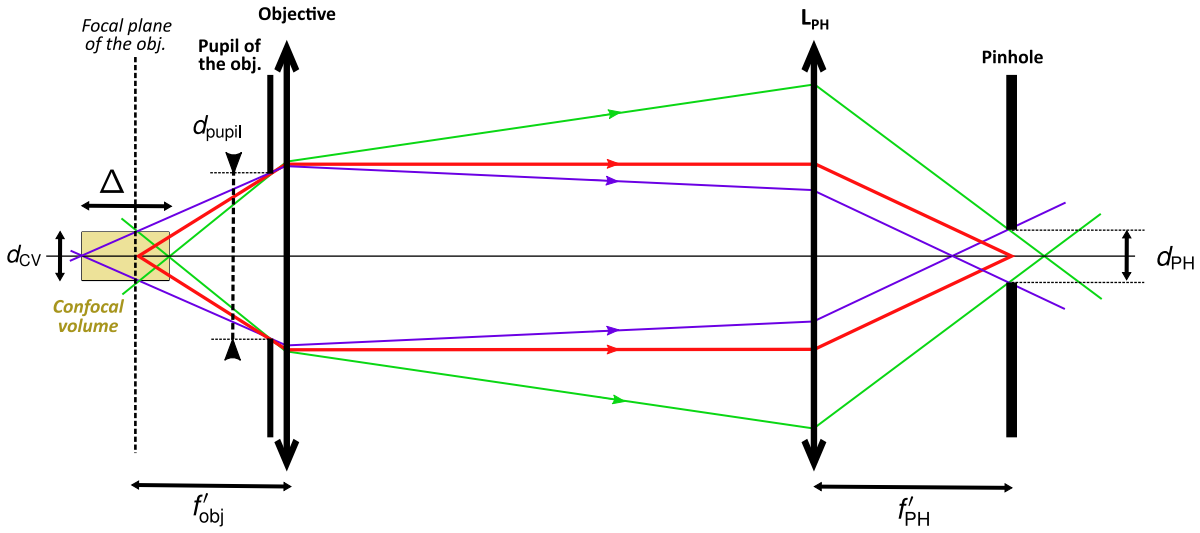

Figure 2.16: Schematic of the description of the confocal volume (in yellow) using geometrical optics. Δ and d_{CV} are the depth and diameter of the confocal volume.

of the tube lens is conventionally 180 mm. Therefore, since the magnification is $M = 180\,\text{mm}/f'_{obj}$, the effective focal length can computed to $f'_{obj} = 3\,\text{mm}$. Consequently, the pupil diameter d_{pupil} can also be calculated $d_{pupil} = 2 \times \text{NA} \times f'_{obj} = 8.1\,\text{mm}$.

Using the various characteristics of the objective, the size of the excitation spot at the focus can be estimated. Considering an Airy function resulting from the diffraction by the pupil of the objective, the first extinction of the circular intensity distribution in the focal plane of the objective is given for a radius R [149]:

$$R = 1.22\frac{\lambda}{d_{pupil}} \times f'_{obj} = 1.22\frac{\lambda}{2\text{NA}} \tag{2.17}$$

with λ the excitation wavelength. The excitation spot diameter can then be expressed as $2R$. For an excitation wavelength $\lambda = 594\,\text{nm}$, the spot diameter is about 540 nm.

Confocal selection

The confocal selection is performed using a pinhole (PH) on which the emission beam is focused using a convergent lens (L_{PH}, with focal length f'_{PH}), and the transmitted light is recollimated using a second lens, as highlighted in violet in Figure 2.16. The focal plane of the objective is thus conjugated to the plane of the pinhole, as shown by the red ray in Figure 2.16. The pinhole thus rejects the light emitted from emitters out-of-focus on the sample, which limits the collection of light from a small volume in the sample, referred to as the *confocal volume*. We can estimate the volume, defined by Δ the depth of the confocal volume (similar to a depth of field) and d_{CV} the diameter of the confocal volume, using geometrical optics considerations. As shown in Figure 2.16, we use two particular rays, namely the rays corresponding to the limit case where the rays are transmitted by

the pinhole after (in blue) or before (in green) focusing after L_{PH}. Given d_{PH} the diameter of the pinhole, we can express:

$$d_{CV} = \frac{f'_{obj}}{f'_{PH}} d_{PH}. \tag{2.18}$$

Moreover, using the definition of the NA:

$$NA = \frac{d_{CV}}{\Delta} \implies \Delta = \frac{d_{CV}}{NA} \tag{2.19}$$

In our setup, we focus on the pinhole using a lens with $f'_{PH} = 75\,mm$, and $d_{PH} = 50\,\mu m$. We can thus estimate $d_{CV} = 2\,\mu m$ and $\Delta = 1.5\,\mu m$, and the total volume is around $4.7\,\mu m^3$.

Excitation

The excitation path in Figure 2.15 is drawn in yellow. Two continuous-wave excitation sources were used for photoluminescence measurements: a 594 nm laser (Mambo 594, Cobolt) and a 532 nm laser (Sapphire 532, Coherent). The power of the excitation beam is tuned using a half-wave plate and a polarizer (additional neutral densities are also sometimes placed in the beam path). The power used in measurements is usually of the order of 250 nW, yielding a power density of around $10^2\,W/cm^2$ (given the diameter of the excitation spot calculated earlier in this section).

Dichroic mirrors are used to reflect the excitation towards the objective and transmit emission after collection from the objective. An additional long-pass filter is added in the detection path (after confocal selection) to block residual light from the excitation laser. For the 594 nm source, a dichroic mirror with a wavelength cut around 600 nm (zt 594 RDC, Chroma) and a 600 nm filter (FEHL600, Thorlabs) are used. For the 532 nm source, we chose a dichroic mirror with a cut at 552 nm (LaserMUX552, Semrock) along with a 532 nm long-pass filter (RazorEdge 532, Semrock). Switching from one source to another is enabled by the use of locking magnet bases for each different dichroic mirror.

Scanning and collection

The microscope objective is mounted on XYZ piezoelectric scanners (Nano-PDQ, Mad City Labs Inc.). The focalization point in the sample can thus be moved with a resolution of 0.1 nm. The sample can also be moved in XY using translational micrometric screws.

The emission collected is then sent through the confocal pinhole and either in a detection part (shaded in green in Figure 2.15) or towards a spectrometer (in blue). The emission intensity is measured using two single-photon counting modules (SPCM-AQRH-13, PerkinElmer), with maximum dark count rate around 250 cts/s. Each APD delivers a TTL signal for each detected photon (min. 2.5 V), with a pulse width of 15 ns, with a 32 ns dead time between pulses. The detection efficiency for photons at 650 nm is around 70%. The pulses from both APDs are summed and counted using an acquisition card (PCIe-6323, National Intruments). A Python program based on Qudi (suite of tools for micro-photoluminescence experiments, developed by the Institute of quantum optics in

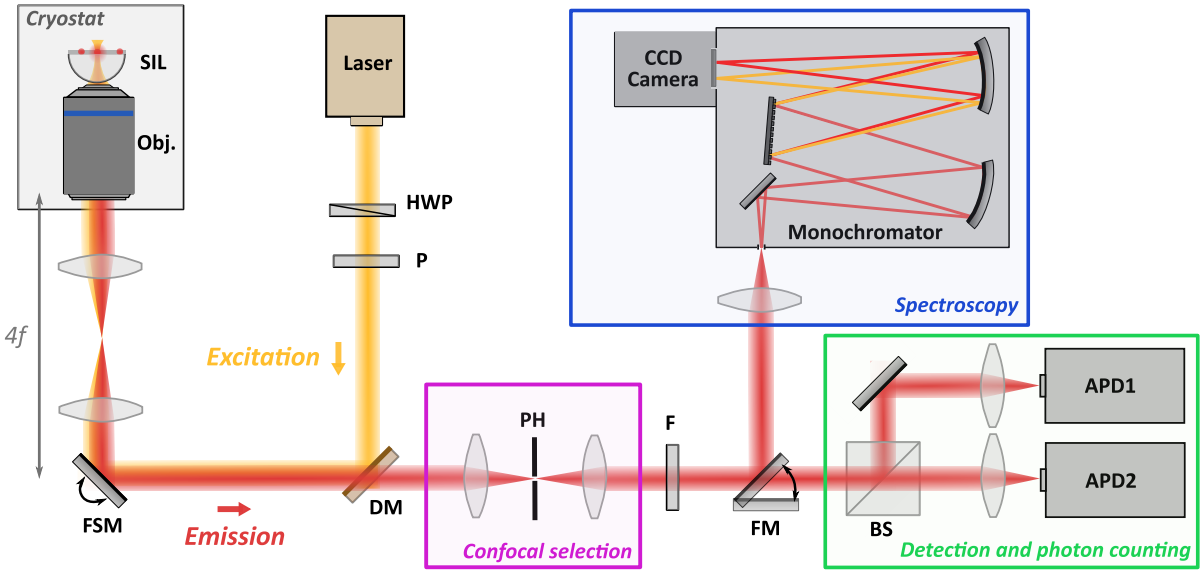

Figure 2.17: Simplified schematic representation of the microphotoluminescence setup for low-temperature measurements. SIL: solid-immersion lens, Obj.: microscope objective, FSM: fast steering mirror, HWP: half-wave plate, P: Polarizer, DM: dichroic mirror, PH: pinhole, F: filter, FM: flipping mirror, APD: avalanche photodiode.

Ulm University[9]) is used to pilot both the piezoelectric scanners and the display of results from the acquisition card. Raster scans of the sample can therefore be performed (usually with an acquisition per position of 10 ms). An optimizer module is also used to automatically position the excitation spot to the maximum intensity position of an emitter (a local raster scan is followed by a 2D Gaussian fit to determine the maximum's position).

Using a flipping mirror, the emission signal can be sent to a spectrometer for spectral measurements. Details for the spectrometric measurements are given in Section 2.4.3.

Low-temperature measurements

In order to change the temperature of the sample, a second microphotoluminescence setup is used where the sample is placed in a cryostat.

The cooldown of samples is performed using a closed-circuit liquid helium cryostat (Montana Instruments Cryostation). The GQD films deposited on SIL substrates are fixed on a home-designed sample holder (in copper) which is then mounted on a gold-plated copper platform, as shown in Figure 2.18. The sample cooldown is enabled by gold contacts linked to the gold platform, which are on one end cooled by the liquid helium circuit (*cold fingers* method). The sample position is controlled using XYZ nanopositioners (Attocube) commanded by a position controller.

Before cooldown, the chamber is pumped using an external pump (TSH 071e, Pfeiffer vacuum) down to 10^{-3} mbar. The cooldown procedure is then triggered on the con-

[9] https://github.com/Ulm-IQO

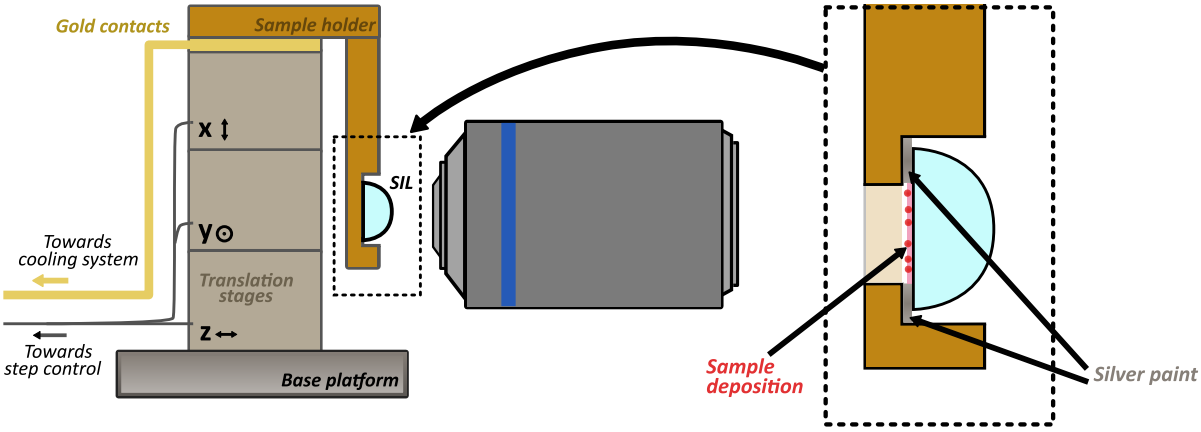

Figure 2.18: Schematic representation of the components in the cryostat chamber. On the right: details of the fixation of the SIL on the sample holder using silver paint.

troller of the cryostat. The temperature is monitored by sensors at different points of the cooldown circuit (labelled *Stage 1* and *Stage 2*) and at the base platform (labelled *Platform*). As shown in Figure 2.19, the cooldown process takes around 180 min. The minimum temperature reached (at the platform) is 7 K (although target temperature is set at 4 K). The difficulty of reaching lower temperatures may arise from the absence of radiation shield around the sample. A home-built radiation shield has been designed to resolve this issue and remains to be tested.

In order to prevent losses due to reflections on the window of the cryostat, a home-built vacuum chamber was designed and appended to the initial chamber of the cryostat, enabling the use of a high NA microscope objective (NA = 0.8, Olympus LMPLFLN 100x). The use of a SIL increases the effective numerical aperture of the system, due its high refractive index $n_{SIL} = 2$, yielding NA = 1.6 for the system {SIL+objective}. The working distance, which has to be larger than the radius of the SIL (2 mm) is 3.5 mm for this objective. Using the same expressions as for the room-temperature setup (described in paragraph 2.4.1), the effective focal length of the objective can be calculated $f'_{obj} = 1.8$ mm, along with the diameter of the excitation spot $2R \approx 450$ nm.[10]

The excitation power used for experiments is around 1-2 µW, which corresponds to a power density of around 10^3 W/cm^2.

Instead of using piezoelectric stages, the sample is scanned using a steering mirror (FSM-300, Newport) conjugated to the microscope objective *via* a 4f system. Given the angular resolution of the FSM (around 1 microrad), the scanning precision on the surface can reach 2 nm. The steering mirror is commanded using a similar Python script to the one used for the other microphotoluminescence setup.

The rest of the setup follows the same configuration as the room-temperature setup described beforehand, except for the addition of a beam expander (not represented in

[10] Since $d_{PH} = 50$ µm and $f'_{PH} = 75$ mm for the low-temperature setup, the confocal volume can also be estimated with $\Delta = 750$ nm and $d_{CV} = 1.2$ µm. The confocal volume is smaller compared to the room-temperature setup, partly due to the lower focal length of the objective.

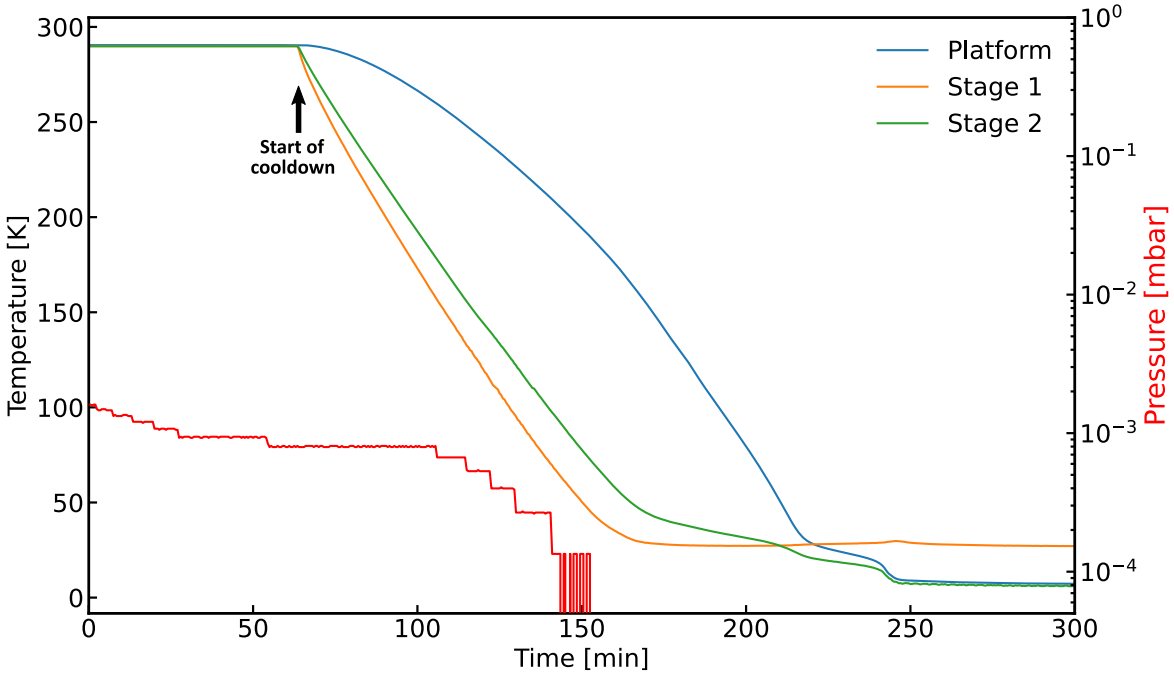

Figure 2.19: Evolution of the pressure (in red) and of the temperature monitored at different points of the cryostat. The pressure captor does not resolve pressures below 10^{-4} mbar.

the scheme for clarity) between the flipping mirror and the focalization lens at the entrance of the spectrometer, consisting of a 50 mm and a 250 mm lens. This beam expander yields a beam with a 1 cm diameter, necessary to achieve a satisfying $f/_{\text{value}}$ matching at the entrance slit (described in more details in the paragraph 2.4.3).

2.4.2 Second-order correlation function measurements

In order to verify if the fluorescence signal collected corresponds to the signal of a single emitter, we can measure the second-order correlation function of the emission from the fluorescent spot. For a intensity signal $I(t)$, the function is defined as:

$$g^{(2)}(\tau) = \frac{\langle I(t)I(t+\tau)\rangle}{\langle I(t)\rangle^2}, \tag{2.20}$$

where $\langle\cdot\rangle$ denotes time average. One can show that the value of the second-order correlation factor for zero delay ($\tau = 0$) can be linked theoretically to the number of emitters probed [150]. Let N be the number of emitters in the collection spot:

$$g^{(2)}(\tau = 0) = 1 - \frac{1}{N}. \tag{2.21}$$

This shows that the correlation of the events « One photon is emitted at time t » with the event « A second photon is also detected at t » vanishes for a single emitter, which

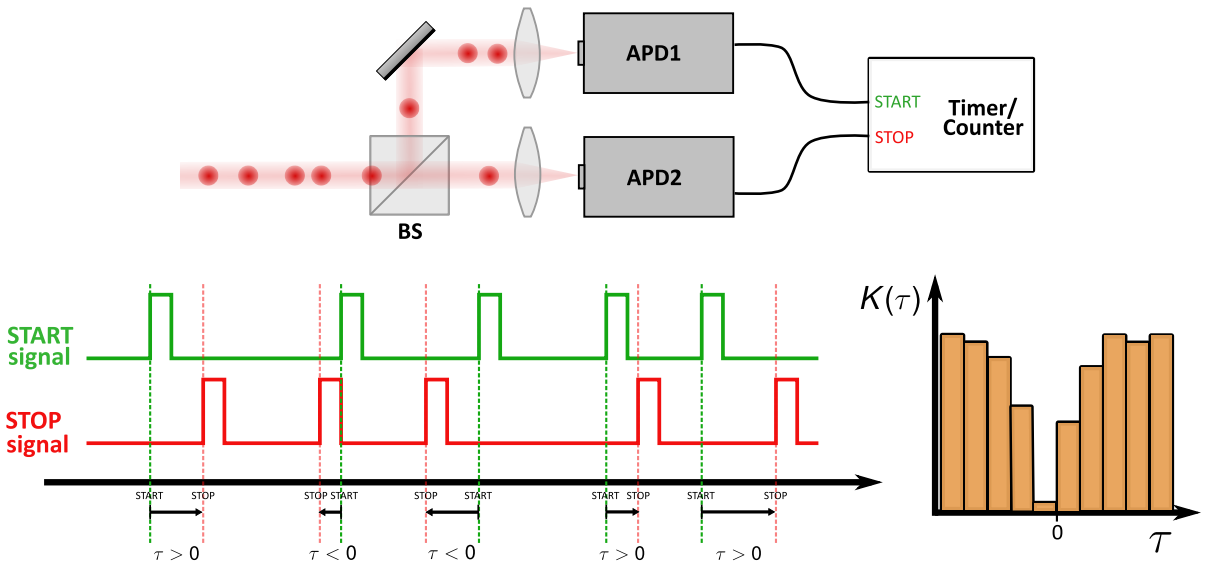

Figure 2.20: (Top) Hanbury Brown and Twiss configuration for $g^{(2)}$ measurements. BS: 50:50 beam-splitter, APD: avalanche photodiode. (Bottom) Example of START and STOP signals sent to the timer/counter (left), the recorded delay is added to the histogram of delay $K(\tau)$ (right).

describes the emission of single photons. For $\tau \neq 0$, using a simple three-level system, one can predict the expression of $g^{(2)}(\tau)$:

$$g^{(2)}(\tau) = 1 - (1 + a)e^{|\tau|/\tau_1} + ae^{|\tau|/\tau_2} \approx 1 - e^{|\tau|/\tau_1}. \tag{2.22}$$

where a, τ_1 and τ_2 can be expessed using the different transition rates [151]. In the case where the system can be approximated to a two-level system, we are left with only the second expression in Eq.2.22. An ideal $g^{(2)}(\tau)$ curve for a single emitter is given in Figure 2.21(a).

Experimentally, the $g^{(2)}$ is measured using two avalanche photodiodes in a Hanbury Brown and Twiss configuration as shown in Figure 2.20. The incident light is separated into the two APDs using a 50:50 beamsplitter. The detection signals delivered from the APDs (TTL pulses) are sent to a timer and counter module. Using the same START-STOP method as described for TRPL measurements, the time delay (positive or negative) between a pulse in the START and in the STOP signal are measured and added to an histogram (labelled here $K(\tau)$). In this case, the START and STOP signals correspond respectively to the detection of a photon by APD1 or APD2. Using this method, we overcome the limit set by the dead time of the APDs, and we are thus limited only by the resolution of the timer[11]. The second-order photon correlation can then be recovered by dividing

[11]That is if we neglect the variations in the detection mechanism of the APD and the internal jitter of the detection and timing circuitry.

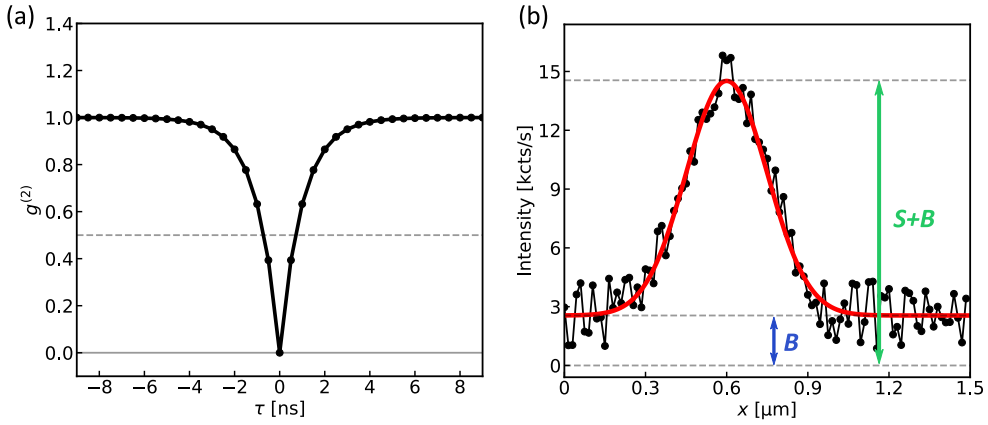

Figure 2.21: (a) Example of a theoretical $g^{(2)}(\tau)$ curve for a single emitter. (b) Example of an intensity profile along a line comprising the studied fluorescent spot (in black) and the Gaussian fit (in red).

$K(\tau)$ by the average photon detection rate per time bin [152]:

$$g^{(2)}(\tau) = \frac{K(\tau)}{\mathcal{N} w R_2} = \frac{K(\tau)}{w R_1 R_2 T} \tag{2.23}$$

where $\mathcal{N}$ is the number of repetitions (*i.e.* the total number of points in the histogram), R_1 and R_2 are the count rates for APD1 and APD2, w is the bin width and T the integration time of the measurement (*i.e.* the total duration of the measurement). Another way to interpret this formula is to notice that wR_1R_2 corresponds to the coincidence rate for a Poissonian source. Therefore, $g^{(2)}$ measures the deviation of the source from an ideal Poissonian source (which would yield a flat $g^{(2)}(\tau)$ curve equal to unity) [153]. Interestingly, if we consider a single-photon emitter, we see that at the beamsplitter, the wavefunction describing the photon will be split along the two possible detection paths. The measurement of the position of the photon will induce the collapse of the wavefunction on either of the two APDs. As a result, each incident photon can be seen as either transmitted or reflected by the beamsplitter, yielding no possible detection simultaneously on APD1 and APD2, which is consistent with the vanishing second-order correlation function at zero delay.

In our case, the detectors used are two silicon-based avalanche photodiodes (SPCM-AQRH-13, PerkinElmer), with 32 ns dead time. The $g^{(2)}(\tau)$ were measured using a time-correlated single-photon counting module (Time Tagger 20, Swabian Intrument) and displayed using a Python program. The resolution of the timer is 1 ps. We also used on different occasions the same card as for TRPL measurements (PicoHarp300, PicoQuant), which has a resolution of 4 ps, along with the dedicated software (PicoHarp). When using the latter counting module, since it does not allow the measurement of negative delays, a delay line is added on the output of APD2 to induce a fixed delay between the two detectors. The zero-delay point of $g^{(2)}(\tau)$ is therefore shifted by the value of the delay.

Background correction

During analysis, the $g^{(2)}(\tau)$ curve calculated with Eq.2.23 can be corrected to take into account the background signal using:

$$g^{(2)}_{cor}(\tau) = \frac{g^{(2)}(\tau) - (1-\rho^2)}{\rho^2} \quad \text{with} \quad \rho = \frac{S}{S+B} \tag{2.24}$$

where S is the intensity of the signal of interest and B the background intensity [154]. The factor ρ is estimated by scanning the fluorescent spot along a line and plotting the intensity profile along this line. An example is given in Figure 2.21(b). By fitting the profile with a Gaussian function with a constant offset, the background signal B can be extracted (corresponding to the constant offset), along with the intensity collected from the position where the $g^{(2)}$ is measured (usually at the maximum intensity of the spot), corresponding to $S+B$. In this example, $S+B = 14.5$ kcnts/s and $B = 2.5$ kcnts/s, yielding $\rho \approx 0.83$.

2.4.3 Spectroscopy measurements

The spectral measurements are performed using a spectrometer constituted of a monochromator (SP-2358, Princeton Instruments) in a Czerny-Turner configuration, coupled in output with a CCD camera (PyLoN:100BR eXcelon, Princeton Instruments) cooled with liquid nitrogen (LN), as schematized in Figure 2.22. The incident light is focalized on the entrance slit of the spectrometer (ES), and sent to a first spherical mirror (M1) which redirects it to the grating (G) as a collimated beam. Depending on the groove density of the grating, the angular dispersion of the diffracted beam will vary. A second spherical mirror (M2) then refocuses the light on the surface of the detector. Due to diffraction by the grating, waves with different wavelengths will focus on different positions of the detector. A calibration in wavelength of the camera (using a Ne-Ar spectral lamp) thus enables the measurement of the spectral composition of the incident light.

In order to efficiently collect the incident light and use the resolution of the spectrometer, the incident beam is focused on the entrance slit in order to match the entrance aperture ratio (or $f/_{\text{value}}$) of the monochromator[12]. Since the incident light has a diameter of around 1 cm, we focalize the beam on the entrance slit using a lens with $f' = 40$ mm in order to match the 3.9 aperture ratio of the monochromator.

On our device, the focal length of the mirrors is 300 mm. Three gratings are available, with different groove densities (150 g/mm, 300 g/mm and 600 g/mm). The camera has a CCD surface composed of 1340×100 pixels, each with a surface of $20\,\mu\text{m} \times 20\,\mu\text{m}$, cooled at -120 °C. Both the monochromator and camera are driven by a dedicated software (WinSpec during the beginning of my thesis, then LightField), which enables the control of the central wavelength and the grating used on the monochromator, and of various

[12] For a lens hit by a collimated beam with diameter d, we have in output $f/_{\text{value}} = f'/d$, with f' the focal length of the lens. In the case of a spectrometer, the $f/_{\text{value}}$ corresponds to the ratio of the projected area of the grating from the entrance slit over the focal length of the mirror. Since the resolution of the spectrometer depends directly on the number of grooves illuminated, an efficient use of the spectrometer will require an optimized matching of the incident light with the $f/_{\text{value}}$ of the monochromator.

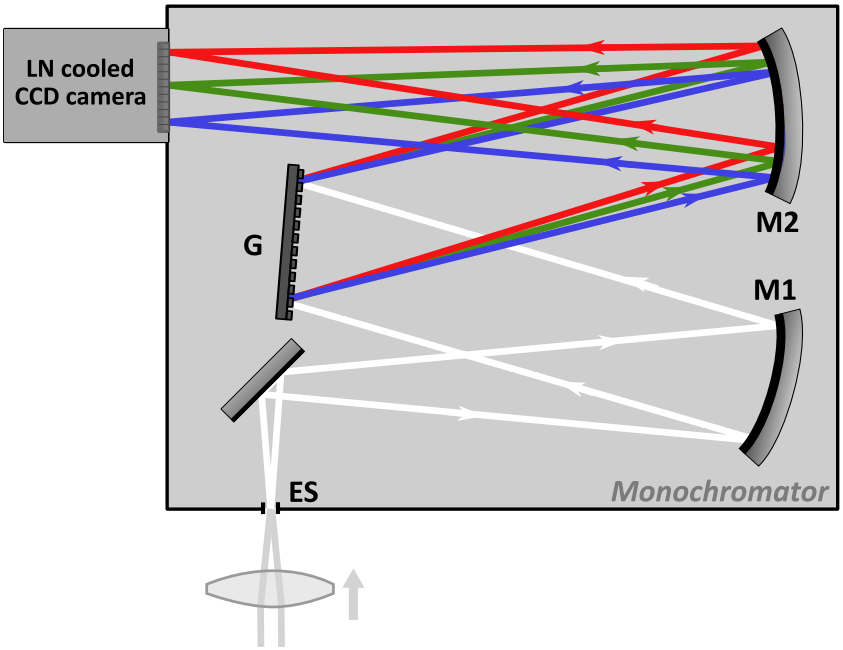

Figure 2.22: Schematic representation of the spectrometer used. ES: entrance slit, M1 and M2: spherical mirrors, G: grating.

acquisition parameters (exposition time, background correction, etc.) on the detector. Spectra are usually measured with an exposure time of 20 s.

Resolution of spectral measurements

Knowing the resolution of the spectral measurements (*i.e.* the minimum linewidth measurable[13]) is essential when dealing with low-temperature spectra.

The resolution of the instrument depends on various parameters. The recorded spectrum results from the convolution of the real spectrum of the analyzed light with the instrumental line profile, which results from various broadening effects. We distinguish the limit due to the method (diffraction by a grating) and the broadening due to slits.

The dispersion in wavelength in our monochromator is performed using diffraction by a reflective grating. Considering that N grooves are illuminated, the interference of N waves yields an intensity I varying with Φ, the phase difference between waves diffracted by two consecutve grooves:

$$I(\Phi) \propto \frac{\sin^2(N\Phi/2)}{\sin^2(\Phi/2)} \quad \text{with} \quad \Phi = \frac{2\pi}{\lambda n}\left(\sin(\theta_d) + \sin(\theta_0)\right), \tag{2.25}$$

where λ is the wavelength of the interfering waves, θ_0 the incident angle on the grating, θ_d the diffracted angle and n the groove density, as shown in Figure 2.23(a). Maxima of

[13]The resolution is more specifically evaluated using the bandpass function of the spectrometer, which gives, in the case of an exit slit, the transmission coefficient for each incident wavelength by the monochromator.

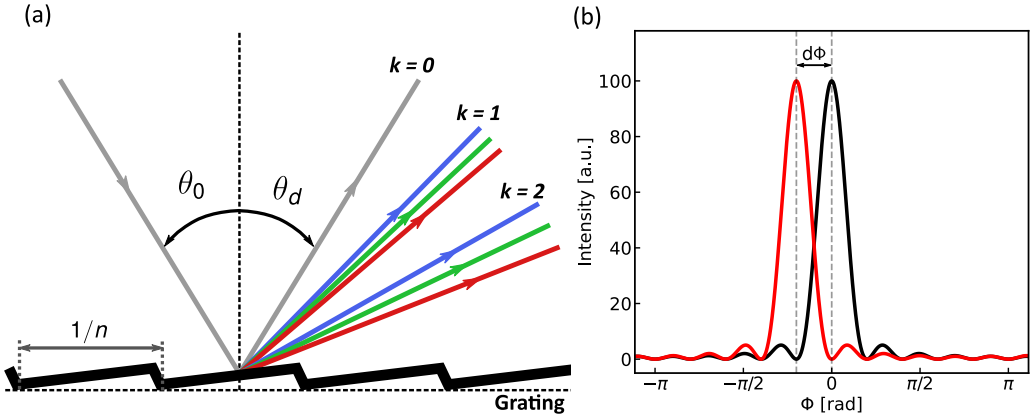

Figure 2.23: (a) Definitions of angles for grating diffraction. Dashed lines indicate the plane of the grating and its normal. θ_0 and θ_d are defined relatively to the normal of the grating's plane. (b) Example of two diffraction patterns respecting the Rayleigh criterion, with $N = 10$.

intensity (*i.e.* constructive interferences) occur for $\Phi = 2k\pi$, with k the order of interference. The associated angular dispersion[14] (at order k) can be computed by differentiating the condition of constructive interferences:

$$-\frac{2\pi}{n}\cos(\theta_d)\mathrm{d}\theta_d = 2\pi k\mathrm{d}\lambda, \tag{2.26}$$

Using the Rayleigh criterion, which states that two signals are resolvable if the maximum of one corresponds to the minimum of the other (see Fig.2.23(b)), one can estimate the next resolvable wavelength $\lambda + \mathrm{d}\lambda$ which can be resolved. Since the phase difference between a consecutive maximum and minimum is $\mathrm{d}\Phi = 2\pi/N$, and at first order:

$$\mathrm{d}\Phi = \frac{2\pi}{\lambda n}\cos(\theta_d)\mathrm{d}\theta_d, \tag{2.27}$$

we directly deduce that $\mathrm{d}\lambda = \frac{\lambda}{kN}$. This value also corresponds to a good estimation of full width at half maximum (FWHM) of the peak.

This can be seen as a fundamental limit of the spectrometer, intrinsic to the use of a diffraction grating to disperse light. One can see that the resolution increases with N the number of grooves and, *a fortiori*, with the groove density of the grating (which is directly linked to the increase of angular dispersion with groove density). I would like here to emphasize that both the angular dispersion and $\mathrm{d}\lambda$ depend on the wavelength (and, more pragmatically, on the central wavelength, *i.e.* the diffracted wavelength at the center of the detector).

In the case of our spectrometer, since the width of the gratings is 68 mm, it is possible to estimate N for various groove densities (if we suppose the ideal case where the whole surface of the grating is used). For a central wavelength around 650 nm and $k = 1$, the

[14] Usually defined as $\frac{\mathrm{d}\theta_d}{\mathrm{d}\lambda}$, its expression is $\frac{kn}{\cos(\theta_d)}$.

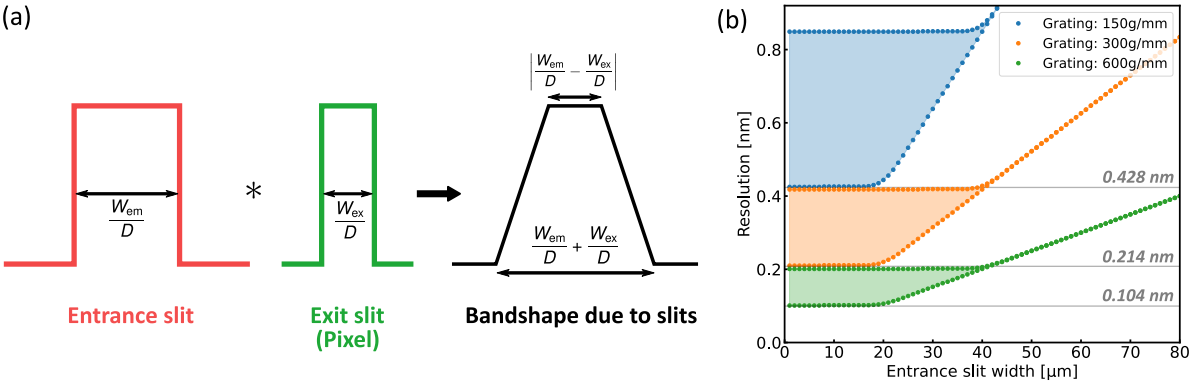

Figure 2.24: (a) Schematic representation of the convolution between the bandpath due to the entrance slit and the bandpath due to the exit slit (or in our case a pixel of the camera). (b) Resolution as a function of the entrance slit width, calculated for the three available gratings, with central wavelength at 650 nm. The lower bound for each grating is given by a grey line. The colored areas correspond to the possible value interval of the resolution, limited by a lower bound (the detected peak is limited by one pixel) and an upper bound (the detected peak is distributed on two pixels).

grating at 150 g/mm ($N = 10200$) yields a FWHM around 6.4×10^{-2} nm, and the one at 600 g/mm ($N = 40800$) yields a FWHM around 1.6×10^{-2} nm.

Other contributions to the resolution of a monochromator are the entrance slit width (tunable) and the exit slit width (tunable) or pixel size of the detector (fixed). In the configuration of our spectrometer, the entrance slit is imaged on the surface of the detector, with no magnification in our case since both spherical mirrors have the same focal length. Neglecting any curvature effect, the linear dispersion D on the detector's surface can be determined by multiplying the angular dispersion by the focal length of the spherical mirror (M2)[15]. If we consider a rectangular entrance slit with width W_{en}, the spectral broadening due to its finite size would result in a rectangular profile with width W_{en}/D. If we now take into account an exit slit with width W_{ex}, the resulting broadening due to both slits would be the convolution of both rectangular profiles, as shown in Figure 2.24(a), which has a FWHM equal to the maximum between W_{en}/D and W_{ex}/D [155]. In the case of a camera, the pixel plays the role of the exit slit. Therefore, given the fixed size of a pixel, if W_{en} is lower than W_{ex} (here the size of a pixel), the effect of slits will be dominated by the pixel size.

For our spectrometer, the width of the entrance slit can be tuned manually and the size of a pixel on the camera is fixed at 20 µm. With a central wavelength at 650 nm, the linear dispersion[16] for the 150 g/mm grating is around 47.2 µm/nm, and for the 600 g/mm

[15] $D = f' \times \frac{d\theta_d}{d\lambda}$.

[16] The spectrometer works with a fixed deviation angle ($\theta_{dev} = \theta_d - \theta_0 = 29.5°$). Using the definition of the linear dispersion and geometric analysis, the linear deviation can be expressed as:
$D = f'nk \times \cos\left(\frac{\theta_{dev}}{2} + \arcsin\left(\frac{k\lambda n}{2\cos(\theta_{dev}/2)}\right)\right)^{-1}$.

one, around 201 µm/nm. In the case where we are dominated by the size of a pixel, the FWHM of the resulting profile with 600 g/mm can therefore be estimated at 9.9×10^{-2} nm (0.29 meV or 70.3 GHz).

Finally, if we convolute the different contributions to the instrument line profile, we can see that the only parameters we can play on to change the resolution is the groove density or the width of the entrance slit. Since the FWHM of the profile due to the pixel size is an order of magnitude larger than the FWHM due to the diffraction profile, the resolution of the spectrometer is thus dominated by the size of a pixel (in the case where the width of the entrance slit is lower than the size of a pixel). In Figure 2.24(b), the resolution (*i.e.* the minimum measurable linewidth) for a central wavelength at 650 nm is calculated for various slit widths and for the three gratings at our disposal. For each grating, two curves are calculated: a lower bound, where the exit slit width corresponds to one pixel (20 µm), and a higher bound, where the exit slit width is estimated at two pixels (40 µm). The higher bound takes into account the case where, when measuring a spectrum equally distributed on two adjacent pixels, the FWHM of the measured profile would be equivalent to two pixels.

Conclusion

In this chapter, I have described the various experimental methods we use to study GQDs, from their synthesis and their inclusion in samples to the various possible spectroscopic measurements at our disposal. As we will see in the next chapters, both ensemble and single-object measurements provide complementary informations on the photophysics of the object.

Chapter 3

Investigation on fluorescent impurities in single-molecule experiments

Contents

Introduction

One may rely on different methods in single-molecule experiments in order to isolate the signal from a single object. Spectral selection by resonantly exciting a chosen object can result in an efficient selection method, since only a few resonant objects with the corresponding transition will be probed among a larger pool of fluorescent objects (notably efficient when considering narrow transitions, for instance at low temperature). Another method, chosen in our group, consists in a non-resonant excitation, which consequently means that all the fluorescent objects absorbing at this excitation energy will emit light, including non-desired objects present in the sample. We must thus resort to spatial selection in order to isolate single objects, which relies on a carefully chosen matrix and a controlled low concentration of objects of interest. However, a possible downside is the difficulty to distinguish the objects of interest from fluorescent impurities in the samples used to embed the object of study. Therefore, before focusing on the study of graphene quantum dots (GQDs), I would first like to discuss the possible impurities encountered in single-molecule experiments, and more particularly impurities sharing spectral features similar to those of GQDs. The work described in this chapter had two main motivations: bringing more insight into the nature of the impurities encountered, and developing experimental conditions to prevent the impurities to interfere with our study of GQDs.

After giving a quick overview of the few studies reported in the literature performed on contamination in single-molecule experiments in a first section, I will describe the single-molecule spectra observed for impurities in our samples at room temperature in a second section. I follow in a third section with the characterization at low temperature and the discussion on the vibrational modes observed for the impurities. Since the origin of the contamination in our case was not clear, we performed tests in order to investigate it, which I describe in a fourth section. Finally, I detail the method chosen in order to minimize the effect of impurities in the observations at room temperature, relying on the thickness of matrix film.

In this chapter, the vast majority of samples are prepared using the protocol given in Chapter 2. If not specified, the solvent used is 1,2,4-trichlorobenzene (TCB) and the solid matrix is polystyrene (PS).

3.1 General context and obstacle for GQD studies

As mentioned in the introduction of this chapter, we choose to study graphene quantum dots (GQDs) by exciting them non-resonantly. The selection of GQDs is therefore performed by diluting the solutions used to prepare the samples for single-object measurements, in such a way that the probability to observe two GQDs in the same probed optical spot becomes negligible. However, if fluorescent impurities are found to absorb at the excitation wavelength, their emission could then be detected, and they would appear as additional bright spots in photoluminescence spatial maps.

We can distinguish three characteristics which make the presence of impurities troublesome for single-molecule studies: (1) localized emission of single photons, (2) rela-

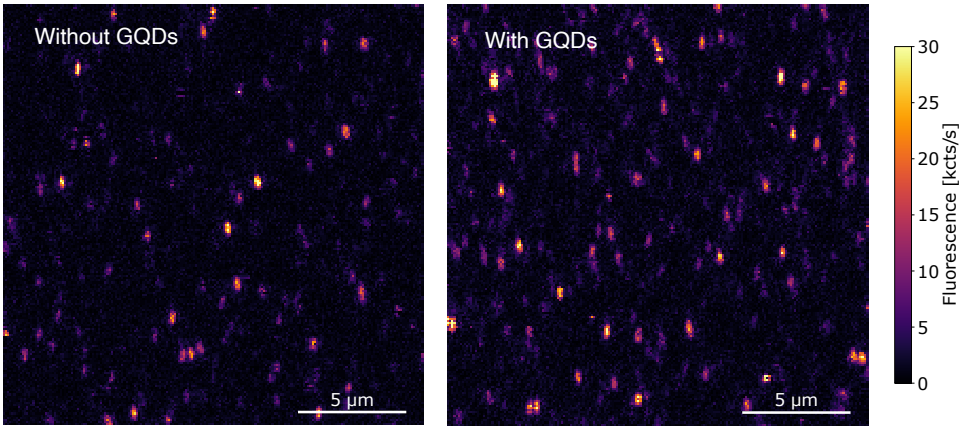

Figure 3.1: Typical map for samples without (left) and with (right) GQDs, prepared with a polystyrene concentration of 1 wt%. All maps are obtained with excitation at 594 nm and 100 W/cm^2.

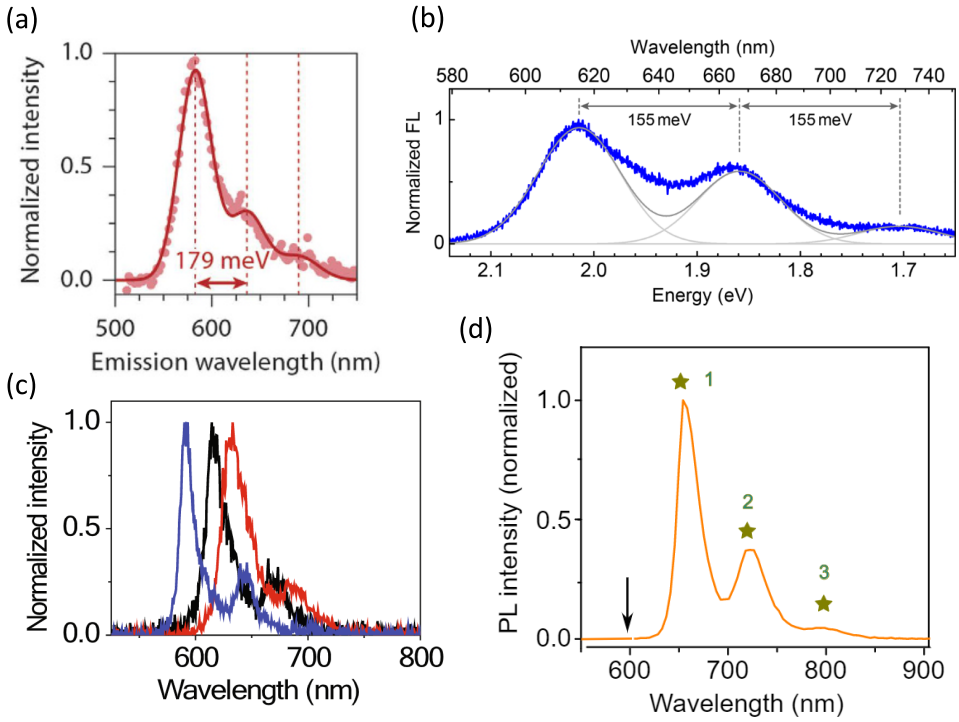

Figure 3.2: (a)-(c) Example of photoluminescence spectra of previously-reported single-photon-emitting impurities: (a) single defects in silica subtrates, from [156], (b) impurity observed in PMMA formulated in anisole, from [157], (c) impurity observed in toluene deposited on glass, from [158]. All spectra were obtained with excitation at 532 nm. (d) Reported spectrum of a single $C_{96}C_{12}$ graphene quantum dot, from [145].

Studied system	Established origin	Source
Polyethylene, n-hexadecane	Organic molecule, common in organic solvents	Fleury *et al.* [159]
Silica substrates	Defects in silica substrates	Rabouw *et al.* [156]
Toluene on cover glass	Impurity in solvent (toluene)	Trinh *et al.* [158]
PMMA prepared in different solvents	Impurity in polymer matrix	Neumann *et al.* [157]

Table 3.1: Example of studies investigating the origin of single fluorescent emitters.

tively high brightness and (3) high concentration in the samples. Their behavior as single-photon emitter makes them undifferentiated to other single emitters of interest investigated at the single-object level. Moreover, the fact that the brightness of the impurities is comparable to the intensity of other single emitters makes them easily observable, and may even hinder the observation of the fluorescent emitters of interest if the impurities' intensity is too high. And finally, the density of impurity spots increases drastically the probability of encountering impurities during measurements. In Figure 3.1, a typical map of a sample with only impurities is compared to a sample where graphene quantum dots are added in the polystyrene matrix, both for a concentration of polystyrene of 1 wt%. As we can see, although there is a clear higher density of spots when GQDs are added, the map with only impurities exhibits spots with the same level of intensity as when GQDs are added.

Multiple studies performed on different systems have reported the observation of impurities. And, to our regret, the origin of the contamination is still to this day not fully understood. One of the first reports of impurities in single-molecule spectroscopy concerned impurities observed in both cristalline n-hexadecane and poly-ethylene [159]. Due to the close resemblance to spectra of organic molecules, this impurity was termed molecule X by the authors. Given the observation of this impurity in two strongly different matrices (the first crystalline, the other polymer), synthesized in the industry via two complete different methods, the authors predicted this impurity to be common in organic solvents. More recently, the observation of emission from defects in silica substrates added a new source of possible emitters in single-molecule experiments [156]. In addition to that, other reports have focused on the observation of impurities in samples with only solvent deposition (toluene for instance) [158], or with various preparation methods of poly(methyl methacrylate) (PMMA) films [157], in order to shed more light on the possible origin of impurities. Neumann *et al.* have in particular demonstrated, using PMMA deposited on perforated silicon nitride membranes, that emitters could be found in zones with no substrate, leading them to conclude that their emitters originate from the PMMA film itself. While the large range of conceivable solvent-matrix systems could hint to a possibly large range of different contaminating emitters, the various reports strikingly exhibit the same spectral structure when performing photoluminescence measurements on single impurities. As shown in Figures 3.2(a), (b) and (c), the spectra

all share a structure with one main peak at wavelength ranging from 560 to 620 nm, followed by weaker redshifted peaks, with an energy split between the peaks of around 155 to 180 meV. Although we do not doubt that the nature of the emitters observed in clean substrates are different than those observed in solid matrices, the close resemblance between the spectra complexifies the possibility of determining the exact origin of the contamination in a given sample. The results obtained for systems close to the one used for the study of GQDs are summarized in Table 3.1. Interestingly, the various studies cited in this table point towards the possibility to observe impurities both in the substrate and in the deposition layer.

We have not found any literature reporting the same combination of solvent and polymer as the one chosen for our experiments. Nonetheless, we do not neglect the possibility that the impurity observed in our samples shares a common structure as impurities observed in other systems.

As it was shown in Figure 3.1, the impurities observed in single-object samples represent an obstacle for a clean study of GQDs, possibly inducing wrong interpretations resulting from their observation, as it has been seen for example in [160]. In our case, an additional difficulty arises from the close resemblance between spectra from impurities and from GQDs in terms of spectral lineshape and emission wavelength. An example of a single-object photoluminescence spectrum measured for a graphene quantum dot is shown in Figure 3.2(d) as reported in [10]. The structure is very similar to the spectra given in Figures 3.2(a)-(c), and to the spectra of impurities observed in our case, as described in the next section. This prevents *a priori* any possible spectral selection by using filters or any discrimination based on the measurement of a spectrum. We therefore need to have more insight on the properties of impurities in order to find discriminating criteria.

3.2 Characterization of impurities at room temperature

To first characterize the properties of impurities, I focus on samples without GQDs. Thus, in Figure 3.3(a), I show a typical raster scan of a sample prepared with only polystyrene (PS) and 1,2,4-trichlorobenzene (TCB), in a concentration of 1 wt% of PS in TCB, with excitation at 594 nm. Each bright spot corresponds to local emitters. By measuring the autocorrelation function (described in Chapter 2), we can determine which spots correspond to single emitters (vanishing autocorrelation function at zero delay, as shown in Fig.3.3(b)). As reported in the literature described in the previous section, the impurities observed in such samples do behave as single-photon emitters.

A typical spectrum measured on these bright spots is shown in Figure 3.4(a). We recover the similar structure as observed for previously-reported impurities, composed of a first strong peak followed by two redshifted peaks with decreasing intensities. In the case of the spectrum shown in Fig.3.4(a), the peaks are located at 597 nm, 653 nm and 718 nm. The energy split between these lines amounts to 178 meV and 172 meV. The structure of the spectrum is characteristic of aromatic compounds, with the first peak (labelled peak **1** for clarity) corresponding to the purely-electronic transition and the redshifted peaks to vibronic replica. The energy split between the successive peaks cor-

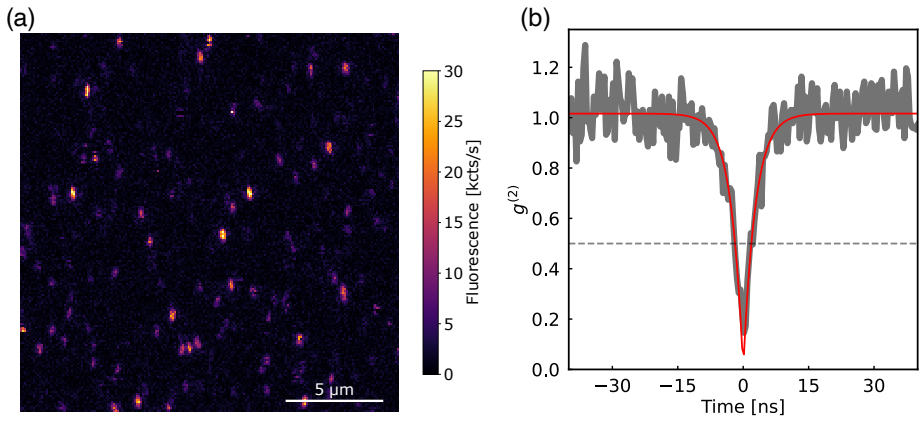

Figure 3.3: (a) Example of a spatial map of a polystyrene film (prepared from a solution at 1 wt% in TCB) at room temperature (excitation at 594 nm, 100 W/cm^2). (b) Typical second-order autocorrelation function measured on diffraction-limited spots.

responds to the energy of the vibrational mode yielding the replicas. In our case, the energy split is consistent with values usually associated with the C=C bond stretching, which reproduces the behavior observed for other impurities and hints to the organic nature of the emitter. However, emitters in different systems have shown similar behaviors, such as defects in silica, which exhibit a similar energy split [156], or even local defects in hBN [161]. Therefore, even if it is tempting to associate the observed impurities to an aromatic compound, given the use of aromatic solvent and matrix, we cannot exclude different origins for our impurities, such as activated defects at the surface of the glass substrate.

We perform measurements on a large number of impurities in order to estimate the dispersion of the spectral features. Since a number of impurity spectra are cut by the 600 nm filter, as it was the case in the spectrum given in Figure 3.4(a), we chose to excite the spectra at 532 nm. Interestingly we note that the spectra of the impurities does not change as the excitation energy is changed, as shown in Figure 3.4(a). This indicates that the light emission results from intrinsic fluorescence from the object and does not depend on the excitation energy, in contrast for example to Raman features. This behavior is for example expected for usual organic molecules. In Figure 3.4(b), the histogram of the position of the most intense peak (peak **1**) is plotted. We can see that the position of peak **1** extends on a large range of wavelength, from 565 nm to 640 nm. This wavelength range is the same as reported for the impurities mentioned in the previous section. If we now look at the distribution of the energy split between peak **1** and **2**, given in Figure 3.4(c), it follows a Gaussian distribution centered around 165 meV, with a standard deviation of 5 meV, which strongly ressembles the distribution centered at 167 meV reported for impurities in toluene [158]. It is interesting to note that the energy presents a much narrower distribution compared to the distribution of peak **1**, indicating that the physical cause of the wavelength dispersion does not affect the vibrational frequency related to the vibronic transition.

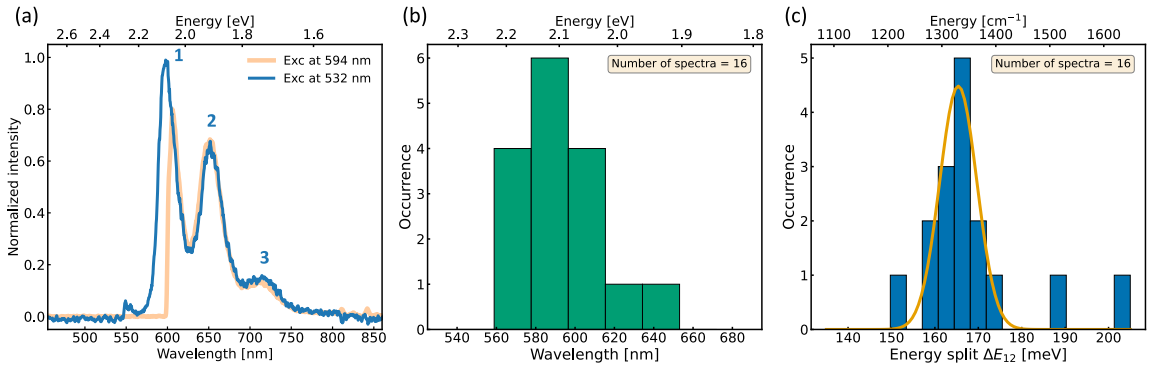

Figure 3.4: (a) Example of a spectrum observed for an impurity at room temperature, excited at 594 nm (in orange) and at 532 nm (in blue). (b) Distribution of the wavelength of peak **1** (with excitation at 532 nm). (c) Distribution of the energy split between peaks **1** ad **2**, fitted to a Gaussian distribution (orange curve).

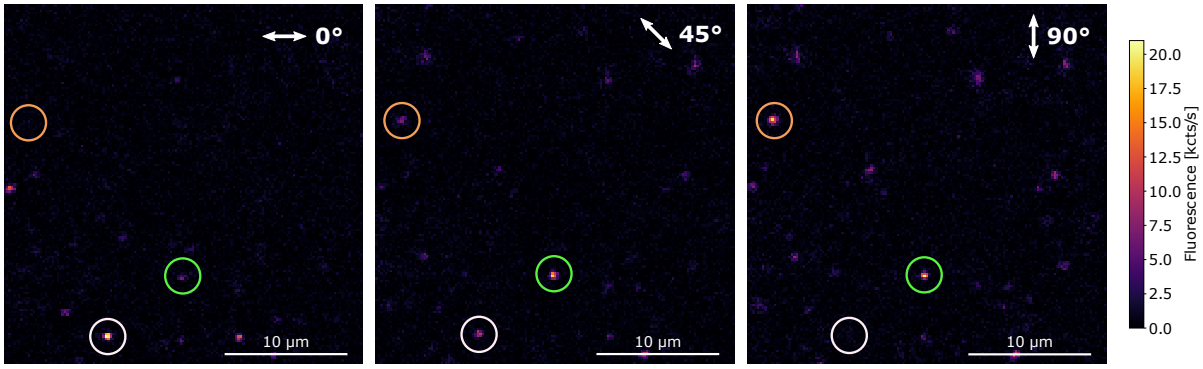

Figure 3.5: Raster scans for three different linear polarizations, oriented at 0°, 45° and 90° (arrows schematically indicate the relative polarization orientation). White circle highlights an emitter with dipole oriented along 0°. Green and orange circles highlight emitters with dipole oriented along 90°.

We probed the polarization-dependence of the emission of impurities by changing the orientation of the linear polarization excitation. In Figure 3.5, maps collected with different orientations (0°, 45° and 90°) are shown. As it can clearly be seen, some spots show a maximum intensity when excited with 0° and become dark with 90° (an example circled in white), while others not excited with 0° polarization are brightened when excited at 90° (an example circled in orange). We recover fluorescence from both spots when excited at 45°, with a lower fluorescence intensity collected. While a more complete study of the polarization dependence should be performed to confirm it, we are confident that this observation results from the dipolar nature of the impurities' fluorescence. This polarization-dependence may guide us on the nature of the contaminating emitter.

To sum up this section, we can say that the single-molecule spectroscopy performed on single impurities yielded results similar to impurities observed by other groups, such as impurities found in toluene [158], or in other solvents [157]. Their behavior is reminiscent of the emission of organic fluorophores and gives clues towards unraveling the nature of the contamination.

3.3 Low-temperature signature of impurities

Using the low-temperature setup, we can cool the samples down to 7 K. Going to low-temperature induces a line-narrowing of the spectral features observed at room temperature, as expected for organic single-emitters at low temperature [71], and enables the observation of additional fluorescence lines which were not resolved at room temperature. The physics of low-temperature spectroscopy will be more extensively discussed in the next chapter when we shall focus on desired emitters. In our present case, we would like to simply describe the behavior, without trying to speculate too much on the interpretation since the exact nature of the discussed object is not yet clear.

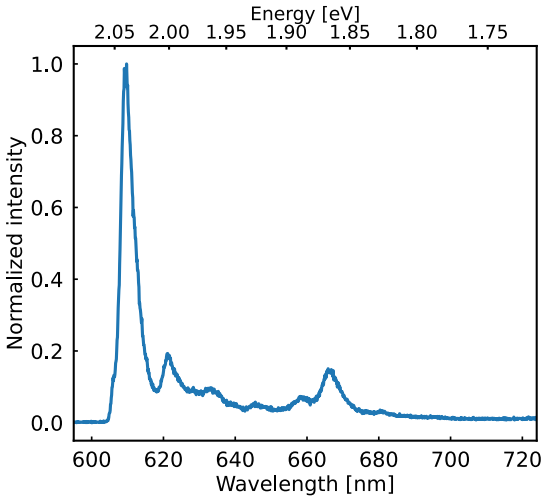

Figure 3.6: Example of a spectrum of a single impurity at low temperature (7 K).

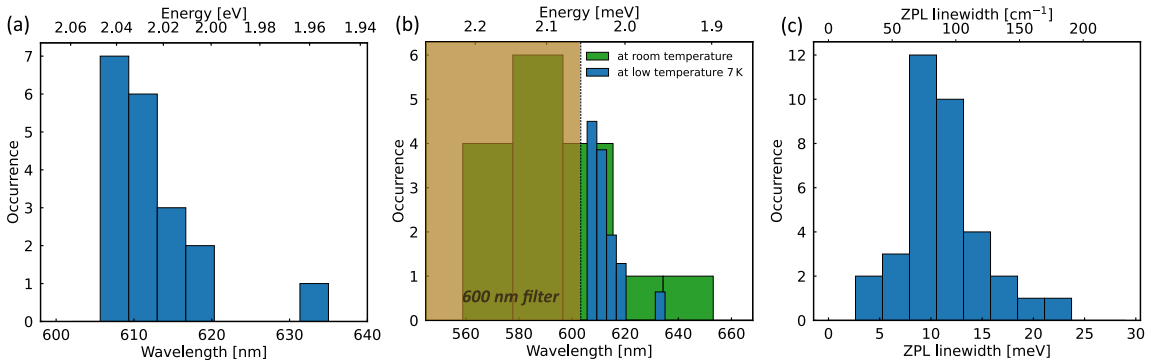

Figure 3.7: (a) Distribution of the wavelength of the ZPL for impurities (excitation at 594 nm) at 7 K (19 spectra). (b) Comparison with the distribution at room temperature (excited at 532 nm). The distribution at 7 K is rescaled for clarity. A shaded area indicates the region cut by the 600 nm filter. (c) Distribution of the linewidth of the ZPL at low temperature.

As shown in Figure 3.6, the spectra observed from impurities exhibit multiple narrow peaks, with one strong peak at high energy, the zero-phonon line (ZPL) here at 609.4 nm, followed by redshifted vibronic peaks, which correspond to electronic transitions accompanied by the creation (or annihilation) of a phonon. We will focus with more details on these spectra exhibiting line-narrowing, which are the spectra likely to be mistaken for GQDs.

Let us first focus on the ZPL. We measured the energy of the ZPL accross multiple samples, with excitation at 594 nm, and plotted the distribution of the ZPL position. As shown in Figure 3.7(a), the ZPL are found below 620 nm (except one around 633 nm), which is consistent with the distribution observed at room temperature. In fact, we can clearly observe that this distribution satisfyingly corresponds to the redmost part of the distribution obtained at room temperature with 532 nm excitation (Fig.3.7(b)). The cut off of the distribution at 600 nm results from the excitation method used at low temperature (excitation at 594 nm and collected light filtered at 600 nm) which prevents the observation of spectra with ZPL at higher energy). Concerning the distribution of the linewidth, the distribution is given in Figure 3.7(c). The distribution is centered at a linewidth value of 11 meV, which is significantly lower than at room temperature (linewidth at around 90 meV). This results from the line-narrowing of the transition as the temperature is lowered, indicating that the broadening at room temperature originates from temperature-dependent phenomena, such as coupling to a phonon-bath [71].

We now focus on the vibronic peaks following the ZPL. Since these peaks correspond to an electronic transition accompanied with the creation (or annihilation) of a phonon, the energy difference between the ZPL and the vibronic features corresponds to the energy of the phonon, directly linked to the frequency of the corresponding vibrational mode. Therefore, we can measure the frequency of the vibrational modes observed for the impurity by measuring the energy redshift of each vibronic peak, as shown in Figure 3.8(a). Accross multiple samples, we manage to isolate 5 characteristic vibrational modes measured on all the impurity spectra observed. The distribution

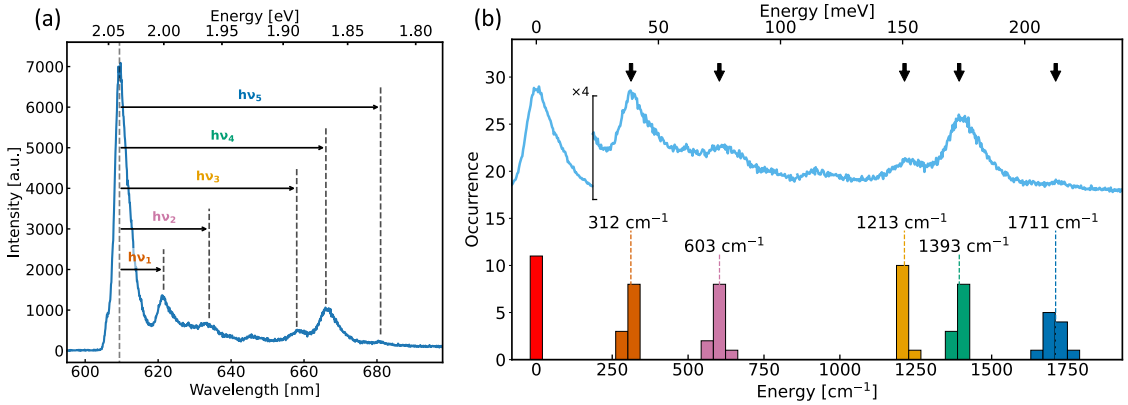

Figure 3.8: (a) Measurement of the energy of the vibrational modes for impurities. The redshift of each vibronic feature relatively to the ZPL (black arrows) correspond to the energy of the vibrational mode. (b) Distribution of the five vibrational modes observed for impurities. A typical impurity spectrum is plotted in blue for clarity and arrows indicate the corresponding modes.

of these 5 modes is given in Figure 3.8(b). The average values of these five modes are 312 cm^{-1}, 603 cm^{-1}, 1213 cm^{-1}, 1393 cm^{-1}, 1711 cm^{-1}, with respective standard deviations of 12 cm^{-1}, 17 cm^{-1}, 10 cm^{-1}, 10 cm^{-1}, 31 cm^{-1}. The different vibrational modes share similar dispersions, except for the mode at highest energy which exhibits a higher dispersion, but this may be due to the difficulty of precisely pinpointing the position of this peak. As indicated at room-temperature for the energy split between the emission peaks, vibrational modes around 1300 cm^{-1} are usually observed in organic compounds. The resolution at low temperature enables us to distinguish three modes around this value (the three high-energy modes). The existence of multiple vibrational modes in this frequency range has been reported for various organic compounds, and are usually associated with stretches of C=C bonds located in different parts of the molecule [162].

We have in our case focused only on five modes for our impurity. However, other observed modes have not been taken into account because of the difficulty of observing them in all the spectra with an appreciable signal-to-noise ratio (*i.e.* high enough to measure their position). For instance, the spectrum represented in Figure 3.8(a) clearly exhibits at peak at 646.5 nm, corresponding to a mode at 940 cm^{-1}.

It is interesting to compare our results with previously-reported impurities. We have chosen to compare the vibrational modes of our impurity with results reported for molecule X in hexadecane [159] and for impurities found in PMMA [157]. Given the conditions in which these impurities are observed, they are *a priori* not related to each other.

In Figure 3.9, we compare the position and the relative intensity of the vibrational modes with values reported for the other systems. The vertical blue lines correspond to the average value of the vibrational modes observed and plotted in Figure 3.8(b). The width of the vertical blue lines correspond to the standard deviation of each vibrational mode. The black vertical lines correspond to vibronic lines reported for each impurity chosen for comparison, with the heights corresponding to the relative values of the os-

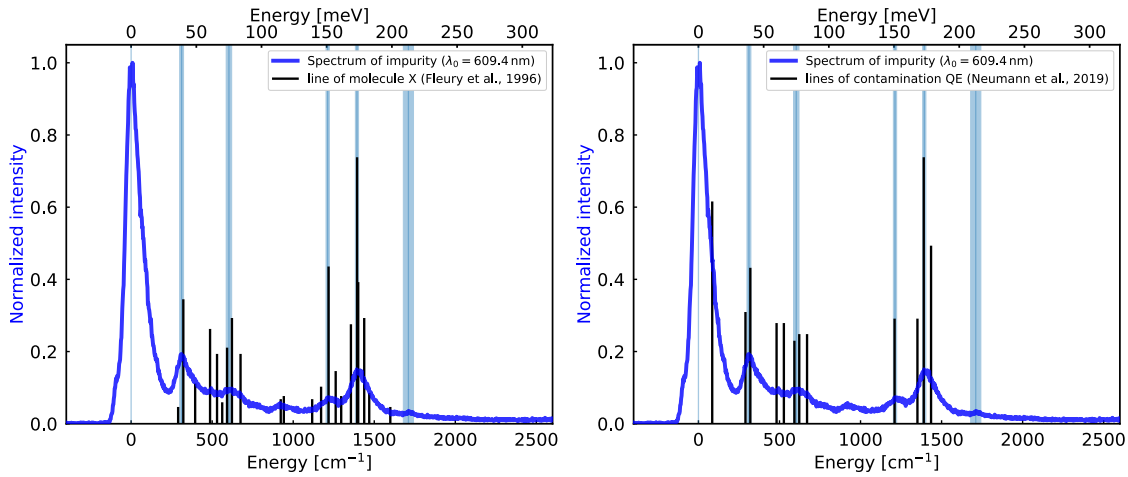

Figure 3.9: Comparison of the vibrational modes of impurities with previously reported systems: with (left) molecule X [159] and (right) a contaminating quantum emitter (QE) [157]. Black lines correspond to reported vibronic transitions for each system, with the height corresponding to the relative oscillator strength of each transition. Blue vertical lines indicate the vibrational modes of the impurity observed in our system, with the width corresponding to the standard deviation of each mode.

cillator strength. We clearly observe a striking correspondence between the modes we observed in our system with the ones reported for the other impurities, in particular the modes at 312 cm^{-1}, 603 cm^{-1}, 1213 cm^{-1} and 1393 cm^{-1}.

As mentioned above, additional modes have not been selected for our impurities due to the difficulty of finding them in all the spectra measured. Nonetheless, these modes can interestingly be observed in other impurity spectra, as it is shown in the comparison with molecule X (left of Fig.3.9) for the mode at 940 cm^{-1}. Moreover, we suspect that other modes observed in other impurities may exist for our impurity but are not resolved with our experimental setup, as for instance at around 500 cm^{-1} (where a faint peak can be distinguished on the blue spectrum).

The observations at low temperature have revealed that the impurities observed in our samples strikingly share spectral features (notably the vibrationnal modes in the vibronic progression) with other impurities associated with organic contamination of solvents observed in other systems.

3.4 Investigation on the origin of the fluorescent impurities

As mentioned in Section 3.1, since no test using our exact combination of solvent, matrix and substrate has been reported to our knowledge, we decided to perform control experiments to investigate the possible origin of the impurities observed and characterized. Given the possible sources of impurities reported in the literature, we distinguish two main origins for the fluorescent impurities observed in our single-objects experiments:

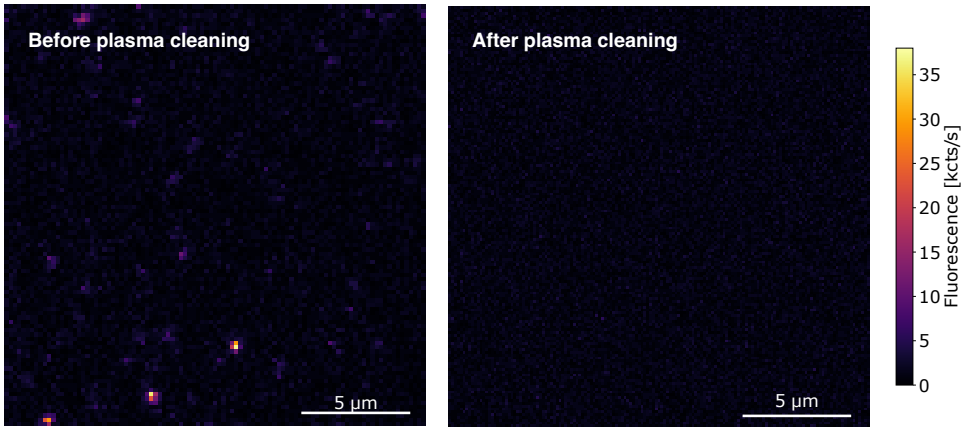

Figure 3.10: Effect of oxygen plasma treatment on Schott coverslip (Excitation at 594 nm and 100 W/cm^2).

they may arise (1) from impurities in the polymer film (originating from solvent or matrix) or (2) from emitters in the substrate.

I will first describe the tests performed on each raw material chosen for our experiments, then rapidly discuss the possibility of contamination during sample preparation. Given the difficulty of precisely determining the origin of the impurities, a small recapitulation of the observations is given at the end of the section in order to give a clearer overview.

Three actors intervene in the fabrication of single-object samples, and can be listed as possible origins: the substrate (Schott coverslip glass), the solid matrix (polystyrene) and the solvent used to dissolve the emitters and the matrix (1,2,4-trichlorobenzene). We will limit our discussion to a few specific tests performed for each of the three actors listed.

Instrinsic emitters in substrates

Let us first focus on the substrate used to deposit the samples. Before discussing the effect of the substrate chosen for the deposition, we will mention the importance of the cleaning process. All the different substrates tested present fluorescent impurities when unpacked. For all the substrates used, we perform oxygen-plasma cleaning in order to eliminate all the organic impurities initially on the subtrates. As reported by various teams [163, 157], we observe no emitters on the surface after treatment, an example is given Figure 3.10 with excitation at 594 nm. We conclude that, for bare cleaned substrates, no contamination can be reported for any of the substrates tested.

We now focus on the tests performed on different substrates when we deposit films. As reported in the literature, depositing films may stabilize or activate surface emitters in substrates [158, 164]. The substrate chosen for single-molecule experiments is D 263® glass from Schott, which is a borosilicate-type glass. We compared the effect of the substrate by testing two other materials: lanthanum-doped glass (S-LAH79), used as solid

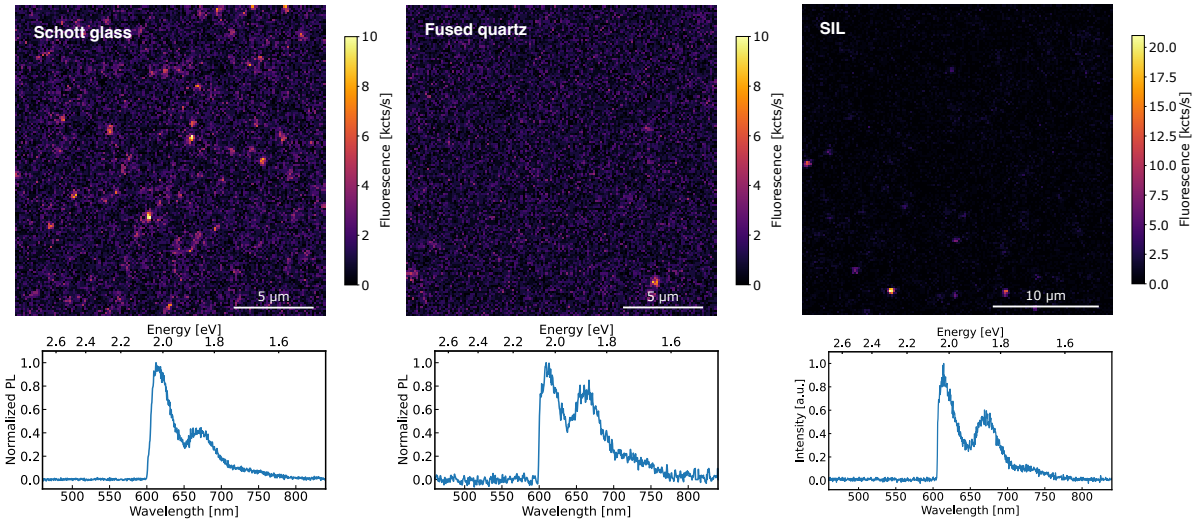

Figure 3.11: Influence of the substrate. Comparison of raster maps on (left) Schott glass, (center) fused quartz and (right) SIL, after deposition of PS films formulated in TCB (Excitation at 594 nm with 100 W/cm^2 for Schott glass and fused quartz, with 1.6 kW/cm^2 for SIL). Typical spectra are given for each sample. The concentration of PS is 5 wt%.

immersion lens (SIL) for single-object experiments on the low-temperature setup (see Chapter 2), and fused quartz coverslips (type GE 124 from EMS). In Figure 3.11, I present spatial maps obtained for plasma-cleaned substrates after deposition of a PS film formulated in TCB via spincoating. On all three substrates, bright spots can be detected, although we note a smaller density of spots for fused quartz than for Schott glass, and the measured PL spectra confirm the observation of the impurity of interest. The observation of impurity is thus not specific to one substrate. Therefore, in the case where the impurity should originate from the substrate, it would be common to all three substrates tested. Since the tested substrates all consist of silica SiO_2, the impurities could result from silica defects[1], as reported in [156]. Nevertheless, we have to keep in mind that no spots were observed before film deposition, indicating that if impurities originate from the substrate, deposition of films is required to observe appreciable fluorescence.

Effect of the matrix

Samples are generally prepared using PS (bought from Sigma Aldrich). In order to compare the effect of the matrix on the presence of impurities, we prepared samples using Zeonex 330R, another commonly-used polymer for single-molecule experiments [165, 166]. In Figure 3.12, we compare maps observed using the two polymers, formulated in TCB. There is no clear difference between the two maps, and the spectra observed with either matrices share the same structure as previously reported. The impurity is thus not specific to one polymer. This indicates that either the impurity results from the solvent used (TCB), either the same impurity is found in both polymers, as suspected by Fleury

[1]The lower density of spots observed with fused quartz could then indicate a higher density of defects in Schott glass than in fused quartz.

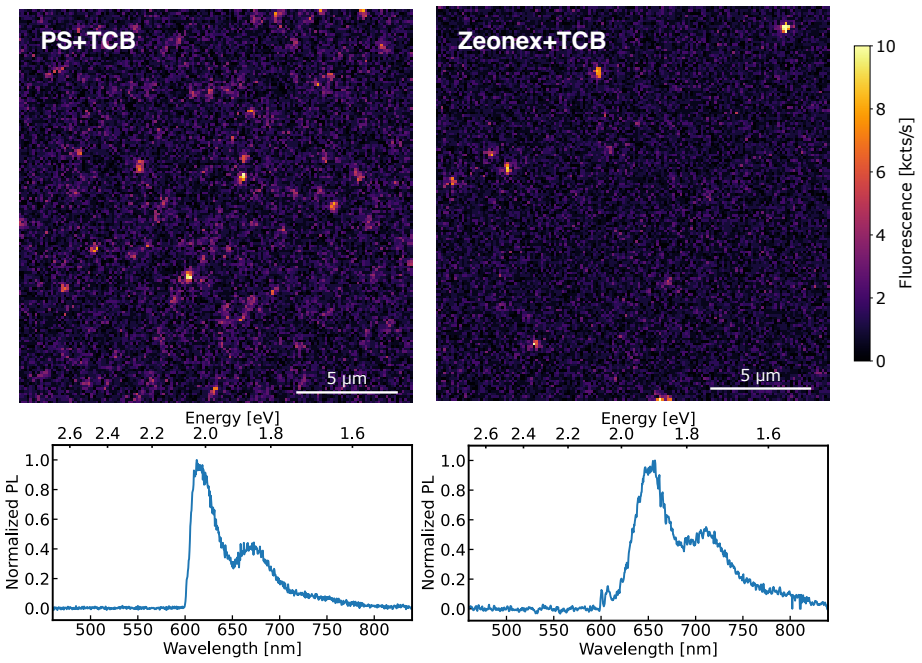

Figure 3.12: Influence of the solid matrix. Comparison of raster maps on films of (left) PS formulated in TCB, 5 wt%, and (right) Zeonex formulated in TCB, 2 wt%, desposited on Schott glass (Excitation at 594 nm and 100 W/cm^2). Typical spectra are given for each sample.

et al. [159].

Effect of the solvent

Finally, we move now to the influence of the solvent on the observation of impurities. We have performed tests with toluene (two types are used, from Sigma Aldrich and from Alfa Aesar, both spectrophotometric grade). The results show that spots can be observed in PS films prepared from either TCB or toluene (see Figure 3.13). No difference between the two types of toluene can be reported. The spectra observed from the spots share once again the same structure. We can therefore conclude that, if the impurity originates from the solvent, this impurity may be found accross various solvents.

Interestingly, we have observed that comparable maps can be observed even without any polymer matrix. By dropcasting (*i.e.* depositing drops of) TCB on the substrate after plasma treatment, impurities can be observed on the surface (although many spots bleach almost instantly when excited), as shown in Figure 3.14, with a density of spots similar to samples with a polymer matrix. The spectra collected from the few stable spots exhibited the same structure as the impurity of interest. This indication shows that the polymer matrix does not significantly contribute to the observation of impurities (except for an increased stability).

We therefore conclude that if impurities are located in the matrix, solvents are the

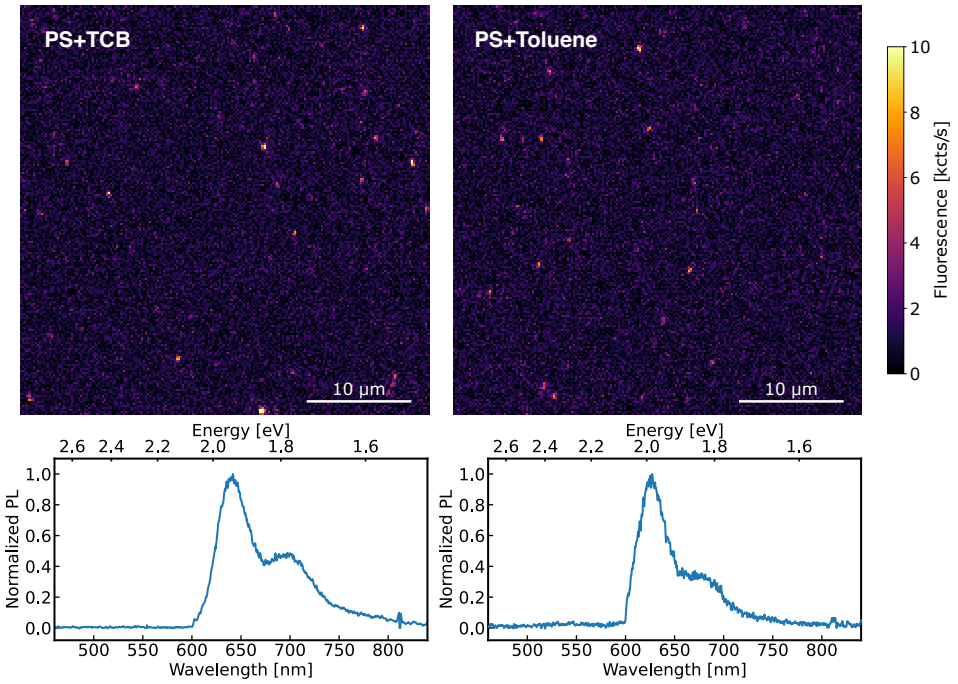

Figure 3.13: Influence of the solvent. Comparison of raster maps on films of PS formulated in (left) TCB and (right) toluene, deposited on Schott glass (Excitation at 594 nm and 100 W/cm^2). Typical spectra are given for each sample. The concentration of PS is 5 wt%.

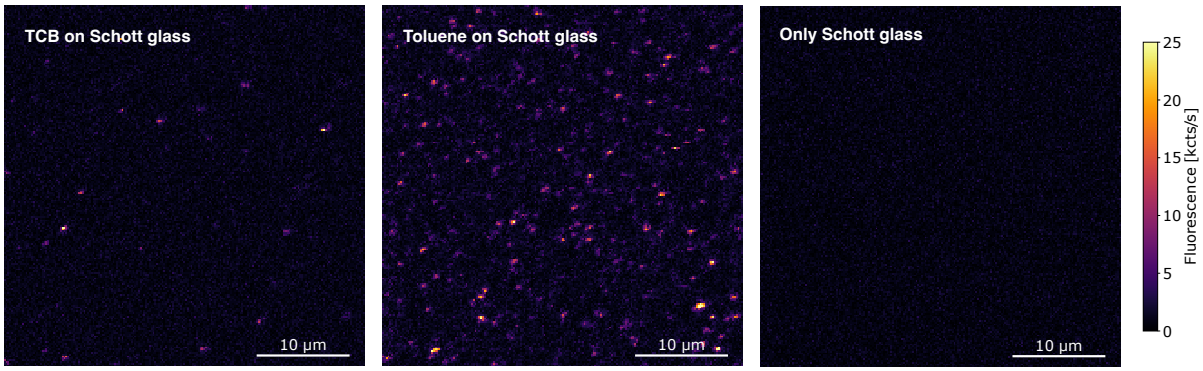

Figure 3.14: Comparison of raster maps on Schott glass after dropcasting (left) TCB, (center) toluene and (right) without any solvent (Excitation at 594 nm and 100 W/cm^2).

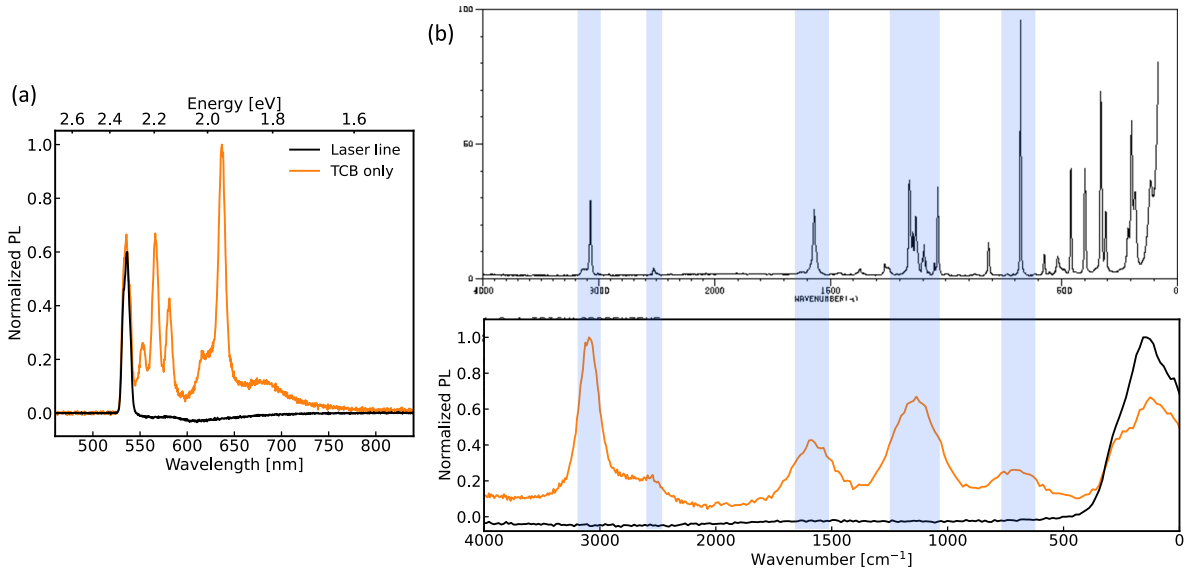

Figure 3.15: Photoluminescence spectrum of TCB in solution, excited at 532 nm. The laser line (black curve) is measured using the scattering of the laser on an empty cuvette. (b) Comparison with reference Raman spectrum of TCB (from chemicalbook.com/SpectrumEN_120-82-1_Raman.htm). The experimental PL spectra are plotted against wavenumber shifts relatively to 532 nm, the excitation wavelength.

main contributor of impurities. By considering impurities in the solvent as fluorescent organic molecules, let us roughly estimate their concentration in the solvent. Using single-molecule measurements, we can estimate impurities to emit with around the same intensity as GQDs (described in the next chapter), as shown in Figure 3.1. In Figure 3.15(a), we can see that, by exciting with high power (around 100 µW), the only peaks appearing in the PL spectrum of TCB correspond to Raman lines of the solvent (which appear broad given the large linewidth of the excitation line). We thus observe no intrinsic fluorescence from the solvent or from impurities contaminating the solvent. Since we can estimate the lowest concentration for which PL signal from GQDs was measurable (*i.e.* where the signal-to-noise ratio allows the appreciation of fluorescence features) to around 10^{-9} mol L^{-1}, we can thus estimate the concentration of impurities in the solvent to be lower than this concentration, given the absence of spectral features in PL spectrum.

Comparatively, we use GQD solutions with concentrations of 10^{-7} mol L^{-1} for single-molecule samples, which is two orders of magnitude above the limit concentration estimated for impurities in the solution. Impurities in the solvent should therefore produce a distinctively-lower density of spots in the resulting polymer film. Since we observe a similar density of impurity spots and GQD spots in samples, we can conclude that it is not possible to interpret the observation of impurities on clean substrates after dropcasting solvent by considering only contaminants in the solvent.

Possible additional experimental loopholes

I do not detail here all the various tests performed concerning other parameters, such as the cleaning of glassware and of surfaces (spincoater, hot plate) during the preparation of samples. Additional care was taken concerning the origin of the various compounds used. For instance, we usually prepare samples using solvents and compounds stored in a glovebox. Suspecting a possible contamination of the glovebox by emitters, we prepared samples using only materials which never went in the glovebox. We also borrowed solvents from other research teams, in case our stock solvents had been contaminated. All these precautions did not induce any appreciable change in the observation of impurities in our samples. We therefore rule out any effect of the experimental environment on the presence of impurities.

Complementary measurements: localization of impurities in samples

As shown by the high number of similar raster scans and spectra presented up until now, it is difficult to clearly identify the origin of the impurities by just changing one parameter. I present here one last experiment performed with the aim of localizing the position of impurities in the sample. Films of PS are usually spincoated on the substrate, yielding a thin homogeneous layer of polymer. As it can be seen in Figure 3.16 where we performed raster scans at different depths (with a step of 400 nm), the impurities seem all localized on a same plane. This is in line with the fact that the spin-coated layer is thin compared to the confocal volume probed (typically aroud 1 µm along the z-axis). Consequently, as soon as we move out of the interface substrate/PS film (labelled z_0), all the spots become simultaneously out of focus (less intense and broader in size). It is therefore impossible to distinguish if the impurities are found on the surface of the substrate or in the film layer.

Interestingly, we can choose not to use spincoating and directly dropcast PS in TCB on the substrate. Inevitably, the layer of the film is thicker than when deposited using spincoating. We present the observation in Figure 3.17. In the depth scan[2] (bottom right pannel), we can estimate the layer of polymer to be of a few µm. The most interesting result is that the spots are not all localized on the substrate/PS film interface. We can in particular observe spots which do not appear at z_0 but become bright inside the film, indicating that emitters are localized not only at the interface with glass but also within the film. Nonetheless, the density of spots is higher at the interface (z_0) than inside the film. Given the observation of spots in the bulk of the film, we can conclude that, although they are not the only source of impurities (as demonstrated in the paragraph on tests with solvents), there are indisputably impurities in the polymer layer, which result from contaminants present in the solvent.

Summary on the origin of the impurity

The origin of impurities is a discussion often avoided given the difficulty of precisely identifying the nature of the emitter, with authors remaining elusive when dealing with

[2] High excitation power is used to enhance the signal-to-noise ratio when performing depth scans

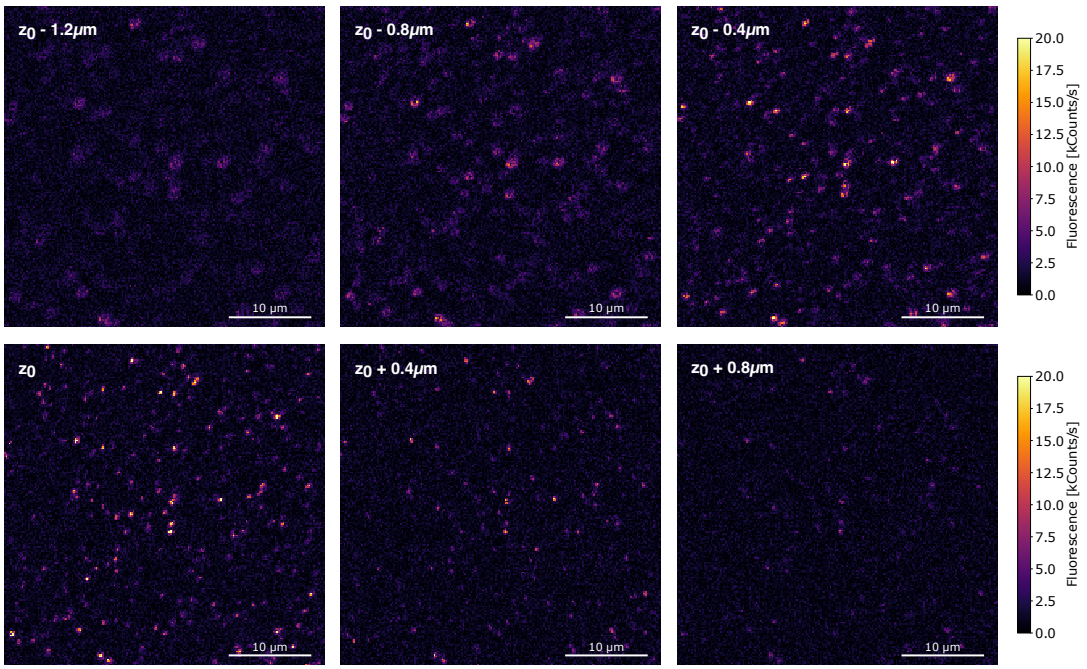

Figure 3.16: Maps at different depths for a sample prepared with spin-coating (Excitation at 594 nm and 100 W/cm^2, PS concentration of 1 wt%). z_0 indicates the interface glass/polymer film. Positive depth variation corresponds to orientation from substrate towards film.

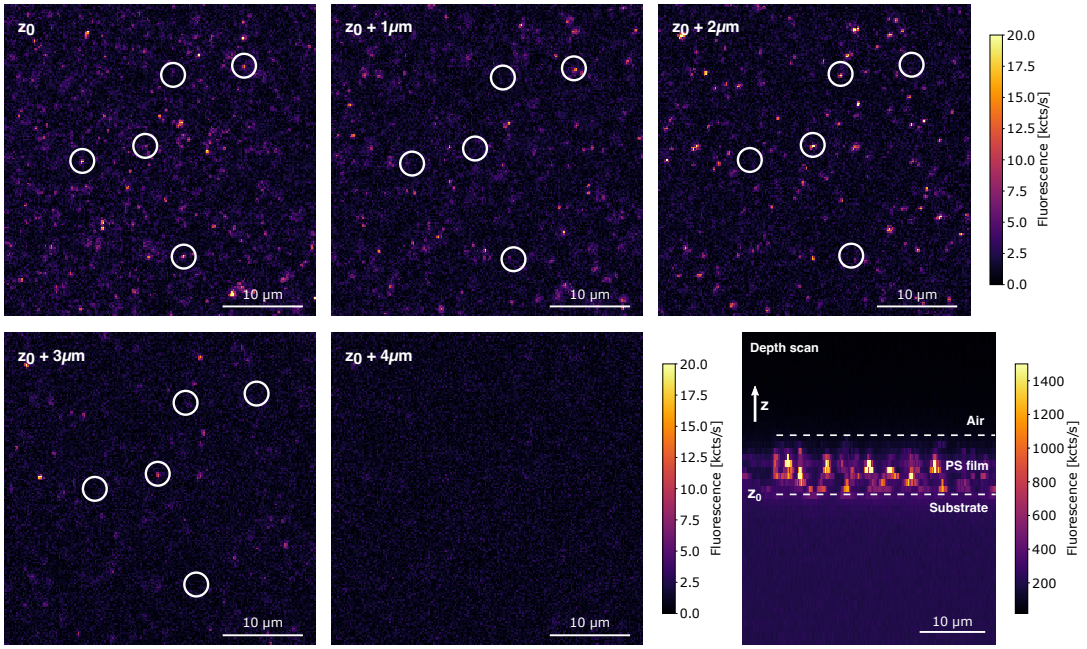

Figure 3.17: Maps at different depths for a sample prepared with dropcasting (Excitation at 594 nm and 100 W/cm^2, PS concentration of 1 wt%). z_0 indicates the interface glass/polymer film. Bottom right: depth scan of the sample along the optical axis (z-axis), showing the polymer film (Excitation at 9 kW/cm^2).

this subject [157].

Concerning our impurities, our tests could not enable us to isolate a single actor in the fabrication of samples as the only origin of impurities in the samples. Substrates alone, after plasma treatment, do not exhibit any emitter. However, as soon as a layer of solvent is deposited on it, emitters are observed. This indicates that either the solvent itself contains impurities, or emitters on the surface of the substrate are activated by the solvent. Such mechanism has just recently been reported by Ronceray *et al.* for surface defects on hBN activated by organic solvents [164]. The authors suspect chemisorption of organic solvent molecules to activate point-defects, resulting in quantum emitters in the visible range. We suspect a similar mechanism to possibly occur in our samples. Given the localization of bright spots in the bulk of the polymer film, we are certain that part of the contamination arises from solvents.

However, the absence of appreciable PL signal from the solvent sets an upper bound for the possible number of spots in single-object samples we can attribute to contaminants in the solvent, which cannot render the density of impurities observed in our samples. Therefore, a reasonable interpretation is that *both sources* (activated substrate defects and contamination from the solvent) are observed in our samples. This interpretation is in line with all the previous reports of impurities found in both substrates and solvents (and polymers).

We do not unfortunately provide a definite explanation to the close resemblance between the vibrational modes observed for our impurities with previously-reported impurities, which seems to indicate that we are observing impurities of the same nature.

3.5 Effect of thickness on the observation of impurities

In order to estimate the effect of the concentration of polystyrene used when preparing samples, multiple control samples with varying concentrations are prepared, ranging from 1 wt% to 5 wt%. Given in Figure 3.18 are maps corresponding to different concentrations of PS in the TCB solution used for film deposition. We clearly observe that as the concentration of polystyrene is increased, the average intensity of the impurity spots decreases. However the surface density of spots does not significantly change.

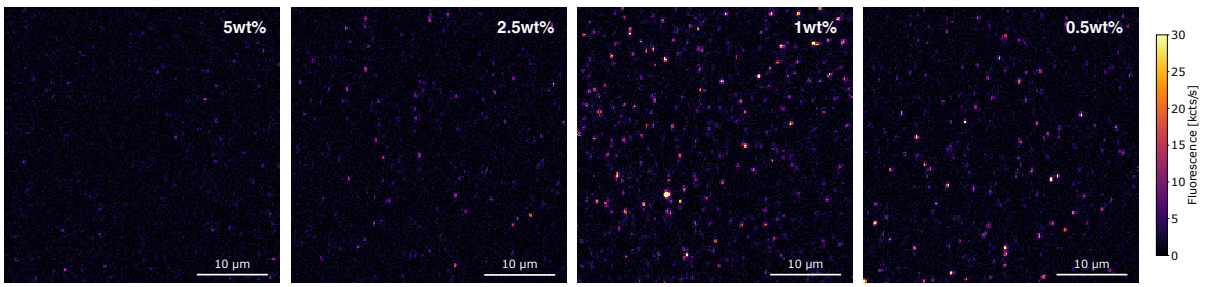

Figure 3.18: Influence of PS concentration on the observation of impurities. Comparison of raster scans with decreasing PS concentration (from left to right), ranging from 5 wt% to 0.5 wt% (Excitation at 594 nm and 100 W/cm^2).

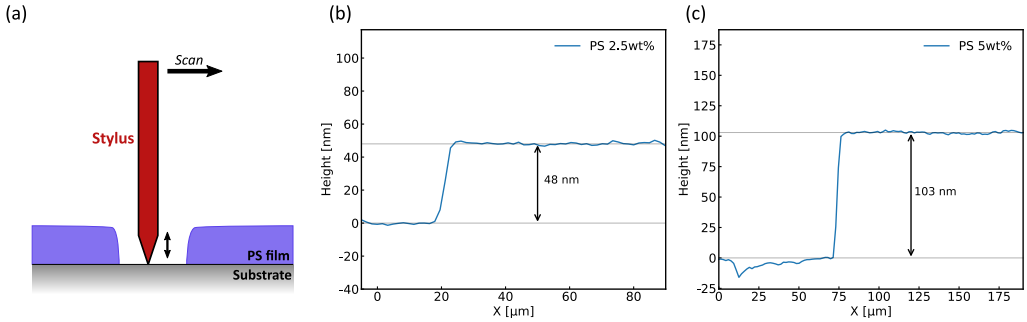

Figure 3.19: (a) Principle of the thickness measurement. The stylus measures a step as it scans the limit between the film and the razor-blade cut, corresponding to the thickness of the PS film. (b)-(c) Example of profiles measured for (b) 2.5 wt% and (c) 5 wt% concentration of polystyrene in TCB.

PS concentration	5 wt%	2.5 wt%	1 wt%
Average thickness	101 nm	43 nm	14 nm

Table 3.2: Effect of polystyrene concentration on the average thickness of the deposition layer.

The concentration of polystyrene should directly influence the thickness of the deposition on the substrate. Using our micro-photoluminescence setup does not allow us to precisely measure the thickness of the PS film deposited, as mentioned in the previous section. We therefore used a stylus-profilometer (KLA-Tencor) to scan the surface of our samples. This method uses a stylus which, in contact with the surface probed, applies a constant force as it scans a specified region. This device can therefore allow a precise measurement of the profile of the surface. For our measurements, we performed razor blade cuts on the surface of various samples, which locally leaves the substrate bare along a trench. As the stylus scans the cut, it will face a step up as it moves from the cut to the PS film (or step down as it moves from the PS film to the cut), as represented schematically in Figure 3.19(a). The difference of height measured at the step corresponds to the thickness of the PS film.

In Figures 3.19(b) and (c), we can observe the steps measured experimentally for two different concentrations of PS. We performed such measurements on various samples, and measured the thickness at different positions on a same sample to evaluate the homogeneity of the deposition. In Table 3.2, the average thicknesses measured for different PS concentration are given. We observe that as the concentration of PS decreases, the thickness of the PS layer decreases. Given our observation in Figure 3.18, this indicates that as the layer of PS increases, the efficiency of the collection of fluorescence from impurities decreases, causing the apparent decrease of the intensity of impurity spots. Due to a lack a time, we have not yet been able to perform calculations on the effect of dielectric layer thickness on the electromagnetic radiation collection, in order to explain our observation. Nonetheless, we enthusiastically admire the low average intensity of impurity spots for 5 wt% concentration. We therefore choose this concen-

tration for single-mocule experiments, as it minimizes the impact of impurities in the observations performed on objects of interest[3].

[3]Interestingly, as it will be seen in the next chapter, the increase of the PS concentration does not induce a significant decrease of the intensity of the spots associated with GQDs, which simplifies the study of single GQDs. Since we would expect the variation of thickness to have the same effect on the intensity of fluorescent spots of GQDs or of organic contaminants from the solvent, we can infer that the effect of thickness may only affect the intensity detected from surface defects. Incidently, the observed decrease of the average intensity of impurity spots is consistent with the estimation made that a larger part of impurities result from surface defects of the substrate than from contaminants from the solvent.

Conclusion

In this chapter, I have summarized the work performed on the investigation of the impurities observed in single-molecule experiments. This chapter comes as a side project in my thesis, and, as such, did not directly provide any additional information on the photophysics of GQDs. However, it was necessary to perform this work in order to safely interpret the experiments performed and described in the following chapters.

I have shown first the spectral characterization of the impurities observed in our case, at both room and low temperature. The spectral features and vibrational modes measured are strinkingly similar to those reported by other teams on different systems. By performing various tests with different substrates, solvents and matrices, we managed to identify that the impurities originate from contamination of the chemical compounds (solvent, matrix) and from the activation of surface defects on the silica substrate. Finally, tests with various polymer concentrations revealed a direct effect of the thickness of the polymer film (controlled by the concentration of polystyrene in the deposited solution) on the intensity of the impurities observed. The results of these tests have a direct impact on the single-molecule experiments with GQDs, by paving the way for a possible selection criterion based on the intensity of spots.

More generally, the work presented in this chapter also adds a brick to the general understanding of impurities in single-molecule experiements. Although the exact nature of the emitter is still to be determined, the impurities behave as single quantum emitters which could be used as such. Moreover, various questions remain unanswered, which may lead to possible investigation routes and to new physics. The possible activation of defects on the surface of silica substrates could unravel a new source of quantum emitters. Another open question is the explanation for the resemblance between the various impurities observed in different organic solvents. The nature of this emitter, which presents characteristic vibrational modes, has still not been determined, and the explanation of its presence is usually avoided.

Since the exact nature of the emitter remains unknown, understanding impurities also enables the development of methods to avoid mistaking them for objects of interest [163]. An example in our case is the choice of using higher concentration of PS for the preparation of samples. These methods can for instance rely on the control of the properties of the impurities. We could envision playing with various parameters, which could passivate the impurities and quench their emission, such as changing the solvent used [164] or applying electric fields (as demonstrated for defect emitters in hBN [167]). Another possiblity is to play on the emitter of interest (GQDs in our case) in order to clearly distinguish them from impurities, either spectrally, by choosing emitters with spectral features distinct from those of impurities, or spatially, by positioning the emitters in a controlled-manner on the substrate (as demonstrated with terrylene in para-terphenyl [168]), which would drastically reduce the probability of being perturbed by impurities.

Chapter 4

Deepened characterization of $C_{96}C_{12}$ GQD spectroscopy

Contents

Introduction

Given the broad variety of graphene quantum dots (GQDs), focusing on a particular geometry is necessary in order to fully grasp the different factors that may influence their properties. In our team, initial studies have already been performed on $C_{96}C_{12}$ (system described in more details in Sec. 4.1) during the PhD thesis of Shen Zhao [145]. Among various results, it has been shown that these objects behave as stable and bright single-photon emitters at room temperature. Building on the photophysical analysis of Shen Zhao, I have focused in my thesis on deepening the understanding of the origin of the emission from these objects. To that end, I have employed methods previously used on this system to confirm and enrich the previously-obtained results, as well as new methods to explore new physical territories. For instance, the first low-temperature studies on this GQD are carried out with the objective to take advantage of the higher spectral resolution conferred by lower temperature to gain insight on photophysical aspects of the GQD. Discussions with various collaborators, in particular chemists from CEA Saclay, Daniel Medina-Lopez and Dr. Stéphane Campidelli, and theoreticians from Université de Mons, Dr. Claire Tonnelé and Pr. David Beljonne, have greatly contributed to the analysis and conclusions described hereafter.

In this chapter, I divide the discussion by successively focusing on the different experimental methods. After first describing the studied $C_{96}C_{12}$ system, measurements performed in solution are described in a second part. In this part, I focus first on the emission from GQDs and on its origin by comparing experimental results to theoretical calculations, before moving to a discussion on the origin of additional peaks, *a priori* not related to single GQD fluorescence. In a third part, I detail the results of single-molecule experiments on $C_{96}C_{12}$ GQDs, both at room and low temperature. Room-temperature results will focus on the statistical studies I have performed to improve our understanding on the dispersion of the properties of $C_{96}C_{16}$ in our samples. I notably discuss the vibrational signature of $C_{96}C_{12}$ and the effect of the environment on the fluorescence emission. All throughout this part on single-molecule experiments, comparison with impurities described in the previous chapter are proposed and discussed. We particularly examine the possibility to confidently distinguish $C_{96}C_{12}$ GQDs from impurities.

4.1 Description of the system and the samples

The graphene quantum dot studied in this chapter is a triangular $C_{96}H_{24}(C_{12}H_{24})_6$ GQD. It is composed of a core of 96 sp^2 carbon atoms arranged in a triangular shape, with 6 alkyl chains of 12 carbon atoms on the side of the core to enhance solubility (as shown in Fig. 4.1). The sidechains are also important in order to decrease the effect of stacking, previously reported for this GQD [141].

The electronic properties of the system are dominated by the 96 π electrons, delocalized on a core showing a D_{3h} symmetry. In the case of our object, due to the presence of the alkyl chains, the whole system presents a C_3 symmetry (invariant by $2\pi/3$ rotations around the central symmetry axis of the GQD). This symmetry induces specific electronic

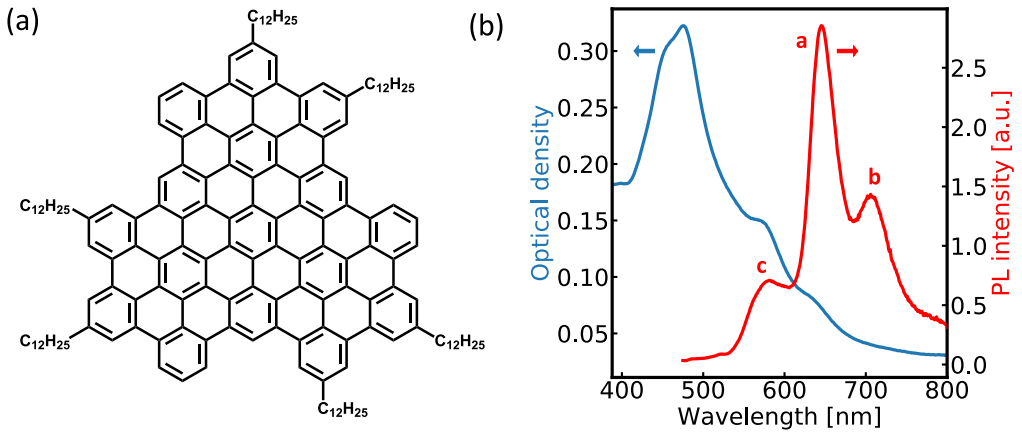

Figure 4.1: (a) Chemical structure of $C_{96}H_{24}(C_{12}H_{24})_6$ (or $C_{96}C_{12}$ for short). (b) Absorption (blue line) and photoluminescence spectrum (red line) of a $C_{96}C_{12}$ dispersion in 1,2,4-trichlorobenzene (TCB). Letters **a**, **b** and **c** identify the three main features.

properties[1], that have been theoretically investigated [44, 36] and that I will present in the following sections. Given the structure of the graphenoid core, the GQD presents a fully benzenoid structure (the structure can be written with either π sextets or "empty" rings), which bestows high stability to the aromatic compound [23].

These objects were synthesized by Dr. Julien Lavie, Daniel Medina-Lopez and Dr. Stéphane Campidelli in CEA Saclay and were delivered to us as powder. The powder was dispersed in 1,2,4-trichlorobenzene (TCB) yielding a concentration of around 3×10^{-5} mol L^{-1} for the stock solution. TCB was chosen for its high tendency to solubilize PAHs [144]. Samples for ensemble and single-object measurements were prepared following the methods described in Chapter 2.
The GQD will be referred to as $C_{96}C_{12}$ hereafter for clarity. Furthermore, we shall refer to single GQDs as GQD monomers, in opposition to dimers (stacking of two GQDs) or more generally aggregates (stacking of multiple GQDs).

4.2 Characterization of the luminescence in ensemble

4.2.1 General characterization of the $C_{96}C_{12}$ dispersion

For a first characterization of the dispersion of $C_{96}C_{12}$ in TCB, absorption spectra were measured. Figure 4.1(b) shows a typical absorption spectrum for a dispersion of $C_{96}C_{12}$ GQD powder, where we distinguish two features at 635 nm and 576 nm, followed by peaks at higher energy (475 nm and 455 nm). The structure observed is reminiscent of typical absorption spectra measured for polycyclic aromatic hydrocarbons (PAHs) [169]. The lines in the spectrum are broad, with no distinct sharp peaks observed.

[1] I will generally refer in the rest of the thesis to the D_{3h} symmetry of the $C_{96}C_{12}$ GQD, although it can be shown that the selection rules for this GQD are direct consequences of its 3-fold rotational invariance (*i.e.* its C_3 symmetry).

Photoluminescence spectra (PL) were measured on a dilution by 1/100 of the stock solution. A typical PL spectrum of such a solution when excited at 450 nm is presented in Figure 4.1. Given previous results obtained for $C_{96}C_{12}$ GQDs [10], we know that the emission from these objects results in a strong peak around 640-650 nm (peak **a**) followed by a vibronic shoulder at around 705-720 nm (peak **b**). These two lines are recovered in our observation in solution. We can observe that the line at 635 nm (the lowest in energy) on the absorption spectrum is slightly blueshifted (27 meV) relatively to the line at 644 nm on the PL spectrum, which is an awaited Stokes shift behaviour for chromophores (compared to 83 meV for hexabenzocoronene or 30 meV for supernaphtalene [60]). This is a good indication that the feature at 635 nm in the absorption spectrum corresponds to the lowest transition of the monomer. Concerning the broad emission at higher energy (peak **c**, between 560 nm to 620 nm), its origin was not clear at the beginning of my thesis and was the subject of an investigation developed in the following sections (in particular Sec.4.2.3).

Effect of the dispersion protocol on the solutions

GQDs were dispersed in TCB using the protocol described in Chapter 2. In order to optimize the dispersion process, we investigated the influence of different dispersion methods on the concentration of GQD monomers present in solution.

An effect of ultrasonication was noticed during the dispersion of $C_{96}C_{12}$ powder in TCB. Before ultrasonication, the powder of $C_{96}C_{12}$ was not dispersed in TCB and remained in the form of millimetric grains in suspension. The intermolecular interaction between PAH is well-known (usually referred to as π-π stacking) and results in the formation of agglomerates or aggregates. While the alkyl sidechains on the $C_{96}C_{12}$ GQD should enhance solubility, the presence of such interactions is non-negligible and explains the difficulty to dissolve the powder of GQD in TCB. Ultrasonication is necessary to overcome the intermolecular interactions and disperse the GQD in the solvent. However, after around 30 s of ultrasonication, no effect of additional ultrasonication time is observed, as shown in Figure 4.2(a). This seems to indicate that after this time, ultrasonication does not induce any increase of the concentration of GQD monomers in solution. If additional agglomerated objects remain in the solution, the strength of the ultrasonication method is not enough to break the bonds between the objects.

As it can be seen in Figure 4.2(b), no effect of the magnetic agitation was noticed in the intensity of the peak at 644 nm in the PL spectrum, which would increase if the concentration of GQD monomers increased in the solution. This indicates that stirring using magnetic agitation does not impact significantly the dispersion of $C_{96}C_{12}$ in solution. Dilution of the solution also yields no clear effect on the relative ratio of lines in the PL spectra, as can be seen in Figure 4.2(c). Moreover, ultrasonication of the solution after dilution did not induce any change in the PL spectrum.

Given our observations, ultrasonication remains the necessary step in dispersing $C_{96}C_{12}$ and was therefore adopted in our protocol. We can note that beside ultrasonication, protocols using shear-mixing have also been shown to be efficient in enhancing the dispersion of nanographene aggregates [118].

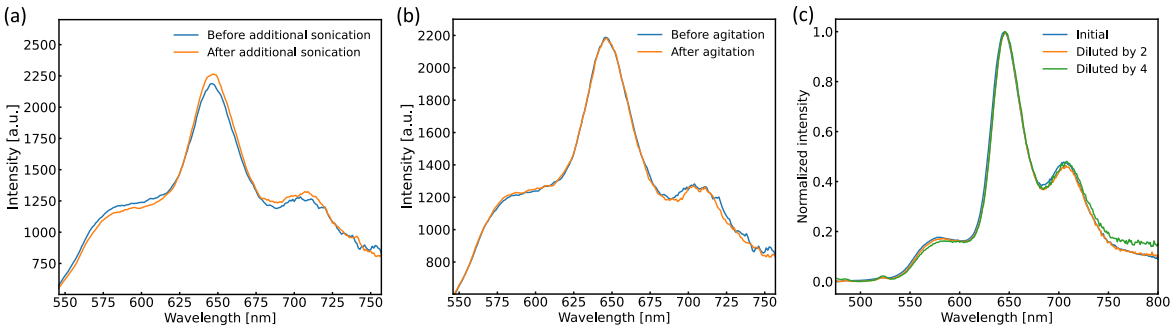

Figure 4.2: Effect of (a) additional ultra-sonication, (b) magnetic agitation and (c) dilution on the PL spectrum of $C_{96}C_{12}$ solution (after the initial 30 s ultra-sonication).

Disparity among different batches

Multiple batches of $C_{96}C_{12}$ were delivered to us by chemist collaborators, and stock solutions were prepared by dispersing the different powders. Among a same batch, the general observations in solution are reproducible. For example, different solutions prepared from the same batch yield the same spectrum, as it can be seen in Figure 4.3. This shows the reproducibility of the spectra when using the same synthesis batch.

However, we have observed that, following the same dispersion protocol, different batches yielded slightly different absorption and PL spectra. In order to keep the description clear and simple, we shall focus in this paragraph on only two different batches, which we will label **A** and **B**. The difference between batches can first be noticed during the dispersion of $C_{96}C_{12}$ in TCB: following the same dispersion protocol described in Chapter 2, we observe after the ultrasonication step a difference in the visual aspect of the solution[2]. Solution with dispersion from batch **A** would result in a homogeneous light brown hue (with no powder left undissolved) while in solution from batch **B**, suspension of micrometric black grains could still be observed.

In Figure 4.4(a), the absorption spectra from the dispersion of the two different $C_{96}C_{12}$ batches are compared. We can clearly see that the absorption band at 635 nm associated with GQD monomers is absent/less intense for the solution from batch **B** than for batch **A**, indicating a relatively lower concentration of GQD monomers in solution. This is confirmed by the observation in PL spectra (Figure 4.4(b)). We can see that the ratio between the lines associated with GQDs and the lines at higher energy is in favor of an enhanced dispersion of GQDs for batch **A** while the line is more faint in batch **B**. Moreover, there are also possibly other additional objets in solution, as can be seen from the slight difference in shape of the emission band at higher energy. The observation made in the spectra therefore matches the visual aspect of the respective solutions: the dispersion of $C_{96}C_{12}$ GQD monomers is more enhanced for batch **A** than for batch **B**, for which the absence of intense PL lines associated with GQD monomers matches the noted difficulty to dissolve grains of powder.

[2]No photographic picture showing the visual aspects of the solutions are provided since the resolution could not render the observation described.

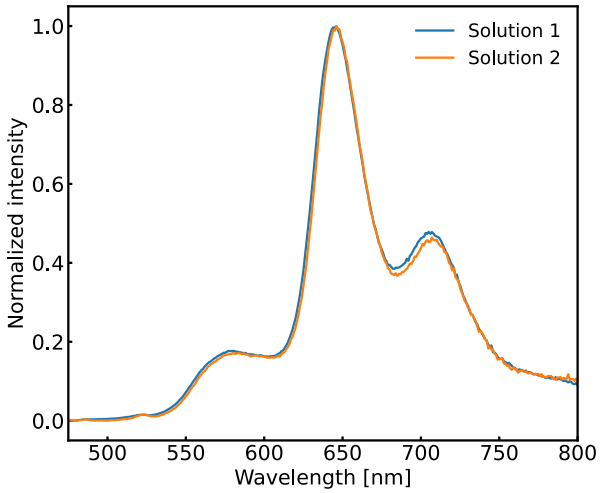

Figure 4.3: Normalized PL spectra of two solutions (labelled arbitrarily 1 and 2) prepared from a same $C_{96}C_{12}$ synthesis batch.

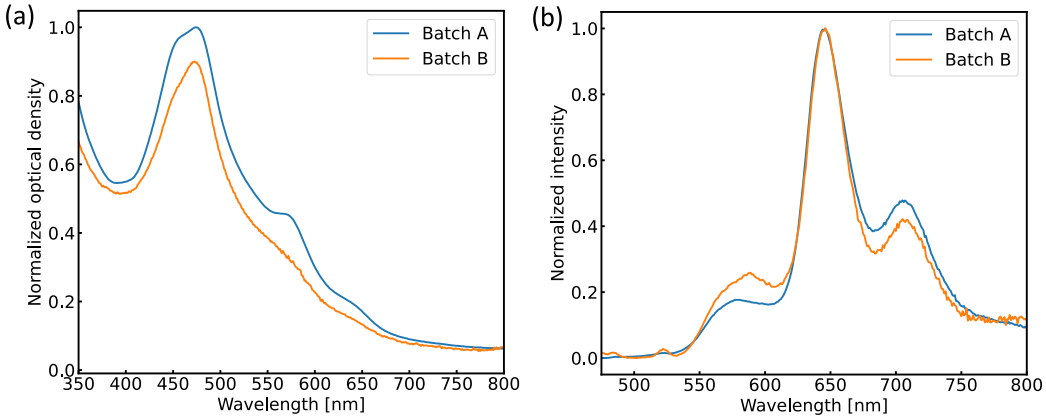

Figure 4.4: Comparison of the (a) absorption and (b) PL spectra of solutions prepared from different $C_{96}C_{12}$ synthesis batches (labelled **A** and **B**). The normalized absorption spectrum for batch **B** is shifted in y for clarity.

4.2.2 Investigating emission from monomers

Photoluminescence excitation and time-resolved PL

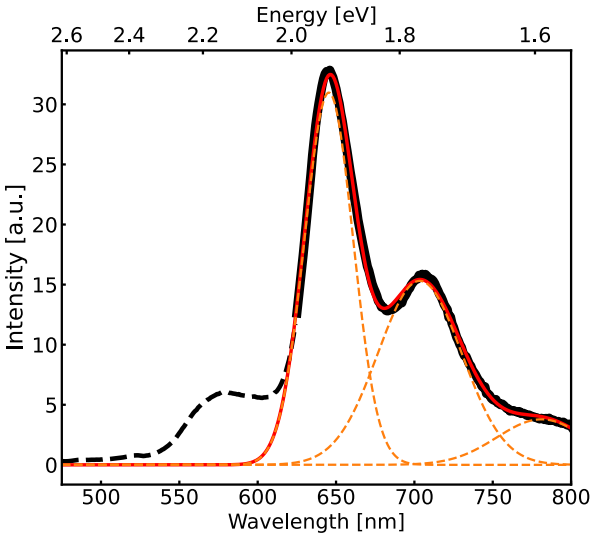

Figure 4.5: Fit of the GQD monomer portion of the PL (solid black) by three Gaussians. The fit is given in red, along with the three corresponding Gaussians (dashed orange).

First, let us focus on the emission from $C_{96}C_{12}$ monomers. As stated hereabove, given the results obtained on this system prior to my work, we know the emission of the monomer to correspond to the lines labelled **a** and **b** in Figure 4.1(b).

As mentioned in the previous section, the emission from $C_{96}C_{12}$ GQDs has been reported to be constituted of one main electronic transition followed by two vibronic replicas considering the spectra measured on single GQDs [10]. To be more quantitative, the part of the PL spectrum corresponding to the emission of $C_{96}C_{12}$ GQDs can be perfectly fitted by three Gaussian functions (although the values for the third Gaussians show a high uncertainty level), as shown in Figure 4.5. The central positions of the three Gaussians are 645 nm, 703 nm and 781 nm, with respective full widths at half maximum (FWHM) of 36.5 nm (109 meV), 62.9 nm (158 meV) and 66.6 nm (136 meV), but we must not put too much emphasis on the fitting parameters of the third Gaussian function given the uncertainty of the fit.

Photoluminescence excitation (PLE) spectra are measured on the different emission lines present in the PL spectrum. Spectra measured with emission at 644 nm and 705 nm yield the same spectral structure, as shown in Figure 4.6(b). This observation is a good indication that the emission lines **a** and **b** originate from the same object and result from the radiative relaxation from the same excited state of the $C_{96}C_{12}$ GQD. To be even more precise, given the Kasha rule stipulating that fluorescence results from the radiative decay from the lowest-lying excited state in the electronic structure of a system, the emission should result from the first excited singlet state of the GQD. This observation also supports the assignment of line **b** to a vibrational replica of line **a**. As a matter of

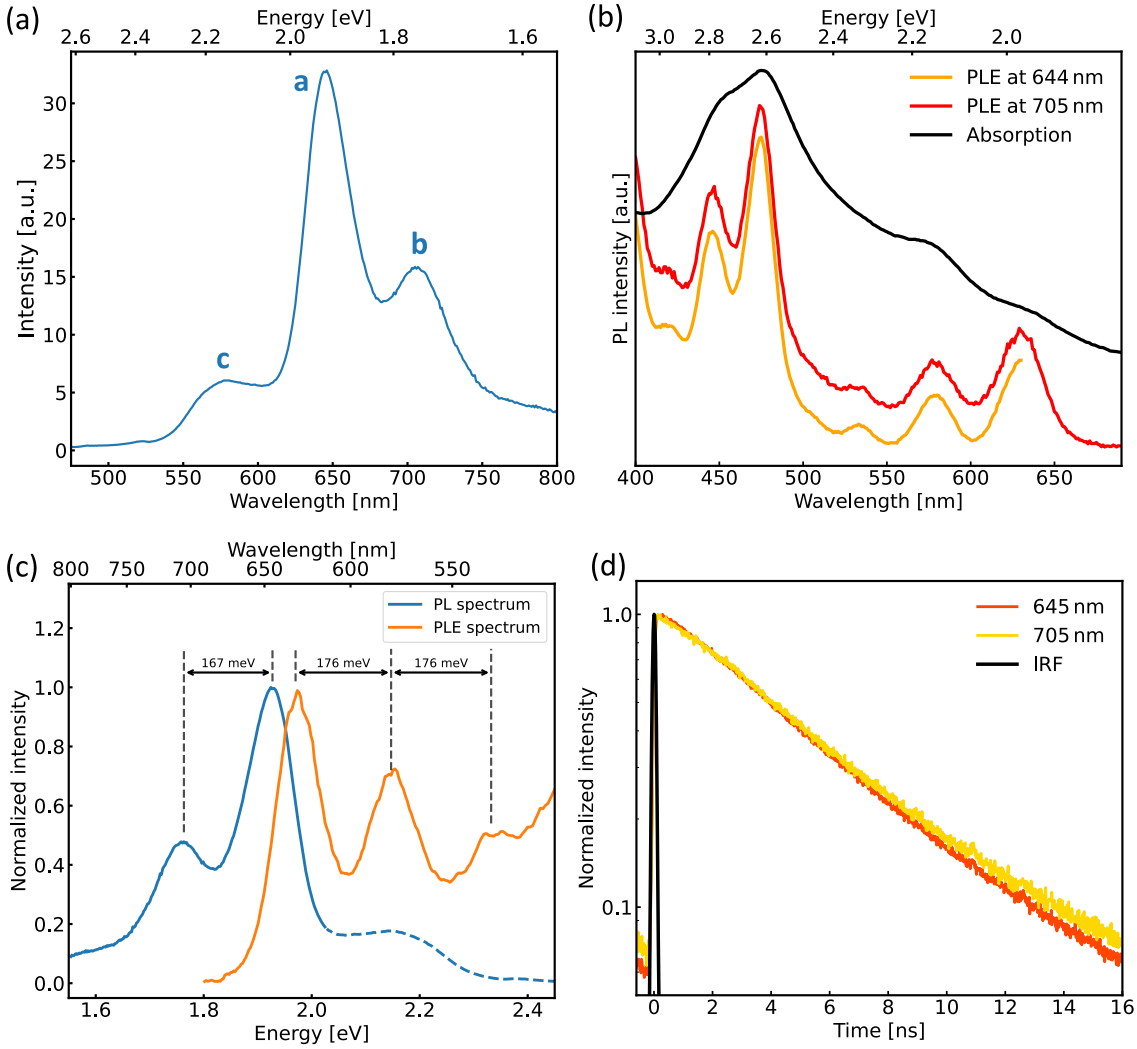

Figure 4.6: (a) Photoluminescence (PL) spectrum of a solution of $C_{96}C_{12}$ dispersion in TCB. (b) Photoluminescence excitation (PLE) spectra collected at peaks **a** (644 nm) and **b** (705 nm), as labelled in subfigure (a). The absorption spectrum is given for comparison. (c) Mirror symmetry between PL and PLE spectra. (d) Time-resolved photoluminescence (TRPL) emission collected at peaks **a** and **b**. IRF: instrument response function.

fact, the energy difference between lines **a** and **b** is at 167 meV, which corresponds to the vibrational frequency of the C=C bond stretching in aromatic compounds expected for PAHs [162].

Moreover, as expected, we recover the general structure of the absorption spectrum in the PLE spectra measured. We measure three transitions at lower energy at 631 nm, 579 nm and 535 nm, followed by stronger lines at 475 nm, 446 nm and 420 nm. The energy difference between the different transitions is equal to 176 meV for the lower-energy transitions and around 170 meV for the stronger lines at higher energy. We thus recover almost the same energy difference as the one observed in emission, with the slight difference arising from possible Herzberg-Teller effects, *i.e.* dependence between electronic states and nuclear configurations [170, 171]. The mirror symmetry observed with the PL spectrum is in good agreement with the Franck-Condon principle (Figure 4.6(c)).

2D PL-PLE maps can be measured on the solution and efficiently summarize observations made up until now. In Figure 4.7, an example of a 2D PL-PLE map is given, where the y-axis corresponds to the excitation wavelength and the x-axis corresponds to the emission wavelength. The bright diagonal corresponds to the line $\lambda_{exc} = \lambda_{em}$ (*e.g.* the situation when the emission is collected in resonance with the excitation). Bright spots correspond to emission maxima. We recover the PL spectrum from Figure 4.6(a) if we isolate the horizontal line at $\lambda_{exc} = 450$ nm, and the PLE spectra from Figure 4.6(b) if we focus on the vertical lines at $\lambda_{em} = 644$ nm and $\lambda_{em} = 703$ nm. The presence of spots arranged into a square (as highlighted with the white dashed line) transcribes the mirror symmetry between absorption and emission. The slight shift of the top left spot of the square relatively to the diagonal line results from the Stokes shift between absorption and emission. Highlighted in green are the features due to the $C_{96}C_{12}$ GQD monomers in solution.

If we come back to the comparison of the PLE spectra to the absorption spectrum, we said that the position of the peaks correspond perfectly. However, we must note that the lines in the absorption spectrum are broader relatively to the PLE spectra (clearly seen in Figure 4.6(c)). The broadening of the lines as we switch from the PLE spectra to the absorption spectrum indicates that there are absorbing objects with transitions close to the ones associated with the GQD monomer which do not result in emission at the fluorescence wavelengths of the monomer and may be attributed as derivatives from GQDs. The broadening may arise from a dispersion in position of the lines of the $C_{96}C_{12}$ monomer. However, if we turn to the 2D PL-PLE map, we observe that the bright spots associated to the emission of $C_{96}C_{12}$ monomers are aligned on a horizontal line (blue dotted lines guide this observation). This indicates that, as we vary the collection wavelength (λ_{em}) accross the emission lines of the GQD, the position of the lines in the PLE remains the same. We could have envisioned the case where the PLE lines would shift as we vary λ_{em}, which would mean that there would be different populations of GQDs emitting in the wavelength range, and explain the broadening observed in the absorption spectrum. However, since it is not the case here, this is a good indication that the emission lines of GQD monomers observed in PL are homogeneous in solution and that the broad width of the lines in the absorption spectrum cannot be the result of the dispersion of the lines of the $C_{96}C_{12}$ GQD monomer.

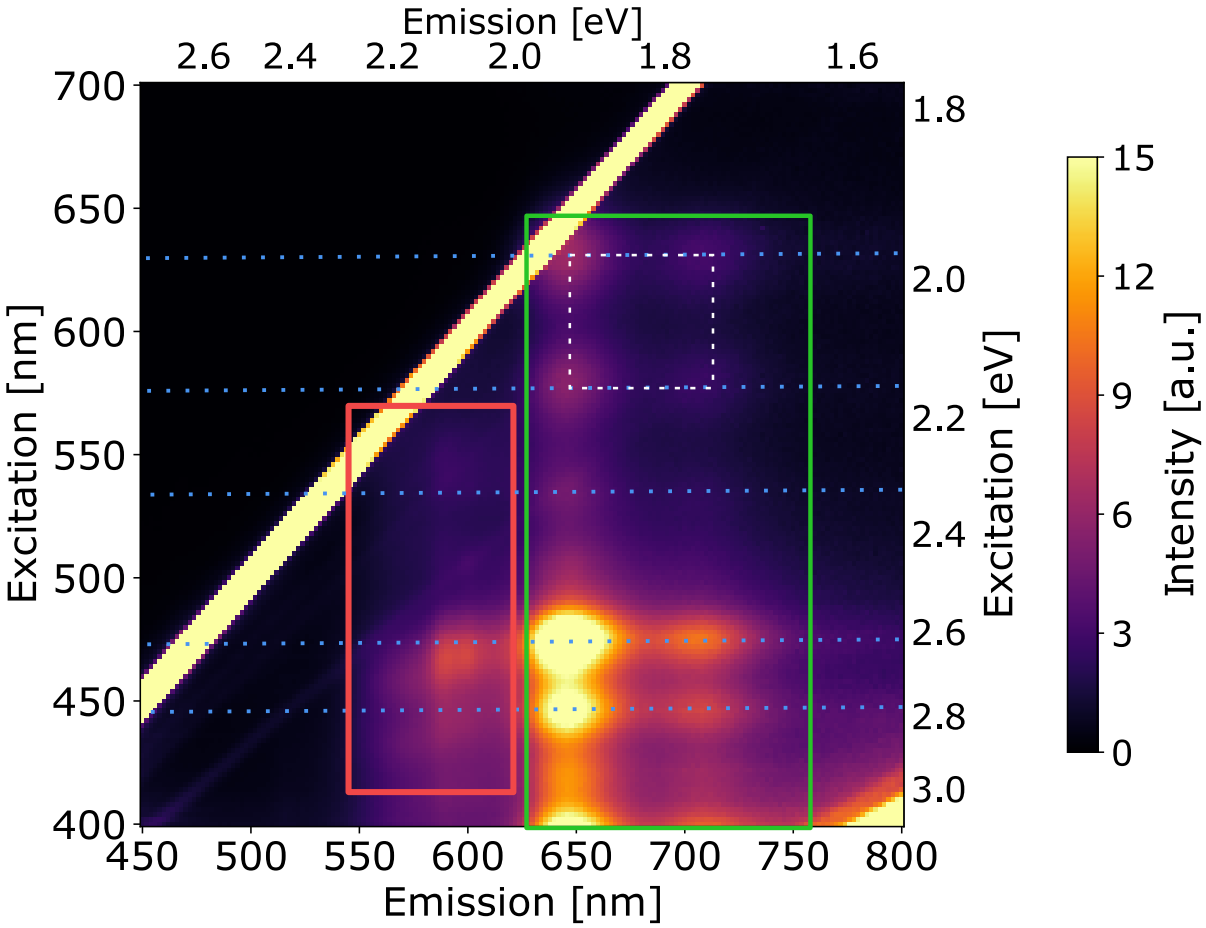

Figure 4.7: 2D PL-PLE spectrum of $C_{96}C_{12}$ solution. The white dashed square highlights the mirror structure between PL and PLE. Green and red plain squares identify the features of GQD monomers and high-energy emitting objects respectively. Blue dotted lines mark the horizontal alignement of the monomer's features (they are placed at the maxima of the PLE spectrum).

If we now look at the emission lines at higher energy (highlighted by the red square), we see features that are not associated with the emission from GQD monomers. We see in particular peaks with maxima not aligned with the horizontal dotted blue lines, indicating the presence of objects absorbing at slightly different wavelengths than GQD monomers but not emitting at the same wavelength. The presence of such objects can account for the apparent broadening of the absorption lines. We will focus on these objects in following sections (see Sec.4.2.3).

Therefore, we expect the broadening of the absorption lines to originate from additional objects derivating from GQDs. Such objects can for instance be associated with the existence of large disordered aggregates in the solution, which for most do not produce any fluorescence emission [117, 118]. We must not neglect the possible presence of additional non-emitting objects (not related to $C_{96}C_{12}$) given the diffuse absorption background observed over the whole spectrum.

Finally, looking at the time-resolved photoluminescence (TRPL) emission curves, the measurements performed at peak **a** and **b** give the same behaviour (Fig.4.6(d)). This is a strong indication that the emission at these two wavelengths result from the same relaxation dynamics of the system, and originate from the decay of the same excited state, therefore supporting the observation already made with the PLE spectra. The decay can easily be fitted by a monoexponential decay, yielding a relaxation time of 4.55 ns. The mono-exponential nature of the relaxation points toward a simple relaxation channel from the populated excited state, and indicates homogeneity in the population of $C_{96}C_{12}$ GQD monomers in solution. For instance, chromophores exhibiting strongly different conformations may show multi-exponential decay in solution [172, 146].

Theoretical aspect of the luminescence of $C_{96}C_{12}$

Given the aromatic nature of the $C_{96}C_{12}$ GQD, it is possible to use nomenclature and results previously obtained for PAHs. Using Clar's notation, it is possible to annotate the transitions observed in the absorption spectrum (and PLE spectrum). The features at lower energy are usually associated to α and p bands and the more intense features at higher energy corresponding to β band (the example of pyrene is given in Figure 4.8(a)). These bands can be explained by looking at the electronic transitions of the PAH. By taking into account the frontier molecular orbitals of the GQD, *e.g.* HOMO (highest occupied molecular orbital), HOMO-1 (molecular orbital right below the HOMO), LUMO (lowest unoccupied molecular orbital) and LUMO+1 (molecular orbital right above the LUMO). In Figure 4.8(b), they are labelled π_{n-1}, π_n, π_{n+1}, π_{n+2} from lowest to highest in energy (due to the nature of these orbitals involving only π electrons of the PAH). Four possible transitions (*i.e.* electronic configurations of the molecular orbitals) can be listed, and combinations of these transitions between orbitals result in four excited singlet states as shown in Figure 4.8(b). In the specific case depicted, the orbitals are not degenerated. The case of degenerated orbitals (which is the case for benzene for example) would induce a degeneracy of the transitions, which would then be splitted via interaction between configurations, as it is the case for configurations $(\pi_{n-1}\pi_n^2\pi_{n+1}^*)$[3] and $(\pi_{n-1}^2\pi_n\pi_{n+2}^*)$

[3]Read state where π_{n-1} is occupied by one electron, π_n occupied by two, and π_{n+1}^* occupied by one.

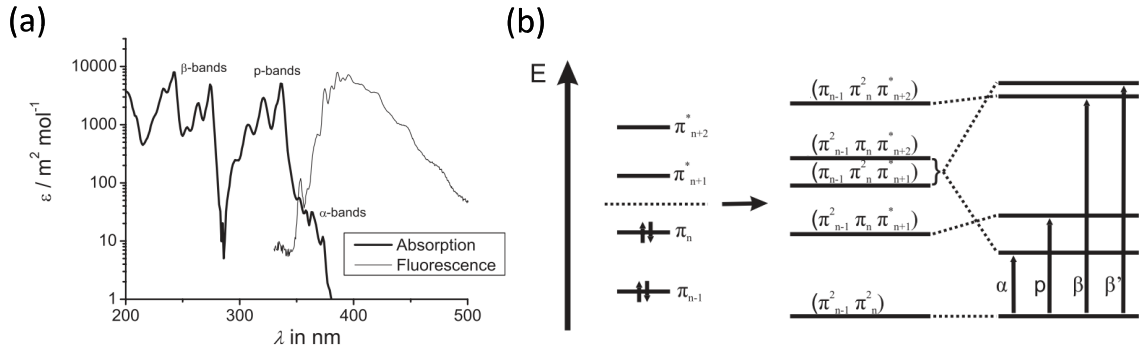

Figure 4.8: (a) Absorption and fluorescence spectra of pyrene in cyclohexane. (b) (From left to right) Energy levels, electronic configurations and resulting transitions of a PAH. Figures adapted from [60].

in Figure 4.8(b). The *p*-band is, by definition, attributed to the HOMO-LUMO transition, and may be below the α-band in some cases, depending on the chosen symmetry of the PAH [173].

Let us now be more specific and focus on the $C_{96}C_{12}$ GQD in order to understand the origin of the emission lines. Given the D_{3h} symmetry of the GQD, the transitions to the two lowest lying states should be forbidden, as was previously reported for systems presenting such symmetries [36]. However, in order to be more quantitative, specific calculations need to be perfomed on our GQD of interest.

With the help of theoreticians Dr. Claire Tonnelé and Pr. David Beljonne, from Université de Mons, we managed to have a deeper look into the photophysics of the $C_{96}C_{12}$ GQD, with calculations specific to its geometry. First, by performing DFT/TDDFT (Density function theory / Time-dependent density function theory), the equilibrium structure of the GQD was calculated, yielding equilibrium geometries with a slightly distorted core. Two equilibrium conformers are obtained (shown in Figure 4.9(a)), differing only by the orientation of the alkyl side-chains: one with in-plane side-chains (in orange) and one with out-of-plane side-chains (in blue). No effect of the orientation of the side-chains were found, the core being unaffected between the two conformations.

Looking now at the energy levels of the GQD in its equilibrium geometry, we recover the first four excited singlet states as described earlier. The results of the calculations are given in Table 4.1 (values computed with LC-ωPBE XCF - a typical exchange-correlation functional - on the equilibrium geometry). The oscillator strength for the two first singlet states S_1 and S_2 vanishes, and the states at higher energy S_3 and S_4 are degenerate and bright. The singlet states can be described as combinations of excitations involving the frontier orbitals. The HOMO and HOMO-1 are delocalized on the 96-carbon-atom core of the GQD and are calculated to be quasi-degenerate (energy difference around 3 meV), and the same applies for the LUMO and LUMO+1 (see Figure 4.9(c)). The main contributions for each state are given in the same table.

The results obtained are close to the general prediction made for PAHs, with transition to S_1 associated with the α-band, S_2, with the contribution of the HOMO-LUMO tran-

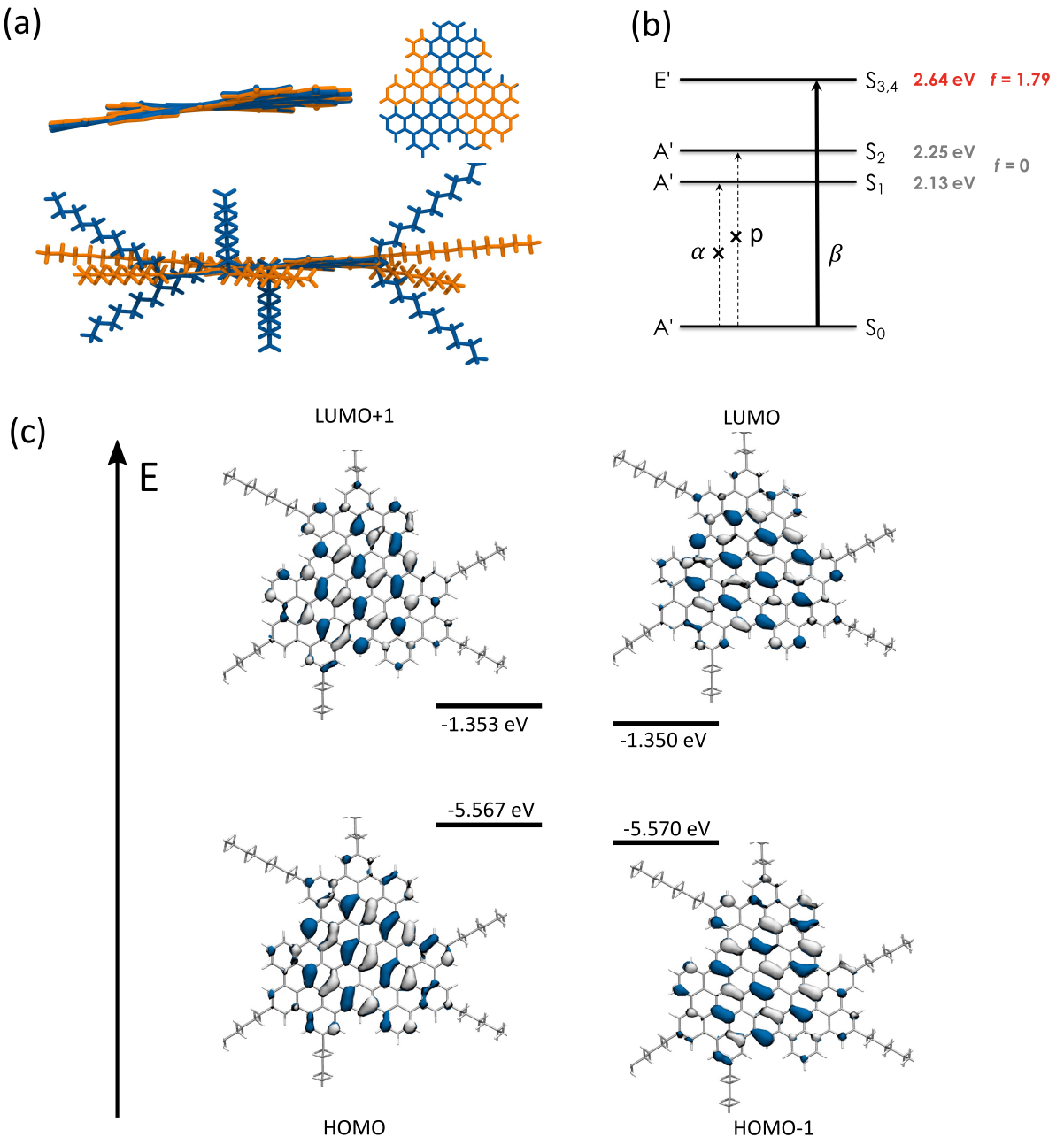

Figure 4.9: (a) Equilibrium geometry of the $C_{96}C_{12}$ GQD conformers without (top) and with (bottom) alkyl side-chains in-plane (in orange) or out-of-plane (in blue). (b) Transitions calculated for the equilibrium geometry. (c) Frontier orbitals of $C_{96}C_{12}$.

State	ΔE (eV)	f	Main contributions (%)	Band attribution
S_1	2.130	0.000	H-1 $\longrightarrow$ L (47) H $\longrightarrow$ L+1 (47)	α-band
S_2	2.251	0.000	H-1 $\longrightarrow$ L+1 (47) H $\longrightarrow$ L (48)	p-band
S_3	2.644	1.791	H-1 $\longrightarrow$ L (44) H $\longrightarrow$ L+1 (44)	β-band
S_4	2.644	1.791	H-1 $\longrightarrow$ L+1 (45) H $\longrightarrow$ L (44)	

Table 4.1: Excitation energies (ΔE), oscillator strength (f) and dominant contributions of the first four excited singlet states (H and L being short for HOMO and LUMO respectively) calculated for the $C_{96}C_{12}$ GQD. The attributed Clar nomenclature is given in the last column.

sition, corresponds to the p-band, and the two high-lying degenerate singlet states form the β-band (see Fig.4.9(b)). The calculated position of the β-band (2.65 eV) reproduces faithfully the intense feature at high energy in the PLE spectra, measured experimentally at 478 nm (2.59 eV). Concerning the transitions at lower energy, looking at the equilibrium geometry of the GQD could not render the observations made due to the vanishing oscillator strength and the non-negligible difference between the calculated α-band position and the measured lowest-lying transition at 631 nm (1.97 eV). Once again, it is important to point out that these results are direct consequences of the D_{3h} symmetry of the system. In order to explain the observation of fluorescence from the GQDs, it is necessary to take into account the processes that could brighten the lowest-lying transitions. As it has been demonstrated in different systems [174, 175], symmetry-breaking of the system could induce changes in its electronic transitions.

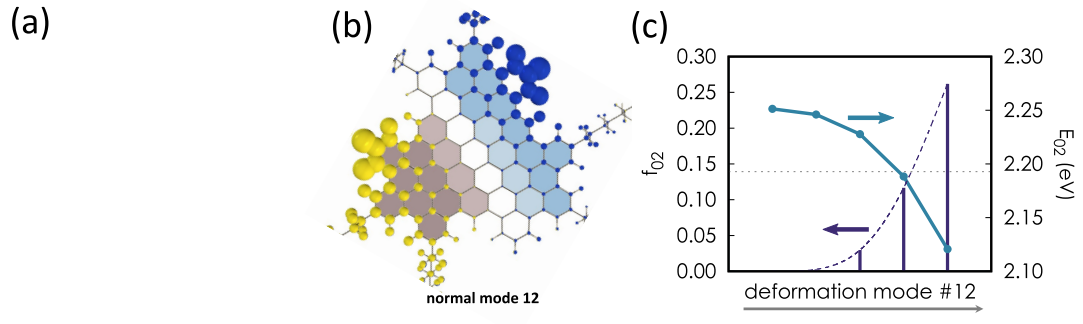

Figure 4.10: (a) Frame calculated in molecular dynamics. Rings filled in blue are distorted downward and those in grey are moving upward relatively to the equilibrium plane (the darker the shade, the stronger the deformation). (b) Normal mode corresponding to the deformation (the same color palette is applied). (c) Evolution of the oscillator strength (verticular bars) and the excitation energy (blue curve) of the $S_0 \longrightarrow S_2$ transition along the normal deformation mode.

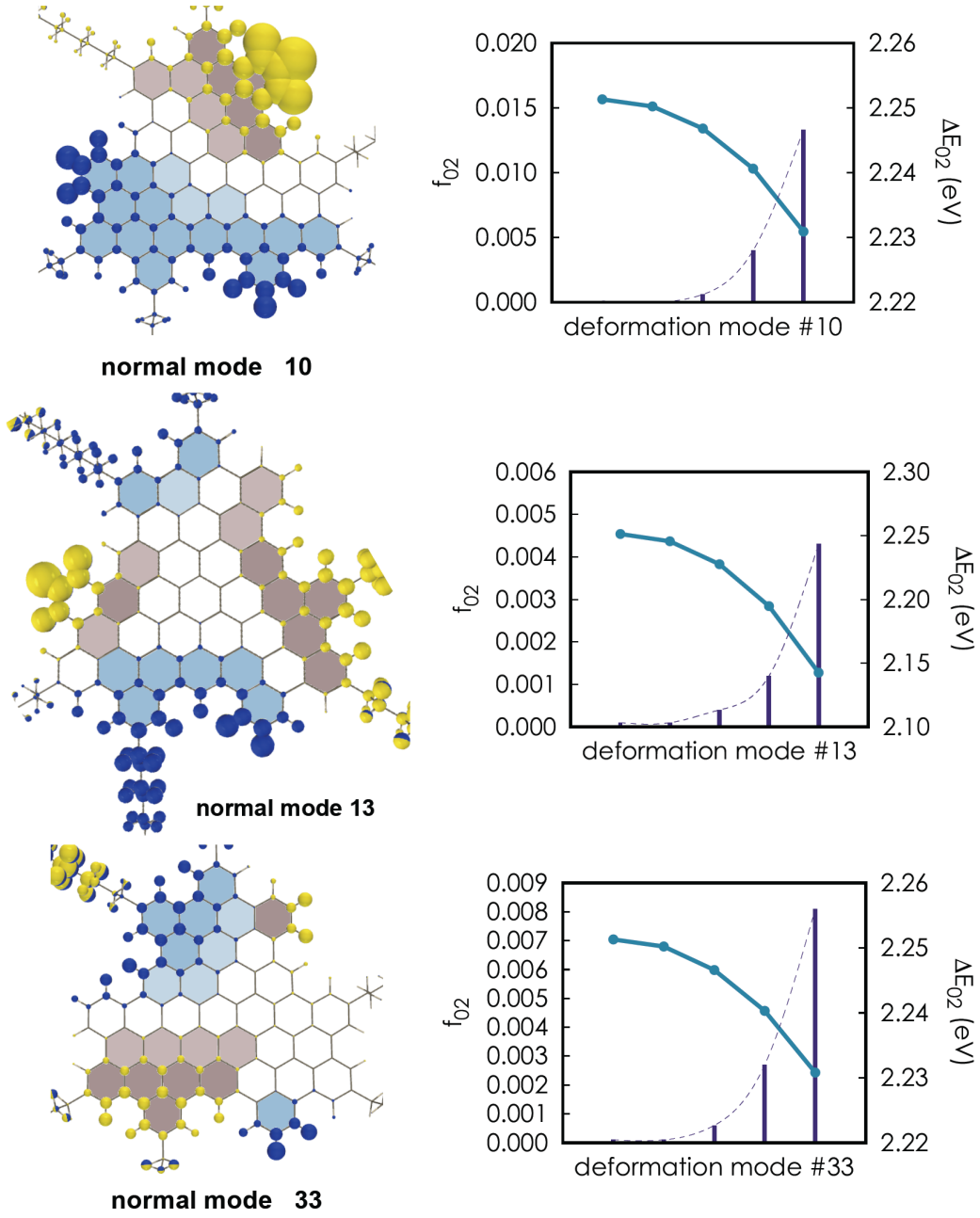

Figure 4.11: Example of different normal modes brightening the $S_0 \rightarrow S_2$ transition, along with the evolution of the oscillator strength (dark blue vertical bars) and the excitation energy of the transition (light blue solid line).

Using molecular dynamics (MD) to simulate the time dynamics of the GQD structure in a solvent, it was possible to observe, as the $C_{96}C_{12}$ GQD deforms, an increase of the oscillator strength of the transition to singlet state S_2. This results from the distortion of the graphenoid core of the GQD, thus breaking the D_{3h} symmetry forbidding these transitions. For example, Figure 4.10(a) shows the geometry of the GQD at a particular time (identified as time frame c325) during calculations using MD, where the rings filled

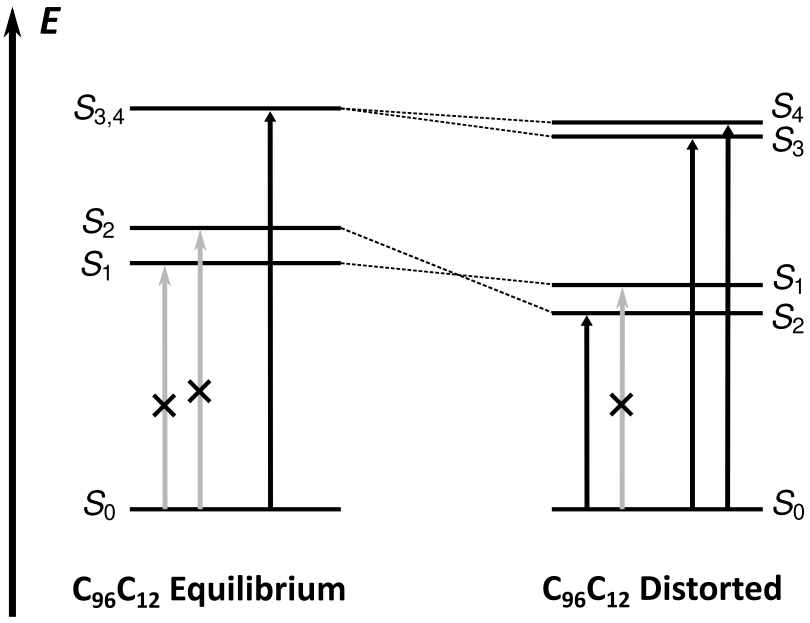

Figure 4.12: Predictive evolution of the energy levels after distortion of the aromatic core of $C_{96}C_{12}$. Light grey arrows indicate forbidden transitions (with non-appreciable oscillator strength).

in blue are distorted downward (away from the reader) and those in grey are moving upward (towards the reader) relatively to the equilibrium plane (the darker the shade, the stronger the deformation). The deformation of the core reproduces a normal vibrational mode (here numbered 12) of the GQD, as depicted in Figure 4.10(b). Focusing on normal mode 12, we can observe that as the amplitude of deformation increases, the oscillator strength of the $S_0 \rightarrow S_2$ increases significantly as shown in Figure 4.10(c). The deformation also induces a redshift of the transition, reaching in the case of normal mode 12 around 150 meV. Multiple other normal modes induce similar behaviors, as given in Figure 4.11. Nonetheless, no deformation has induced any appreciable brightening of the $S_0 \rightarrow S_1$ transition. This observation has also been theoretically predicted for other systems [44, 38]. A degeneracy lift is also observed between S_3 and S_4.

Given the redshift of the $S_0 \rightarrow S_2$ transition during deformation, we therefore suspect that $S_0 \rightarrow S_2$ becomes the lowest-lying excited singlet state, from which emission is observed. Another possibility would be that transition $S_0 \rightarrow S_1$ remains the lowest-lying state but not observable due to the quasi-vanishing oscillator strength associated with it. However, the latter possibility is improbable given the relatively high fluorescence quantum yield reported for the $C_{96}C_{12}$ GQD (underestimated to 35% [10]).

The theoretical calculations performed for the $C_{96}C_{12}$ GQD unravel new understanding on the origin of the fluorescence observed for this object. The importance of the D_{3h} symmetry-breaking via vibrational coupling to explain the intensity-borrowing effect for the forbidden low-lying transitions clearly stresses the importance of the geometry of the GQD on its electronic properties.

4.2.3 Discussion on the origin of the additional line

Coming back to the fluorescence spectra obtained for the dispersion of $C_{96}C_{12}$ in solution, a few unclear observations remain to be discussed, notably the observed features that are not associated *a priori* with the emission of $C_{96}C_{12}$ GQD monomers.

Concerning the additional emission line at higher-energy (labelled **c** in Fig.4.6(a)), multiple hypotheses for its origin are considered. Since PL measurements on the solvent alone yielded no emission, it can be asserted that the origin is the addition of the powder of $C_{96}C_{12}$. Emission from higher energy states is unlikely given Kasha's rule and the reported high brightness of the object [10]. This conclusion was later confirmed in single-molecule experiments (see Sec.4.3.1). Therefore, the object emitting the additional emission line can either have a distinct origin from GQDs (synthesis by-products) or be a derivative of monomer GQDs (for instance aggregates or degraded GQDs).

Characterization of the additional emission line

The fluorescence of the object ranges from 560 nm to 605 nm, with a maximum around 580 nm (labelled peak **c** in Figure 4.6(a)). The energy shift between peak **a** and **c** is around 223 meV. The TRPL measurement at peak **c** yields a different decay dynamics than for $C_{96}C_{12}$ monomers, with a shorter lifetime and a multi-exponential behavior (see Figure 4.13(a)). This is a good indication that the high energy emission is not resulting from the same fluorescent object.

Leaving the solution stored under inert atmosphere in glovebox, we observed the gradual decay of the emission peaks associated with $C_{96}C_{12}$ monomers in favor of an increase of the emission band at higher energy, as shown in Figure 4.13(c). In particular, peaks **a** and **b** decrease with the same decay rate, once again highlighting their common origin from GQD monomers. For multiple solutions, we observe also the presence of an iso-emissive point (a stationary point as the spectrum evolves through time). In the case of the solution presented in Figure 4.13(c), the iso-emissive point is at 616 nm. The observed dynamic points toward a conversion of population between the GQD monomers and the objects emitting at higher energy. Therefore, the high-energy emission cannot stem only from synthesis by-products. Once again, the observation is in favor of an interpretation that the objects emitting at higher energy are derivatives from GQD monomers.

Given the stability of the $C_{96}C_{12}$ GQD due to its fully benzenoid structure, and the precautions of storing the solution under inert conditions, it is very unlikely that the observed conversion results from the degradation process of the GQD into a new emissive species. Therefore, we interpret that the objects emitting at high energy correspond to aggregates of $C_{96}C_{12}$ GQDs.

Such conversion of monomer population into aggregates has been observed accross different samples, examples are given in Figure 4.14. It is important to note that the evolution of the PL curve differs for different samples, with different structures observed for the aggregate emission or different positions of the iso-emissive point. The variety of possible aggregates formed can explain that the evolution may vary for different samples. Moreover, as shown in Sec.4.2.1, the $C_{96}C_{12}$ solutions themselves show disparity in

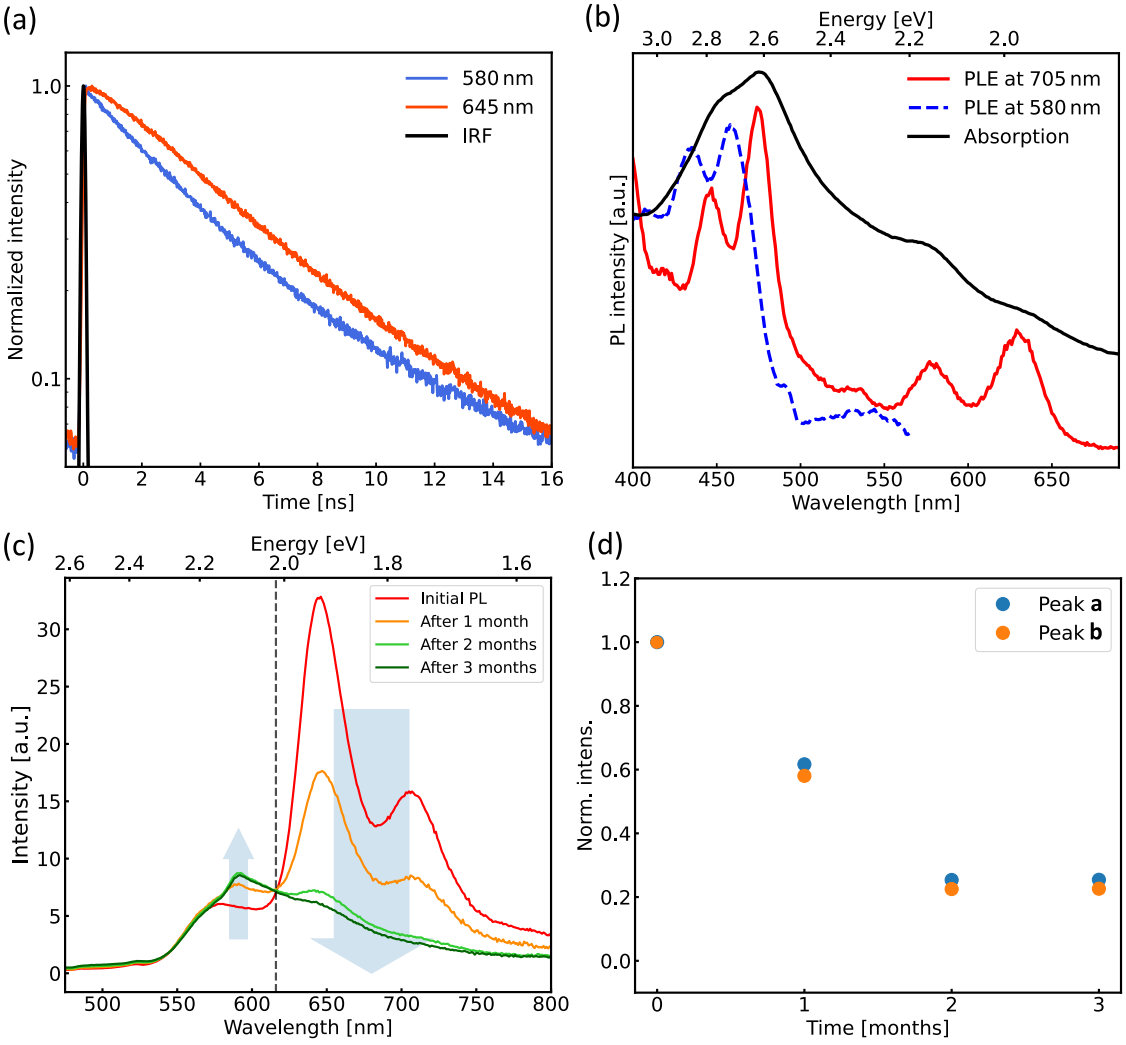

Figure 4.13: (a) Time-resolved photoluminescence (TRPL) emission collected at peaks **a** (644 nm) and **c** (580 nm), as labelled in Figure 4.6(a). (b) Photoluminescence excitation (PLE) spectra collected at peaks **a** and **c**. (c) Time evolution of the PL of a $C_{96}C_{12}$ solution, stored in glovebox between measurements. (d) Time-evolution of fluorescence emission collected at peaks **a** and **b** associated with monomers.

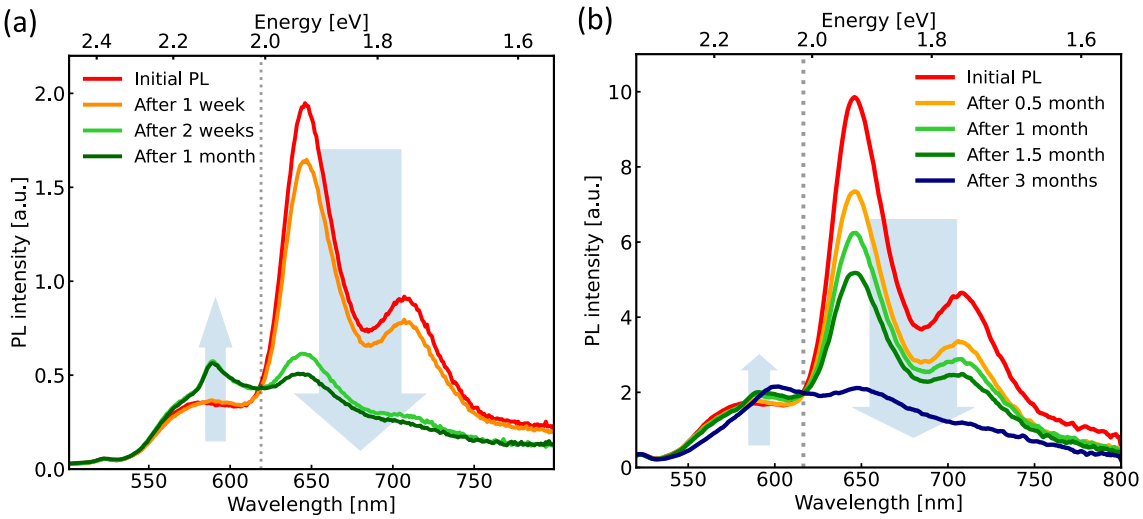

Figure 4.14: Examples of PL time evolution showing the presence of an iso-emissive point, observed for different solutions.

their initial composition after dispersing powder from different batches, which resulted in variations of the evolution of the solution's composition over time.

PLE spectra measured with emission at the wavelength of peak **c** is given in Figure 4.13(c) and shows a structure similar to the PLE spectra collected at the emission wavelengths of GQD monomers, but blueshifted by 115 meV (when looking at the most intense line). The wavelength of the lines of the PLE are 455 nm, 433 nm and 411 nm. The energy split between the lines is 153 meV. The value is lower than for the GQD monomers, which may indicate a lowering of the energy of the C=C bond stretching in the object. The resemblance between the PLE collected on line **c** with the PLE collected for GQD monomers is in line with the attribution of line **c** to a derivative of monomer GQDs, and is thus also consistent with the formation of aggregates.

Transmission electron microscopy (TEM) images of $C_{96}C_{12}$ samples deposited on a monolayer CVD graphene were taken by Dr. Hanako Hokuno in CEA Grenoble. On the images, we can clearly observe the presence of single GQDs (or aggregates of few GQDs) by the characteristic honeycomb structure, as circled in yellow in Figure 4.15. Also on the TEM images, structures composed of planar objects parallely-stacked (circled in red in Fig 4.15) can be identified as corresponding to long stacks of GQDs, here lying on their side. These columnar structures confirm the tendency of GQDs to form aggregates via stacking [141], and once again bolsters the conclusion of aggregate formation of $C_{96}C_{12}$ in solution.

Effect of aggregation on the electronic transitions: DFT/TDDFT calculations

In order to support the observations in solution and predict the effect of aggregation on the optical transitions, we turned to theoretical computations.

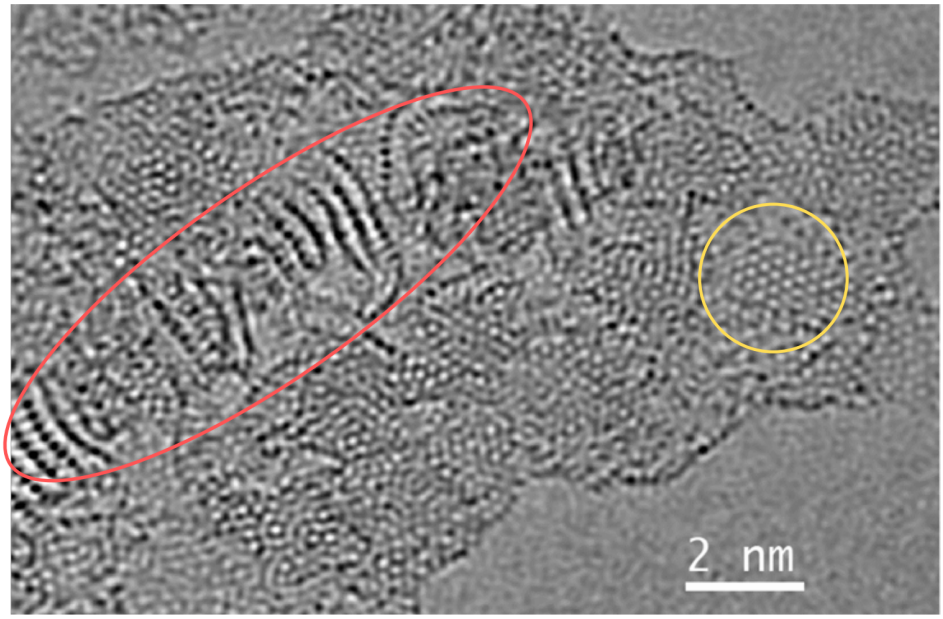

Figure 4.15: Transmission electron microscopy (TEM) image of a $C_{96}C_{12}$ GQD sample deposited on a monolayer of CVD graphene (signal due to the graphene support layer was removed during data treatment). We observe GQD monomers (yellow circle) and stacks of GQDs (red ellipse).

Building up on the calculations performed on single GQDs, theoreticians simulated the transitions of a dimer of $C_{96}C_{12}$ GQD. By first optimizing the structure of a dimer, calculations show that the most stable configuration for a dimer is composed of two GQDs co-facially separated by 3.48 Å (typical for $\pi - \pi$ interaction and consistent with previously reported results [141]) and with a twist angle between the two GQDs of $23° \pm 2°$ (see Figure 4.16(a)). Computing the transitions of the dimer in its equilibrium geometry yielded a blueshift of the optical transitions of about 30 meV. When focusing on the low-lying singlet states of the system, the oscillator strength of the first ten transitions amounts to around 0.004, which is two orders of magnitude below the value obtained for monomers. Therefore, calculations are in line with the spectral signatures of aggregates observed experimentally, reproducing the weaker fluorescence efficiency and the blueshift of the transitions.

Focusing on the effect of vibrations on the transitions of the dimer, molecular dynamics coupled with TDDFT calculations were performed on the dimer. We learn that the amplitude of the deformations of the graphenoid core of the GQD is weaker than for monomers, a reasonable result given the proximity of the two GQDs in the dimer. The amplitude of the out-of-plane deformation of the GQD can be monitored by following the distribution of the branch twist dihedral angle relatively to the median plane, *i.e.* the twist angle along the dashed line in Figure 4.16(b). By plotting the distribution of the dihedral angle computed using molecular dynamics for the dimer and the monomer, we can therefore compare quantitatively the amplitude of deformation for the dimer and the monomer. In Figure 4.16(c), the distribution of angles for each GQD composing the

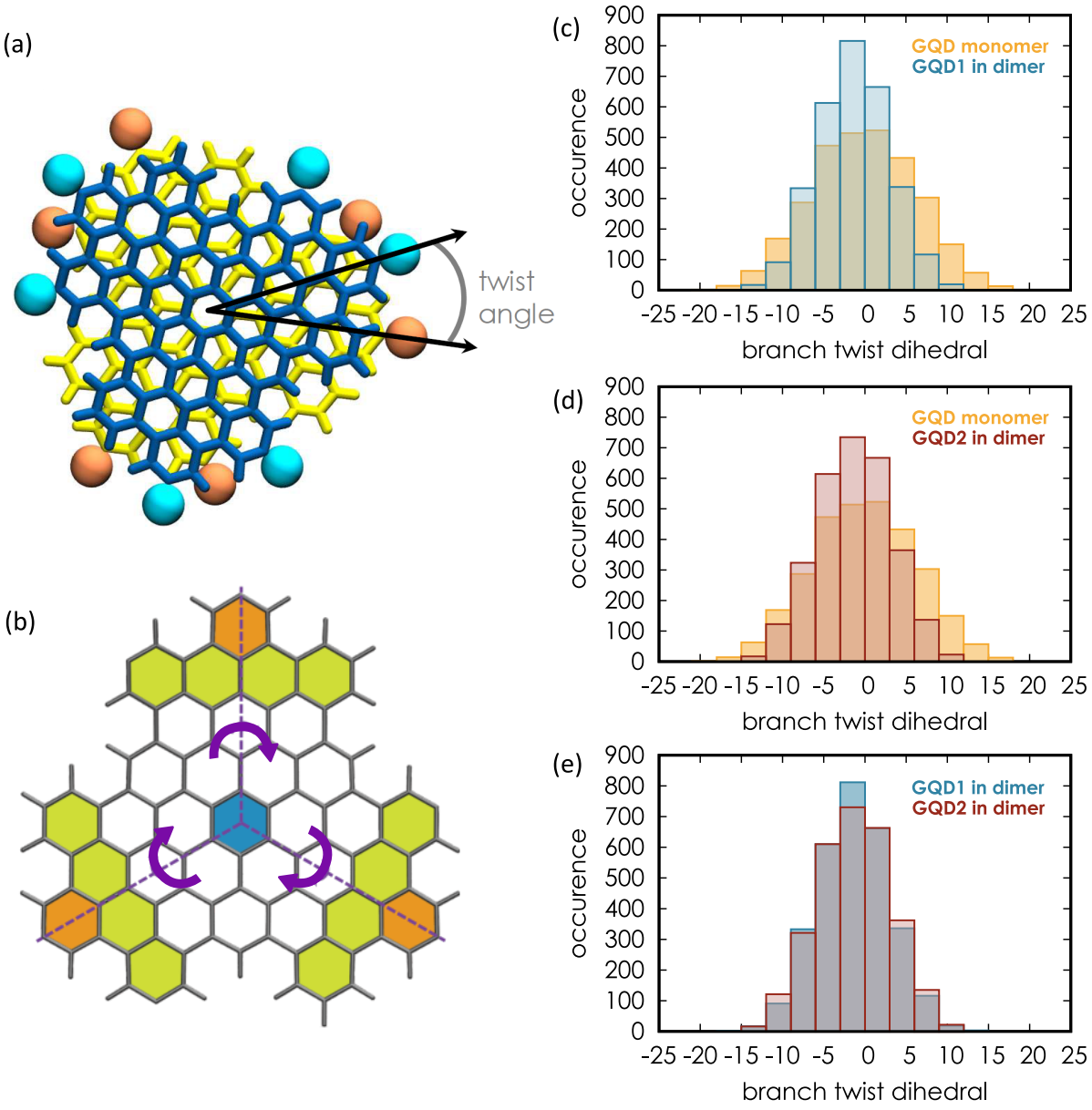

Figure 4.16: (a) Structure of the stable configuration of the dimer. The spheres correspond to the position of the alkyl sidechains. (b) Out-of-plane distortion mode of the graphenoid core. Dashed purple lines indicate the axis along which the twist of the plane is monitored. (c)-(e) Comparison of the distribution of dihedral angles due to the deformation represented in Fig.(b) for GQDs in the dimer (blue and red) and a GQD monomer (yellow).

dimer is compared with the distribution of a monomer. We can clearly see that the distribution is broader for the monomer than for the GQD in dimer, with standard deviation of $\sigma = 6.2°$ for the monomer versus $\sigma = 4.4°$ and $4.2°$ for the GQDs in a dimer (unsurprisingly, the two GQDs in the dimer share the same distribution). Consequently, in contrast to the results in monomers, vibrations do not induce any significant brightening of the low-lying transitions. It is interesting to note that this result was not straightforward, since dimerization may induce deformations of the chromophores constituting the dimer. In some cases, it may result into a brightening of the forbidden transition, as it was reported for H-aggregates of merocyanine dyes [176].

The calculations are therefore very satisfactory when compared to experimental results concerning the blueshift of the transitions induced by aggregation along with the lowering of the radiative decay rate. In the case of the dimer considered for calculations, the computed blueshift remains lower than the value measured experimentally (of around 110 meV as observed in the PLE spectra).

Finally, in the calculations presented in this section, we have limited ourselves to the study of the dimer in its equilibrium geometry. It could be interesting to see how considering deviations from the equilibrium geometry may change the results obtained. Even if such calculations have not been perfomed using DFT/TDDFT, we can speculate the possible dependence of the transitions levels on various geometric parameters, for instance on the size of the aggregate (*i.e.* the number of monomers constituting the aggregates) or the twist angle between the monomers consistuting the aggregate. In particular, increasing the size of the aggregate is predicted to induce higher energy shifts during aggregation [177, 178], we can tentatively suspect a similar behavior in our system.

Exploiting the PL time evolution

Coming back to the time evolution of the PL spectrum, assuming the formation of aggregates emitting at higher energy, we can exploit the measurements to estimate different characteristics. For example, the time evolution of the PL spectrum can give us access to an estimation of the kinetic of the aggregation process. As a first simple approach, one can first consider only a dimerization process.

Let us consider the following dimerization process, between monomer A and dimer A_2, characterised by the reaction constant K (expressed in Eq.4.7), and by k and k' the reaction rate constant of the dimerization reaction and its counterpart respectively:

$$2\,A \underset{k'}{\overset{k}{\rightleftharpoons}} A_2 \tag{4.1}$$

Let C be the concentration of the monomer and C_D the concentration of the dimer. Therefore, in the sample, we have $C + 2C_D = C_{tot}$, where C_{tot} is a constant. The kinetic equation for the reaction reads:

$$-\frac{1}{2}\frac{dC}{dt} = kC^2 - k'C_D = kC^2 - \frac{k'}{2}(C_{tot} - C) \tag{4.2}$$

where the first term corresponds to the formation of monomers, and the second term to the separation of dimers into monomers. By introducing characteristic parameters $k^* = \frac{k'}{2kC_{\text{tot}}}$, and $\tau^* = 1/(2kC_{\text{tot}})$, the kinetic equation can be nondimensionalized

$$\frac{\mathrm{d}\tilde{C}}{\mathrm{d}\tilde{t}} = -(\tilde{C}^2 + k^*\tilde{C} - k^*) \tag{4.3}$$

where $\tilde{C} = C/C_{\text{tot}}$ and $\tilde{t} = t/\tau^*$. The resolution of this equation yields:

$$\tilde{C} = \frac{\tilde{\alpha}(\tilde{C}_0 - \tilde{\beta}) - \tilde{\beta}(\tilde{C}_0 - \tilde{\alpha})\mathrm{e}^{-\tilde{t}(\tilde{\alpha}-\tilde{\beta})})}{(\tilde{C}_0 - \tilde{\beta}) - (\tilde{C}_0 - \tilde{\alpha})\mathrm{e}^{-\tilde{t}(\tilde{\alpha}-\tilde{\beta})}} \tag{4.4}$$

with $\tilde{\alpha} = \frac{k^*}{2}(\sqrt{1+4/k^*} - 1)$ and $\tilde{\beta} = -\frac{k^*}{2}(\sqrt{1+4/k^*} + 1)$.

By realizing that I_M and I_D, the intensity of the fluorescence peak associated respectively to monomers and to dimers, are proportional respectively to C and C_D, one can fit the temporal evolution of I_M and I_D with the following temporal evolutions:

$$\begin{aligned} I_M &= \frac{\alpha(I_0 - \beta) - \beta(I_0 - \alpha)\mathrm{e}^{-t(\alpha-\beta)/\tau}}{(I_0 - \beta) - (I_0 - \alpha)\mathrm{e}^{-t(\alpha-\beta)/\tau}} \\ I_D &= \gamma\left(\frac{\Gamma}{2} - \frac{\alpha(I_0 - \beta) - \beta(I_0 - \alpha)\mathrm{e}^{-t(\alpha-\beta)/\tau})}{2[(I_0 - \beta) - (I_0 - \alpha)\mathrm{e}^{-t(\alpha-\beta)/\tau}]}\right) \end{aligned} \tag{4.5}$$

where we have introduced $I_M = \gamma_M C$, $I_D = \gamma_D C_D$ and I_0 the initial value of I_M, as well as the following parameters in order to fit the time evolution of the fluorescence intensity:

$$\begin{aligned} \alpha = \gamma_M C_{\text{tot}}\tilde{\alpha} \quad \text{and} \quad \beta = \gamma_M C_{\text{tot}}\tilde{\beta} \\ \tau = \frac{\gamma_M}{2k} \quad \text{and} \quad \gamma = \frac{\gamma_D}{\gamma_M} \quad \text{and} \quad \Gamma = \gamma_M C_{\text{tot}} \end{aligned} \tag{4.6}$$

The dimerization reaction equilibrium constant K can be expressed as:

$$K = \frac{C_{D,\infty}}{C_\infty^2} = \frac{k}{k'} = \frac{1}{2k^* C_{\text{tot}}} \tag{4.7}$$

with $C_{D,\infty}$ and C_∞ the concentrations of dimers and monomers when the equilibrium is reached.

We can fit the curves obtained experimentally using Eq.4.5. Using the dynamics of Figure 4.17, the fit yields $k^* = 0.379 \pm 0.1$. If we estimate the total concentration in our sample to $C_{\text{tot}} \approx 3.10^{-5}$ mol/L, we can evaluate $K \approx 4.10^4$. The high value of the equilibrium constant ($K \gg 1$) is coherent with the hypothesis of favorable dimerization process in our sample (the equilibrium favors the products, here the dimer, relatively to the reactant, here the monomers)[4].

[4]As a side remark, if one would *a priori* expect an equilibrium to be established between monomers and dimers (or aggregates) in solution and thus observe an effect of the dilution on the concentration of monomers in solution, the absence of effect of dilution on the ratio between peak **c** and peak **a** may be due to the stabilization of the system as it aggregates. The resulting energy barrier may induce a kinetic quench (or at least a very slow dynamic on the timescale of the experiments). Such observations have already been reported on for stackings of graphene quantum dots [179].

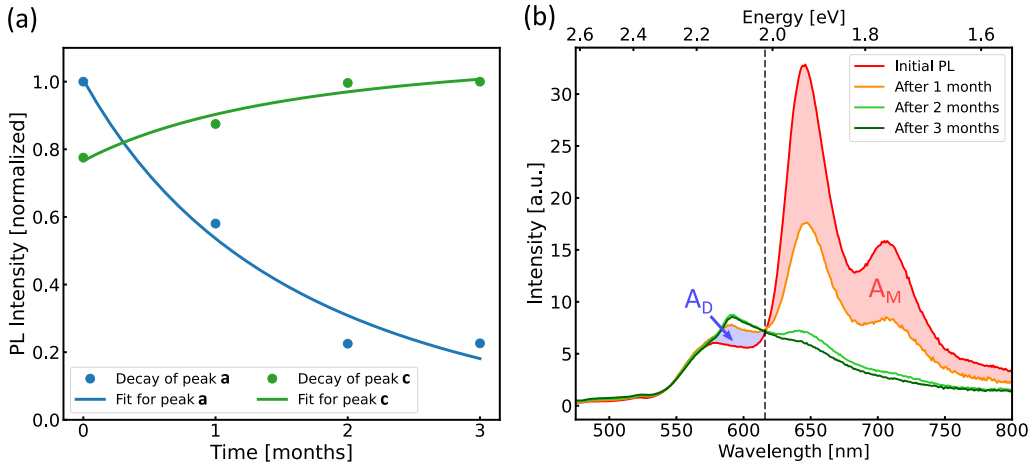

Figure 4.17: (a) Time evolution of peaks **a** and **c**, with fit using Eq.4.5. (b) Time evolution of the PL spectrum of the $C_{96}C_{12}$ solution. The area between the curve of the initial PL and the curve after 1 month left (A_D, in blue) and right (A_M, in red) of the iso-emissive point correspond respectively to the increase of the concentration of aggregates and to the decrease of the concentration of monomers.

It is also possible to estimate the ratio of fluorescence quantum yield using the time evolution of the PL. We observe that the total fluorescence intensity is not conserved during the aggregation process. It indicates a difference of fluorescence quantum yield between single GQDs and aggregates. Let F_M be the flux of emitted photons by single GQDs, which is related to the product $\Phi_M \sigma_M C$, where Φ_M is the quantum yield for monomers, C their concentration and σ_M their absorption cross section. Therefore, a variation ΔC of the concentration of monomers will induce a variation $\Delta\Phi_M$ of the flux Φ_M. If we introduce similar physical quantities for aggregates (with subscript $_D$), we can express the ratio of the fluorescence quantum yields:

$$\frac{\Phi_D}{\Phi_M} = \frac{\Delta F_D \times \sigma_M \times \Delta C}{\Delta F_M \times \sigma_D \times \Delta C_D}. \tag{4.8}$$

If we make now the assumption that only dimers are formed during the aggregation process, we obtain $\Delta C_D = -\Delta C/2$. We can also make the assumption that the absorption cross section for the dimer is twice as large as the one for the monomer. Since F_D and F_M can directly be assessed by integrating the PL peaks associated with each fluorescent species, we use the variation of the area under the PL curve to evaluate the ratio Φ_D/Φ_M. If we note A_M the area integrated between the initial PL curve and the PL curve measured after 1 month on the right side of the iso-emissive point (*i.e.* for single GQDs), shaded in red in Figure4.17(a), and A_D the area similarly integrated but on the left side of the iso-emissive point, shaded in blue, we can obtain:

$$\frac{\Phi_D}{\Phi_M} = \frac{A_D}{A_M}. \tag{4.9}$$

We estimate the ratio to $\Phi_D/\Phi_M \approx 9.5 \times 10^{-2}$, indicating a lower quantum yield for the

aggregate than for the GQD monomer, a behavior which has been observed for other chromophores [180]. Given the reported value for Φ_M around 35%, we can estimate the quantum yield of the aggregate to be around 3.3%.

Observation of synthesis by-products

Although the observation of aggregation of GQDs in solution has been confirmed, it is possible that additional fluorescent objects, including possible side-products resulting from the synthesis of $C_{96}C_{12}$ GQDs are present in our samples. During the characterization of the synthesis batch by Dr. Stéphane Campidelli in CEA Saclay, MALDI-TOF spectra were measured and analyzed. In Figure 4.18 are given the mass spectrum measured on a $C_{96}C_{12}$ batch, along with zooms on different parts of the spectrum. For each zone, simulations (in blue) are performed to verify if the speculated structure adequately reproduces the given spectrum. The main peak, detailed in Figure 4.18(b), corresponds to the awaited peak for $C_{96}C_{12}$ monomers (with the expected isotopic pattern). At slightly higher m/z ratio, we recover peaks shifted by around $\Delta m/z = 12$ relatively to the monomer peak, which can be associated with non-closed products. In Figure 4.18(c), we show two examples of two dehydrogenated GQD, labelled **M2** and **M3**, lacking respectively 5 and 8 C – C bonds. The simulation shows that the peaks in this region can correspond to GQDs where 5 to 8 C – C bonds were not formed due to an incomplete Scholl reaction. In Figure 4.18(d), the peaks match the signature of a monochlorinated GQD (structure labelled **M4**). This is not surprising since chlorination of GQDs is often observed during the synthesis of GQDs, specifically during the Scholl reaction. Coming now to the region circled in green, the attribution is more complex. While the periodicity of $\Delta m/z = 34$ encourages us to interpret these lines as structures with increasing numbers of chlorine atoms, the positions do not match a structure composed simply of multi-chlorinated $C_{96}C_{12}$ GQDs. A possibility could be the presence of a complex with a Fe atom (coming from the $FeCl_3$ used during the Scholl reaction), along with a OH group (structure **M5**).

The observations in MALDI-TOF prove the presence of synthesis by-products in the $C_{96}C_{12}$ GQD batch. While it does not change the interpretation made until now concerning the formation of aggregates in the solution, we can safely say that the by-products may also participate to the presence of additional peaks in the spectra observed in solution[5].

To conclude this section, we can summarize the results obtained for the $C_{96}C_{12}$ GQD in solution. With the objective of fully understanding the spectral measurements carried out in solution, we identified peaks resulting from the fluorescence of GQD monomers (peaks **a** and **b**), which result from the brightening of forbidden transitions due to distortion of the GQD's aromatic core. The additional features (peak **c**) are due to the presence of additional fluorescent objects, comprising GQD aggregates. As we move to single-object experiments, we use the solution samples studied in this part on experiments in

[5] If these objects were to be fluorescent, they would most probably emit at a different wavelength than GQD monomers, given the strong change in their molecular structure compared to GQDs (presumably blue-shifted due to the reduced delocalization of the π electrons).

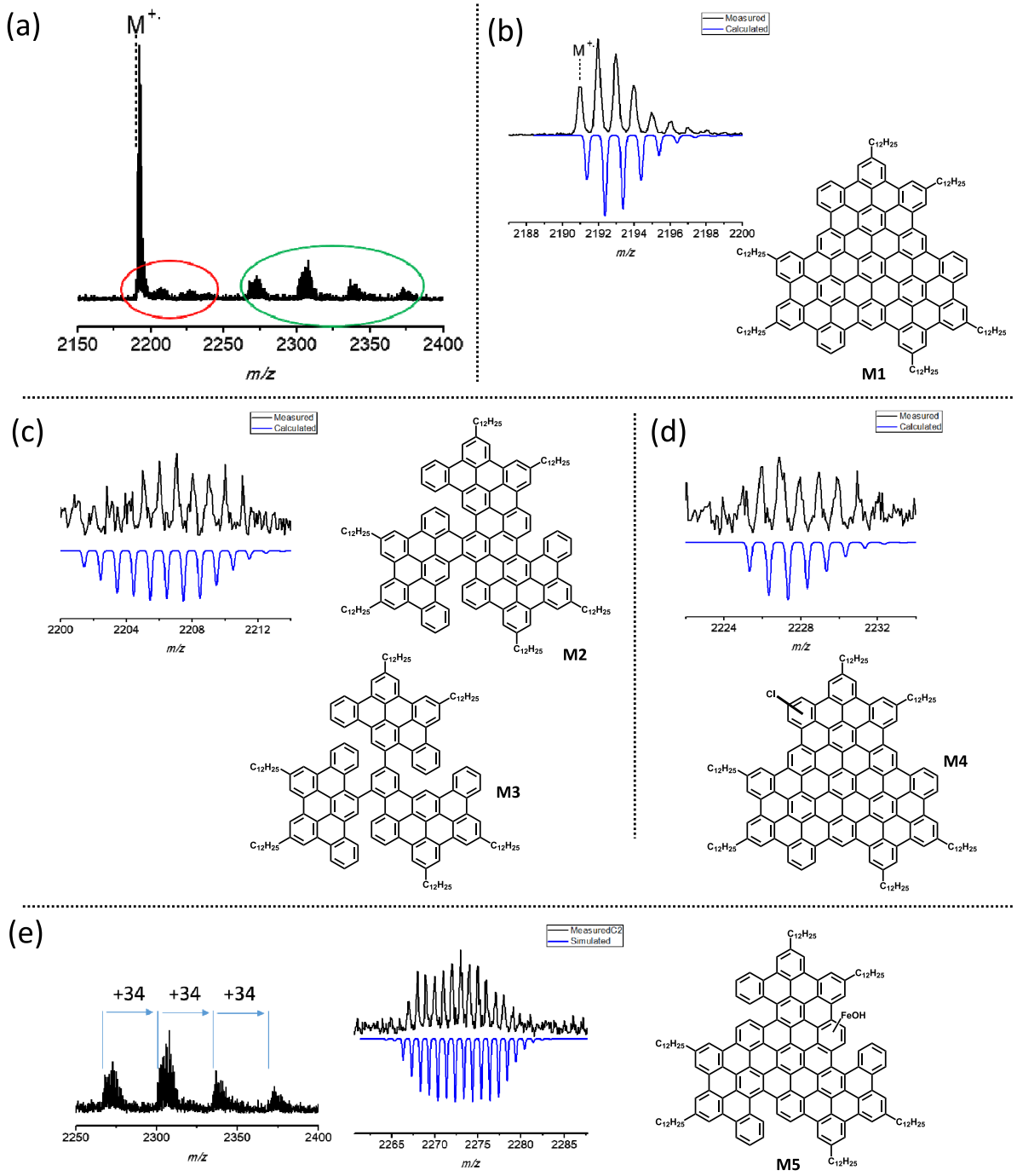

Figure 4.18: (a) MALDI-TOF spectrum of a $C_{96}C_{12}$ batch. (b),(c),(d) Zooms in the mass region circled in red, and the respective possible structures associated. (e) Zoom in the mass region circles in green, and example of speculative structure.
M1: $C_{168}H_{174}$, Exact mass: 2191.3616
M2: $C_{168}H_{184}$, Exact mass: 2201.4398
M3: $C_{168}H_{190}$, Exact mass: 2207.4888
M4: $C_{168}H_{173}Cl$, Exact mass: 2225.3226
M5: $C_{168}H_{181}FeO$, Exact mass: 2270.1400

solution to prepare the single-molecule samples. We will assuredly embed aggregates and other fluorescent species observed in the solution in the solid matrix.

4.3 Single-molecule study of $C_{96}C_{12}$

Although observations made in solution allowed us to identify the presence of various fluorescent objects including GQD aggregates, it also showed the limit of ensemble measurements. In order to probe the intrinsic properties of the $C_{96}C_{12}$ GQD and not be disturbed by ensemble effects or by the presence of the additional fluorescent objects, it is necessary to isolate the $C_{96}C_{12}$ GQDs. This can be achieved using single-molecule spectroscopy, as it will be demonstrated in this section. I first studied the GQDs at room temperature in order to check the distribution of their properties, before venturing to low temperature to probe with higher resolution the spectral signature of these objects.

In order to keep the discussions clear, I will refer to the additional objects present in the GQD solution (aggregates, synthesis by-products) as **by-products** while the contaminating emitters in single-molecule samples described in the previous chapter will be referred to as **impurities**.

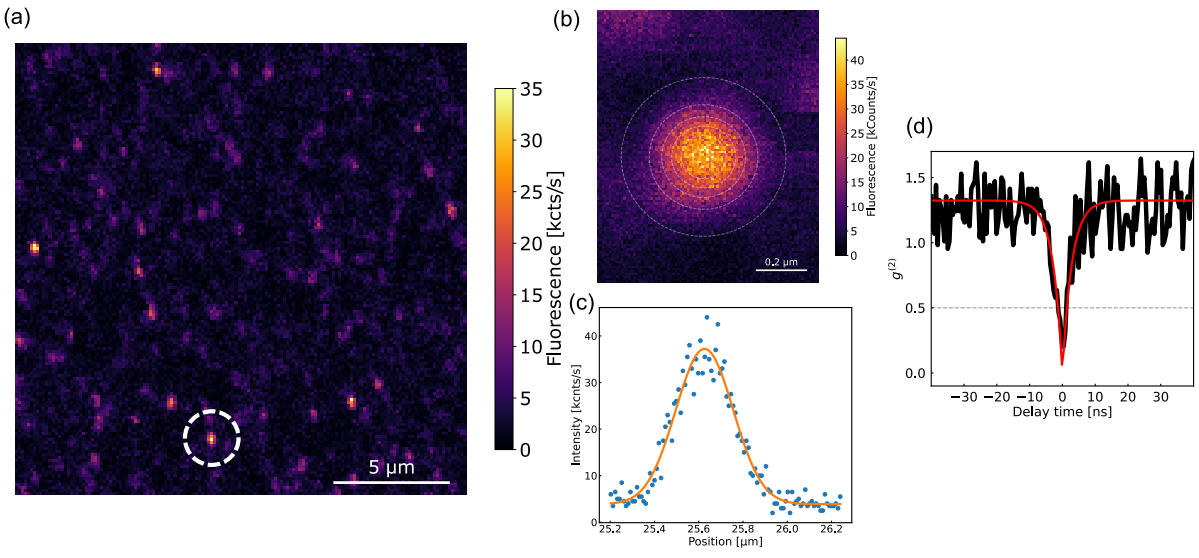

Figure 4.19: (a) Typical spatial map observed in micro-PL with excitation at 594 nm, 100 W/cm^2 power. A white circle highlights a typical GQD spot. (b) Zoom on a diffraction-limited spot, white circles indicate the contour of the 2D Gaussian fit, and (c) slice of the spot along the horizontal axis, with a Gaussian fit (in orange). (d) Typical anti-correlation function measured on a diffraction-limited spot. The antibunching at zero-delay ($g^{(2)}(\tau = 0) < 0.5$) indicates the presence of a single emitter.

4.3.1 Room-temperature characterization

Spatial maps and observation of single GQDs

Samples of $C_{96}C_{12}$ GQDs for single-molecule studies were prepared using the protocol described in Chapter 2. For room-temperature studies, GQDs embedded in polystyrene (PS) were deposited on glass substrate. The different samples studied were placed in the room-temperature micro-photoluminescence (micro-PL) setup described in Chapter 2.

An example of a spatial map obtained by scanning a sample with a 594 nm laser is presented in Figure 4.19(a). We can distinguish bright spots, corresponding to localized emission from fluorescent objects. While it is possible to find large spots, sometimes presenting non-circular shape, which correspond to agglomerates of fluorescent objects, most of the spots exhibit a circular structure smaller than 1 µm. A closer look at the spots show the expected profile for a diffraction-limited spot, which can be fitted by a 2D Gaussian function (Figure 4.19(b)). We recover from the fit a standard deviation of the intensity distribution of 130 nm, which corresponds very well with the predicted value in Chapter 2 (considering that the diameter can be described as 4σ, σ the standard deviation). Therefore, this observation confirms the presence of single GQDs in the sample. Of course, it is possible that two fluorescent objects close to each other may show the same diffraction-limited signature. Therefore, to confirm that only single objects are observed in the diffraction-limited spots, second-order autocorrelation functions $g^{(2)}$ are measured on these spots. On most of the stable spots, we measured an antibunching signature, with the $g^{(2)}(\tau)$ function droping below 0.5 at zero delay $\tau = 0$, indicating the presence of a single emitter in the spot, as shown in Figure 4.19(c).

In order to maximize the probability of finding single emitters, the concentration of the sample must be carefully chosen. In Figure 4.20, we show the effect of concentration on the spatial maps observed, when excited at 594 nm, with around 100 W/cm^2 of excitation power. The different dilutions are obtained from the same stock solution. We can clearly notice the effect of concentration of the solution used to prepare samples on the density of spots observed in the spatial maps. This is a good indication that the presence of GQDs is undoubtedly detectable by our setup. In our study of $C_{96}C_{12}$ GQDs,

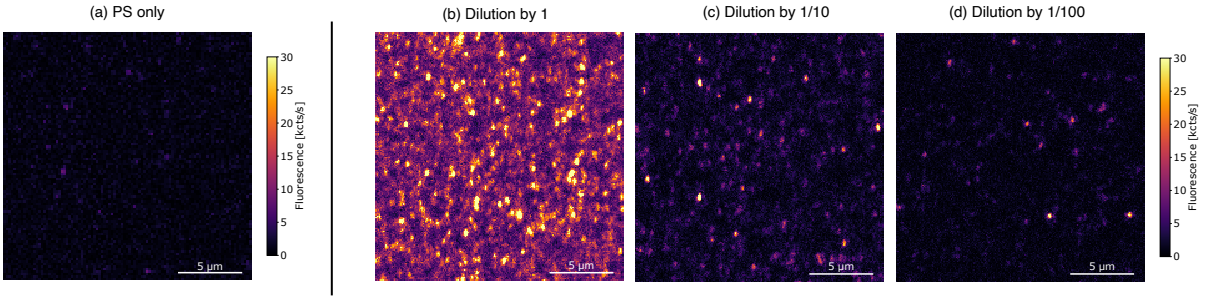

Figure 4.20: (a) Typical map for a sample without GQDs (only polystyrene). (b)-(d) Typical map for samples prepared from (b) a non-diluted, (c) a dilution by 1/10 and (d) a dilution by 1/100 of a stock solution. All maps are obtained with excitation at 594 nm and 100 W/cm^2.

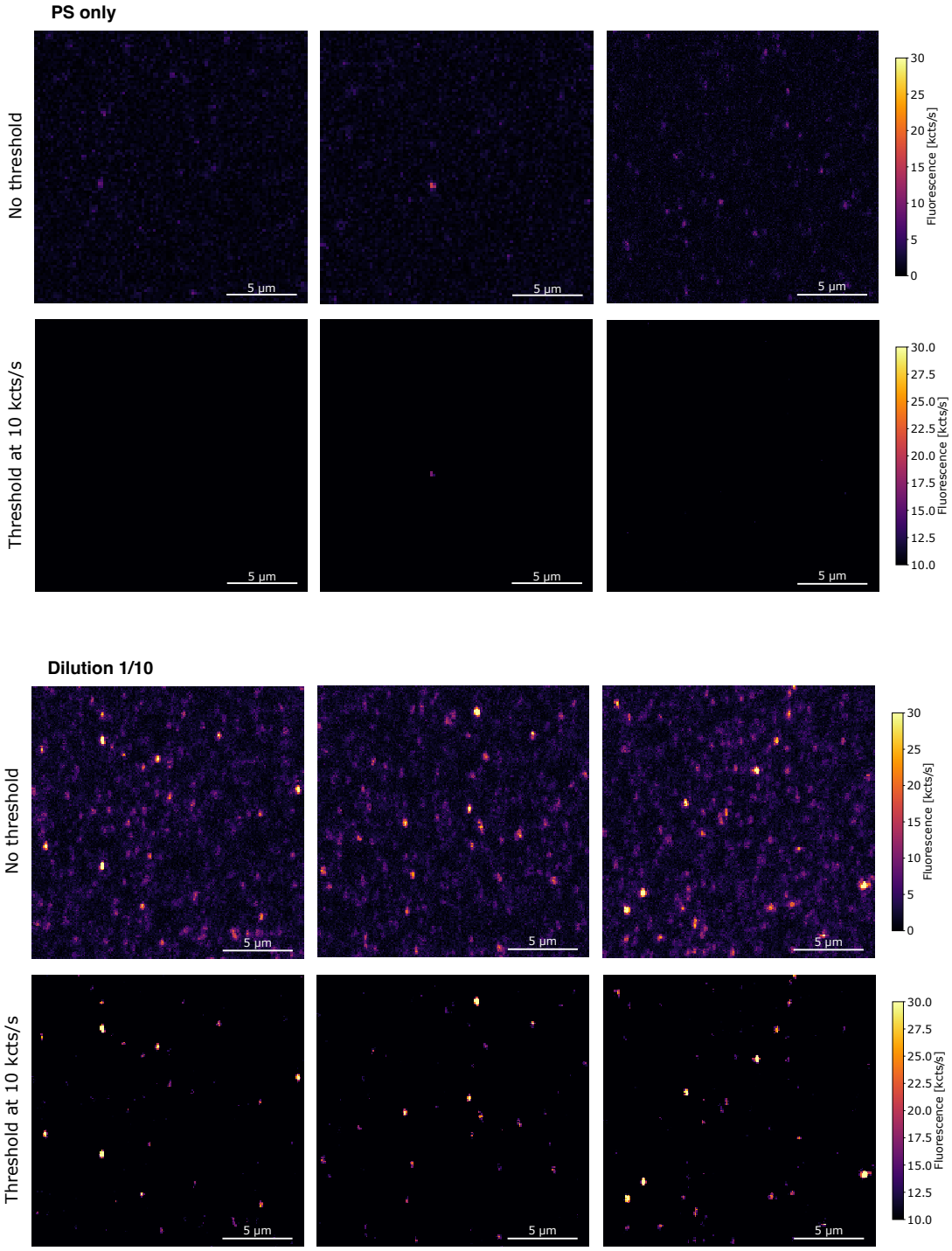

Figure 4.21: Effect of threshold on maps of dilution 1/10 samples.

Threshold	PS only samples		GQD samples		Average error per map
	Total # of spots	Average density	Total # of spots	Average density	
10 kcts/s	58	1.2 spots/map	558	17 spots/map	7%
12 kcts/s	42	0.8 spots/map	460	14 spots/map	6%
15 kcts/s	15	0.3 spots/map	303	9.2 spots/map	3%

Table 4.2: Number of bright spots observed on 51 maps (of size 20 µm × 20 µm) without GQDs and 33 maps with GQDs, along with the average number per map for different intensity thresholds. The average error corresponds to the fraction of bright spots in a map possibly due to impurities.

we decided to choose concentrations which lead to maps similar to the one labelled "Dilution 1/10" (labelled this way because prepared from a stock solution diluted by 10), where the density of spots is low enough to ensure the observation of single GQDs, but high enough to have an appreciable number of objects to study. Let us note that for the maps measured here, the polystyrene layer is around 100 nm thick (as shown in Chapter 3), which is lower than the depth of the confocal volume of the setup (*i.e.* the depth of field). This means that the setup does not allow us to selectively collect fluorescence from only one layer of the sample, although the piezoelectric translation stages have a spatial resolution low enough to selectively favor the collection of fluorescence from one layer relatively to others. Consequently, the concentration has to be chosen so that we prevent any layering of multiple objects in the sample [6].

As developed in the previous chapter, the presence of impurities in the samples makes the analysis of experimental observations laborious since the impurities present characteristics of aromatic compounds. The maps in Figure 4.20 clearly indicate that the increase of the concentration of $C_{96}C_{12}$ GQDs in the sample is accompanied with an increase of the density of bright spots (with intensities around 30 kcounts/s) while no bright spots above 10 kcounts/s can be detected in the map of a PS only sample. The level of signal is similar to previously reported for this GQD in these conditions [145]. Therefore, focusing only on bright spots can be a good method to circumvent artefacts from impurities.

A more quantitative criterion can be elaborated to assess the efficiency of this method. For different values of threshold, it is possible to estimate the average number of discernable spots for 20 µm × 20 µm maps collected for samples with and without GQDs (as shown in Figure 4.21). In Table 4.2, the number of spots distinguished for a set of maps with (labelled *GQD samples*) and without GQDs (labelled *PS only samples*) is given for different threshold values. The number of maps amounts to 33 maps for samples with GQDs and 51 maps without GQDs. As the threshold increases, both the number of impurity spots and GQD spots decrease. However, the average error, defined as the average fraction of spots on a map with GQDs which originate from impurities, decreases with

[6] Actually, if the concentration is chosen so that single GQDs are observed in raster scans, it should naturally also be low enough to prevent layering.

increasing threshold. We can clearly conclude that setting a threshold for the intensity of the spots in order to minimize the chance of including impurities in our analysis is an efficient method. It is interesting to add that the average error calculated here may be overestimated, since we observe that the spots in "PS-only" samples usually bleach very quickly when excited, resulting in a lower number of bright spots due to impurities actually studied unintentionally. For the following spectral study of $C_{96}C_{12}$ GQDs, we aim to use a threshold at 10 kcounts/s[7].

Preliminary analysis of single-object spectra

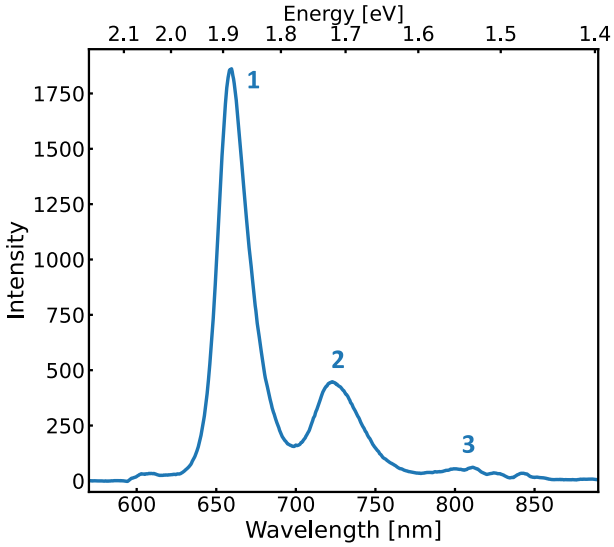

Figure 4.22: Typical spectrum of single $C_{96}C_{12}$ GQD at room temperature. Obtained with excitation at 594 nm and 100 W/cm^2.

Focusing on the diffraction-limited spots showing single-emitter signature, we can measure the spectrum of the fluorescence coming from these spots. As expected from measurements in solution and previously reported values [10], the wavelength of emission of the $C_{96}C_{12}$ should be around 640-650 nm. In Figure 4.22, a typical spectrum observed when exciting at 594 nm is given. The spectrum is composed of two to three peaks, the third peak being faint in intensity and often difficult to observe clearly. We shall label the peaks in increasing wavelength peaks **1**, **2** and **3**, as shown in Figure 4.22. This structure is coherent with the observations in solution, with the first peak corresponding to the main electronic transition, and the second peak to the first vibronic replica. The third peak could correspond to a second vibronic replica (*i.e.* creation or annihilation of two phonons during the transition).

[7]Since the absorption of GQDs is sensitive to the polarization orientation [10], dim spots may correspond to GQDs excited with a polarization orientation almost orthogonal to their absorption dipole orientation. The use of an intensity threshold leads us to neglect these GQDs. Nonetheless, since we expect an homogeneous distribution of the orientation of GQDs in the polystyrene matrix, this threshold should not bias the final conclusions.

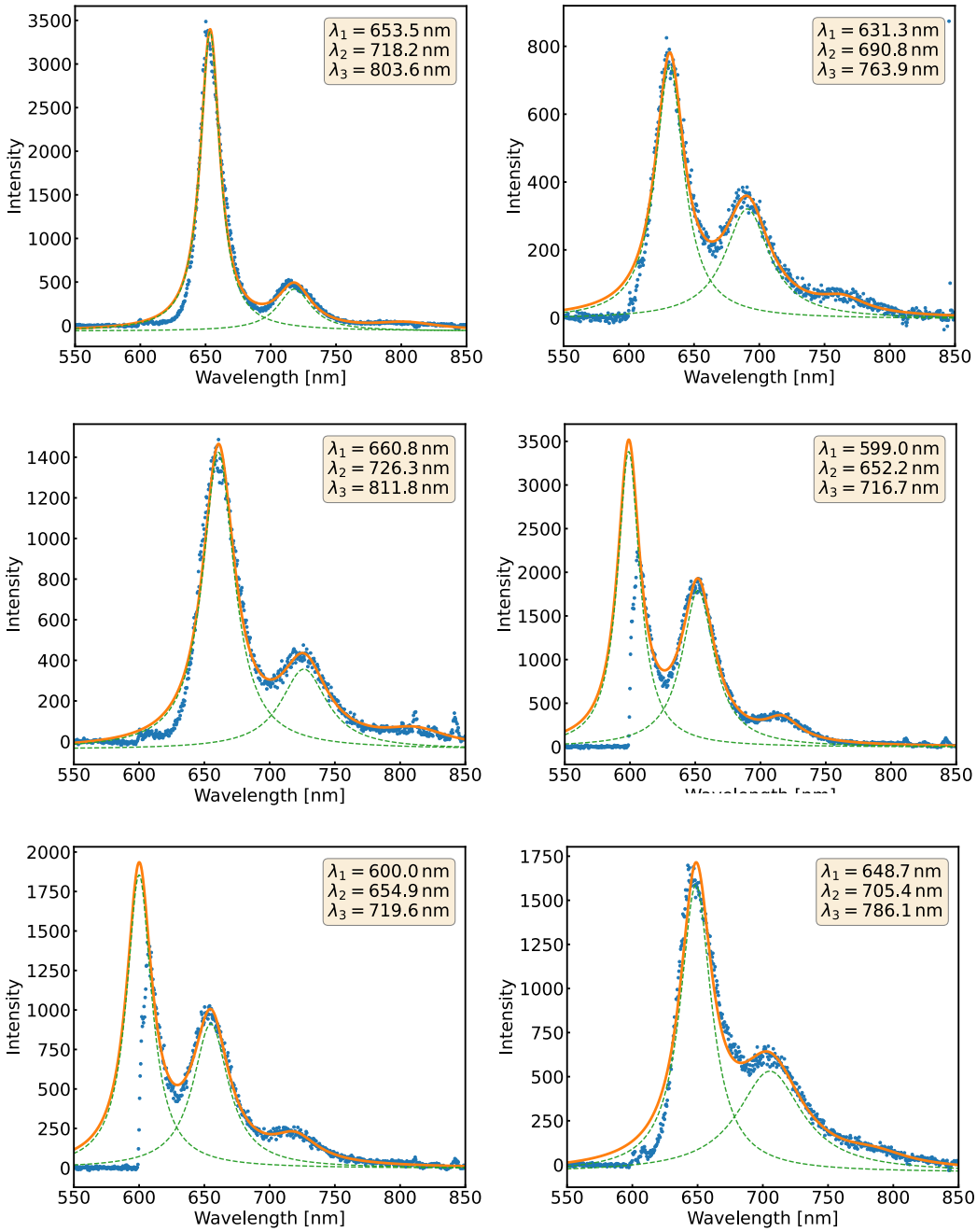

Figure 4.23: Examples of spectra observed in micro-PL and taken into account *a priori* as GQDs. Spectra are fitted with three Lorentzian functions. Only points above 600 nm are considered for the fit.

In order to have more insight into the behavior of the GQDs in single-molecule samples, we decided to perform measurements on a large number of spots accross different samples and therefore increase the statistics used for our interpretation.

For the spots observed when excited at 594 nm, we distinguish spectra with slight differences, although all share the expected general structure described earlier (a few are shown in Figure 4.23). We use Lorentzian functions to fit the different peaks and extract the position of the peaks and their linewidths. We note that spectra with peak **1** around or below 608 nm are affected by the presence of the dichroic mirror at 595 nm and the 594 nm filter. The fit of these spectra are more difficult, as shown on the bottom left of Figure 4.23.

We decide to first focus on the energy of peak **1**, corresponding to the purely electronic transition. In Figure 4.24(a), a histogram of the wavelength λ_1 of peak **1** is given, for a total number of 52 spectra analyzed. The distribution can be described by two contributions, one peaked at around 655-660 nm and the other, less peaked, centered around 625 nm. This distribution is consistent with observations previously made by Shen Zhao [145], as shown in Figure 4.24(b), although in our case, the majority of spectra has peak **1** at a wavelength above 640 nm (32 above 640 nm, 20 below 640 nm). A possible explanation for this observation is the existence of two families of GQDs in our samples, resulting from the possiblity of finding them in one of two different states (*e.g.* charge states, conformation states). For instance, embedding organic emitters in a crystalline matrix presenting two distinct insertion sites in the host structure could result in the observation of two different sets of properties due to the effect of the matrix, as reported for various systems [181, 81]. However, given the chosen polymer matrix, with a continuous range of different hosting environments, this does not represent a reasonable explanation for the given distribution for $C_{96}C_{12}$.

If we compare the distribution of λ_1 with the PL spectrum observed in solution, we recognize in the family of spectra with λ_1 around 650 nm the expected spectra for GQD

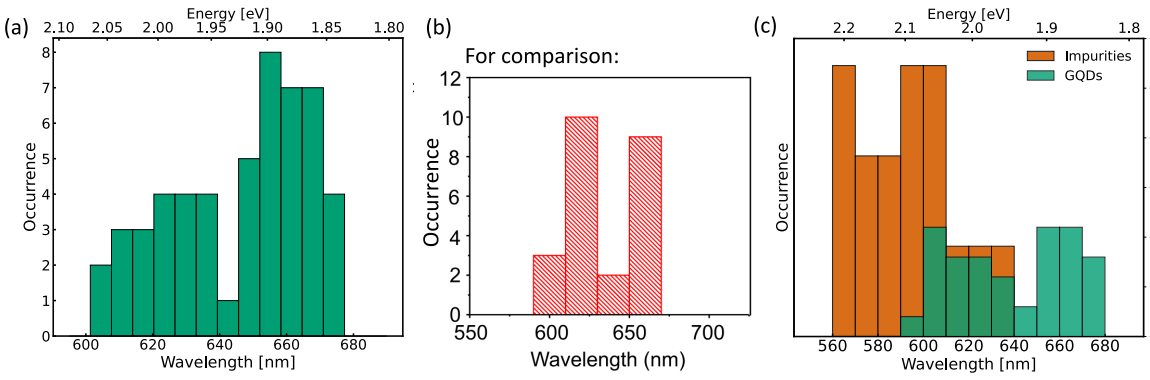

Figure 4.24: (a) Distribution of the energy of peak **1** (on 52 spots). (b) Distribution measured by Shen Zhao on similar samples (on 25 spots), adapted from [145]. (c) Comparison with the distribution of peak **1** measured for impurities. The distributions are rescaled for comparison.

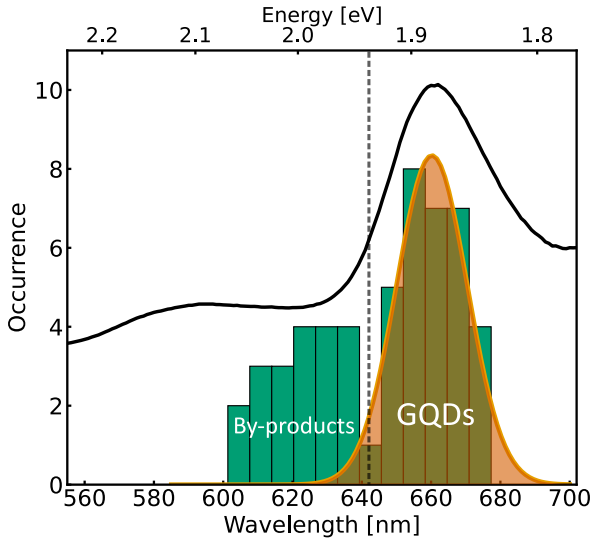

Figure 4.25: Comparison of the distribution of λ_1 with the PL spectrum in solution (solid black line, redshifted by 45 meV) and attribution to the emitting species. The orange curve indicates the Gaussian fit of the distribution above 640 nm.

monomers in solution, although slightly redshifted. However, we are left with the spectra of spots with λ_1 at slightly higher energy.

In order to investigate the origin of the spectra with λ_1 below 640 nm, we decide to compare the distribution of wavelength observed on our samples with GQDs with the distribution of peak **1** for spectra coming from impurities (described in Chapter 3). Impurity spectra have a peak **1** distributed around 585-590 nm, with a few going up to 640 nm. We plot both distributions in Figure 4.24(c). As can clearly be seen, the spectra at higher energy observed in our samples (*i.e.* with $\lambda_1 < 640$ nm) could perfectly correspond to impurities, since the distribution of wavelength for impurities, in red, stops exactly around 640 nm. However, given the criterion based on intensity thresholds described in the previous section, the impact of impurities should be limited in our statistics. In the case of this histogram, if we assume all the spectra with λ_1 below 640 nm to be impurities, they would represent around 35% of the spots studied, which is significantly larger than the predicted 7% in the previous section. We therefore expect other objects to account for the spectra observed at higher energy.

Experiments in solutions have revealed the presence of fluorescent by-products in the solution samples, in particular the formation of aggregates, emitting at transitions blueshifted relatively to the transitions of the $C_{96}C_{12}$ GQD. We could thus explain the observation of spectra at higher energy by the presence of aggregates and other by-products embedded in the polymer matrix. For instance, calculations for GQD dimers predicted a blueshift of around 30 meV, which, if we consider a GQD emitting at 645 nm, would result theoretically to a dimer emitting at 635 nm. Moreover, if we compare the distribution with the PL spectrum observed in solution, as shown in Figure 4.25, we can see that the histogram reproduces the solution PL spectrum (a slight shift is applied to

the PL spectrum in solution in order to match the portion of the histogram attributed to GQDs with the PL peak corresponding to GQD monomers).

Therefore, we can be assured that the spectra observed above 640 nm correspond to single GQDs. Concerning the spectra below 640 nm, although a few impurity spectra may be observed in our statistics, we are confident that they correspond predominantly to by-products observed in solution. Given the results of this section, we can see that the combination of the criterion based on intensity and a discrimination based on the position of peak **1** results in an efficient selection of spectra corresponding effectively to $C_{96}C_{12}$ GQDs.

Intrinsic properties of single-GQD spectra

We focus now only on the spectra with $\lambda_1 > 640$ nm, corresponding to $C_{96}C_{12}$ GQDs.

We can first consider the distribution in wavelength of peak **1**. It can be fitted using a Gaussian distribution (see Fig.4.25), yielding a central wavelength at 660 nm and a standard deviation of the distribution of 10.2 nm. This dispersion can be compared to the emission linewidth of single GQDs. We thus compute the FWHM of line **1** of single GQD spectra. The histogram of the linewidth is presented in Figure 4.26, highlighting a mean linewidth of around 30 nm, much larger than the peak **1** wavelength distribution. Interestingly, the narrow distribution of peak **1** indicates that the polystyrene matrix hosting the GQDs does not strongly impact the emission wavelength of the GQDs, despite the expected strong disorder and variations in the local environment for such matrices.

Moreover, the average linewidth value is comparable to the FWHM of peak **a** in solution measured at around 35 nm (Figure 4.5). This comparison is consistent with the interpretation of a homogeneous population of GQD monomers in solution. Indeed, we observed in solution that the emission peak **a** showed no indication of inhomogeneous

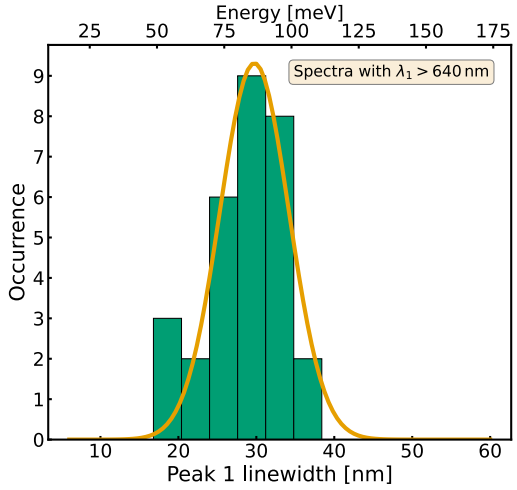

Figure 4.26: Distribution of the linewidth of peak **1** considering only GQD spectra (with $\lambda_1 > 640$ nm). The orange solid line shows the Gaussian fit of the distibution, with central linewidth of 30 nm and standard deviation of 4.4 nm.

broadening. To recover the same linewidth as in PL spectra in solution was also expected, since it was reported that TCB is a good solvent for the dispersion of aromatic compounds and the observation of narrow lines in their spectra [144].

We note that the average value of λ_1 is slightly redshifted relatively to the position of peak **a** associated with GQD monomers in solution (by around 45 meV). This may be due to the change of dielectric environment as we move from TCB solvent to polystyrene matrix.

By exciting the GQDs at higher energy, we can probe if emission from higher singlet states can be observed for the $C_{96}C_{12}$ GQD.

With a 532 nm laser, aligned on the confocal microscope used for micro-PL, it is possible to perform the same experiments as with the 594 nm laser. To excite on collocal spots with both excitation sources enables the study of the effect of excitation energy on the spectra, as shown in Figure 4.27. For spectra collected on the same spot, we observe that the spectrum (including position of the peaks, their relative intensities and linewidths) does not change as the excitation energy is increased. This is a strong indication that no emission from higher singlet states is observed for $C_{96}C_{12}$ GQDs, and the photophysics of these objects follows Kasha's rule (*i.e.* observation of fluorescence from the lowest singlet state, corresponding here to peak **1**). This observation on the single-object level confirms the analysis of the experiments in solution, where the observation of fluorescence at higher energy was conclusively not associated with the emission from $C_{96}C_{12}$ GQD monomers. Moreover, this observation confirms that the emission results from intrinsic fluorescence of the $C_{96}C_{12}$ GQD and its electronic states. This behavior contrasts with the emission collected from GQDs produced using top-down methods [52, 50], where the emission is dominated by defect states (see Fig.4.27(c)).

Let us now focus on the vibronic replicas (lines **2** and **3**). In Figure 4.28(b), the distribution of wavelength λ_2 of peak **2** is plotted alongside the distribution of peak **1** for spectra with $\lambda_1 > 640$ nm. The distribution of λ_2 reproduces the distribution of λ_1 but is globally redshifted. We plotted the energy split ΔE_{12} between peaks **1** and **2** for the different spectra measured (as shown in Figure 4.28(a)). As shown in Figure 4.28(c), the energy split is indeed comparable for the different spectra, yielding a distribution centered at 169 meV (1350 cm^{-1}) which can be fitted by a Gaussian with a standard deviation of 3.7 meV. For comparison, this value is one order of magnitude lower than the average linewidth measured for peak **1** at around 85 meV (30 nm), highlighting the narrow dispersion of the energy split.

The energy difference ΔE_{23} between peaks **2** and **3** can also be measured for the different spectra. We take into account only the spectra where the position of the third peak can clearly be pinpointed, which explains why the number of spectra used for the histograms (13 spectra) is lower than for the previous histogram. In Figure 4.28(d) the distribution of ΔE_{23} is plotted for spectra with $\lambda_1 > 640$ nm. The distribution is similar to the one of ΔE_{12}. The center position of the distribution at 182 meV is slightly higher in energy relatively to the distribution of ΔE_{12} and a Gaussian fit yields a similar standard deviation (at 3.5 meV). Therefore, the similarity of ΔE_{12} with ΔE_{23} is consistent with the assignment of peaks **2** and **3** to successive vibronic replicas.

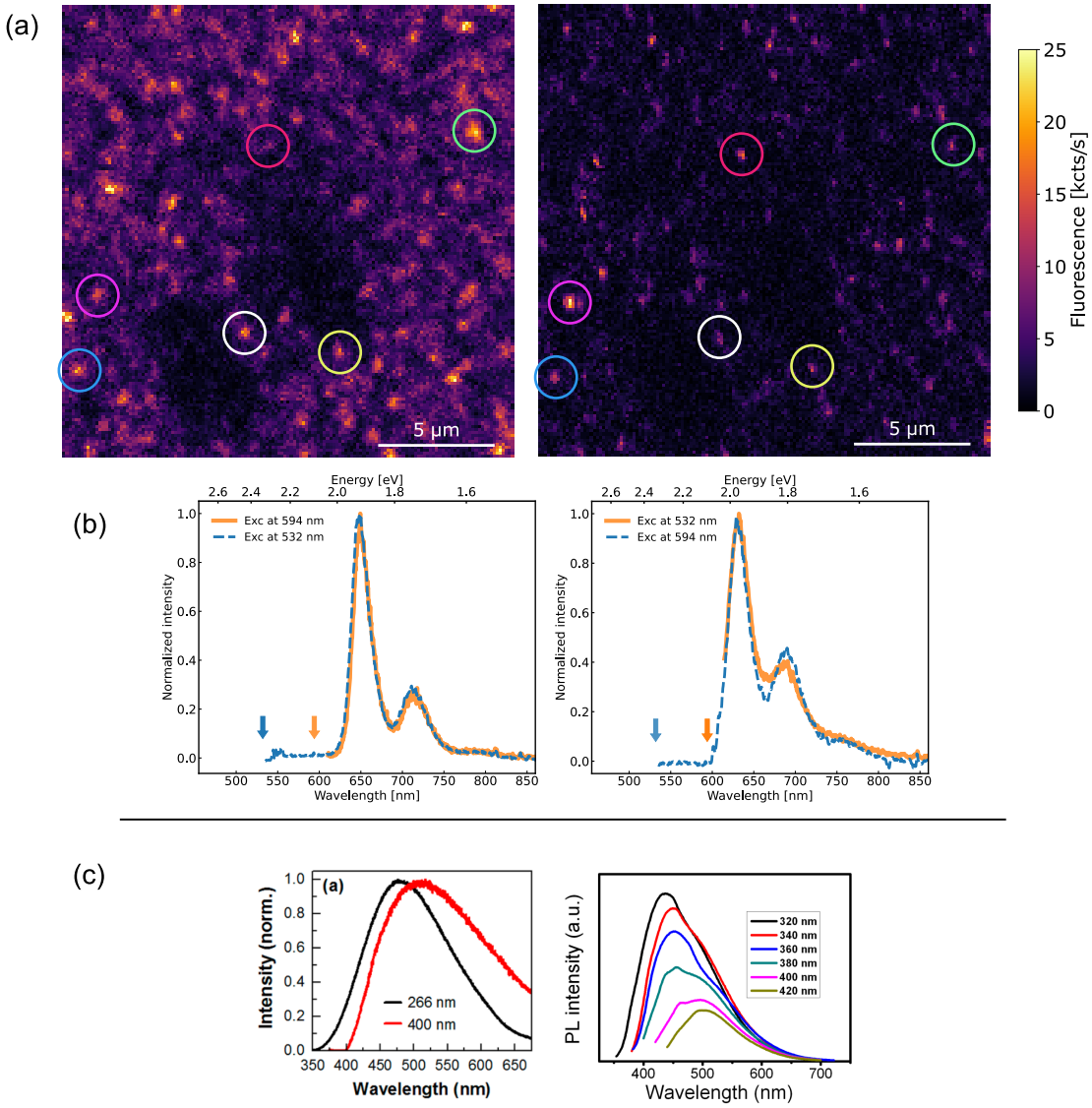

Figure 4.27: (a) Example of maps obtained with (left) 594 nm and (right) 532 nm excitation. Color circles highlight collocal spots in the two maps. (b) Example of spectra measured by exciting at 594 nm and 532 nm. (c) Comparison with ensemble spectra of GQDs obtained via top-down method, from [52] (left) and [50] (right).

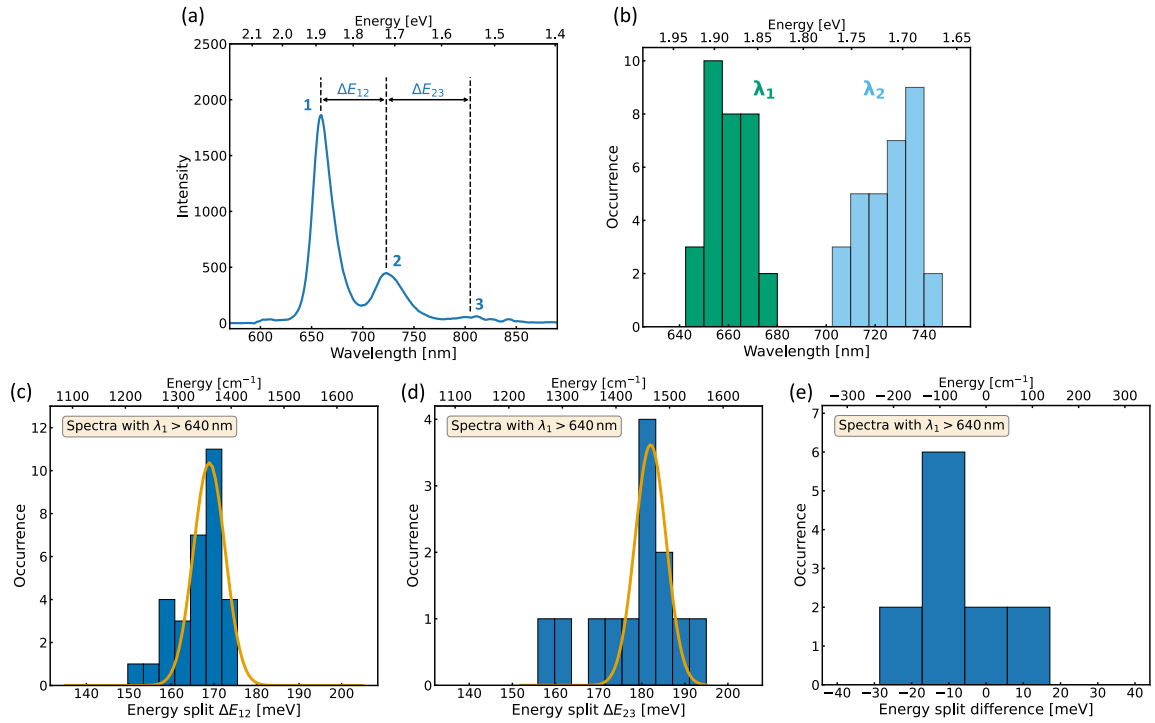

Figure 4.28: (a) Definition of ΔE_{12} and ΔE_{23} on a typical GQD spectrum. (b) Distribution of the wavelength of peak **1** (in green) and peak **2** (in blue) for GQD spectra ($\lambda_1 > 640$ nm). (c)-(e) Distribution of ΔE_{12}, ΔE_{23} and $\Delta E_{12} - \Delta E_{23}$ for GQD spectra.

The energy split difference $\Delta E_{12} - \Delta E_{23}$ can finally be plotted (Figure 4.28(e)). The histogram indicates a weak average difference between the two energy splits (around -5.7 meV) and confirms the aforementioned global shift of the distribution of ΔE_{23} relatively to the one of ΔE_{12}.

The distributions of the different quantities discussed hereabove show relatively narrow dispersion, especially if we compare with distributions performed on GQDs obtained via top-down methods [182], which exhibit larger standard deviations by almost one order of magnitude for energy-split values in similar polymer matrices. This result highlights once again the benefit of bottom-up synthesis for the production of GQDs with narrowly-dispersed optical properties.

Comparison with by-products

We decide to focus now on the spectra with peak **1** below 640 nm, which we associated primarily to by-products observed in solution.

Looking at the distribution of the wavelength peak **1**, we can see that the distribution is broader and less peaked than for single GQDs. Since we attribute these spectra to by-products, the observed dispersion of λ_1 may result from the presence of aggregates with different sizes or configurations in the sample. Concerning the linewidth of peak **1** (given in Figure 4.29(b)), we can see that it is centered at 33 nm, close to the average value measured for GQDs. However, the standard deviation of the distribution is significantly

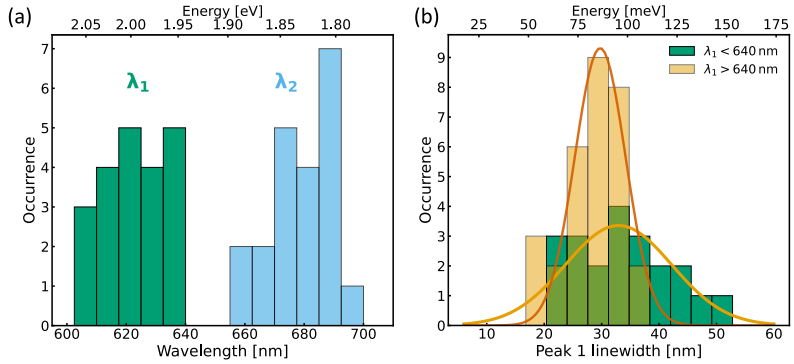

Figure 4.29: Distribution of (a) λ_1 and λ_2 and of (b) the linewidth of peak **1** considering only by-product spectra (with $\lambda_1 < 640$ nm).

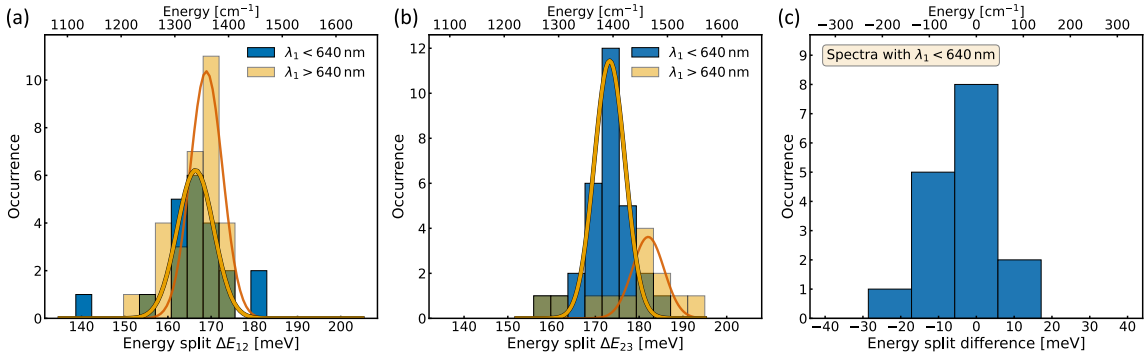

Figure 4.30: Distribution of (a) Distribution of ΔE_{12}, (b) ΔE_{23} and (c) $\Delta E_{12} - \Delta E_{23}$ considering only by-products spectra (with $\lambda_1 < 640$ nm).

larger than for GQDs (9 nm for by-products compared to 4 nm for GQDs). Since we do not expect the by-products to show a stronger sensibility to local perturbations than GQDs, the distribution results intrinsically from the population of emitters, and is in line with the possible presence of various aggregates or by-products[8].

Similarly to GQDs, we can see that the distribution for λ_2 has the same dispersion as the distribution of λ_1 (Fig.4.29(a)) but redshifted. The energy splits ΔE_{12} and ΔE_{23} are plotted in Figures 4.30(a) and (b). In contrast to the distribution observed for λ_1 or for the linewidth of peak **1**, the distributions of the energy split are narrow. In order to compare with the energy splits measured for GQDs, we fitted the distribution using Gaussian functions. We observe that for ΔE_{12}, the distribution is centered at 166 meV, with a standard deviation of 4.2 meV, and for ΔE_{23}, the distribution is centered at 173 meV with a standard deviation of 3.5 meV. The distributions have the same standard deviation as the distributions for the GQDs, but are shifted towards lower energy. If we look at the energy split

[8]This observation is also coherent with the observation of a multi-exponential decay dynamics when performing time-resolved photoluminescence measurements in solution at wavelengths below 640 nm, as described in Subsection 4.2.3.

difference (Fig.4.30(c)), we recover the same distribution as for GQDs, with a central value slightly shifted relatively to zero difference. The similarity in dispersion for the energy splits between GQDs and the by-products shows that all the fluorescent objects included in the by-products share to some extent the same vibrational modes as the $C_{96}C_{12}$ GQDs. Moreover, the striking difference between the broadened dispersion of the linewidth of peak **1** and the reproducible dispersion for the energy splits indicates that the origin of the dispersion of the linewidth of peak **1** does not seem to affect the vibrational mode responsible for the vibronic replicas. Once again, these observations are consistent with the attribution of the by-products to GQD-like objects such as aggregates, which are expected to exhibit vibrational modes close to the ones of GQDs. Interestingly, we can note that, similarly to the observation on the histograms, we also observed a weaker value of the energy split for the aggregates than for the GQD monomers in solution when looking at the PLE, as mentioned in Subsection 4.2.3.

If we summarize the observations from the discussion on the peaks observed for single-GQD spectra, we have observed that when looking at the distribution in wavelength of peak **1**, we observe two families of emissive objects. While the awaited GQDs emitting at around 650 nm are observed, emission at higher energy (below 640 nm) can be attributed to by-products from the GQD solution and impurities, although the latter should be less visible given the intensity criterion developed in the previous section. Nonetheless, while it is possible to distinguish the GQDs based on the wavelength of the first peak, we have observed that spectra from by-products and impurities are indistinguishable. We can hence see the limit of the spectral analysis at room temperature. Going down at lower temperature will eventually bring more insight into this subject.

4.3.2 Low-temperature spectroscopy and vibrational characterization

Single-molecule spectroscopy at low temperature

Using the low-temperature micro-PL described in Chapter 2, we perform experiments at cryogenic temperatures (around 7 K). Samples are prepared following the same protocol as for room-temperature samples, where the substrate is changed for a solid-immersion lens (see Methods for more details) for larger numerical aperture. In Figure 4.31(a), I present a spatial map observed on a sample with $C_{96}C_{12}$ GQDs, with an excitation at 594 nm, 2×10^3 W cm^{-2} power. We can then reproduce the same characterization as at room temperature. Bright spots can be fitted by a 2D Gaussian with a standard deviation of 100 nm (Fig.4.31(b)), which is slightly lower than for the room-temperature setup, and perfectly corresponds to the calculated value for a diffraction-limited spot (see Chapter 2). The power used is usually around 2 to 2.5 µW, generating an excitation power density of around 2×10^3 W cm^{-2}. This power density, although higher than for room-temperature experiments (around 100 W cm^{-2}), yields the same level of fluorescence signal as in room-temperature maps[9]. This may be due to losses during the collection of

[9]The power density may be overestimated since the power of the excitation beam is measured before the entrance window of the vacuum chamber. Losses may occur at this interface.

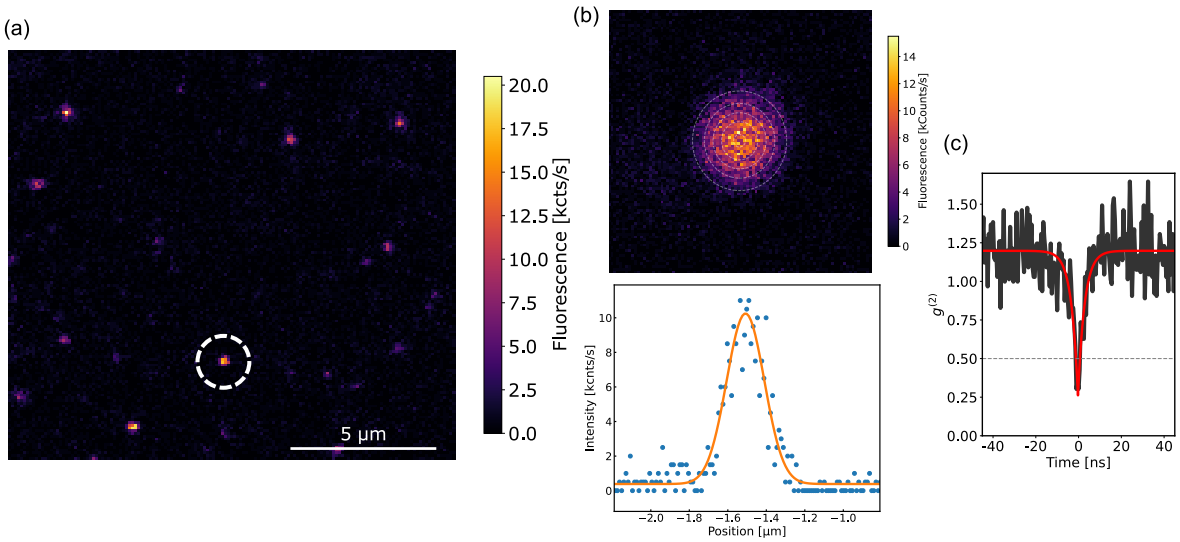

Figure 4.31: (a) Spatial map observed at low temperature, excitation at 594 nm, 1.6×10^3 W cm^{-2} power. White circle indicates a typical diffraction-limited spot. (b) (top) Zoom on a diffraction-limited spot, white circles show the contour of the 2D Gaussian fit, and (bottom) slice of the spot along the horizontal axis, with a Gaussian fit (in orange). (c) Typical anti-correlation function measured on a diffraction-limited spot. The antibunching at zero-delay ($g^{(2)}(\tau = 0) < 0.5$) indicates the presence of a single emitter.

the fluorescence signal (especially as it hits the window of the vacuum chamber), which must be compensated by a higher excitation power.

On such spots, we can measure a second-order autocorrelation function to verify the single-emitter nature of each spot, and we recover the awaited antibunching (as shown in Figure 4.31(c)). Measurements at low temperature were always preceded by tests at room temperature to ensure the quality of the sample (density of spots, observation of spectra corresponding to single $C_{96}C_{12}$ GQDs).

In Figure 4.32, we plot a typical low-temperature spectrum of $C_{96}C_{12}$ GQD. In stark contrast to room-temperature spectra, the spectrum collected at low temperature is richer, constituted of many weak lines which were not resolved at room temperature due to broadening processes. The low-temperature spectrum is composed of one sharp line, the zero-phonon line (ZPL), which arises from purely-electronic transitions (without creation or annihilation of phonons), along with a broad band and additional less intense peaks redshifted relatively to the ZPL. The weak broad band decreasing from the ZPL corresponds to the *phonon wing* of the ZPL, which results from the weak coupling of the GQD to a large number of vibrational modes from the surrounding matrix (for example to a branch of phonons in the matrix) [70]. The additional peaks correspond to transitions accompanied by the creation (or annihilation) of a phonon of various vibrational modes, each peak associated with a vibrational mode of the GQD. Considering a linear coupling of electronic levels to phonons, the energy difference between the ZPL and the line of a vibronic transition can be assigned to the energy of one phonon of the vibrational mode corresponding to the transition, *i.e.* to $h\nu_{\text{vib}}$ where ν_{vib} corresponds to the frequency of

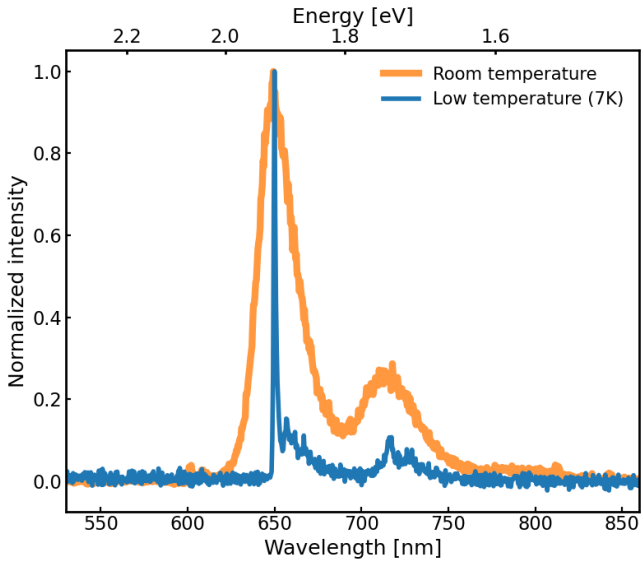

Figure 4.32: Typical spectrum of a single $C_{96}C_{12}$ GQD at 7 K, with excitation at 594 nm. Typical room-temperature spectrum plotted for comparison.

the vibrational mode. A similar structure has been described for impurities (see Chapter 3). We will describe in more details the observations for the ZPL and the vibrational modes of $C_{96}C_{12}$ in the following paragraphs.

It is also interesting to note that, apart from spectra exhibiting narrow lines similar the one shown in Figure 4.32, a few spectra studied at low temperature conserve the structure shown for room temperature, with two to three broad peaks.

Focus on the vibrational fingerprints

We first focus on the peaks in the spectra of $C_{96}C_{12}$ corresponding to vibronic transitions. These peaks are less intense and present a broader linewidth compared to the ZPL, which is a common observation for spectra at low temperature [183], due to the short decay lifetime of the vibronic states [71, 184].

As mentioned before, the frequency of the vibrational mode responsible for each vibronic transition can be extracted from the energy redshift of the corresponding peak relatively to the ZPL. On the spectrum shown in Figure 4.33(a), we can pinpoint four distinct peaks (labelled modes **1** to **4** in increasing order of energy), and measure four associated vibrational frequencies. These four characteristic lines can be observed for $C_{96}C_{12}$ spectra accross different samples. Plotted in Figure 4.33(b), the histogram of the energy of the four different lines is given for the GQD spectra measured at 7 K, along with the position of the ZPL set at zero energy. The average position for each distribution is 183 cm^{-1}, 397 cm^{-1}, 1362 cm^{-1}, 1576 cm^{-1}. We can sort these lines into two sets. At high energy (modes **3** and **4**), the value of the vibrational modes coincide with the frequency usually associated with C=C stretching modes in PAHs [162]. These modes therefore correspond to *localized* vibrations in the GQD. On the other hand, the two low-fequency modes (modes **1** and **2**) should correspond to vibrational modes *delocalized* on

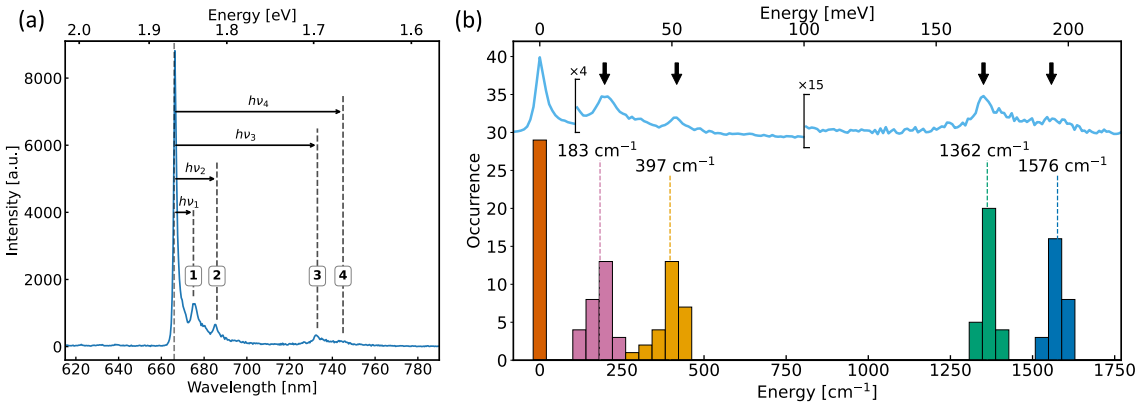

Figure 4.33: (a) Example of four pinpointed peaks resulting from vibronic transitions for $C_{96}C_{12}$ GQDs. The peaks are labelled **1** to **4**. The energy redshift relatively to the ZPL gives the energy of the vibrational mode (black arrows). (b) Distributions of the four vibrational modes observed at 7 K. A typical spectrum is given on top of the distribution. Successive zooms on the spectrum are applied for clarity.

the whole GQD. The delocalized nature of these modes should bestow on them a strong dependence on the size and the geometry of the GQD. Such delocalized vibrations have been observed for various graphene-based materials.

Similarly to carbon nanotubes, for which it is possible to link a characteristic vibrational mode, the *radial breathing mode*, to the diameter of the nanotube [185], it is possible to define such a mode for graphene nanoribbons (GNR). For GNR, theoretical studies of Raman-active modes using mechanical modelization [186, 187] or symmetry analysis [188] revealed the existence of a *radial breathing-like mode* (RBLM), or simply breathing-like mode. This mode results from the deformation of the GNR along it lateral direction (see Figure 4.34(a)). The frequency of the mode scales as $1/w$, w the width of the GNR. In the same manner, a length-dependent mode has also been reported, referred to as *longitudinal compressive mode* (LCM), which corresponds to the longitudinal deformation of the GNR along its long axis (see Figure 4.34(b)). This mode scales as $1/L$, L the length of the nanoribbon [189], and has a lower frequency than the RBLM given the stronger delocalisation of the vibrational mode.

We decided to try a naive estimation of an analogous vibrational mode for our GQD. In the case of GQDs, mechanical modelization of the system using continuum elasticity theory was proposed recently [190]. The model, which faithfully reproduced previously-reported numerical and experimental results for GNR, predicts for a circulary-shaped GQDs:

$$\omega_{\mathrm{RBLM}} = \frac{x}{R + \delta R}\sqrt{\frac{c_{11}}{\rho_{2D}}}, \tag{4.10}$$

with c_{11} a coefficient in the 2D elastic stiffness matrix (in Voigt notation), ρ_{2D} the mass density and x a material-dependent numerical factor. The additional factor δR takes into account the specificity of the edges of the system and strongly depends on the nature of

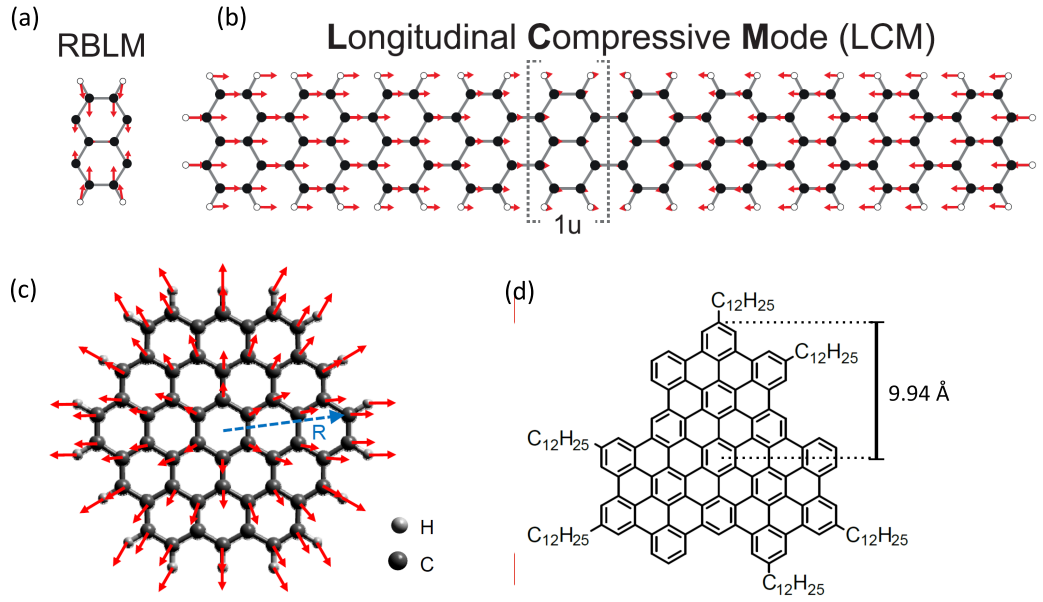

Figure 4.34: Atomic motion during (a) radial breathing-like mode (RBLM) and (b) longitudinal compressive mode (LCM) in graphene nanoribbons. The RBLM mode is shown on only one unit of the for a periodic ribbon. Adapted from [189]. (c) Atomic motion for the radial breathing-like mode for a circular GQD with radius R. From [190] (d) Estimation of the typical radius for $C_{96}C_{12}$ GQD.

the edges and on the presence of side-groups. For hydrogen-terminated objects, Liu and co-workers propose the value $\delta R = 0.9$ Å for the correction [191]. For graphenoid objects, $c_{11} = 352.6\,\mathrm{N/m}$, $\rho_{2D} = 0.743 \times 10^{-6}\,\mathrm{kg/m^3}$ and $x = 1.963$. Using these parameters, we obtain:

$$x\sqrt{\frac{c_{11}}{\rho_{2D}}} = 42.7 \times 10^3\,\mathrm{m.rad.s^{-1}} = 2.27 \times 10^3\,\text{Å}.\mathrm{cm^{-1}}. \tag{4.11}$$

By evaluating the radius of the $C_{96}C_{12}$ GQD to 9.94 Å (knowing the length of a C=C bond in aromatic compounds to be about 1.42 Å, see Figure 4.34(c)), the calculation yields: $\omega_{\mathrm{RBLM}} \approx 209\,\mathrm{cm^{-1}}$. We recover the same order of magnitude as the low-frequency modes observed at low temperature. This quick computation is thus satisfactory considering the strong approximations made. In order to obtain the vibrational modes specific to the $C_{96}C_{12}$ GQD, it is essential to perform calculations on the precise geometry, in particular by taking into account the anisotropy of the GQD and its particular geometry.

Using computational chemistry methods, theoretician colleagues from Université de Mons, Pr. David Beljonne and Dr. Claire Tonnelé, optimized the geometry of the $C_{96}C_{12}$ in the gas phase and computed the vibrational normal modes of the system. In Figure 4.35 are depicted low-frequency modes calculted for the GQD. These modes are characterized by in-plane collective breathing and bending of the graphenoid core, with associated energy values consistent with the values measured experimentally. The calculations are therefore in-line with the experimental observation. We do not observe all the modes in

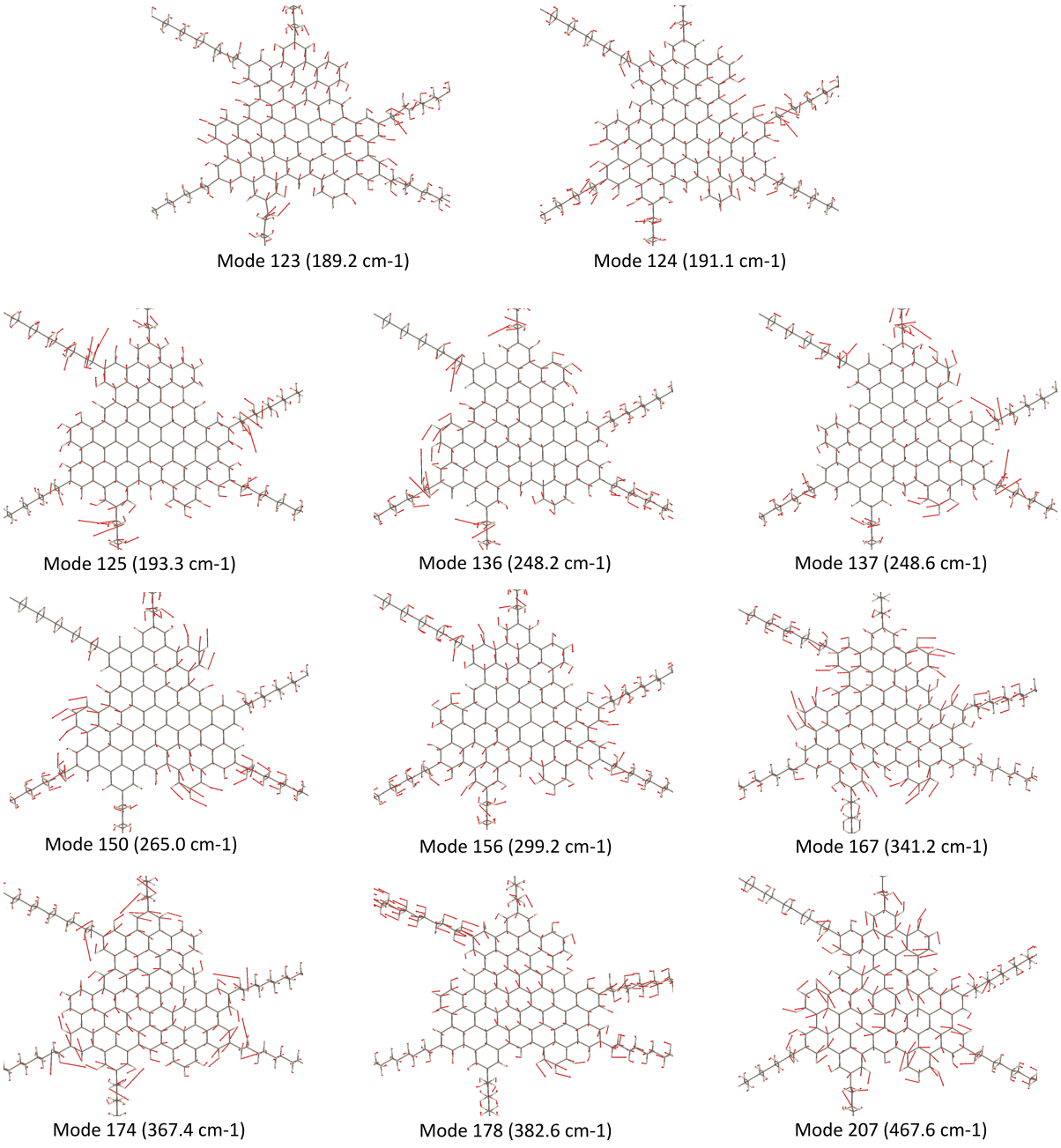

Figure 4.35: Normal vibrational modes calculated for the $C_{96}C_{12}$ GQD.

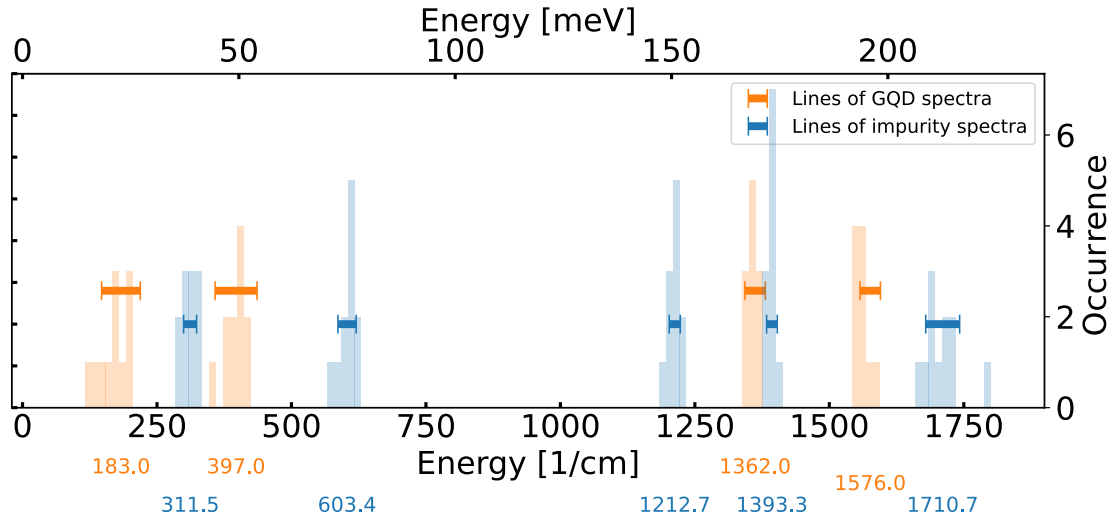

Figure 4.36: Comparison of the characteristic vibrational modes of GQDs (orange) and impurities (blue). The horizontal bars indicate the standard deviation for each mode. The colored numbers below the graph indicate the mean value of each mode in cm^{-1}.

the fluorescence spectrum since only the modes resulting in a significant Franck-Condon factor (*i.e.* an appreciable overlap of the partaking wavefunctions) will yield an appreciable emission peak in the fluorescence spectrum.

Pushing the resolution even higher might enable the observation of weaker lines which are for the moment hidden by the broadening of the vibronic lines at 7 K.

Coming back to Figure 4.33, we can estimate the dispersion of the different observable modes. For the two low-energy modes, the standard deviation is 36 cm^{-1} and 39 cm^{-1} respectively for modes **1** and **2**, while for the two high-energy modes, we find a standard deviation of 19 cm^{-1}. Observing a narrower dispersion for high-energy modes is consistent with our assignment: localized vibrational modes will tend to be less sensitive to environmental perturbations, while delocalized ones will be more sensitive to local changes of the GQD's environment (*e.g.* strain induces by the matrix, dielectric environment).

The characteristic nature of the low-frequency vibrational modes observed at low temperature leads us to identify them as **fingerprints** of the studied GQD.

As described in the previous chapter on impurities, we know their spectra to also present specific vibrational modes. In order to study only the spectra from $C_{96}C_{12}$ GQDs, we choose to consider only spots exhibiting the characteristic vibrational modes of $C_{96}C_{12}$ GQDs. This selective process achieves its purpose if the vibrational modes of impurities are not mistakable with the characteristic modes of the $C_{96}C_{12}$ GQD. Shown in Figure 4.36 are both the sets of vibrational modes observed for impurities and for $C_{96}C_{12}$. We can satisfyingly appreciate the absence of overlap between the dispersions of the various vibrational modes: vibrational frequencies measured for $C_{96}C_{12}$ are unquestionably dif-

ferent from the ones for impurities, and the two sets are perfectly distinguishable from one another. The difference between the two objects is most noticeable when looking at the low-frequency modes, since the modes at higher energy, typical for aromatic compounds, are more delicate to tell apart. Moreover, since we have never observed the characteristic frequency modes assigned to GQDs in control samples prepared without GQDs, in which only spectra with impurity vibrational modes are observed, our interpretation is indisputable.

This selection criterion is used for the rest of the study.

Characterization of the ZPL

We now focus on the ZPL of $C_{96}C_{12}$ GQDs.

The linewidth of an emitter is a good metric of how its properties are affected by its environment and deviate from the intrinsic characteristics. It is also an important parameter for applications in quantum technologies where a lifetime-limited linewidth is desired. Indeed, the linewidth γ of the transition (in units of frequency) can be expressed as [70]:

$$\gamma = \frac{1}{2\pi T_1} + \frac{1}{\pi T_2^*} \tag{4.12}$$

where T_1 is the natural lifetime of the excited state and T_2^* the *pure dephasing* time, which corresponds to any effect of decoherence of the transition. This decoherence process is generally attributed, for molecules, to the coupling to a phonon bath (mainly low-frequency vibrational modes) which, by coupling to the electronic states involved in the optical transition, dissipates the coherence of the transition. Theory thus predicts that, as the temperature of the system increases, the broadening effects due to the coupling to the environment are activated, with the density of activated modes in the phonon bath depending on the temperature following an Arrhenius-type activation dependence at low temperature. The example of pentacene in p-terphenyl is given in Figure 4.37(c) (from [192]) where the linewidth increases by multiple orders of magnitude between 4 to 10 K. The behavior measured has enabled the authors to estimate the activation temperature to around 38 K for this system. Moreover, since the broadening process depends on the coupling to the phonon bath, we expect a dependence of the linewidth measured to the chosen host matrix. In particular, in the case of a polymer matrix, we expect even larger broadening effect than in crystalline hosts. For instance, the linewidth at 1.7 K for single terrylene molecules in polymer matrices have been observed to be more than one order of magnitude larger than the natural linewidth observed in crystalline matrices [193]. This is attributed to the broadening processes which are still active at this temperature.

To address this question, we measure the linewidth of narrow emission line directly on the low-temperature spectra. The precision of the measurement relies on the experimental apparatus, and more specifically on the gratings in the spectrometer (with 150, 300 and 600 g/mm). We show in Figure 4.37(a) the measured profile of the ZPL using three gratings (with entrance slit width of 60 µm). Given the increased dispersion with increasing groove density, the finest resolution is obtained using the 600 g/mm grating, which

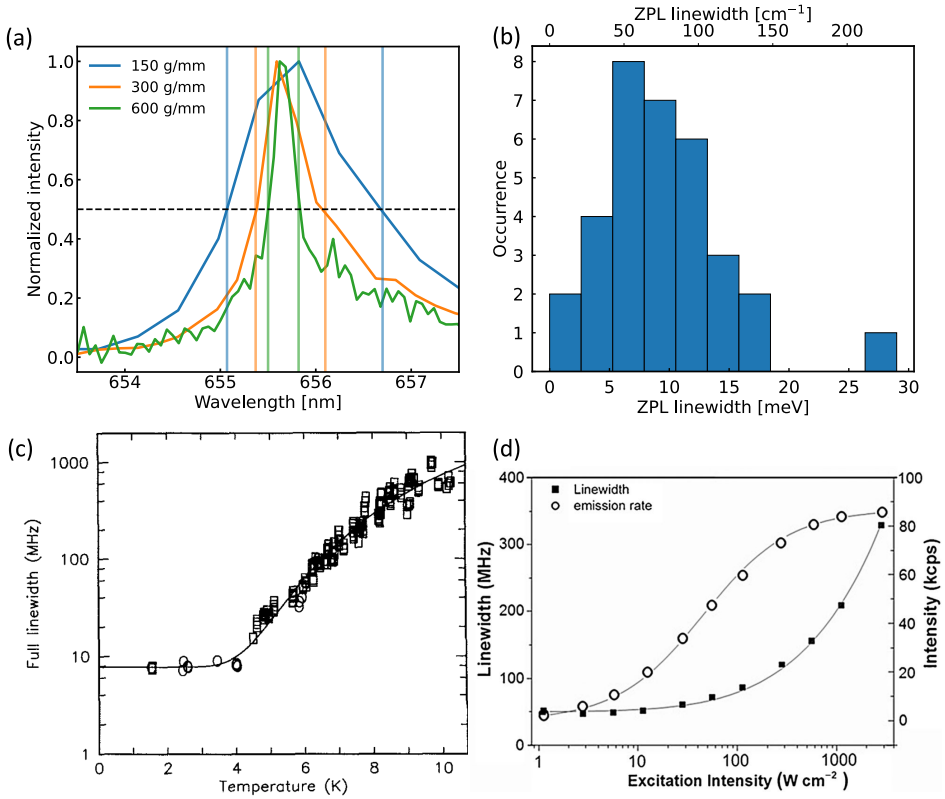

Figure 4.37: (a) Comparison of the ZPL linewidth measurement with 150, 300 and 600 grooves/mm gratings. (b) Distribution of the ZPL linewidth for $C_{96}C_{12}$ GQDs at 7 K (total of 29 spots). (c) Temperature dependence of the ZPL linewidth observed for pentacene in p-terphenyl, from [192]. (d) Excitation-power dependence of the ZPL linewidth for terrylene molecules in para-Dichlorobenzene, from [72].

exhibits a linewidth of 0.3 nm (0.86 meV) which corresponds to the resolution limit for this grating. For the other two gratings, the resolution limit is 1.2 nm for the 150 g/mm grating, 0.7 nm for the 300 g/mm grating. Given the necessity to measure linewidths down to 0.86 meV, we only worked with the 600 g/mm grating.

The distribution of the linewidth, given in Figure 4.37(b), shows that we observed linewidths ranging from around 1 meV to almost 20 meV. The linewidth is significantly narrowed relatively to room-temperature spectra, as shown in Figure 4.32. However, we are still orders of magnitude above the lifetime-limited linewidth, which, given the measured lifetime of 4.55 ns for $C_{96}C_{12}$, should be around 35 MHz (0.15 µeV).

Multiple effects may lead to a broadening of the emission line, and identifying the phenomena at play in our case may provide hints for improvement.

First of all, we must keep in mind that experimentally, as we measure the linewidth, we should also take into account the effect of spectral diffusion, which may be expressed as an additional temperature-dependent term in the apparent linewidth of the transition [194, 71][10]. The spectral diffusion phenomena will be described more extensively in the dedicated section (Sec.4.3.2).

Then, apart from the aforementioned effect of temperature, we have not discussed the effect of power on the spectra of $C_{96}C_{12}$ GQDs. It has been shown that the excitation power may have, for instance, an effect on the linewidth of the ZPL [195, 196]. This has been observed on various systems [192] and I show an example of such line broadening in Figure 4.37(d) for terrylene molecules in para-dichlorobenzene, from [72]. The curves illustrate the effect of saturation on the linewidth of the ZPL (which increases almost linearly with the excitation power) and the count rate. The effect of saturation occurs when the excitation power is around I_{sat} the saturation intensity, a parameter which depends on various characteristics of the system (*e.g.* the absorption cross-section at the wavelength of excitation). For the system presented in Figure 4.37(d), I_{sat} is at 3.6 W cm^{-2}, which is orders of magnitude below the power density used for our experiments (2×10^3 W cm^{-2}). However, for $C_{96}C_{12}$ GQDs, the value of I_{sat} has been reported at 28×10^3 W cm^{-2} for an excitation at 594 nm [10], which is more than one order of magnitude above the excitation power used in our case[11]. We can therefore infer that the excitation power does not significantly contribute to the broadening of the ZPL line, and that other broadening processes are dominant in our case. We have not yet performed any power-dependence experiments at low temperature, which could exhibit more explicitly the influence of power on the linewidth.

Therefore, the broad linewidth of the ZPL lines is to be attributed to the significant increase of linewidth with temperature. The broad dispersion of linewidth for $C_{96}C_{12}$ spectra in the sample can therefore be accounted for by, for example, a spatially inho-

[10] Actually, spectral diffusion phenomena occur on a large range of timescales. The contribution of these phenomena to the broadening of the spectral lines depends on the time resolution of the spectral measurements, as it is described in Ref. [77].

[11] We keep in mind that the saturation intensity may depend on the linewidth and the resolution of the excitation beam. In our case, the same excitation parameters are used than for measuring the saturation curve reported in [10].

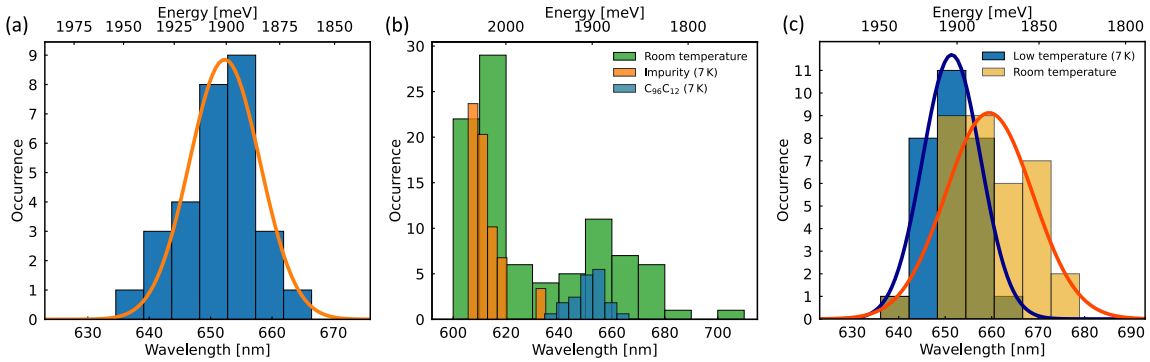

Figure 4.38: (a) Distribution of the ZPL position for $C_{96}C_{12}$ spectra at 7 K. The distribution is fitted by a Gaussian function (orange curve). (b) Comparison of the distribution observed at room temperature (in green) with the low-temperature distribution of impurities (in orange) and GQDs (in blue). (c) Comparison of the distribution of ZPL position at low temperature (in blue) with the wavelength distribution assigned to GQDs (rightmost family of spectra in Figure 4.24(c)) (in orange). The corresponding Gaussian fits are plotted.

mogeneous distribution of the temperature in the sample[12]. Another possibility may be also the activated spectral diffusion processes for each GQD, which depend locally on degrees of freedom in the matrix [197]. It is difficult to precisely determine which process dominates the dispersion in linewidth, since the degrees of freedom activated also depend on temperature. To give an order of magnitude, it has been reported that for terrylene in polystyrene, a dispersion of linewidth with standard deviation of around 1 GHz (4 µeV) can be observed at 1.7 K [193]. We can see that it is orders of magnitude below the standard deviation we measured for GQDs in polystyrene at 7 K, which indicates that we can confidently attribute the dispersion to temperature dependences.

Let us now have a look at the position of the ZPL. Across 29 analyzed spots, the resulting distribution exhibits a Gaussian profile centered at 651.3 nm, which can be fitted to extract a standard deviation of 5.9 nm (Figure 4.38(a)). The Gaussian dispersion in wavelength of the ZPL is coherent with the polymeric nature of the host matrix. Inhomogeneity at the local scale in the matrix can induce dielectric screening of the excitons or induce local strain. A striking observation is the absence of spectra with ZPL below 630 nm, observed in distributions at room temperature. This satisfyingly proves that the spectra at higher energy in the distribution at room temperature indeed corresponded to impurities and by-products, and confirms the efficiency of our selection criterion based on the frequency of vibrational lines.

Interestingly, if we plot the distribution of spectra (without any selection on wavelength or intensity) alongside the distribution of impurities at low temperature, we would recover the two families of spectra discerned in the wavelength distributions at room

[12]Since the cryostat used for the experiment relies on cold contacts (cold fingers) to cool the sample, it could result that the whole sample may not have reached the indicated temperature, resulting in single GQDs being at slightly different temperatures.

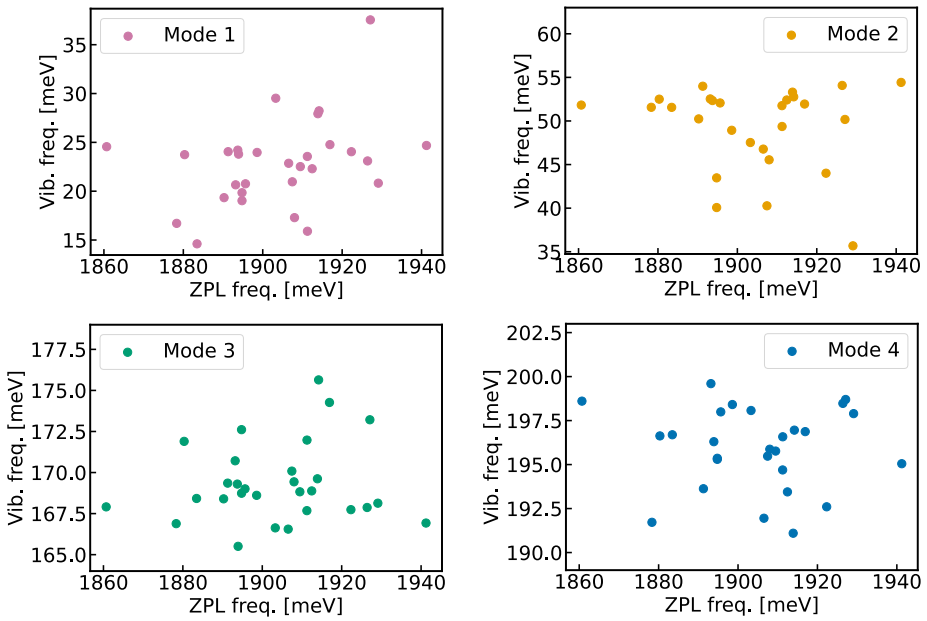

Figure 4.39: Energy of vibrational modes **1** to **4** plotted against the ZPL position.

temperature (see Fig.4.38(b)). Of course, we must note that we do not observe any family of spectra which we would associate with by-products at low temperature. We suspect that the absence of by-product spectra in our study results from a selection bias on the spectra selected for study. As mentioned earlier in this chapter, we observe at 7 K spectra which exhibit lines broader than for GQD spectra. Since only spectra with measurable frequency modes have been taken into account, by-product spectra may have been overlooked if they exhibited no narrow lines at 7 K. A strong blue-shift of the spectra of by-products at low temperature could also cause them not to be efficiently excited at 594 nm.

In order to explore a little more the possible origin of the dispersion ZPL, we investigate possible correlations between the dispersion of the characteristic vibrational modes with the dispersion of the ZPL. The energy of the different vibronic modes are plotted against the position of the ZPL, as shown in Figure 4.39. For instance, we would expect from a naive perspective that, if the dispersion of the ZPL position was due predominantly to strain imposed on the GQD, it would also induce consequent shifts of the energy of the vibrational modes. Such effect should therefore lead to correlations between ZPL position and vibrational energy. However, we observe no correlation for all four modes with the dispersion in wavelength, which indicates a different origin for the observed dispersions (or a result of many different causes).

If we compare closely the dispersion of the distribution at room temperature (the Gaussian distribution at high wavelength centered at 660 nm) with the distribution at low temperature, we can notice a small blueshift of the average value of the distribution for the distribution at low temperature (Fig.4.38(c)). It would be interesting to follow the

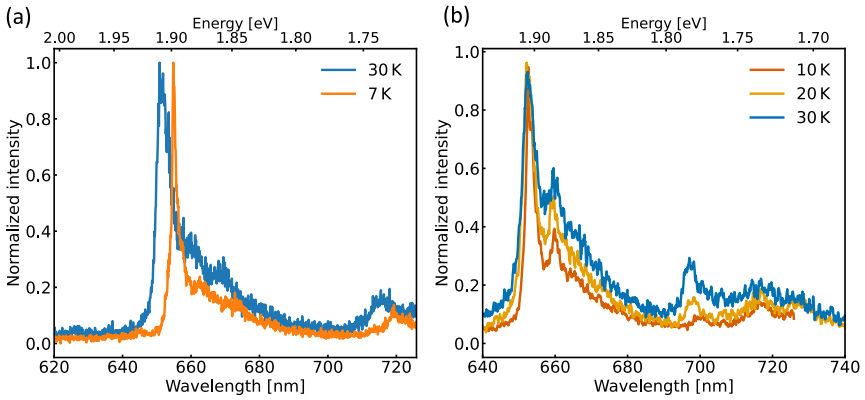

Figure 4.40: Two examples of temperature evolution of GQD spectra.

temperature-dependence of the spectrum, in order to see if this blueshift is observable for each single-GQD spectrum. However following a same spot during the cooldown of the cryostat has proven to be arduous. As the sample is cooled down to the target temperature, drifts of the piezoeletric steppers complexifies the observation of collocal spots for different temperatures. First tests have been carried out for a few spots, but the results remain limited. As shown in Figure 4.40(a), the aforementioned line-narrowing of the ZPL accompanying the cooldown of the system can be noticed for this GQD studied at both 7 K and 35 K, along with a global redshift of the spectrum. On a second example given in Figure 4.40(b), we observe only a broadening of the linewidth of the ZPL with no energy shift, along with an apparent decrease of the Debye-Waller factor[13]. A more precise tracking of the evolution is required to probe more accurately the temperature dependence of these physical quantities. The use of marked substrates by lithography should facilitate such measurements and is planned for future experiments.

There and back again: comparison with impurities

We have already compared the vibrational frequencies of $C_{96}C_{12}$ GQDs and impurities, and elaborated our selection criterion based on it.

As it has been mentioned earlier, the distribution of the ZPL energy of $C_{96}C_{12}$ and of impurities do not overlap either, as it could be seen in Figure 4.38(b). Moreover, if we plot the distribution of linewidth for impurities and $C_{96}C_{12}$ (in Figure 4.41), we observe that at the temperature of study (7 K), the spectra from impurities have broader ZPL linewidth than spectra from $C_{96}C_{12}$, while they both shared the same linewidth at room temperature. This discrepancy may be due to the different way GQDs and impurities interact with the environment (*e.g.* stronger coupling for instance to the vibrational modes of the matrix). This shows that characteritics of the ZPL could also help distinguish $C_{96}C_{12}$ GQDs

[13]The factor is defined as the ratio between the intensity of the ZPL over the total intensity of the transition (intensity of the ZPL and of the corresponding phonon wing) [72, 198]. Simultaneously, the phonon wing rises and broadens with increasing temperature [199]. In our case, a precise numerical estimation of the Debye-Waller factor is impossible given the difficulty to distinguish the phonon wing associated with the ZPL from the peaks due to intra-molecular vibrations.

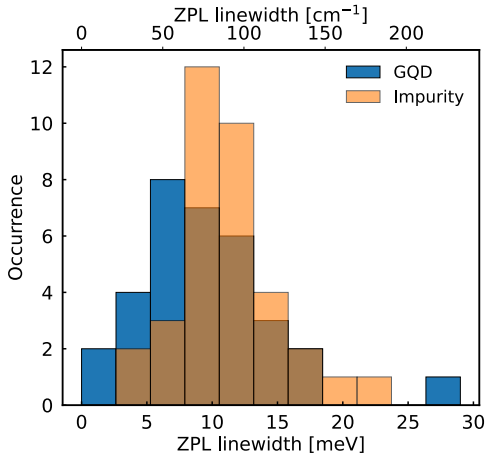

Figure 4.41: Comparison of the linewidth distribution of GQDs and impurities at 7 K.

from environing impurities. We can note that we already had a hint at room temperature at the fact that only spectra with first-peak wavelength distributed around 650 nm actually corresponded to GQDs. Given the complete absence of spectra with ZPL below 630 nm, it is worth emphasizing again that this criterion has proven to be more accurate than the selection based on spot intensity at room temperature.

Effects of the environment on the spectral features

As mentioned in the discussion on the linewidth of ZPL, *spectral diffusion*, the temporal shift of the energy of the ZPL, or *frequency jitter*, can also induce broadening of the emission lines. Single-molecule spectroscopy has enabled the observation of spectral diffusion for single systems [200], resulting in numerous studies discussing the origin of this phenomenon. Moreover, such phenomena can occur on a wide range of timescales, from nanoseconds to days (for tunneling times in glassy systems) [201].

In order to study spectral diffusion, time traces of the ZPL energy can be measured by performing a series of spectral measurements. In our case, the exposure time for each spectral measurement is of the order of 1 s – 10 s, which means that processes on shorter timescales cannot be probed and would only yield a homogeneous broadening of the measured spectra lines. Nonetheless, we manage to observe spectral diffusion for $C_{96}C_{12}$ GQDs in the traces measured. For all our measurements, the temperature of study is 7 K and the excitation wavelength is 594 nm, with power at around 2×10^3 W cm^{-2}. In Figure 4.42, two traces are shown, comparing the trace of a stable spot (on the left) with the trace of a spot subject to spectral diffusion (on the right). Out of 22 time-traces measured, 14 have shown a stable evolution on the timescale probed. In the traces showing spectral diffusion, we always observe jumps between discrete energy values, as shown in the right trace of Figure 4.42. In this particular case, the ZPL energy jumps to an energy blueshifted by 5 meV during 120 s before returning to its original energy. This type of behaviour is usually associated with a coupling of the emitter to a tunneling two-level system (yielding the jump between two discrete frequencies) [202, 197] or to the trap-

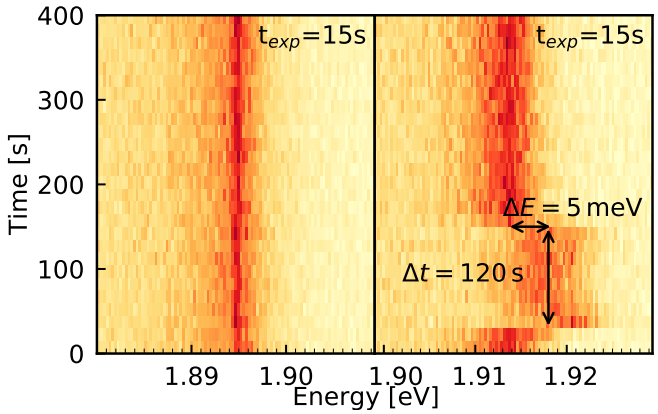

Figure 4.42: Example of ZPL time traces for two different GQDs, one without apparent spectral diffusion (left) and the other showing a spectral jump (right). The exposure time is 15 s.

ping/detrapping of charge carriers on local defects [203]. Tunneling two-level systems may correspond to a large variety of local degrees of freedom, *e.g.* the reorientation of sidechains in the matrix, which can tunnel from one state to another. The energy shift during spectral jumps, as well as the duration of the jump, vary according to the studied GQD. This is not surprising since the coupling of the GQD to any environing perturbation is dependent on the distance of the GQD to the perturbation. The GQD therefore probes its immediate surroundings, which yields a large dispersion of possible behaviors (linewidth, spectral diffusion) in polymer matrices [77].

This dispersion of behavior can also be witnessed when considering the difference between the states concerned by the spectral jump. We examinate the case of two spots, with the time traces shown in Figure 4.43. For both emitters, labelled here GQD1 and GQD2, the spectral jump occurs between two states (labelled states **1** and **2** for each GQD) characterized by two distinct frequencies. We plotted the distribution of the ZPL energy shift (center of Fig.4.43) and of the integrated intensity (right of Fig.4.43) for GQD1 and GQD2 in their two different states. For GQD1, no clear difference in the ZPL position distribution between the two states, while the intensity is weaker in state **2** than in state **1**. For GQD2, the opposite behavior is observed: there is a clear broader distribution of the ZPL position in state **2** than in state **1**, while the integrated intensity remains the same in average.

We can interpret these two behaviors by two different causes for the spectral jump. The cause of its spectral jump leads GQD2 to a state in which the GQD may be prone to be coupled with additional two-level systems, which results in an apparent unstability of the ZPL energy. Complementarily, we tentatively deduce that jumping to state **2** may lead to an enhanced coupling of the excited state of GQD1 to non-radiative decay channels, leading to an increase of the non-radiative relaxation rate, while not significantly inducing coupling to other two-level systems.

Nonetheless, when we look at the vibrational modes of the GQD during states **1** and

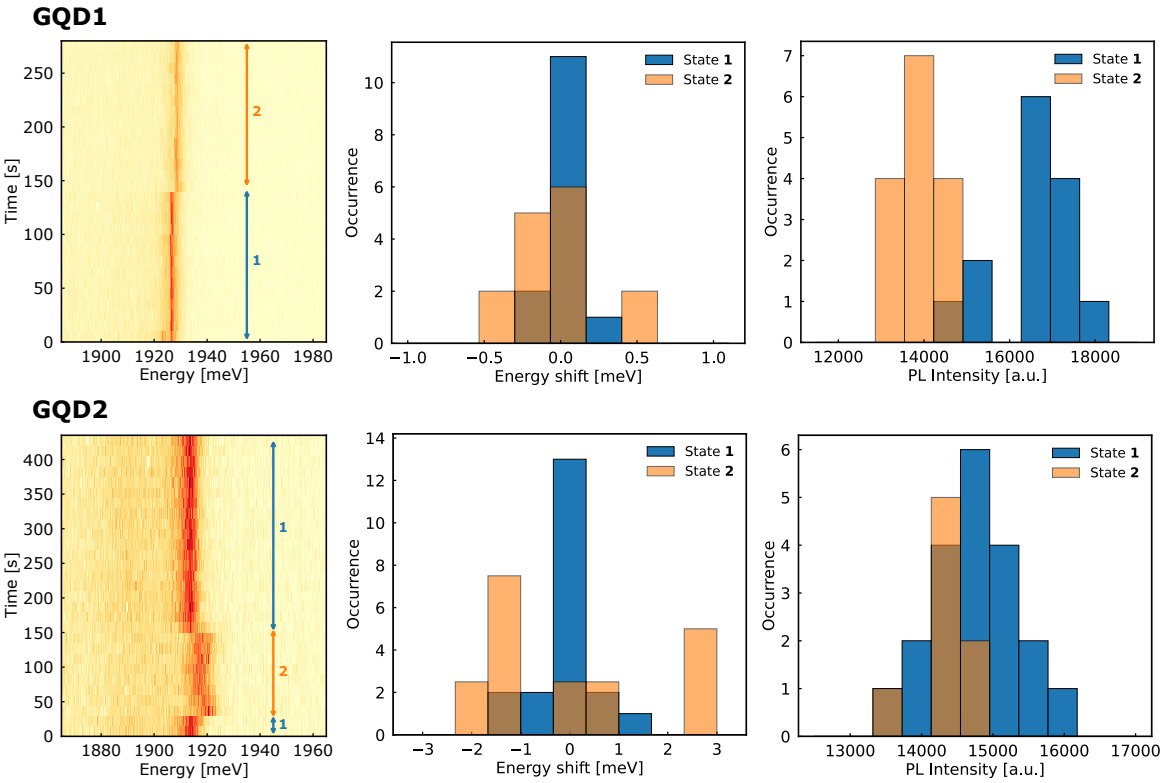

Figure 4.43: Time trace (left), distribution of the energy shift relatively to the average value (center) and distribution of the integrated PL intensity (right) for the states **1** and **2** of two different GQDs. States **1** and **2** correspond to the two states at play in the spectral diffusion of the GQD (indicated in the time traces). Exposure time of 10 s for GQD1 and 15 s for GQD2

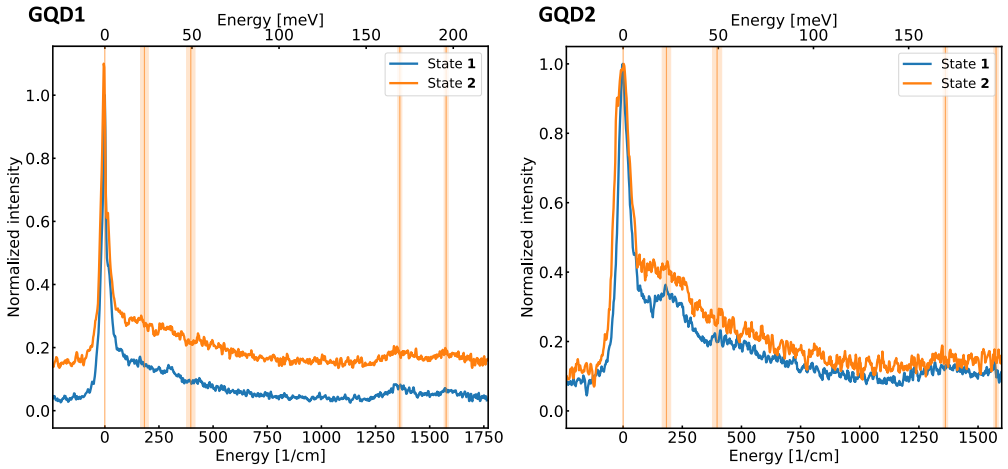

Figure 4.44: Comparison of the vibrational modes for spectra measured in the states **1** and **2** for the two GQDs of Fig.4.43.

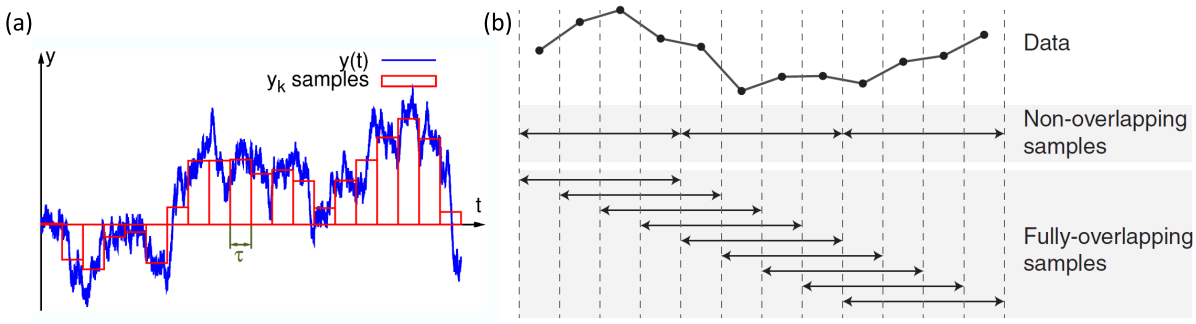

Figure 4.45: (a) Example of sampling of a $y(t)$ trace by periods of τ for Allan variance calculation. The red bars correspond to the amplitude of y_k, average of $y(t)$ over each period. From [204] (b) Comparison between the sampling of a data set for the computation of the Allan deviation (Non-overlapping samples) and the overlapping Allan deviation (Fully-overlaping samples). The successive arrows correspond in each case to the time period over which successive y_k are calculated. Adapted from [205]

states **2**, we report no change of the vibrational frequencies for both GQD1 and GQD2, as shown in Figure 4.44, along with no change in the relative intensities of the vibronic peaks. This observation indicates that the spectral diffusion does not alter the coupling between the electronic states and the vibrational modes of the GQD. This could very well be consistent with the effect of local charge fluctuation (charge trapping) which would induce a global shift of the vibronic levels through Stark effect.

In order to be more quantitative in our analysis, we can use statistical tools when investigating the origin of the spectral diffusion. In our case, we turn to the *Allan deviation*, usually manipulated in metrology to study the stability of clocks and oscillators [206]. Derived from the commonly used standard deviation, the Allan deviation $\sigma_y(\tau)$ can be defined for a time-evolution of the frequency $y(t)$ as:

$$\sigma_y(\tau)^2 = \frac{1}{2}\left\langle (\bar{y}_{k+1} - \bar{y}_k)^2 \right\rangle, \tag{4.13}$$

where $\langle\rangle$ corresponds to an ensemble average, τ is the integration time the Allan deviation is calculated at, and $\bar{y}_{k+1}$ and $\bar{y}_k$ the average value of $y(t)$ over time τ for two successive sections of $y(t)$. To give a more explicit definition of $\bar{y}_k$, we can picture the case where we decide to average $y(t)$ over periods of time τ. As shown in Figure 4.45(a), this can be done by dividing the time axis by periods of τ and marking the successive time positions t_k, separated by time τ. Therefore, the average value $\bar{y}_k$ between time t_k and $t_k + \tau = t_{k+1}$, can be defined as:

$$\bar{y}_k = \frac{1}{\tau}\int_{t_k}^{t_k+\tau} y(t)\mathrm{d}t. \tag{4.14}$$

$\sigma_y(\tau)^2$ is known as the Allan variance.

Power law	Noise type
τ^{-1}	White phase noise
$\tau^{-1/2}$	White frequency noise
τ^{0}	Flicker frequency noise
$\tau^{1/2}$	Random walk frequency noise (or random telegraph noise, RTN)

Table 4.3: Power laws for the Allan deviation, and the associated noise type.

Given the definition of the Allan deviation, we see that for a set of N discrete measurements of the frequency performed by steps of time τ_0, the minimum value of τ for the calculation of the Allan deviation will be τ_0, while the maximum value will be $N/2\times\tau_0$, since we always require at least two samples $\bar{y}_k$ to compute $\sigma_y(t)$ (and the resulting confidence interval would make the estimation useless). An alternative definition, referred to the *overlapping Allan deviation*, can solve this issue by considering not the difference between successive $\bar{y}_k$, but between averages of $y(t)$ over periods τ separated by the sampling time τ_0. It can be seen as performing a moving average of $y(t)$ by steps τ_0, see Figure 4.45(b). This yields:

$$\sigma_y^2(\tau = m\tau_0) = \frac{1}{2}\frac{1}{N-2m}\sum_{i=1}^{n-2m}(\bar{y}_{i+m} - \bar{y}_i)^2 \tag{4.15}$$

The overlap has been shown not to induce any bias in the resulting Allan variance [207]. We will use this method in our analysis.

The Allan variation is usually expressed using power laws [204]:

$$\sigma_y^2(\tau) = \sum_{i=0}^{4} C_i \tau^{i-2} \tag{4.16}$$

Similarly to the analysis of power spectral density, it is possible to associate the successive powers of τ with different types of jitter dynamics (or *noise*). In Table 4.3 are given the different power laws for the Allan deviation along with the associated noise type.

We can note that $y(t)$ is usually normalized by the nominal frequency of the studied oscillator and has thus no unit. In our case, we decide to express $y(t)$ in eV, the values measured for the Allan deviation therefore serving as estimates of the standard deviation of the trace.

We propose the use of this tool on 4 time series of $C_{96}C_{12}$ GQDs, summarized in Figure 4.46. For comparison, we plot alongside the Allan deviation the profile evolution associated with white noise ($\tau^{-1/2}$) and random telegraph noise ($\tau^{1/2}$). White noise corresponds to a signal which exhibits a flat spectrum (or, equivalently, to a signal modelled by a series of uncorrelated random variables with zero mean and finite variance), while random telegraph noise corresponds to sudden step jumps in a signal between discrete values (following a memoryless stochastic process).

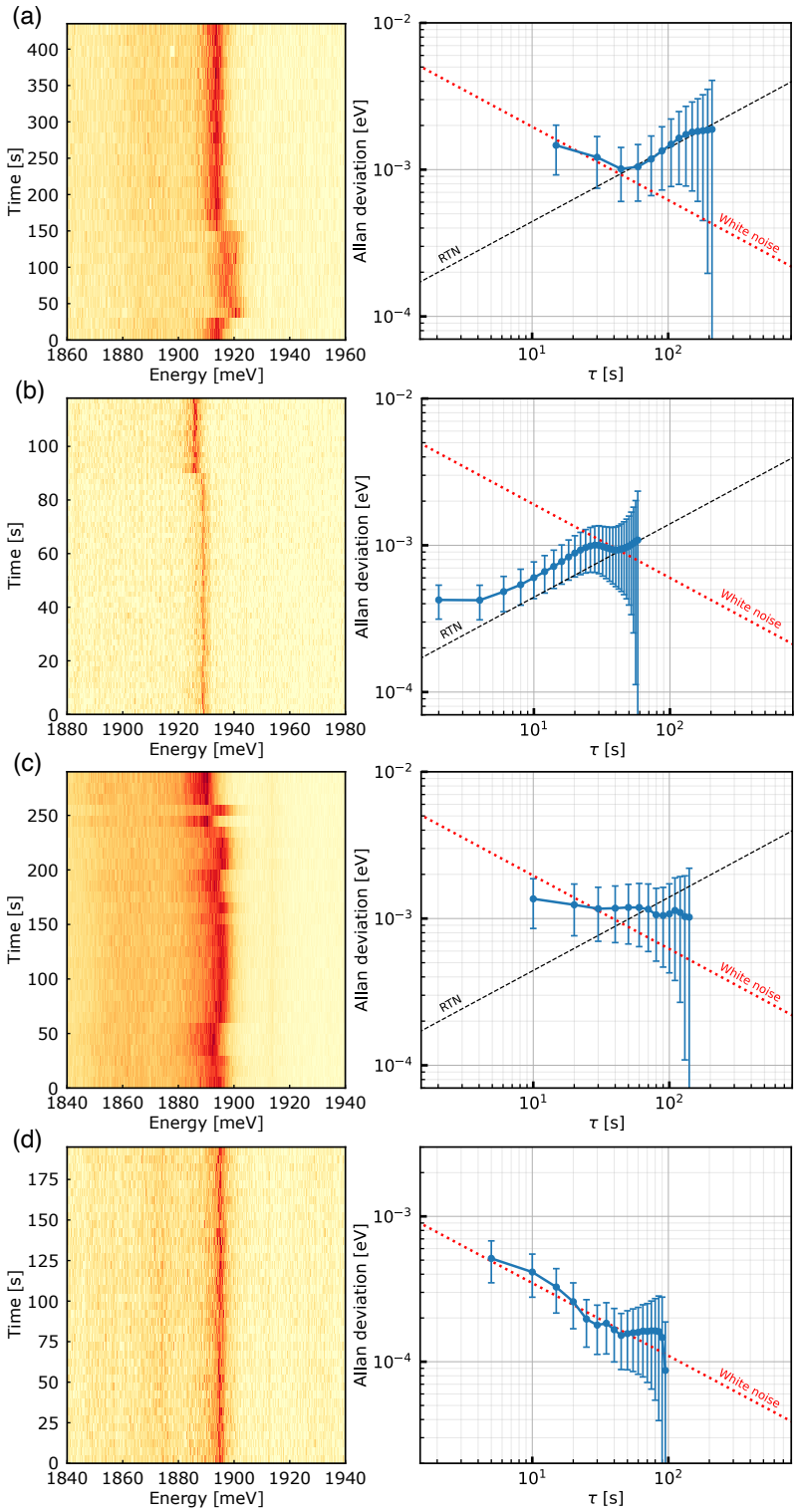

Figure 4.46: Time trace and associated Allan deviation for (a),(b),(c) three GQDs presenting spectral diffusion and (d) a stable GQD. Black and red lines indicate power law slopes of repectively random telegraph noise (RTN) and white noise. The exposure times are respectively 15 s, 2 s, 10 s and 5 s.

For time trace (a) (corresponding to GQD2 in Figure 4.43), the Allan deviation shows two distinct linear portions (in log-log scale). For low values of τ, the Allan deviation exhibits a slope corresponding to white frequency noise, while the second portion shows the signature of random telegraph noise (RTN). This can be easily interpreted when comparing to the time trace. On the scale of the exposure time τ_0 of the spectrum (low τ), the dispersion is dominated by the spectral diffusions which may happen at lower timescales, while, when looking at timescales of 60 s and above, we can see that the evolution of the trace is dominated by the spectral jump (which can be seen to occur on this particular timescale on the time trace). Indeed, simulations can easily show that when considering spectral jumps (for instance due to trapping/detrapping of charge carriers in the vicinity of an emitter) on timescales smaller than the resolution of the timetrace (*i.e.* the exposure time), we can witness white noise arising in the dynamics [208]. Considering a similar process but with a characteristic timescale longer than the resolution, we recover the expected random walk noise. In particular, in the case where we observe jumps between only two states, this would indicate the presence of only one trapping site in the vicinity of the emitter.

The time trace (b) presents a profile close to the time trace (a). However, the Allan deviation exhibits only a random telegraph noise signature, even at short timescales. An explanation we can propose relies on the amplitude of the jump. In the case of trace (a), the amplitude of the jump is of the order of the jitter before the jump, while in the case of trace (b), the jump has a relatively higher amplitude. The deviation is therefore dominated by the jump, yielding the random telegraph noise. These observations have been comfirmed by simple simulations[14].

Looking now at trace (c), we now observe both the amplitude of the jump and of the instantaneous jitter, similarly to trace (a). However, the characteristic timescale of the jumps is of the same order of magnitude as the resolution of the time trace. The resulting Allan deviation is almost flat, resulting from a compensation between the two noises. This can also be easily verified by naive simulations (see Figure 4.47(f)). However, when considering power laws indicated in Table 4.3, τ^0 should correspond to flicker noise. This type of noise can arise when we consider for example an accumulation of charge traps not in the direct vicinity of an emitter [208]. However, since the time trace seems to show only two distinct states, which should result in a random telegraph noise, the first interpretation seems more adequate.

Finally, for comparison, we study a typical stable time trace, here trace (d). We recover the expected white frequency noise. Once again, this may hint to additional spectral diffusion processes at lower timescales which, when averaged during measurement, broaden the ZPL and result in the slight shifts of the ZPL.

Our method using real-time tracking has its limits: it cannot resolve timescales lower than the exposure time necessary to measure a spectrum. Other methods, based on statistical studies of photon emission during the spectral diffusion, can lead to a more pre-

[14] We can easily generate a trace based on a white noise with a standard deviation, and impose arbitrarily a jump in the simulated trace, as shown in Figure 4.47. By computing the Allan deviation for the case where the jump is of the order of the standard deviation, we observe the two slopes ((d) and (e)), while when the jump has a larger amplitude (a), we observe only the random walk noise.

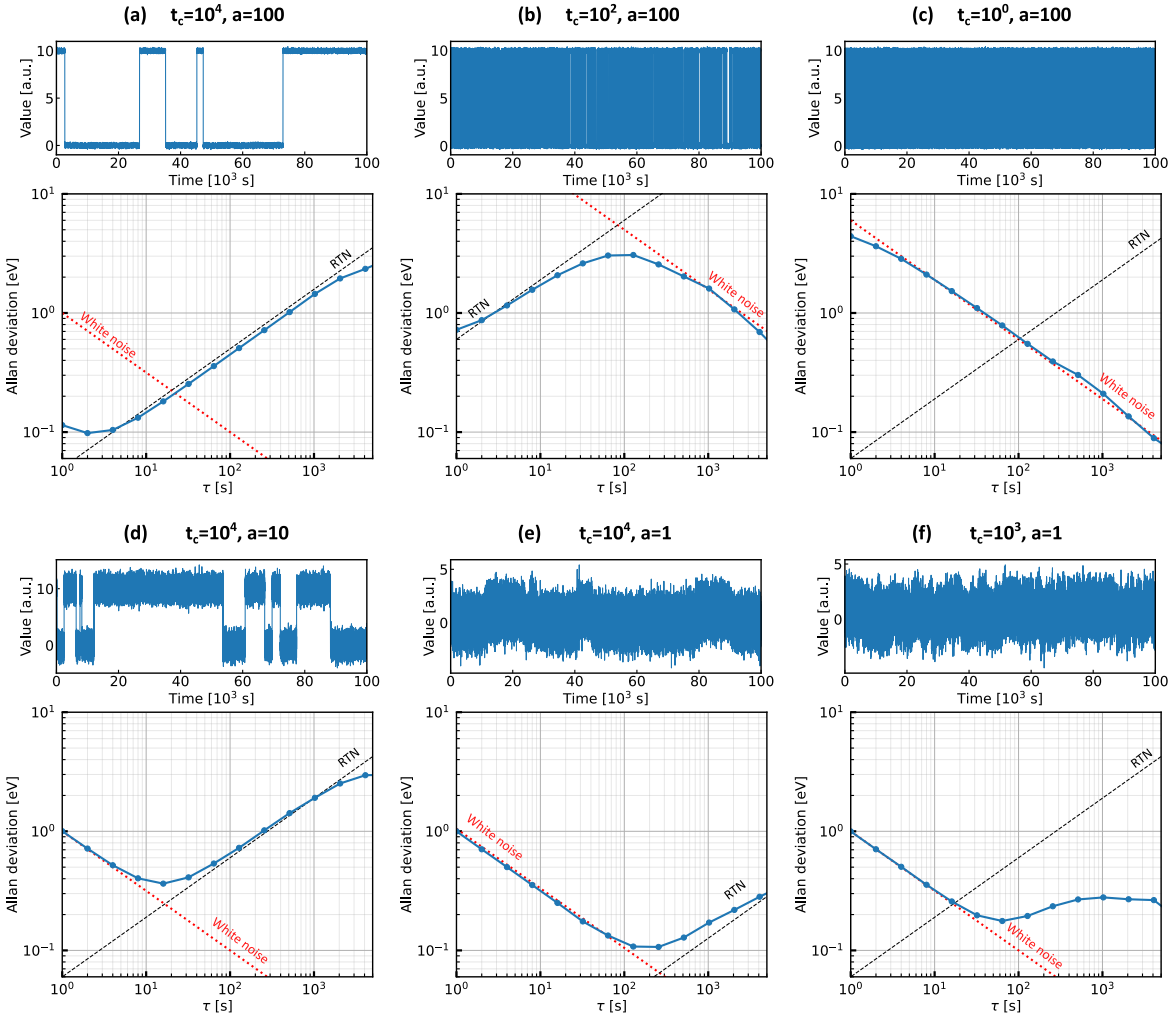

Figure 4.47: Simulation of time traces and associated Allan deviation. The trace is simulated using normal distribution centered on zero (reproducing the effect of low-timescale spectral diffusion), with jumps determined by an exponential-distributed dwell time (Poissonian process). t_c is the ratio between the correlation time (characteristic decay time of the exponential distribution) and the resolution of the trace (here set at 1s). a corresponds to the ratio between the amplitude of the jump and the standard deviation of the normal distribution. By changing t_c (simulations (a),(b),(c)), we switch from a purely RTN (dominated by the discrete jump) to purely white noise (the resolution not low enough to resolve the jumps yielding white noise in average). By decreasing a ((a),(d),(e)), we enhance the influence of white noise at short time scales. (f) shows a case where a is set to unity, choosing t closer to unity induces both noise contributions to compensate, which yields a flat Allan deviation in the range of $\tau \sim t$.

cise estimation of the various timescales of the process [202]. Subnanosecond resolution has been reached for instance by probing the correlation between the photon emission in two frequency windows of the spectral diffusion process [209]. The method proposed is therefore only limited by the resolution of the correlation measurement, although rigorous spectral selection must be achieved. Recently, the use of a highly-dispersive medium has been proposed to replace the interferometric spectral selection [210].

Moreover, the possibility to decrease the probability of observing spectral diffusion is an on-going subject of study in order to increase the stability of single emitters [201]. For instance, one could change the host matrix chosen to embed the emitters. However, using cristalline matrices does not necessarily prevent the observation of spectral diffusion, as observed for example of dibenzoterrylene in 2,3-dimethylanthracene [211]. Apart from changing the guest-host system used, the influence of various factors can be probed, such as temperature or excitation power. For instance, changing the excitation wavelength may result in an inhibition of the spectral diffusion for an emitter, as shown recently on emitters in hexagonal boron nitride (hBN) [212]. While keeping in mind that the wide range of possible causes for spectral diffusion forces us to consider each guest-host system individually, with each its own dependence on the experimental parameters, continuous studies on this subject can only enrich our understanding of this phenomenon.

Conclusion

In this chapter, I reviewed the advances in our understanding of the photophysics of $C_{96}C_{12}$. The work I presented here results from experiments using various spectroscopic methods. I described for each method the resulting interpretations we could propose with the help of collaborators.

In solution, the understanding of the composition of the sample is motivated by the need to precisely identify the origin of the different peaks observed in various spectroscopy measurements. We have identified and characterized the lines of $C_{96}C_{12}$ in solution and, with the help of theoretical calculations, we provided a precise explanation of the origin of the various transitions observed. Interestingly, a symmetry-breaking process is established and results in the observed fluorescence. In addition to that, we have observed the signature of the formation of aggregates which results from the stacking of $C_{96}C_{12}$. The blueshift of the electronic transition and lower fluorescence quantum yield observed experimentally are verified theoretically. The results of this work has been published recently [213].

Single-molecule measurements are complementary to measurements in solution. While ensemble measurements in solution enable the measurement of averaged properties of the GQD, studying at the single-object level gives us have more insight into the property of single GQDs and reveals the dispersion of various properties. We have for instance shown that the fluorescence from GQDs results from intrinsic emission from the object, which is noteworthy in comparison to top-down GQDs. Other benefits of the bottom-up approach can be noted when looking at the dispersion of wavelength or energy shifts, which we observe to be narrower for bottom-up GQDs.

The experiments performed using the cryostat have yielded the first low-temperature results for such GQDs. We have successfully isolated GQDs and observed line-narrowing processes on their spectra, along with the appearance of vibronic transitions unresolved at room-temperature. Moreover, we have underlined how the vibrational frequencies can be considered fingerprints of the $C_{96}C_{12}$ GQD since directly linked to the size and geometry of the object. We have also exhibited the phenomenon of spectral diffusion for a fraction of GQDs probed and proposed tools to analyze this phenomenon. Our work on the vibrational characterization of $C_{96}C_{12}$ GQDs at low-temperature has resulted in a paper published recently [214].

Concerning the impurities in single-molecule experiments examined in the previous chapter, we know their presence in samples to be a source of possible misinterpretations. The possibility to unambiguously distinguish GQDs from impurities is a crucial step in order a recover clear results for GQDs. The development of criteria to discriminate GQDs from impurities was tested by comparing the results for impurities described in the dedicated chapter with the results in samples containing GQDs. We have shown that room-temperature selection based on intensity, though not showing a high level of selectivity, can decrease the contamination of the GQD data by impurities and help assign the origin of various observations (*e.g.* dispersion of transition wavelength). The low-temperature measurements helped establish a robust criterion using the characteristic vibrational modes of the GQD, which in return confirm assumptions made at room

temperature.

Moreover, beyond the deepened understanding of the properties of the $C_{96}C_{12}$ GQD and of our samples, this chapter was also a chance to develop multiple general tools and methods which can be useful for future studies of different GQDs.

Of course, we have, along the different sections of this chapter, pointed out possible improvements which may orient the possible future studies on this GQD. Concerning the system itself, the use of long alkyl sidechains in order to prevent the stacking of GQDs has proven to be not as efficient as wished, as shown by the formation of aggregates in solution. Adding different side-groups, such as tert-butyl groups, may lead to an enhanced inhibition of the aggregation process and increase the probability of observing monomers in solution. However, although the general electronic properties should not be altered by such a change since they depend mainly on the graphenoid core of the GQD, the disorder which originated from the side-groups may induce changes in the coupling between the electronic states and the intramolecular or environing vibrational modes.

As mentioned throughout the section concerning single-object studies, the choice of a polymer matrix leads to a large variety of environments and of possible disorders for the GQDs embedded. Using crystalline matrices, for instance Sh'polskii matrices, may help decrease the coupling of the GQD to its environment. It would result in the possiblity to probe the intrinsic limits of the GQD, in particular in experiments at low temperature.

In order to observe a possible lifetime-limited linewidth for the ZPL, we would need to reach lower temperatures (4 K and below). A home-designed radiation shield has been prepared for the cryostat and may help reach the desired temperatures. Moreover, since we are already limited in our case by the resolution of the spectrometer, a measurement of the linewidth of narrower spectra lines is impossible. In order to increase the precision of the measurement of linewidths, we would either need to increase the groove density of the diffraction grating of the spectrometer, or use a tunable laser with ultra-narrow linewidth to scan the transition. The use of Sh'polskii matrices, crystalline host matrices of long alcane molecules, has been shown to greatly enhance the line narrowing of ZPL due to the resulting homogeneous and inert environment for emitters [193, 77]. Preliminary tests have been carried out at room temperature, but this type of matrices remain to be tested for low-temperature experiments.

In our global aim to link properties to structure for GQDs, a thorough undestanding of the observations for different measurement methods for a particular GQD (in solution or single-molecule experiments) comes as a necessary step before moving on to other geometries. For instance, we have highlighted the need of symmetry-breaking of the GQD in order to explain the observed emission from $C_{96}C_{12}$, implemented in the case of $C_{96}C_{12}$ by a coupling to the vibrational modes of the GQD. We could now induce this symmetry-breaking by directly considering systems with different symmetries, and investigate the difference in signature compared to $C_{96}C_{12}$, which will be developed in the next chapter.

Chapter 5

Towards new geometries: optical investigation of rod-shaped GQDs

Contents

Introduction

The extensive study on the triangular-shaped $C_{96}C_{12}$ GQD has enabled us to gain insight into the manipulation of GQDs, both in solution and at the single-object level, and underlined the importance of symmetries in the emission properties of GQDs. It has also shed some light on a few drawbacks for its use at the single-object level, such as the formation of aggregates and the presence of by-products. Although we established methods to bypass these shortcomings using selection criteria, developing new methods to isolate a GQD and probe its intrinsic properties without obstacle would be beneficial for not only experimental measurements but also the use of GQDs for applications. In this perspective, we focus on a new class of rod-shaped GQDs, which have recently been synthesized with high purity using efficient bottom-up routes by Daniel Medina-Lopez and Dr. Stéphane Campidelli in CEA Saclay. Since they exhibit a different symmetry than $C_{96}C_{12}$, comparing them with $C_{96}C_{12}$ could provide some insight into the influence of geometry on the optical properties of GQDs. Moreover, the addition of bulky side-chains, in contrast to the alkyl side-chains on $C_{96}C_{12}$, should help tackle the issue of intermolecular interaction between GQDs.

After describing the structure of the rod-shaped GQDs in a first section, I focus first on the effect of geometry on the optical properties of GQDs by studying the $C_{96}tBu_8$ GQD, a rod-shaped GQD sharing the same number of carbon atoms in its graphenoid core as $C_{96}C_{12}$ but arranged in a different geometry. The study is performed both in solution with ensemble characterization, and at the single-object level. In a final part, I describe the effect of size on the optical properties of GQDs by studying objects from the same symmetry class, but of different sizes.

5.1 Description of rod-shaped GQDs

5.1.1 Description of the system

In this chapter, we focus on a family of graphene quantum dots presenting a rod-shaped structure. Similarly to the triangular $C_{96}C_{12}$, the $C_{96}tBu_8$ GQD is composed of an aromatic core constituted of 96 carbon atoms, but in a different spatial arrangement, as shown in Figure 5.1. In the case of $C_{96}tBu_8$, 8 *tert*-butyl side-chains are added on the periphery of the aromatic core. The steric effect of such groups prevents stacking between GQDs and increases the solubility of the system (as shown in following sections).

The electronic properties of $C_{96}tBu_8$ are dominated by the 96 π electrons delocalized on the core and its D_{2h} symmetry. Similarly to the triangular-shaped $C_{96}C_{12}$ GQD presented in the previous chapter, the rod-shaped GQD presents a fully-benzenoid structure and is therefore predicted to exhibit a high stability [23].

Similar rod-shaped GQDs have been synthesized, but with different core sizes: a smaller GQD, with a 78-carbon-atom core and 6 *tert*-butyl side-chains, and a longer GQD, with a core with 114 carbon atoms and 10 *tert*-butyl side-chains in its periphery. They are respectively labelled $C_{78}tBu_6$ and $C_{114}tBu_{10}$, and their chemical structure is given in Figure 5.1.

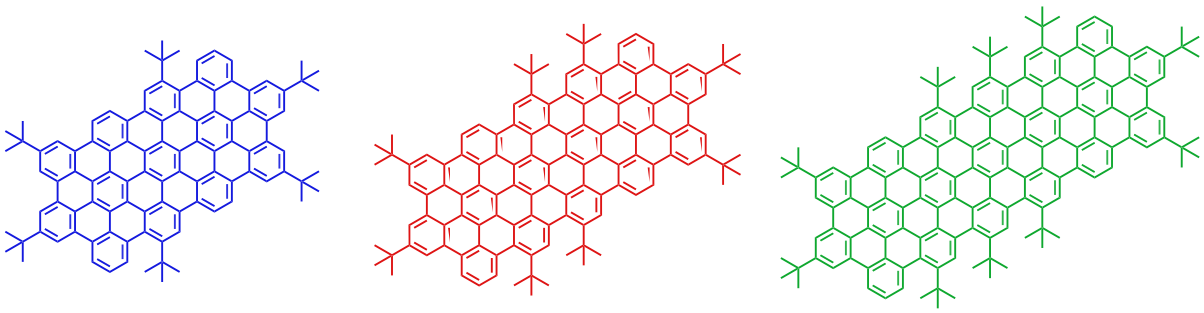

Figure 5.1: Chemical structure of $C_{78}tBu_6$, $C_{96}tBu_8$ and $C_{114}tBu_{10}$ GQDs.

The rod-shaped GQDs were synthesized by Daniel Medina-Lopez and Dr. Stéphane Campidelli at CEA Saclay, and were delivered to us as powder.

5.1.2 Purification of synthesis batch

Synthesis batches were purified by the chemists using various methods. In particular, it is possible to use column chromatography to eliminate by-products of the synthesis. In Figure 5.2, the comparison between MALDI-TOF mass spectra measured before (*i.e.* right after the Scholl reaction) and after purifications shows the clear decrease of peaks not associated with the GQDs (identified as the **M+** peaks). The disappearance of these peaks highlights the efficiency of the purification step. In the insets of the bottom line subfigures, the isotopic distribution of the compound **M+** is compared to a simulated distribution, with a perfect agreement between the two, comforting us in the synthesis of the desired product.

It is also possible to appreciate the elimination of non-desired compounds using optical spectroscopy. An example is given in Figure 5.3 for the synthesis batch of $C_{96}tBu_8$ dissolved in 1,2,4-trichlorobenzene (TCB). Similarly to the results described for the triangular $C_{96}C_{12}$ GQD, we can observe in the photoluminescence spectrum before purification both the fluorescence of GQD monomer, and the fluorescence at higher energy resulting from other by-products dissolved in the solution. The purification process developed for the rod-shaped GQDs successfully eliminates the by-products, and we are thus left after purification with only the fluorescence of the $C_{96}tBu_8$ monomer, with no fluorescence signal at higher energy (in stark contrast to PL spectra measured on solutions of $C_{96}C_{12}$). The possibility to efficiently purify the synthesis batches represents a significant asset for the production of high-purity samples, as compared to other systems such as the $C_{96}C_{12}$ which are hampered by the presence of undesired by-products.

In the case of $C_{78}tBu_6$ GQD, we observe the presence in the mass spectrum of a series of peaks at a value of m/z around 2597 (out of the range of Figure 5.2), corresponding to the presence of dimers of $C_{78}tBu_6$ GQDs, hinting a tendency of this GQD to stack. No peaks in the mass spectra of the other two GQDs may hint to the formation of dimers.

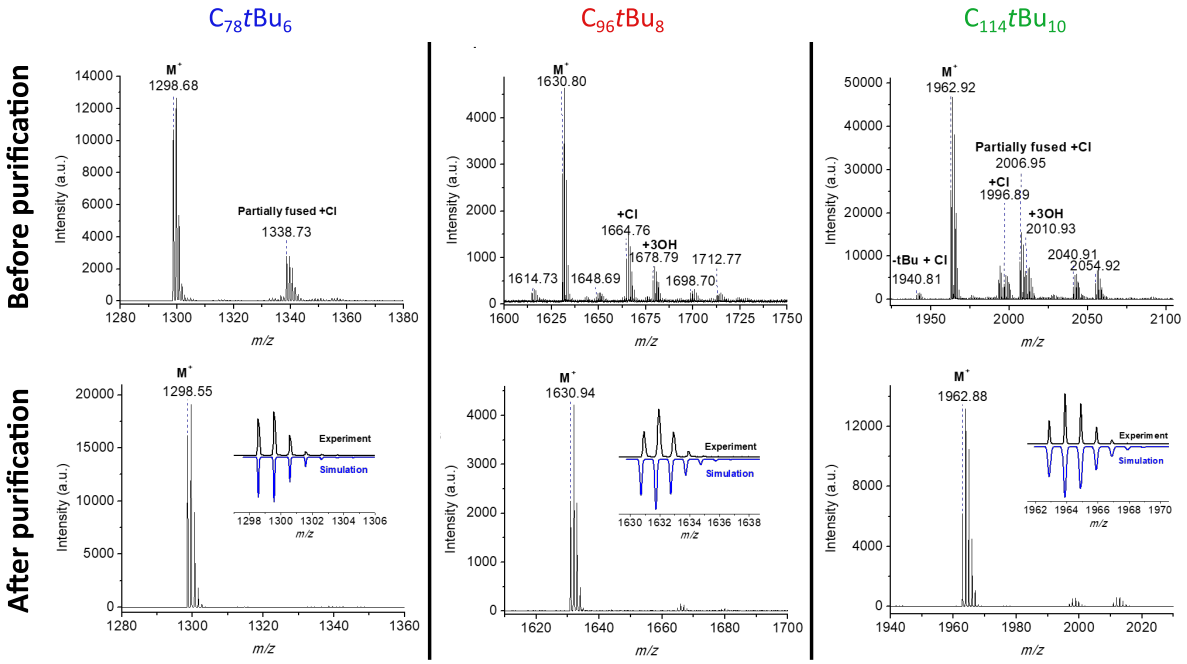

Figure 5.2: MALDI-TOF mass spectra (top) before and (bottom) after purification of the three GQDs. Inserts correspond to the zoom on the M+ peak (black) and a comparison to the simulated spectra (blue).

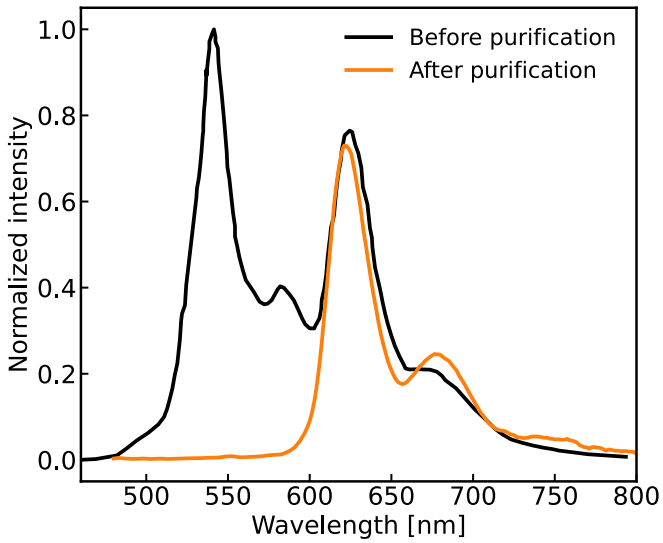

Figure 5.3: PL spectrum of the $C_{96}tBu_8$ synthesis batch dispersed in TCB before (black) and after (orange) purification.

5.1.3 Description of samples

The powders delivered by the chemists were dispersed in 1,2,4-trichlorobenzene (TCB). No specific ultra-sonication or stirring step was necessary to disperse the GQDs, in contrast to the $C_{96}C_{12}$ GQDs, indicating an enhanced solubility for the rod-shaped GQDs.

Single-object samples were prepared using the protocol described in Chapter 2. The matrix used is polystyrene (PS), prepared in TCB, with a concentration of 5 wt% in the solution deposited on substrate (Schott coverslip).

5.2 Exploring new geometries: rod-shaped $C_{96}tBu_8$

As mentioned in the previous paragraph, the graphenoid core of $C_{96}tBu_8$ GQD shares the same number of atoms as the $C_{96}C_{12}$ GQD, but arranged in a different geometry, changing the symmetry class from D_{3h} for $C_{96}C_{12}$ to D_{2h} for $C_{96}tBu_8$. By analyzing the experimental results for the rod-shaped GQD, we will therefore probe the effect of the reduction of symmetry on the optical properties of the GQD.

5.2.1 Ensemble characterization in solution

General characterization

The absorption spectrum measured on a solution of $C_{96}tBu_8$ in TCB is given in Figure 5.4(a). The general structure is similar to absorption spectra recorded for $C_{96}C_{12}$ and other PAH: the spectrum exhibits a progression of lines at lower energy from 615 nm to 550 nm, followed by a series of peaks at higher energy (with wavelengths below 500 nm). Distinct peaks can be observed in the spectrum, and their position can be measured with good accuracy. From lowest to highest in energy, the position of the lines are: 612 nm (**a**), 598 nm

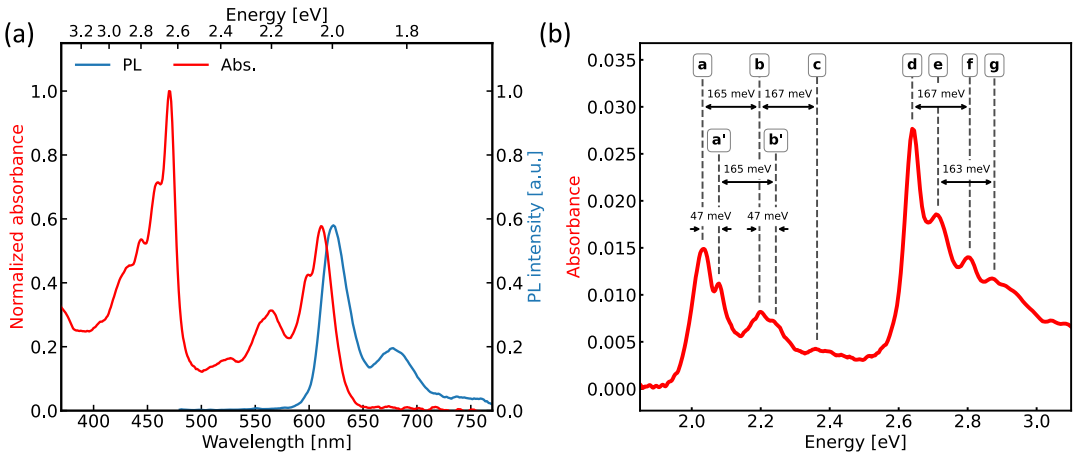

Figure 5.4: (a) Absorption and PL spectra of $C_{96}tBu_8$. (b) The labelling of the peaks in the absorption spectrum, and associated energy split.

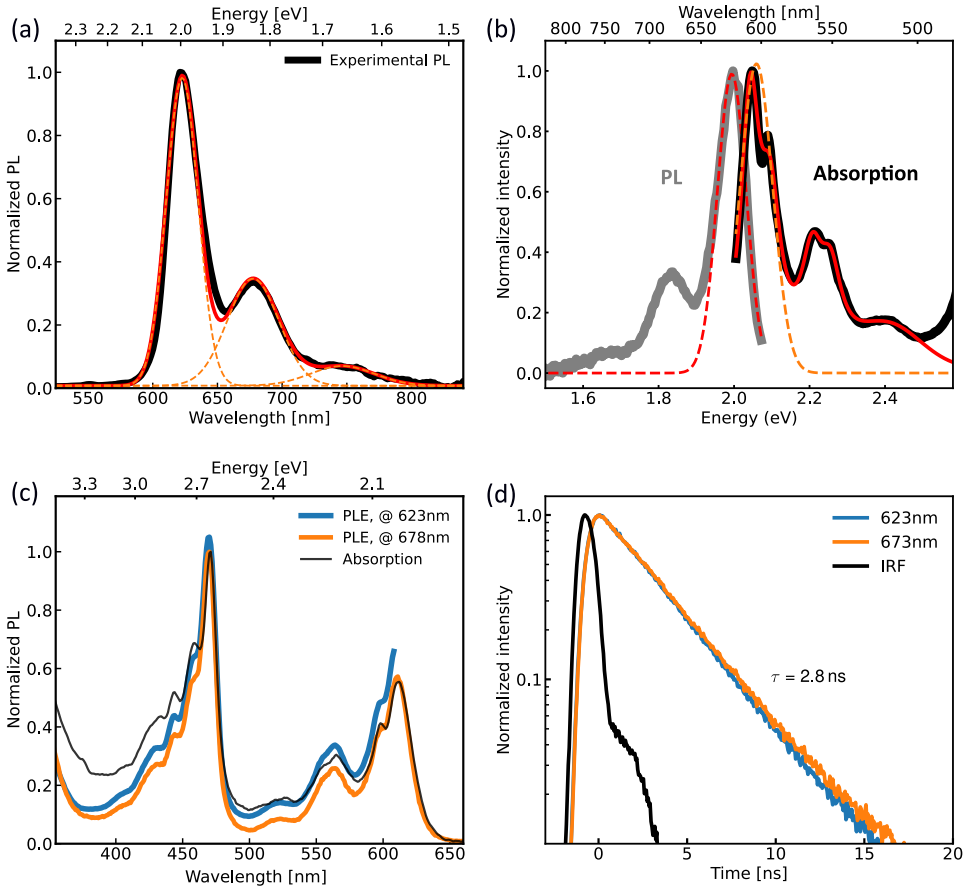

Figure 5.5: (a) PL spectrum of $C_{96}tBu_8$ in TCB (excited at 450 nm). The spectrum is fitted using three Gaussian functions (orange dashed curve). (b) Mirror symmetry between PL and absorption. The red dashed line gives the Gaussian fit of the main peak of the PL spectrum. The red solid line represents the multi-Lorentzian fit of the absorption spectrum. The orange dashed line represents the Gaussian fit of both peaks **a** and **a'**. (c) PLE spectra collected at the two main emission peaks (623 nm and 678 nm). The absorption spectrum is plotted for comparison. (d) Time-resolved PL decay collected at the same two wavelengths. Mono-exponential fit yields a decay lifetime of 2.8 ns

(**a'**), 566 nm (**b**), 554 nm (**b'**), 526 nm (**c**), 471 nm (**d**), 458 nm (**e**), 443 nm (**f**) and 432 nm (**g**), with the lettering of the transitions given in Figure 5.4(b). In comparison to the absorption spectrum of the triangular-shaped $C_{96}C_{12}$ GQD, the features are sharper, which indicates a higher solubility of the GQDs in the solution, and a reduced influence of aggregation (as reported for different PAH systems, for instance in [117]). Indeed, the observation of narrow lines is characteristic of polycyclic aromatic hydrocarbons exhibiting high solubility [128]. The energy difference between the peaks is given in Figure 5.4(b). Following usual peak assignment, we can attribute peak **a** to the lowest purely-electronic transition and the following peaks (**a'** to **c**) to vibronic replicas, with energy shifts relatively to peak **a** measured at 47 meV (**a'**), 165 meV (**b**), 212 meV (**b'**) and 332 meV (**c**). Interestingly, we recover with line **b** and **c** the expected vibronic replicas for aromatic compounds (similarly to $C_{96}C_{12}$ GQDs), with the energy split value of 165 meV corresponding to the C=C bond stretching in the aromatic core.

At higher energy, the intense peaks (**d** to **g**) correspond presumably to β-bands (using Clar's notation). Interestingly, the energy split between **d** and **f** (and between **e** and **g**) yields 167 meV (163 meV), corresponding to the same expected vibronic replica for aromatic compounds as observed for the lower-energy peaks. This observation encourages us to consider peaks **f** and **g** as vibronic replicas of transitions **d** and **e** (considered as purely electronic) respectively. Another possibility would be that only peak **d** corresponds to a purely-electronic transition, and the following peaks are associated vibronic replicas (peak **e** would in that case correspond to a vibronic peak with an energy of 75 meV). Comparison to theory, in the next section, will bring more insight on the assignment.

Plotted in Figure5.5(a), the photoluminescence (PL) spectrum when excited at 450 nm shows a structure similar to the one obtained for $C_{96}C_{12}$ GQDs, composed of one strong peak at 622.7 nm followed by a weaker peak at 677.5 $\pm$ 0.3 nm and a third at around 745 nm (values extracted by fitting with three Gaussians). The first peak is attributed to the purely-electronic transition, while the two other peaks correspond to replicas at 161 meV. The general mirror symmetry between absorption and PL is therefore respected, with a Stokes shift of 38 meV, although we do not observe the sharp features present in the absorption spectrum. We can compare for instance the width of the absorption peak **a** measured at 58.73 $\pm$ 0.01 meV (estimated using a Lorentzian fit, see Figure 5.5(b), with the solid red line) with the 89.63 $\pm$ 0.01 meV width of the first PL peak (see dashed red line for the Gaussian fit). Interestingly, fitting both transitions **a** and **a'** with a single Gaussian (in dashed orange in Figure 5.5(b)) yields a width of 101.2 $\pm$ 0.5 meV, bringing us closer to the width of the first PL peak.

The photoluminescence excitation (PLE) spectra collected at 623 nm and 678 nm exhibit the same structure as shown in Figure 5.5(c), indicating that the two emission peaks result from the emission from the same excited level. Moreover, the PLE spectra share the exact same structure as the absorption spectrum, in terms of transition energies and linewidth. This is in stark contrast to the observations for $C_{96}C_{12}$ GQDs, and represents a strong indication that the solution is composed almost exclusively of single $C_{96}tBu_8$ GQD

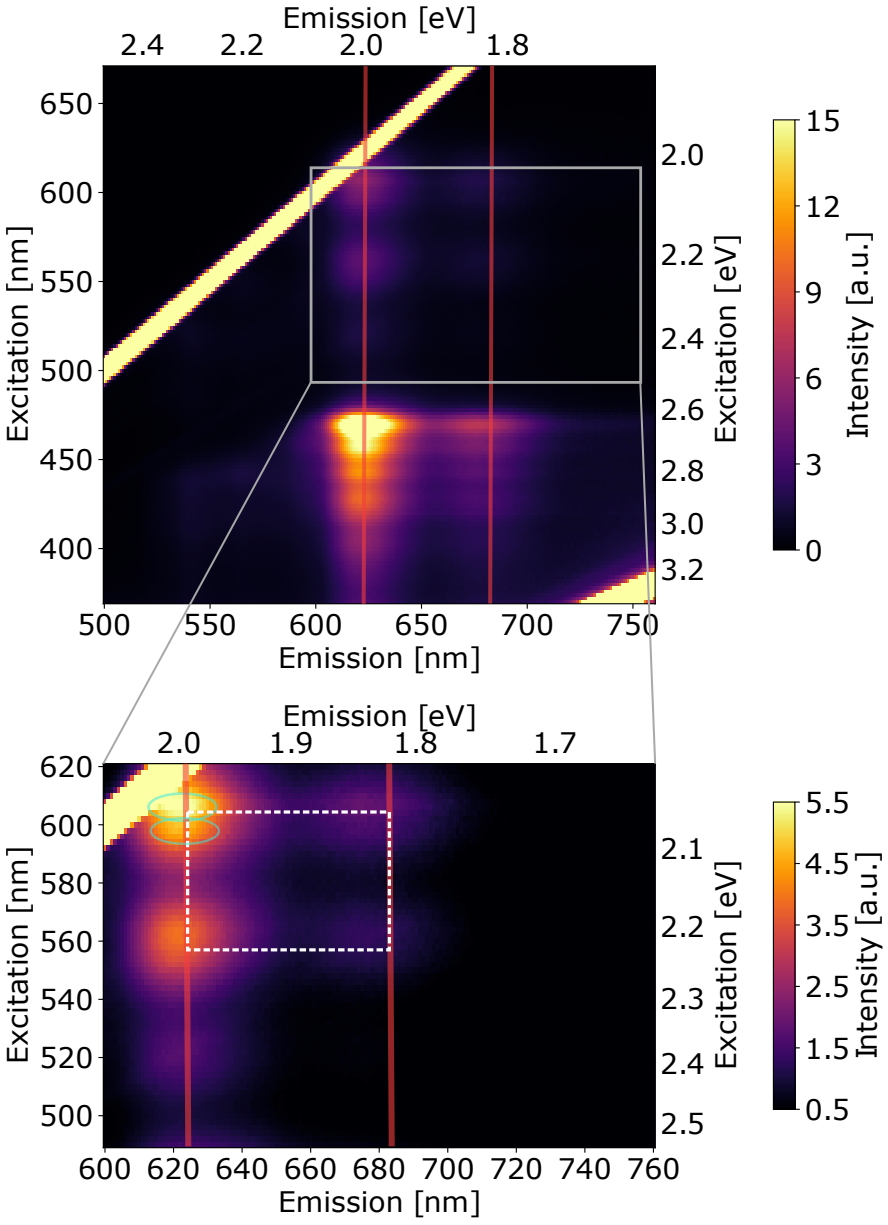

Figure 5.6: 2D PL-PLE map for $C_{96}tBu_8$ in TCB. A zoom on the low energy region (delimited by the grey line) is given in the bottom map, with the intensity colorscale rescaled for clarity. Red lines indicate the emission wavelengths of $C_{96}tBu_8$ GQD. Green lines circle the features associated with the **a** and **a'** peaks in the absorption spectrum. Dashed white lines highlight the square structure associated to the mirror symmetry.

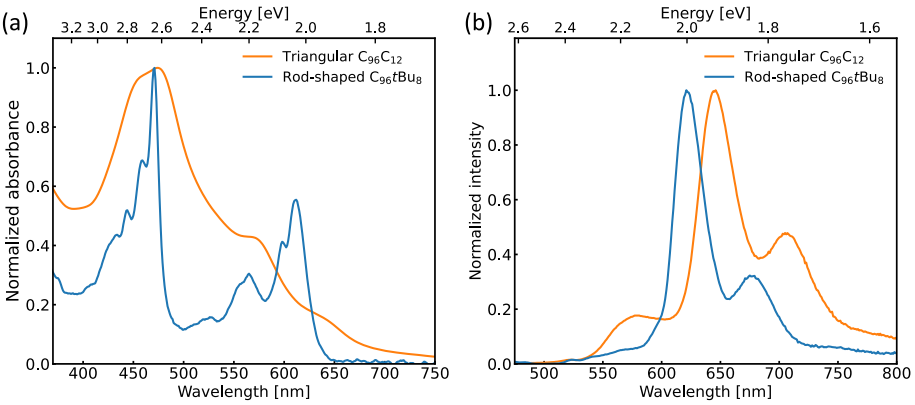

Figure 5.7: Comparison of the (a) absorption and (b) photoluminescence spectra of the $C_{96}tBu_8$ and $C_{96}C_{12}$ GQDs.

monomers, with no aggregates in solution[1].

With time-resolved photoluminescence curves measured at 623 nm and 674 nm (shown in Figure 5.5(d)), we can verify that the dynamics is the same for both transitions, following a mono-exponential decay with a lifetime of 2.8 ns, and confirming the attribution of the peak at 674 nm to a vibronic replica.

The 2D PL-PLE map confirms once more the homogeneity of the composition of the solution. We recognize the features attributed to $C_{96}tBu_8$ GQDs, with the characteristic square structures resulting from the mirror symmetry between absorption and PL spectra (in white dashed line). If other emitting objects different from $C_{96}tBu_8$ were present in the solution, we would observe features not aligned with the ones associated with the $C_{96}tBu_8$ GQD. In particular, if we look at the features at low energy in Figure 5.6, with a reduced intensity colorscale for more clarity, we distinguish no additional features close to the diagonal $\lambda_{exc} = \lambda_{em}$, indicating the absence of other fluorescent objects in the solution.

Finally, before closing the description of the observations on $C_{96}tBu_8$ in solution, I compare in Figure 5.7 the absorption and PL spectra with the ones measured for $C_{96}C_{12}$. As mentioned earlier, the linewidth of the peaks in the absorption spectrum is significantly larger for $C_{96}C_{12}$ than for the $C_{96}tBu_8$ GQD. For the PL spectrum, the two GQDs share the same structure (ignoring the peak at high energy for $C_{96}C_{12}$, attributed to aggregates and other by-products), with an energy shift between the two main peaks of 21 nm (65 meV). Moreover, the linewidth of the peaks is not significantly different between the two GQDs. Given that for both GQDs, these PL lines result from the emission of single GQDs (*i.e.* monomers) in solution, we can therefore assume that the homogeneous broadening of the PL lines is comparable for both GQDs.

[1]As mentioned in the previous chapter on $C_{96}C_{12}$ GQDs, the difference between the absorption spectrum and the PLE spectrum arises from the presence of non-fluorescent absorbing species.

Comparison with theoretical calculations

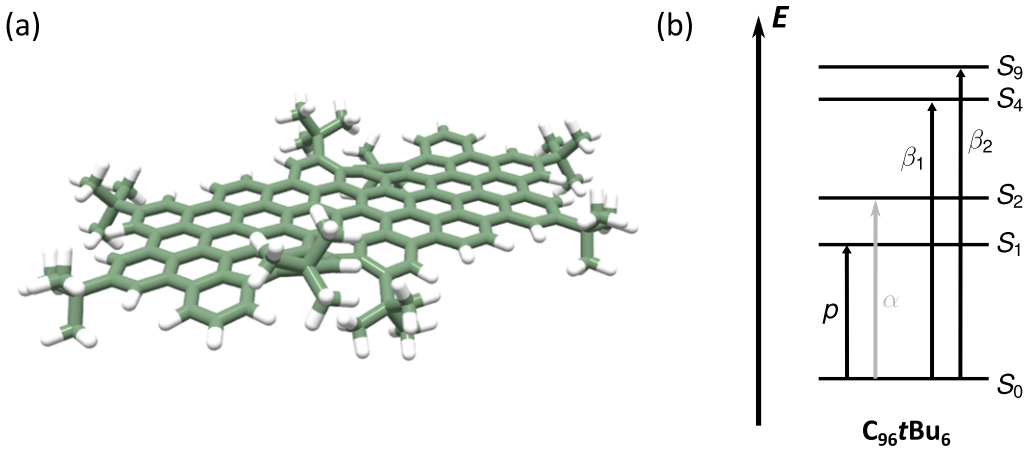

Figure 5.8: (a) Calculated equilibrium geometry for $C_{96}tBu_8$. (b) Bright energy levels and associated Clar's notation for rod-shaped $C_{96}tBu_8$.

The results in solution obtained for rod-shaped $C_{96}tBu_8$ GQD can be compared with theory. Similarly to $C_{96}C_{12}$, Clar's formalism can be used to describe the transitions of $C_{96}tBu_8$. Nonetheless, we expect a change in the electronic levels of the $C_{96}tBu_8$ GQD compared to $C_{96}C_{12}$, due to a change of symmetry. Indeed, according to theory, the symmetry lowering from D_{3h} to D_{2h} is accompanied by a brightening of the low-lying excited singlet states and a splitting of the degenerated higher singlet states [44, 38][2].

Theoretical calculations on $C_{96}tBu_8$ were performed by Dr. Silvio Osella and Prof. David Beljonne (Université de Mons). Using DFT, the stable geometry of the $C_{96}tBu_8$ GQD is calculated in its ground state. The resulting geometry shows that the aromatic plane is slightly twisted due to steric hindrance induced by the *tert*-butyl groups, as shown in Figure 5.8(a). The transitions are computed using DFT/TDDFT from the optimized geometry. The bright transitions calculated are given in Table 5.1. Interestingly, the four principal transitions (*i.e.* corresponding to the α-, p- and β-bands in Clar's notation) do not correspond to the four lowest singlet states (additional dark singlet states are predicted in-between). This is expected for systems like $C_{96}tBu_8$ with lower symmetry [44, 215]. Nonetheless, these four states can be described with transitions involving primarily the frontier molecular orbitals of the GQD (HOMO, HOMO-1, LUMO and LUMO+1), as it was the case for $C_{96}C_{12}$. Given the calculations, the lowest transition to singlet state S_1 in the case of $C_{96}tBu_8$ is bright (oscillator strength near unity) and can be described primarily by the HOMO to LUMO transition, and thus by definition corresponds to the p-band. The calculated energy for state S_1 corresponds perfectly to the lowest transition **a** (at 612 nm) in the absorption spectrum. Directly above it, the second singlet state corresponds to the α-band, with a significantly lower oscillator strength. Although many systems present an α-band below the p-band [60], as it was the case for $C_{96}C_{12}$, it is not uncommon for the

[2]Taking into consideration distortions of the $C_{96}C_{12}$ GQD led to the same effect, as a result from the symmetry-breaking.

State	ΔE (eV)	ΔE (nm)	f	Principal contribution	Band attribution
S_1	2.021	615	1.01	H $\longrightarrow$ L	p-band
S_2	2.173	572	0.01	H-1 $\longrightarrow$ L	α-band
S_4	2.579	482	0.62	H $\longrightarrow$ L+1	β_1-band
S_9	2.732	455	1.19	H-1 $\longrightarrow$ L+1	β_2-band

Table 5.1: Excitation energies (ΔE), oscillator strength (f) and principal contribution of the first four bright singlet states (H and L being short for HOMO and LUMO respectively) calculated for the $C_{96}tBu_8$ GQD. The attributed Clar nomenclature is given in the last column.

p-band to find itself below the α-band [216] (we can cite for example pentacene [217]). In the case of $C_{96}tBu_8$, this result notably accounts for its appreciable fluorescence. Moreover, the distortion of the plane may also contribute to the presence of the p-band below the α-band. It was indeed reported that deformation of the aromatic core of elongated nanographenes (due to steric effects of functionalization groups) could lead to an inversion between the α- and the p-band [34], and thus to an increased emission of the GQD [215].

The two bright β-bands are effectively split, with a predicted energy split of 0.15 eV. These two states correspond well with the narrow peaks **d** (471 nm) and **e** (458 nm) of the absorption spectrum. This attribution is in line with the attribution of peaks **d** and **e** to purely-electronic transitions. As a result, given the narrow linewidth of the peaks

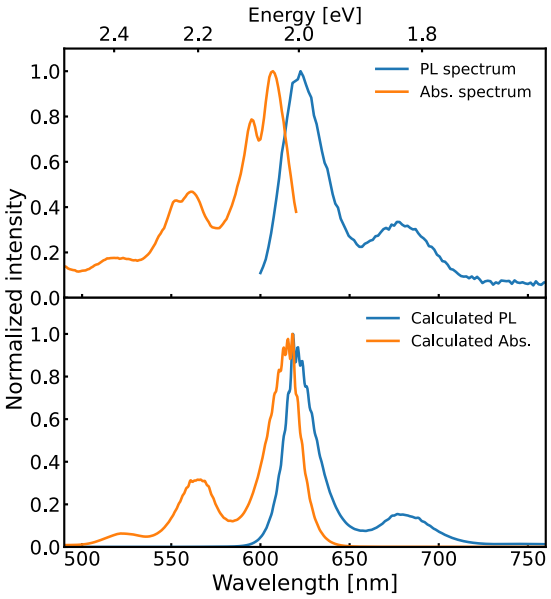

Figure 5.9: Comparison of the absorption and photoluminescence spectra measured experimentally (top) with theoretical calculations (bottom).

resulting from the high solubility of the $C_{96}tBu_8$, the splitting between the two β-bands can be resolved in the absorption spectrum.

Deeper characterization is performed by taking into account vibrational effects, which enables a simulation of the spectra for the first optical transition. The structural distortion between S_0 and S_1 is described using the ground-state normal modes. The spectral lineshape is then calculated using a displaced harmonic oscillator model in the Franck-Condon approximation. The linewidth of the spectrum in simulation is accounted for by thermal population of low-frequency modes[3]. The results is given in Figure 5.9. There is a good correspondance between the simulated spectra and the experimental results. Looking at the PL spectrum, we recover that the width of the PL line can be fully reproduced by taking into account the vibrational modes, and is in good agreement with the absence of inhomogeneous contribution. Moreover, calculations show that the $S_0 \rightarrow S_1$ transition is coupled to two vibrational modes of the GQD with frequencies at around 166 meV and 205 meV, which correspond satisfyingly to the peaks **b** and **b'** resolved in the absorption spectrum (measured at 165 and 212 meV), confirming the attribution of these two peaks to vibronic transitions. The larger unresolved peak **c** is also reproduced and corresponds well to the $0-2$ vibrational peak of the same modes.

There remains the interpretation of peak **a'**. According to calculations, no vibrational mode with a frequency close to the value observed for peak **a'** (47 meV) was found to significantly couple to the $S_0 \rightarrow S_1$ transition. We suspect therefore that peak **a'** does not correspond to a vibronic peak. One possibility is that this peak corresponds to the formation of stable dimers. However, no effect of concentration has been observed on the spectra measured. As shown in Figure 5.10, the position, linewidth and relative ratio

[3]A tiny inhomogeneous contribution is added to smoothen the spectra.

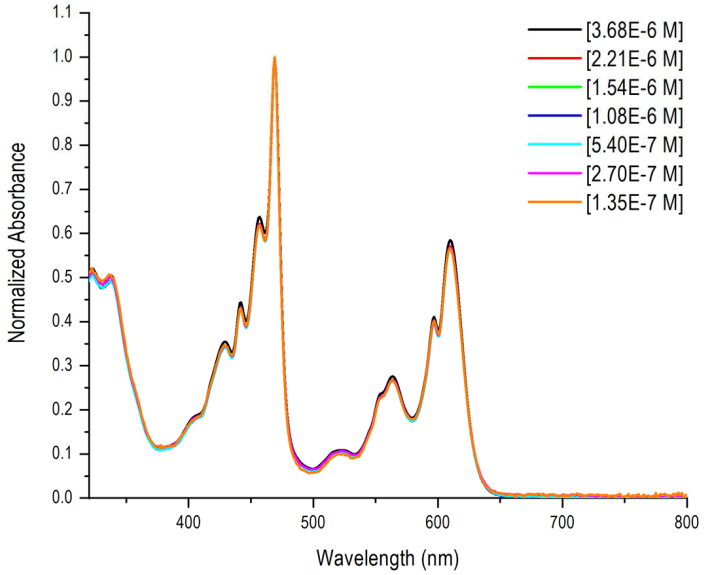

Figure 5.10: Effect of concentration on the absorption spectrum of $C_{96}tBu_8$ in TCB.

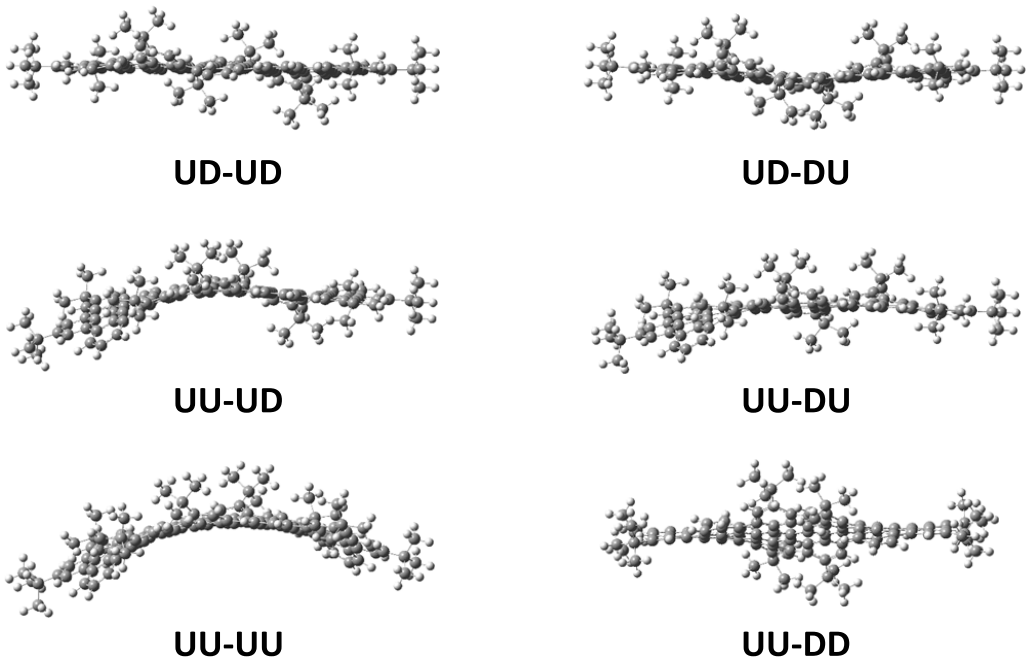

Figure 5.11: Representation of the six conformers of the $C_{96}tBu_8$ GQD. The four letters (U for up, D for down) indicate the relative position the *tert*-butyl groups relatively to the molecular plane.

of the peaks does not change with the concentration. Moreover, no peak in the MALDI-TOF mass spectra indicated the presence of aggregated $C_{96}tBu_8$ GQDs.

Another possiblity is to attribute peaks **a** and **a'** to the presence of different stable conformers. Since the 8 *tert*-butyl groups distort the aromatic core, their position relatively to the plane of the GQD produce different stable geometries of the GQD (to be more precise, only the four *tert*-butyl groups attached to the center of the GQD induce a distortion of the core). Given the symmetry of the system, there results 6 different conformations, which can be identified by the relative position of the four *tert*-butyl groups (U for up or D for down, relatively to the aromatic core). The calculated molecular structure of the conformers are given in Figure 5.11, and the energy calculated for each conformers is given in Table 5.2. Calculations show that the energy of the first transition slightly varies over a 18 meV range. Although the value is lower than the energy split between **a** and **a'** (47 meV), the order of magnitude is coherent and lends weight to this interpretation. Moreover, the stabilization of the various conformers depends on the environment (*i.e.* solvent), which can thus lead to a change of the energy range.

We still note a few unresolved details when adopting this hypothesis. By looking at the PL-PLE 2D map in Figure 5.6, we can see that the spot corresponding to the absorption peak **a'** (circled in green) is perfectly aligned with the emission wavelength of peak **a** (*i.e.* shares the same x-coordinate as peak **a**), which indicates that the object responsible for peak **a'** rigorously emits light at the same wavelength the object yielding peak **a**. We would have expected a shift of peak **a** which would account for a shift of the emis-

Conformer	S_1	S_2	S_4	S_9
UD-UD	2.017	2.168	2.571	2.728
UD-DU	2.015	2.169	2.571	2.731
UU-UD	2.016	2.175	2.570	2.744
UU-DU	2.022	2.175	2.571	2.736
UU-UU	2.013	2.181	2.572	2.758
UU-DD	2.031	2.182	2.574	2.738

Table 5.2: Energy (in eV) of the four principal transitions calculated for the various conformers of the $C_{96}tBu_8$ GQD.

sion peak for the conformer yielding peak **a'**[4]. Moreover, calculations showed that other transitions were affected by conformers. For instance, the $S_0 \rightarrow S_9$ transition (which we associated with peak **e**) should be affected, with a variation of the energy over a range of 30 meV. However no peak which could correspond to an effect of conformers can be observed in the absorption spectrum[5]. It is possible that the peak that should result from the existence of different conformers may be too weak in intensity and be hidden by neighboring peaks, for example peak **f**.

Steric effects of bulky side-chains are known to distort the molecular plane of PAH [117, 40] and may restrain the delocalization of the wavefunction on the whole sp^2 system. Looking at the electronic density distribution calculated for the various transitions, we can see that it is delocalized on the whole GQD, thus indicating that the consequences of the D_{2h} symmetry are preserved. If we focus on the resulting transition dipole moments, they are polarized along different directions of the GQD. As predicted by Cocchi and co-workers for similar elongated systems [44], the transitions of $C_{96}tBu_8$ are polarized along either the longitudinal (transitions $S_0 \rightarrow S_1$ and $S_0 \rightarrow S_9$) or transverse (transition $S_0 \rightarrow S_4$) direction relatively to the long axis of the GQD, as shown in Figure 5.12. The $S_0 \rightarrow S_2$ transition dipole, not shown in the Figure, is oriented along the transverse direction. These calculations reproduce successfully the results of Cocchi and co-workers, who calculated that, on flat D_{2h} systems, the four main transitions are composed of two longitudinal and two transverse transition dipoles, with the p-band exhibiting a longitudinal transition dipole. Interestingly, these results provide an additional approach to probe the peak assignment, by performing polarization-dependent measurements.

Fluorescence anisotropy measurements

In order to verify experimentally the calculation of the transition dipoles, we performed anisotropy fluorescence measurements, using the method described in Chapter 2. Since it is necessary to correlate the relative orientation of the absorption polarization to the emission polarization, the GQDs must be ideally immobilized between absorption and

[4]Since the $S_0 \rightarrow S_1$ transition energy changes for different conformers, both the absorption peak and emission peak should be affected by this change.

[5]We exclude the possibility of peak **e** to correspond to a "conformer peak" associated with **d**, since calculations predict no change of the $S_0 \rightarrow S_4$ transition energy for the different conformers.

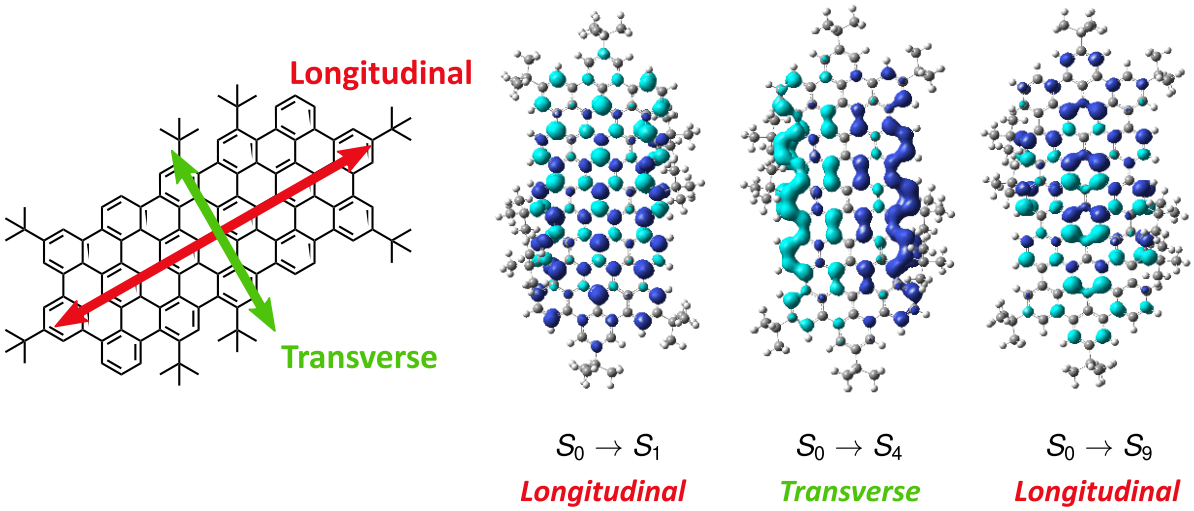

Figure 5.12: Transition densities for the three bright transitions of $C_{96}tBu_8$, and direction of the associated transition dipole. On the left is given the definition of the longitudinal and transverse directions of the GQD.

fluorescence emission for steady-state measurements. A viscous solvent, castor oil, is thus added to minimize the reorientation of the GQD during measurement, as mentioned in Chapter 2. After a few seconds of stirring castor oil with TCB, the mixture yields a stable homogeneous phase. In Figure 5.13(a), I show the PL spectrum of the solution of $C_{96}tBu_8$ in the mixture of TCB and castor oil. We recover the main emission peak of $C_{96}tBu_8$ GQDs at 629 nm. The other features observed result from the intrinsic fluorescence of the castor oil solvent used (this is clear when comparing with PL spectrum of castor oil, plotted in the same figure). Fortunately, the main emission peak of $C_{96}tBu_8$ does not overlap with features from castor oil, and we can thus assume that the fluorescence collected at this wavelength results almost exclusively from $C_{96}tBu_8$.

The PLE spectrum collected at 629 nm, along with the associated anisotropy curve, is given in Figure 5.13(b). The PLE spectrum corresponds perfectly to the spectrum measured without castor oil (see Figure 5.15(b) for comparison), which indicates that we are indeed primarily observing $C_{96}tBu_8$ GQDs. The anisotropy curve is relatively flat at high wavelength, reaching a maximum value of $r_{max} = 0.37$, and oscillates at shorter wavelengths between local extrema, which are reached for wavelengths which satisfyingly correspond to the position of PLE peaks. The measurement of the anisotropy r does not give an absolute information on the polarization direction of a transition, but compares the polarization direction of each excited transition with the polarization of the emission transition. In the case of the curve in Figure 5.13(b), since the PLE is collected at 629 nm, corresponding to the electronic transition $S_1 \rightarrow S_0$, the anisotropy curve gives information on the relative orientation of the polarization of each absorption transitions excited. As expected, r is maximum and close to 0.4 for high λ_{exc} since the emission and absorption of a same electronic transition are usually collinear. All the transitions with $\lambda_{exc} > 500$ nm share the same anisotropy factor (we do not observe any strong variation of the anisotropy). This observation is in good agreement with the attribution of all the

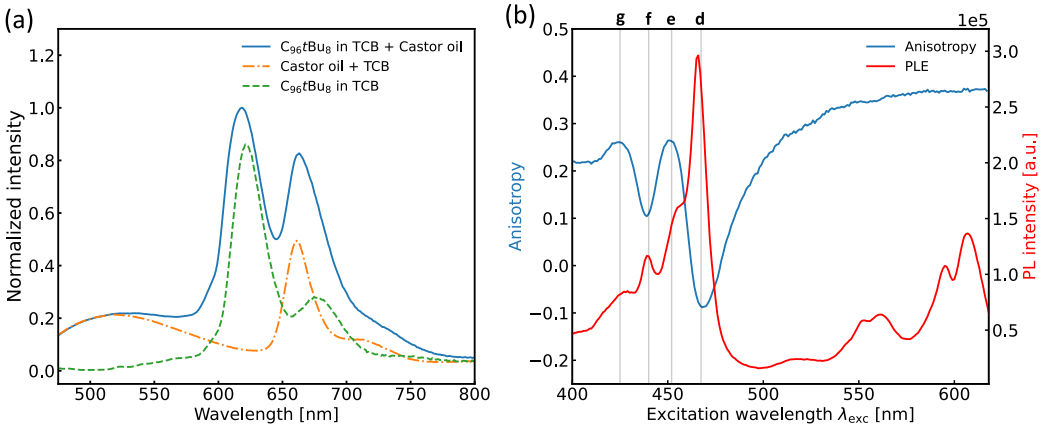

Figure 5.13: (a) PL spectrum for $C_{96}tBu_8$ in TCB and castor mixture (10/90 wt%). PL spectra of the mixture without $C_{96}tBu_8$ (orange dash-dotted line) and of $C_{96}tBu_8$ in TCB only (green dashed line) are given for comparison. (b) PLE spectrum (red) and anisotropy curve (blue) collected at 629 nm.

lines labelled **a** to **c** as related to the same electronic transition (namely $S_0 \longrightarrow S_1$). Below 500 nm, the anisotropy reaches minima for peaks **d** and **f** and maxima for peaks **e** and **g**. These peaks thus correspond to transitions to higher excited singlet states.

In order to better visualize the transitions, we can compute the parallel and perpendicular components of the PLE. For each wavelength, the anisotropy can be decomposed as a parallel and perpendicular contribution $f_{\parallel}$ and $f_{\perp}$ (with the sum of both equal to unity):

$$r = f_{\parallel} r_{\parallel} + f_{\perp} r_{\perp} \tag{5.1}$$

where $r_{\parallel}$ and $r_{\perp}$ are the value of the anisotropy for a parallel and perpendicular transition respectively. Theoretically, $r_{\parallel} = 0.4$ and $r_{\perp} = -0.2$. In our case, we know that depolarization effects can occur, which prevent the anisotropy to reach the theoretical 0.4 value for parallel absorption and emission dipoles. Instead, we evaluate the value $r_{\parallel}$ by measuring the maximum value of $r_{\max}$ (reached usually by r for λ_{exc} close to the collection wavelength, as it is the case for $C_{96}tBu_8$). Using the experimental curve in Figure 5.13(b), we estimate:

$$r_{\parallel} = r_{\max} = 0.37 \quad \text{and} \quad r_{\perp} = -\frac{r_{\max}}{2} = -0.185$$

If we introduce $\tilde{I}_{\parallel}$ and $\tilde{I}_{\perp}$ the two components of the PLE intensity[6], they can thus be

[6]It is important to note that the components $\tilde{I}_{\parallel}$ and $\tilde{I}_{\perp}$ of the PLE spectrum are different from $I_{\parallel}$ and $I_{\perp}$, which are the PLE intensity collected with a polarization parallel and perpendicular to the excitation polarization respectively. For instance, one can easily convince oneself that the PLE collected with a polarization parallel to the excitation may result from a transition with a dipole transition either parallel or perpendicular to the emission dipole orientation depending on the orientation of the GQD.

expressed as:

$$\begin{aligned}\tilde{I}_{\parallel}(\lambda) &= f_{\parallel}(\lambda) I_{\text{tot}}(\lambda) = \frac{r(\lambda) - r_{\perp}}{r_{\parallel} - r_{\perp}} I_{\text{tot}}(\lambda) \\ \tilde{I}_{\perp}(\lambda) &= f_{\perp}(\lambda) I_{\text{tot}}(\lambda) = \frac{r_{\parallel} - r(\lambda)}{r_{\parallel} - r_{\perp}} I_{\text{tot}}(\lambda)\end{aligned} \tag{5.2}$$

where $I_{\text{tot}}(\lambda)$ correspond to the PLE spectrum measured. The result is given in Figure 5.14. In this figure, we can visually appreciate the peaks corresponding to transitions with dipole orientation parallel and perpendicular to the emission dipole orientation. It is interesting to compare this result with the dipole orientation of the transitions calculated using DFT/TDDFT. As discussed in the previous section, the three brightest transitions $S_0 \longrightarrow S_1$, $S_0 \longrightarrow S_4$ and $S_0 \longrightarrow S_9$ exhibit transition dipoles either longitudinal or transverse relatively to the long axis of the GQD (see Figure 5.12). Satisfyingly, we can see that peak **d** experimentally exhibits a dipole orientation perpendicular to the emission, which is in perfect agreement with the attribution of this peak to the $S_0 \longrightarrow S_4$ transition (which indeed exhibits a transition dipole orthogonal to the $S_0 \longrightarrow S_1$ transition). Moreover, concerning the possible attribution of peak **e** to the $S_0 \longrightarrow S_9$ electronic transition, since the measured transition dipole for this peak is parallel to the dipole for transition $S_0 \longrightarrow S_1$, it thus shares the same orientation as the one predicted for $S_0 \longrightarrow S_9$. We

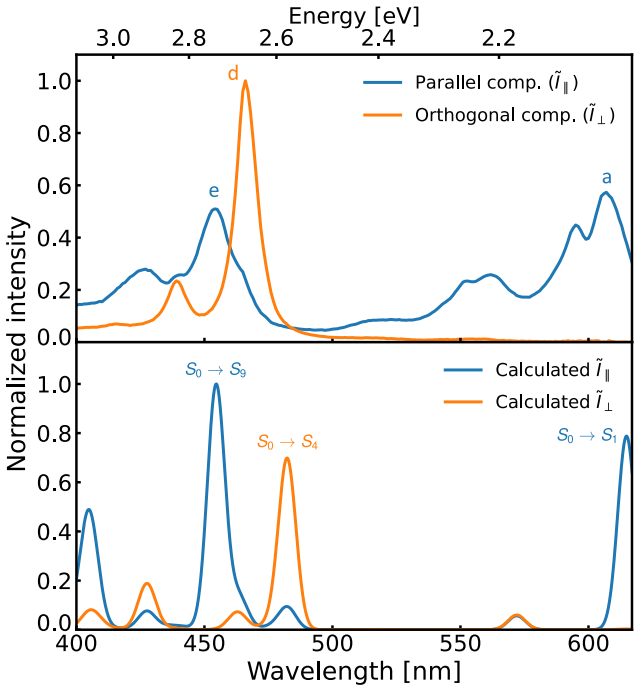

Figure 5.14: (Top) Intensity of the parallel (blue) and perpendicular (orange) components of the PLE. (Bottom) Calculated transitions for dipole polarization along (blue) or perpendicular (orange) to the long-axis of the $C_{96}tBu_8$ GQD.

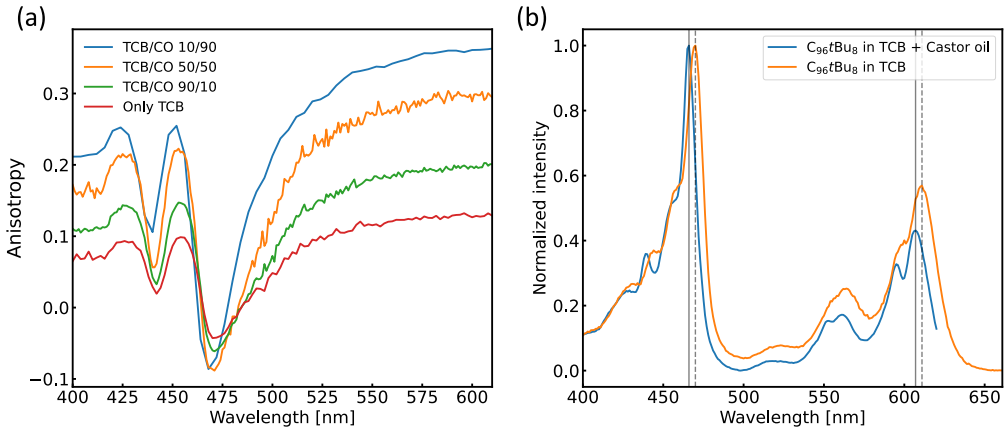

Figure 5.15: (a) Anisotropy PLE spectrum for different concentrations of castor oil (ratios are in wt%). CO stands for castor oil. (b) Comparison of PLE with (in blue, collected at 629 nm, ratio TCB/CO 10/90 wt%) and without (in orange, collected at 678 nm) castor oil.

can furthermore note that since peak **e** does not share the same orientation as peak **d**, it is unlikely that peak **e** corresponds to a vibronic replica associated with the same electronic transition[7].

In Figure 5.15(a), the anisotropy curve collected at 629 nm is given for different concentrations of castor oil added to the solution of $C_{96}tBu_8$ in TCB. As the concentration of castor oil decreases, the amplitude of the curve decreases, *i.e.* the variations of the anisotropy is less pronounced. Consequently, the value reached by the anisotropy for high λ_{exc} deviates from the theoretical 0.4 (in the case where depolarization effects occur on an infinitely-short timescale, we would observe a flat curve at 0). This observation underlines the effect of viscosity for steady-state anisotropy photoluminescence. As the ratio of castor oil diminishes, the viscosity of the solvent decreases along with the rotational diffusion time (*i.e.* correlation between absorption and emission polarizations decreases faster).

Moreover, as the concentration of castor oil increases, we can observe a shift of the anisotropy towards higher energy. This blueshift of the features, evaluated at 25 meV, can also be appreciated when looking at the PLE spectra, in Figure 5.15(b), and is attributed to an effect of the solvent on the energy levels of the $C_{96}tBu_8$ GQD.

In order to avoid adding viscous solvents such as castor oil to prevent depolarization effects during measurement, one can use time-resolved measurements of the anisotropy. An advantage of this method is the possiblity to estimate an absolute value of the anisotropy. However, since we have only one pulsed source at a fixed wavelength of 483 nm, it is only possible to perform a time-resolved anisotropy measurement at one precise

[7] In the framework of the Born-Oppenheimer approximation, the transition dipole should depend solely on the electronic part of the wavefunction, and thus all the vibronic replica of the same electronic transition should share the same transition dipole orientation.

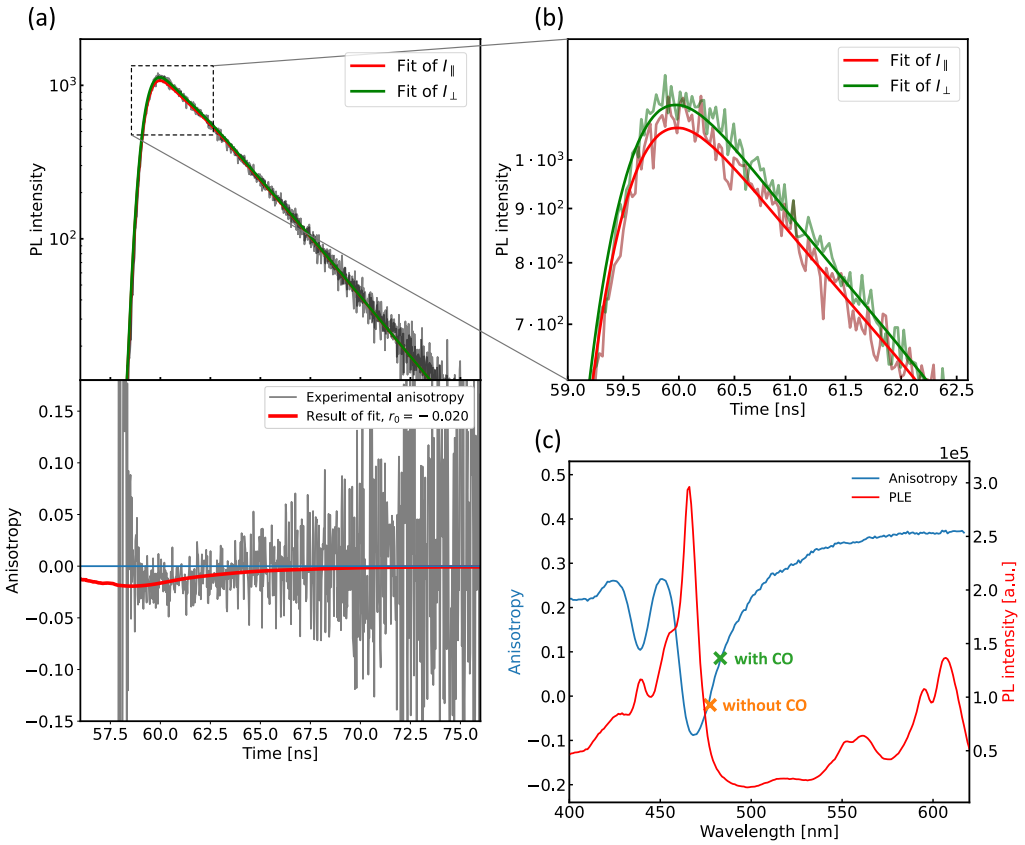

Figure 5.16: (a) Time-resolved photoluminescence (top) and anisotropy (bottom) curves for solution of $C_{96}tBu_8$ in TCB. Excitation at 483 nm, collection at 629 nm. (b) Zoom on the top of the time-resolved intensity curves in figure (a). (c) PLE and anisotropy curve collected at 629 nm (in steady-state, with solution of $C_{96}tBu_8$ in TCB/castor oil). The orange and green crosses indicate the value obtained using time-resolved anisotropy measurements with solution without and with castor oil respectively.

excitation wavelength. Using a solution of $C_{96}tBu_8$ in TCB, we recover the time-resolved photoluminescence (TRPL) curves of $I_{\parallel}$ and $I_{\perp}$ given in Figure 5.16(a). The difference between the two curves is faint, and for clarity, a zoom on the top of the TRPL curves is shown in Figure 5.16(b). The gap between the two curves is due to the anisotropy of the photoluminescence, and the amplitude of the gap decreases with time. The characteristic time of the decrease is related to the rotational diffusion of the GQDs in the solution. If the anisotropy at this wavelength was equal to zero, the two curves would coincide, with no gap between them. Using these two curves, the time-evolution of the anisotropy r can be computed (given in Figure 5.16(a) bottom).

A simultaneous fit of both $I_{\parallel}$ and $I_{\perp}$ can lead to an evaluation of the fundamental anisotropy r_0 (value of r in the absence of rotational diffusion), which can be evaluated as the value of r at zero delay, *i.e.* before any rotational diffusion takes place [218]. Using the definition of the anisotropy r (Eq. 2.5), one can write:

$$I_{\parallel} = \frac{I_{\text{tot}}}{3}(1+2r) \quad \text{and} \quad I_{\perp} = \frac{I_{\text{tot}}}{3}(1-r) \tag{5.3}$$

where I_{tot} corresponds to the total intensity emitted. Considering a monoexponential decay of both the fluorescence and the anisotropy, the time-evolution yields:

$$I_{\parallel}(t) = \frac{I_0 e^{-t/\tau}}{3}(1+2r_0 e^{-t/\tau_{\text{rot}}}) \quad \text{and} \quad I_{\perp}(t) = \frac{I_0 e^{-t/\tau}}{3}(1-r_0 e^{-t/\tau_{\text{rot}}}) \tag{5.4}$$

with τ the fluorescence lifetime and τ_{rot} the rotational correlation time. The curves are fitted using Eq. 5.4 convolved with the instrument response function (IRF), with the fit plotted in Figure 5.16(a). The fit of the anisotropy can then be plotted, which is also performed by taking into account the IRF[8]. The fit yields a value of $r_0 = -0.020 \pm 0.002$, with $\tau_{\text{rot}} = 3.3 \pm 0.3$ ns. τ_{rot} share the same order of magnitude as the fluorescence lifetime of $C_{96}tBu_8$, which explains why the anisotropy spectrum could still be measured even without the addition of castor oil. The value of r_0 can be compared to the anisotropy measured in steady-state in the mixture with castor oil (by taking into account the 25 meV blueshift) and satisfyingly corresponds as it can be seen in Figure 5.16(c) (orange cross). The same measurement can be made for a solution with castor oil, on which the steady-state measurements were performed, and yields a satisfactory value for the anisotropy, as shown by the green cross in Figure 5.16(c), corresponding to the time-resolved measurement. The fact that both measurements using the time-resolved method yield values in line with the steady-state measurement shows that the addition of castor oil effectively prevented any rotational diffusion during the measurement of the anisotropy in steady-state and validates the ensuing interpretations.

5.2.2 Preliminary results of single-molecule experiments

Results in solution showed promising results in terms of homogeneity in the sample. The narrow features of the spectra in solution hint at an absence of aggregation between the GQDs, which is an asset for the manipulation of single $C_{96}tBu_8$ GQDs. In order to test the use of $C_{96}tBu_8$ at the single-object level, single-molecule experiments were performed.

[8] We use the expression $r_{\text{measured}} = \frac{IRF(t)*[r(t)I(t)]}{IRF(t)*I(t)}$, with $I(t)$ the fluorescence intensity decay [219].

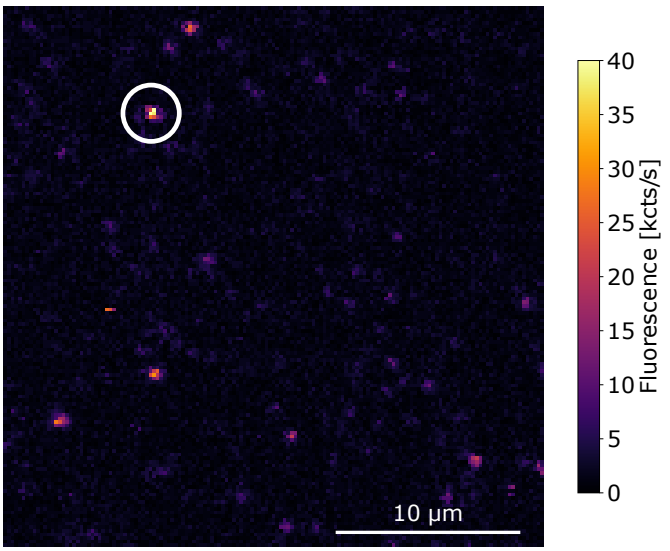

Figure 5.17: Raster scan of a sample of $C_{96}tBu_8$ in PS. Excitation at 594 nm, 130 W/cm^2.

Spatial map description

The maps observed with the micro-photoluminescence setup are similar to the ones measured for $C_{96}C_{12}$ samples, as it can be seen in Figure 5.17. The samples are composed of $C_{96}tBu_8$ embedded in a polystyrene matrix, as described in Section 5.1.3 excited using the 594 nm laser, with excitation power of 130 W/cm^2. It is possible to observe diffraction-limited spots, as circled in Figure 5.17, which correspond to single $C_{96}tBu_8$ GQDs embedded in the polystyrene layer. The concentration of the solution used here is selected in order to maximize the number of single $C_{96}tBu_8$ GQDs observed in maps.

Samples were prepared using solutions of different concentrations in $C_{96}tBu_8$ GQDs. As shown in Figure 5.18, we can appreciate the decrease of the density of bright spots along with the concentration of the solution used. This observation demonstrates that the bright spots observed effectively correspond to $C_{96}tBu_8$ GQDs added in the matrix. With an excitation power of 130 W/cm^2, we collect a signal from $C_{96}tBu_8$ GQDs of around 20 kcts/s, which is around same order of magnitude as for $C_{96}C_{12}$ GQDs on the same setup. It is thus possible to use the same selection criterion as for $C_{96}C_{12}$ GQDs based on the intensity of the spots in order to select only the spots corresponding to $C_{96}tBu_8$ GQDs. Indeed, using the intensity threshold selection, no bright spots can be observed on samples with only polystyrene (no GQDs embedded).

Single-object spectroscopy at room temperature

On each single diffraction-limited spot, spectra were measured, with an example given in Figure 5.19(a). The spectrum shows the same lines as the spectrum in solution, with a first main electronic transition at 618 nm (labelled **1**), and two vibronic replicas at 676 nm and 743 nm (labelled **2** and **3** respectively). The linewidth of the first peak can be estimated using a Lorentzian fit, yielding a full width at half-maximum of 24.0 ± 0.1 nm. If we compare with the spectrum in solution, as given in Figure 5.19(b), we can see that the

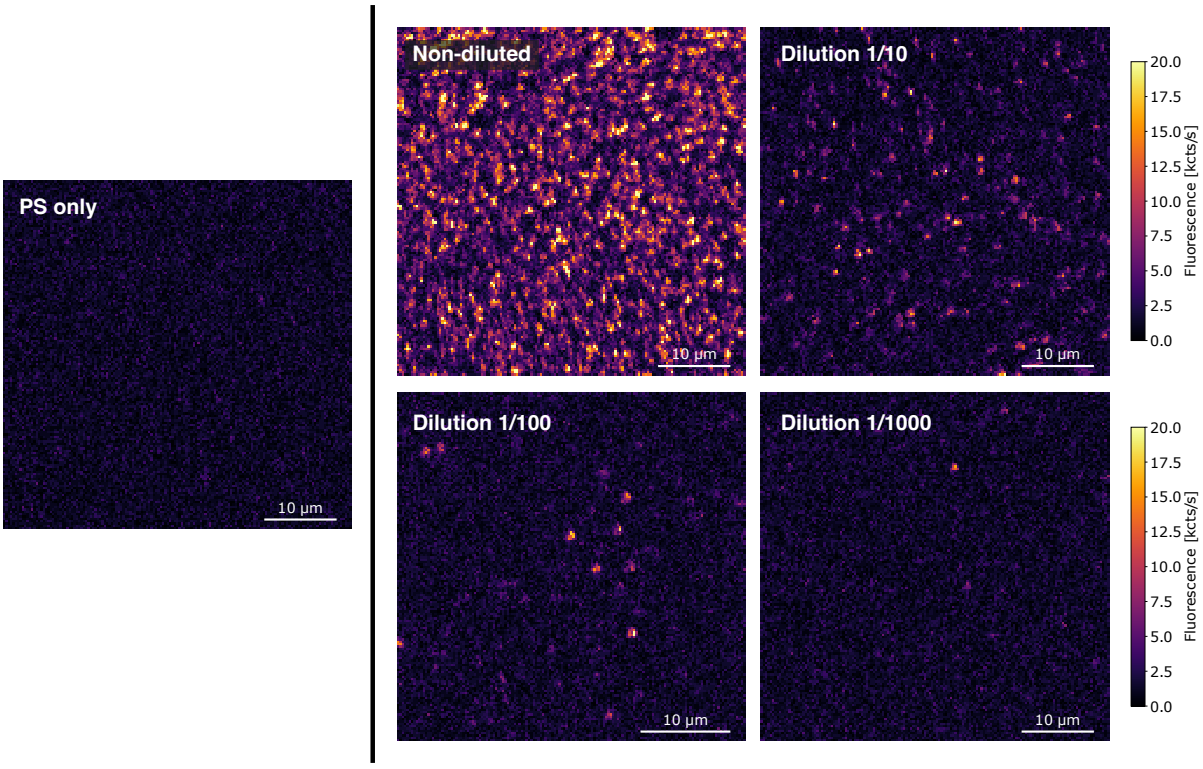

Figure 5.18: Effect of the concentration of $C_{96}tBu_8$ of solutions used for sample preparation. Excitation at 594 nm, 130 W/cm^2.

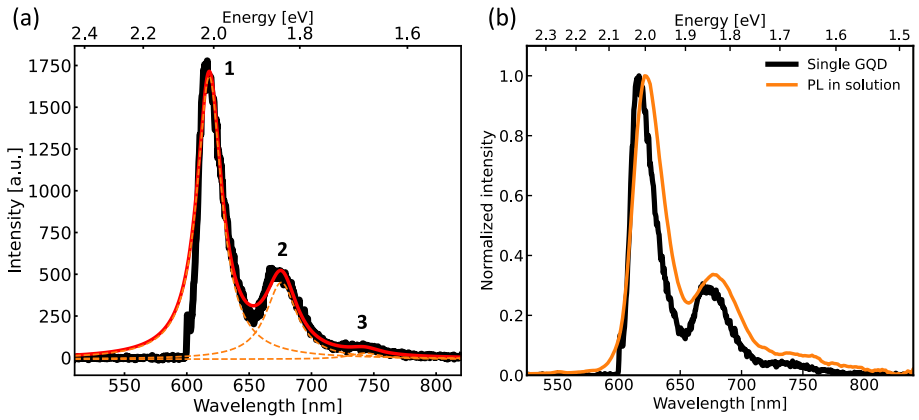

Figure 5.19: (a) Example of a spectrum of a single $C_{96}tBu_8$ GQD (excited at 594 nm). The fit using three Lorentzians (each given in dashed orange) is plotted in the red curve. (b) Comparison with the PL spectrum in solution. For all plots, the orange curve corresponds to a Gaussian fit of the distribution.

position of the lines is slightly blueshifted relatively to the PL lines in solution, which results presumably from energy shifts due to a change of the environment between TCB and PS. Nonetheless, the width of the lines is satisfyingly identical between the single GQD and the PL in solution. This is in line with the observed homogeneity in solution, and is consistent with the theoretical calculations. As mentioned in Section 5.2.1, the broadening of the PL lines in solution is fully accounted for by the thermal population of the vibrational modes of the GQD.

By performing systematic spectral measurements on the spots observed, we recover the distribution in wavelength λ_1 of the peak **1**. As shown in Figure 5.20(a), the distribution is narrow, centered at 619 nm with a standard deviation of around 3.75 ± 0.06 nm, significantly narrower than the distribution observed for $C_{96}C_{12}$ GQDs at room temperature (which was around 10.2 nm if we looked only at spectra above 640 nm). This narrow distribution is a clear consequence of the homogeneity of $C_{96}tBu_8$ GQDs present in the sample, and the absence of by-products in the solution (aggregates, synthesis by-products). Another consequence of the homogeneity is the narrow distribution of the full width at half maximum (FWHM) of the peak **1**, as shown in Figure 5.20(c), centered around 27.5 nm, with a standard deviation of 1.9 nm, which is much lower than observed for $C_{96}C_{12}$ at 4.4 nm. Moreover, we do not observe any peaks from impurities, indicating that the selection criterion is effective.

To be more precise, the absence of impurities in the distribution is indicated by the high concentration of bright spots corresponding to $C_{96}tBu_8$ GQDs in the samples. If we plot the distribution of wavelength for different concentrations of $C_{96}tBu_8$ (*i.e.* concentration in the solution used for sample preparation), we observe that as the concentration of $C_{96}tBu_8$ decreases, and thus the density of $C_{96}tBu_8$ spots in the samples, the distribution broadens, as shown in Figure 5.20(b). There is no significant difference between the samples *Dilution 1/1* and *Dilution 1/10*, with standard deviations of 2.4 and 2.5 nm

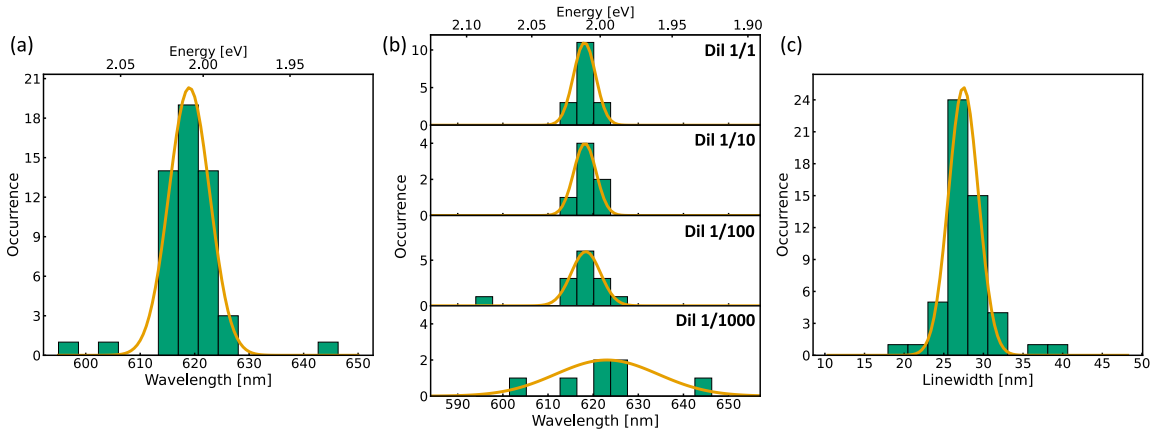

Figure 5.20: (a) Distribution of wavelength λ_1 of peak **1** (53 spectra). (b) Comparison of the distribution of λ_1 for different concentrations of $C_{96}tBu_8$. (c) Distribution of the FWHM of peak **1**.

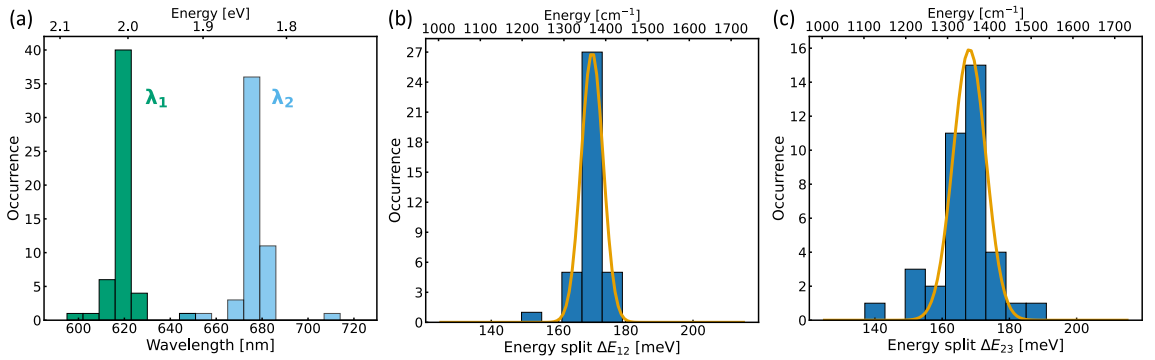

Figure 5.21: (a) Distribution of both λ_1 and λ_2. (b) Distribution of energy split ΔE_{12} between peaks **1** and **2** (38 spectra). (c) Distribution of energy split ΔE_{23} between peaks **2** and **3**. For all plots, the orange curve corresponds to a Gaussian fit of the distribution.

respectively. As we move to higher dilutions, the broadening of the distribution is more significant, with a standard deviation of 6.3 nm for *Dilution 1/100* and 11.4 nm for *Dilution 1/1000*. The broadening accounts for the presence of impurities in the sample, as described in Chapter 3, which become more noticeable as the density of $C_{96}tBu_8$ spots decreases.

If we now consider peak **2** of the single GQD spectra, the distribution of their position share the same dispersion as for peak **1** as illustrated in Figure 5.21(a) where both distributions are plotted. The narrow distribution of the position of both peaks leads to a narrow distribution of the energy split ΔE_{12} between peaks **1** and **2**[9]. As shown in Figure 5.21(b), the distribution is centered at 170 meV with standard deviation of 3.27 ±

[9]The number of spectra used for the distribution of the energy splits is slightly lower than for the distribution of λ_1, since only spectra where the position of peak **3** could be estimated were used.

0.01 meV. The distribution of ΔE_{23}, the energy split between peaks **2** and **3**, is on the other hand broader, centered at 168.1 ± 0.2 meV with standard deviation of 4.9 ± 0.2meV. The broader distribution observed for ΔE_{23} results mainly from the difficulty to pinpoint precisely the position of peak **3** due to the weak intensity of the peak. The value obtained for both energy splits is consistent with the vibrational mode associated with C=C bond stretching in aromatic compounds, as observed for the PL spectrum of the GQD in solution.

Single-object experiments show promising results for the use of $C_{96}tBu_8$ GQDs as single emitters. The homogeneity of the properties of the GQD, and its low tendency to produce aggregates represent essential features to that end.

5.3 Exploring different sizes: comparison with $C_{78}tBu_6$ and $C_{114}tBu_{10}$ GQDs

As shown in the previous section, comparing $C_{96}tBu_8$ GQDs and $C_{96}C_{12}$ GQDs showed that, in addition to the higher solubility and lower stacking-tendency of the $C_{96}tBu_8$ GQD, the electronic energy levels of $C_{96}tBu_8$ differ from the levels of $C_{96}C_{12}$ due to the change of symmetry between the two objects, which nonetheless share the same number of delocalized π-electrons in their aromatic core. We now focus in this section on GQDs sharing the same symmetry as $C_{96}tBu_8$, but with different core sizes (see Figure 5.22), and thus presenting a different number of delocalized π-electrons. By comparing the experimental results with the observations made for $C_{96}tBu_8$, it is possible to study the effect of size on the electronic properties of the GQD.

5.3.1 Comparing the energy levels

The study performed in solution on the $C_{96}tBu_8$ GQD has been reproduced for the $C_{78}tBu_6$ and $C_{114}tBu_{10}$ GQDs. The absorption spectra of the three GQDs are plotted in Figure 5.24(a). The first striking observation is that as the size of the GQD decreases, the absorption

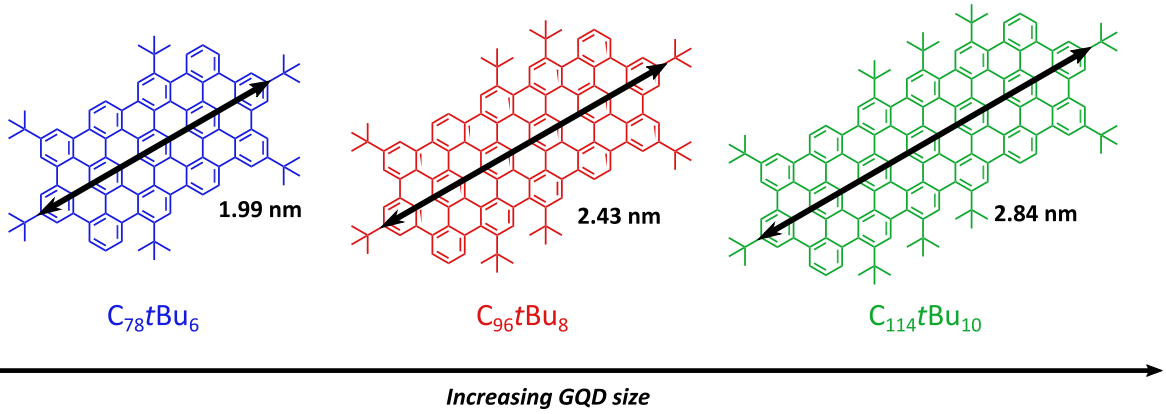

Figure 5.22: Comparison of the size of rod-shaped GQDs.

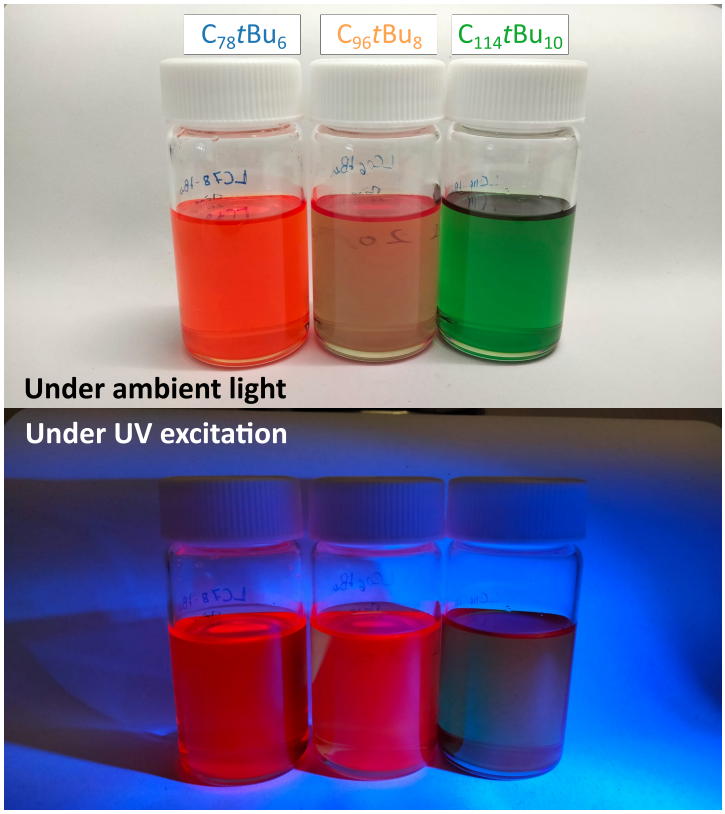

Figure 5.23: Stock solutions of $C_{78}tBu_6$, $C_{96}tBu_8$ and $C_{114}tBu_{10}$ GQD under ambient light (top) or UV light (365 nm) (bottom).

spectrum is blueshifted, resulting from a lower delocalization of the π electrons or, similarly, a stronger confinement of the electronic wavefunction. The wavelength of the lowest transition (peak **a**) is at 558 nm for $C_{78}tBu_6$, 612 nm for $C_{96}tBu_8$ and 654 nm for $C_{114}tBu_{10}$. This sensitivity to the GQD size proves that the electonic distribution remains fully delocalized on the whole GQD (as it will be shown in Figure 5.27(b)). The three spectra share a similar structure with sharp features, with a first series of peaks at lower energy (which we associated with the p-band), followed by more intense peaks at higher energy (the β-bands). Although we do not observe the same sharp transitions which we labelled **a'** and **b'** for $C_{96}tBu_8$ (attributed to stable conformers of the $C_{96}tBu_8$ GQD) in the absorption spectra of $C_{78}tBu_6$ and $C_{114}tBu_{10}$, all the other peaks can be identified (they are recalled in Table 5.3). If we look at the PL spectra, given in Figure 5.24(b), the same blueshift can be observed as the size of the GQD decreases, with a main peak at 569 nm for $C_{78}tBu_6$, 622 nm of $C_{96}tBu_8$ and 668 nm for $C_{114}tBu_{10}$. The linewidth is comparable for all three GQDs. Being able to tune the transition energy over a range of 100 nm represents a great asset for the use of GQD for various applications such as optoelectronics.

The time-resolved photoluminescence curves collected at the main emission peak for each GQD are given in Figure 5.24(c). $C_{114}tBu_{10}$ exhibits a mono-exponential decay with a lifetime of 2.3 ns, $C_{96}tBu_8$, as stated earlier in the chapter, also exhibits a mono-exponential decay with a lifetime of 2.8 ns, and $C_{78}tBu_6$ has a slightly more complex be-

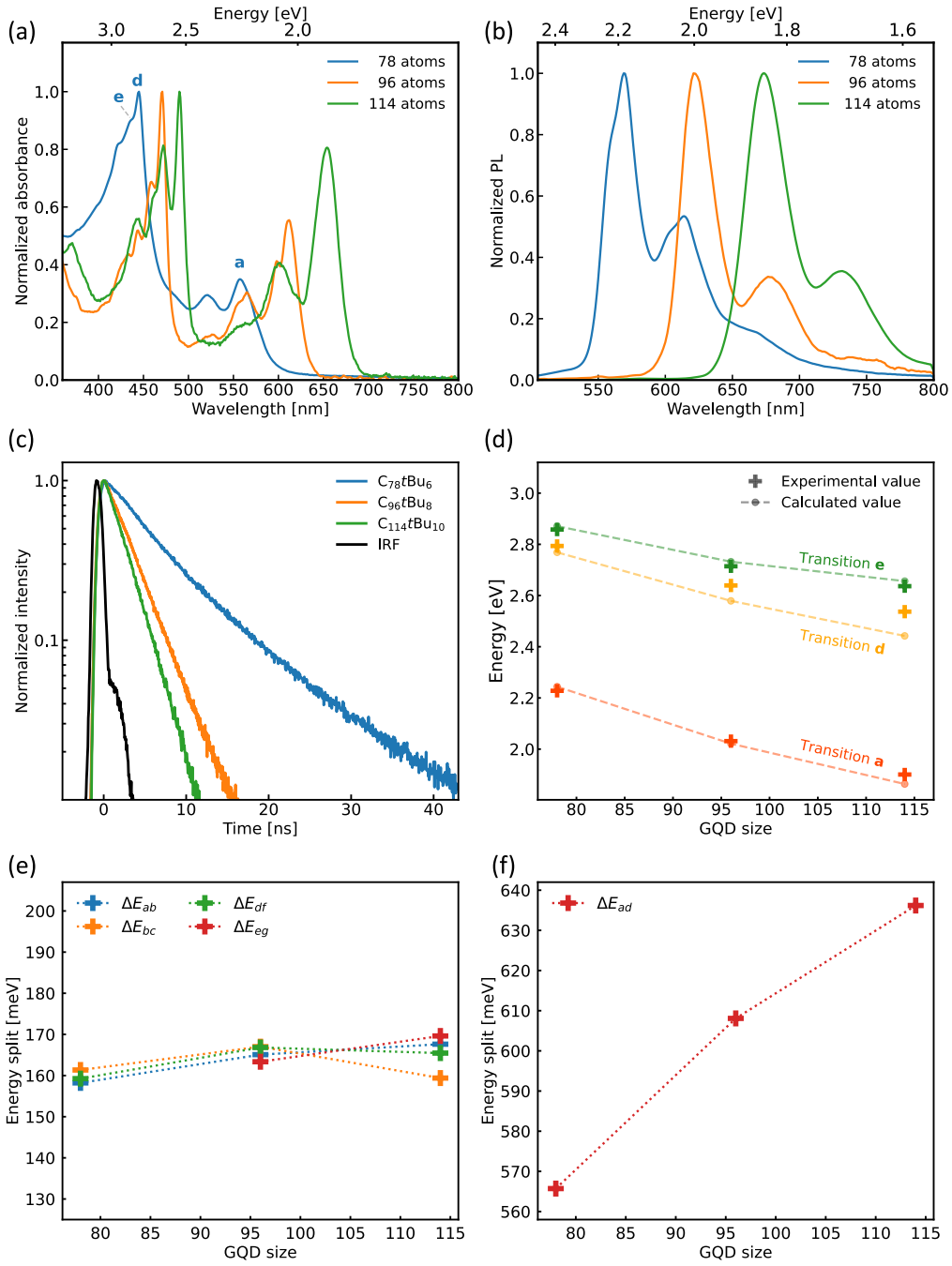

Figure 5.24: (a) Absorption and (b) PL spectra for all three rod-shaped GQDs in TCB. (c) Time-resolved decay curves collected at the emission peak for each GQD. (d) Comparison of the transition energy measured experimentally with the calculated energy of the bright transitions. (e) Energy split between peaks (following the labelling used for $C_{96}tBu_8$) suspected to be vibronic replicas. (f) Evolution the energy split between p- and β-bands.

Peak	Nature of transition	State for $C_{78}tBu_6$	State for $C_{96}tBu_8$	State for $C_{114}tBu_{10}$	Band attribution
a	**Electronic trans.**	S_1	S_1	S_1	
a'	Conformer*				
b	Vibronic replica				p-band
b'	Vibronic replica*				
c	Vibronic replica				
d	**Electronic trans.**	S_4	S_4	S_5	β_1-band
e	**Electronic trans.**	S_6	S_9	S_{10}	β_2-band
f	Vibronic replica				β_1-band
g	Vibronic replica				β_2-band

Table 5.3: Absorption peak attribution for the three rod-shaped GQDs (in order of increasing energy) and associated singlet state number calculated using DFT. Electronic trans.: purely-electronic transitions. Starred transitions are observed only for the $C_{96}tBu_8$ GQD.

havior, but we can estimate the fluorescence lifetime to 4.3 ns (more details are given in the next section). Thus as the size of the GQD increases, the fluorescence lifetime decreases. A possible explanation is the higher density of non-radiative decay channels for larger GQDs[10].

The recovery of the same peaks observed for $C_{96}tBu_8$ directly results from the shared D_{2h} symmetry of the GQDs. Theoretical calculations, using computational methods similar to the ones used for $C_{96}tBu_8$, yield the same structure of electronic levels. In particular, the lowest excited singlet state always corresponds to a bright HOMO to LUMO transition, *i.e.* to the p-band of the spectrum. The two next bright transitions are the splitted β-bands, which correspond to transitions to higher singlet states (to S_4 and S_6 for $C_{78}tBu_6$, to S_4 and S_9 for $C_{96}tBu_8$, and to S_5 and S_{10} for $C_{114}tBu_{10}$ [11]). As shown in Figure 5.24(d), the position of peaks **a**, **d** and **e** of the absorption spectra match perfectly the predicted bright transitions mentioned. This satisfying agreement between experiment and theory is also a testimony of the facility of the dispersion of the rod-shaped GQDs: we can easily have access to the intrinsic properties of the objects, even in solution.

Since the electronic transitions are satisfyingly recovered, we can focus on the other peaks. In the section concerning $C_{96}tBu_8$, we attributed peaks **b** and **c** to vibronic replicas of peak **a**, peak **f** to a replica of peak **d** and peak **g** to a replica of peak **e**. If we plot the energy split between the mentioned transitions, they all share the same value around 160 – 167 meV, characteristic of aromatic compounds, as shown in Figure 5.24(e). This pleasing observation confirms the attribution of these peaks to vibronic replicas, as it was hypothesized in the study of $C_{96}tBu_8$.

[10] One could test this possiblity by comparing the measured fluorescence lifetime to the value of the extinction coefficient for each GQD using the Strickler-Berg equation.

[11] The different numbering of the singlet states corresponding to the β-bands for the three GQD sizes results from the existence of various dark singlet states. Their number and relative position to the bright singlet states varies from one GQD size to another.

Finally, we can note that the energy split between peaks **a** and **d**, or in other words the split between the p- and β_1-band, increases with the size of the GQD (see Figure 5.24(f)). We can easily understand this behavior considering that, as we lower the symmetry from D_{3h} to D_{2h}, the degeneracy of the HOMO and HOMO-1, and of the LUMO and LUMO+1 is lifted, and as we increase the length of the GQD, we move further away from the D_{3h} case, and we thus accentuate the energy split between the frontier molecular orbitals. As a result, the energy split between the different bright transitions increases with size. This behavior is in opposition to the energy split between vibronic replicas, as mentioned in the previous paragraph, which does not vary with the size of the GQD.

Given the shared symmetry for all three rod-shaped GQDs, we observe the same general structure of the electronic transitions accross the different GQDs, as summarized in Table 5.3. Changing the size while keeping the geometry plays essentially a role on the position of the electronic transitions. The frequency of the vibronic replicas are on the other hand not affected by the change of size.

5.3.2 Comparing the solubility: focus on the $C_{78}tBu_6$ GQD

I would like here to focus on the $C_{78}tBu_6$ GQD, which presents slightly different results than for $C_{96}tBu_8$ and $C_{114}tBu_{10}$ GQDs. As mentioned in the previous section, there is no reason which would lead to differences in the structure of the electronic energy levels between the three rod-shaped GQDs (since it is dominated mainly by the D_{2h} symmetry of the core). The differences must then result not from the electronic of the graphenoid core, but from other factors, for instance the side-chains used.

When looking at the absorption spectrum presented in Figure 5.25(a), we can clearly see that, although the various peaks observed in other rod-shaped GQDs are recovered, the lines are broader. As mentioned in Section 5.1.2, the presence of dimers has been observed in the MALDI-TOF mass spectra. The presence of small aggregates could explain the broadening of the absorption spectrum. The fact that such broadening is observed only for $C_{78}tBu_6$ and not for the other rod-shaped GQDs may result from the absence of distortions due to steric effects of the *tert*-butyl groups. As mentioned in the discussion concerning $C_{96}tBu_8$, the four *tert*-butyl groups at the center of the GQD caused a distortion of the aromatic core due to their adjacency to each other. If we look back at Figure 5.22, we can see that there are no neighboring *tert*-butyl groups for $C_{78}tBu_6$, leading to a weaker distortion of the aromatic core[12].

If we now look at the PL spectrum in Figure 5.25(a), when excited at 450 nm, we can see that we recover the same three peaks as observed for the other GQDs but in the case of the $C_{78}tBu_6$ GQD, the two first peaks[13] show a splitting of around 35 meV (between 560 and 569 nm, and between 604 and 614 nm). The origin of the splitting is not yet clear. We could expect, similarly to the $C_{96}tBu_8$ GQD, that these would result from the

[12]Moreover, the *tert*-butyl groups will also have a lower tendency to be out-of-plane relatively to the aromatic core, thus possibly enhancing the possibility of two neighboring $C_{78}tBu_6$ GQDs to interact and form dimers.

[13]The intensity of the third peak, at around 662 nm, is too low to resolve a splitting.

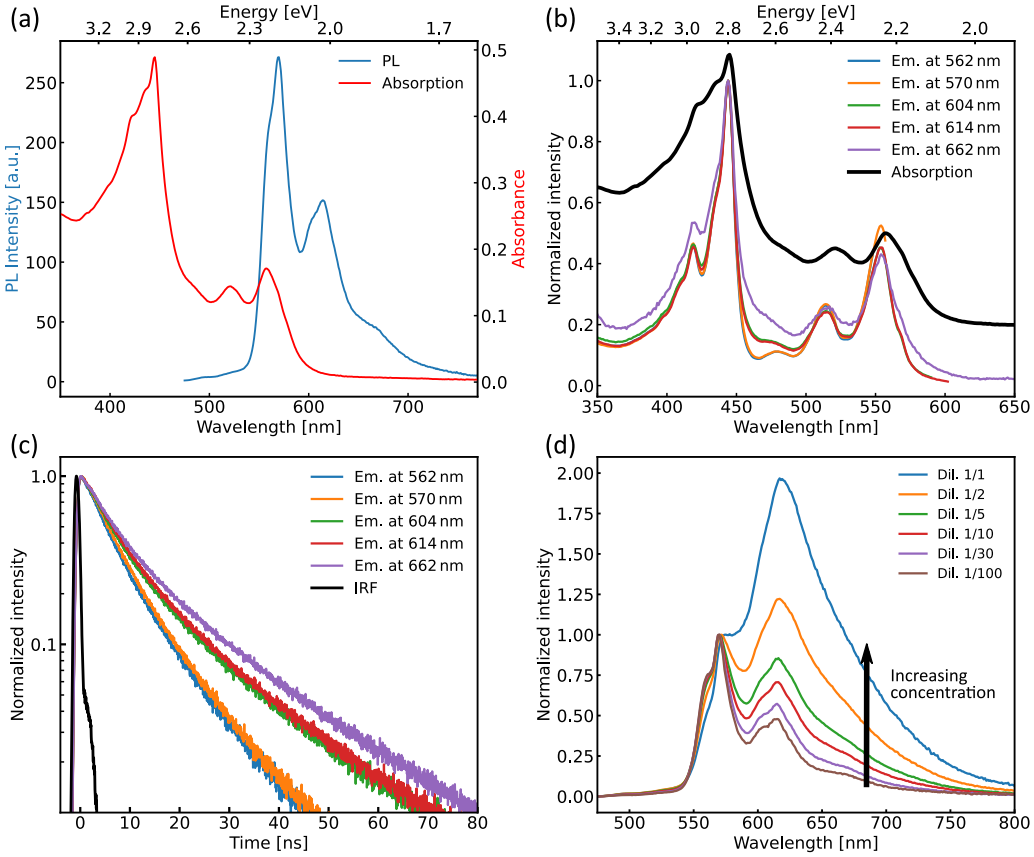

Figure 5.25: (a) PL (excited at 450 nm) and absorption spectrum of $C_{78}tBu_6$ in TCB. (b) PLE spectra collected at the emission peaks of $C_{78}tBu_6$. The absorption spectrum is plotted for comparison. (c) Time-resolved PL curves collected at the emission peaks of $C_{78}tBu_6$. (d) Concentration dependence of the PL spectrum of $C_{78}tBu_6$.

simultaneous presence of different stable conformers of $C_{78}tBu_6$ GQD. However, given the absence of significant steric effects, we would not expect a significant energy splitting due to conformers.

In order to get more insight, PLE spectra are collected at the wavelength position of the various peaks, and plotted in Figure 5.25(b) alongside the absorption spectrum. The different PLE spectra are identical for the different collection wavelengths, indicating that all the lines presumably result from the same absorption transitions (and non-radiative relaxation). If the splitting of the peaks in the PL spectrum resulted from the presence of different emitting species, we would have expected different PLE spectra when collected at the emission wavelengths of the emitting species. Moreover, the position of the peaks in the absorption spectrum are recovered in the PLE spectra, indicating that these transitions indeed correspond to the $C_{78}tBu_6$ GQD. Moreover, if we look at the time-resolved PL decay collected at the same wavelengths, as plotted in Figure 5.25(c), we can see that the curves associated with the same pair of splitted peaks share the same decay dynamics, indicating that the decay yielding both peaks result from the same relaxation

channels, which is not consistent with an attribution of the splitting to the presence of different emissive species. The origin of the splitting must therefore be intrinsic to the $C_{78}tBu_6$ (and not from the formation of different emissive species such as aggregates). Further studies on the subject may be necessary to fully understand it. On the other hand, the decay dynamics differ for each pair of peaks in the PL spectrum, yielding three different decay dynamics as shown in Figure 5.25(c), which is in strong contrast to the observation for $C_{96}tBu_8$ and $C_{114}tBu_{10}$, for which all the various decay curves shared the same dynamics. This observation can be explained if we now consider the effect of concentration on the PL spectrum.

We performed concentration-dependent experiments, as shown in Figure 5.25(d). In this figure, we can appreciate the appearance of a broad structureless band centered around 614 nm in the PL spectrum as the concentration of $C_{78}tBu_6$ increases. This behavior is typical to the formation of excimers, particularly given the identical PLE spectra measured accross the PL spectrum. Excimers (abbreviation for *excited-state dimer*) are species resulting from the interaction between a fluorophore in its excited state and another in its ground state. The formation of excimers occurs after the excitation of a fluorophore, which means that excimers share the same absorption spectrum as the monomer (and thus share similar PLE spectra if the non-radiative decay channels are comparable).

By independently fitting the three decays shown in Figure 5.25(c) using bi-exponential dynamics, we recover for all three the same two lifetimes: one component with a short lifetime at 4.3 ns, and a second component with a longer lifetime at around 12 – 16 ns. As the collection wavelength increases, the ratio between short and long-lifetime components evolves in favor of an increase of the long-lifetime component. Interestingly, this analysis is consistent with the formation of excimers. It has been observed in various systems that the fluorescence lifetime of the excimer is longer than for the monomer [220, 221]. We therefore attribute the short lifetime to the exponential decay of the $C_{78}tBu_6$ GQD (monomer) while the long lifetime to the emission of the excimer. The relative increase of the long-lifetime component in the decay curves as we look to the red side of the PL spectrum therefore illustrates the increased contribution of the emission of excimers in the PL spectrum.

Focusing on the study of $C_{78}tBu_6$ shows that, although the electronic properties of the GQD is dominated by the π-electrons of the graphenoid core, side-groups may play an essential role in the observation of the electronic transitions. In the case of rod-shaped GQDs, while one would expect larger PAHs to be more prone to aggregation, only the $C_{78}tBu_6$ exhibited a signature associated with intermolecular interaction yielding excimer emission, possibly due to the absence of strong steric hindrance between GQDs.

5.3.3 Comparing the transition dipole moments

We have seen that the position of the electronic transitions calculated theoretically are satisfyingly reproduced experimentally. If we now focus on the transition dipole moment of the different transitions, we can investigate the influence of the GQD size on

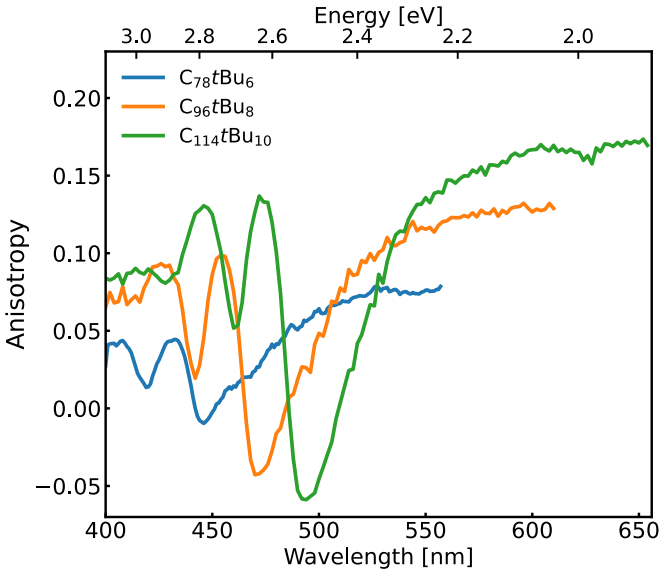

Figure 5.26: PLE anisotropy spectra collected for solutions of GQDs in TCB at 570 nm ($C_{78}tBu_6$ GQD), 622 nm ($C_{96}tBu_8$, GQD) and 674 nm ($C_{114}tBu_{10}$ GQD).

their orientation and amplitude. Performing PLE anisotropy measurements, similarly to solutions of $C_{96}tBu_8$ GQDs, the relative orientation of the transition dipole moments can be probed. In Figure 5.26, the anisotropy curves collected at the main emission peak for each GQD in TCB are plotted. All three anisotropy curves share the same profile, with a relatively flat curve for the p-band, and oscillations over the β-bands (as detailed in the section focusing on $C_{96}tBu_8$ GQDs). The blueshift of the curve for smaller GQDs is a direct consequence of the shift of the transitions with GQD size. The amplitude of the variation of the anisotropy curve decreases for smaller GQDs, which stems from (1) increased depolarization effects due to rotational diffusion as the size of the fluorescent object decreases and (2) an increase of the fluorescence lifetime for smaller GQDs (and thus an increased disposition to correlation loss between absorption and emission polarizations). Since castor oil was not used for these measurements[14], the effect of rotational diffusion is not negligible. However, the measurement proves that the theoretical predictions are respected, and that the polarization of transition dipoles is reproducible for the different sizes of rod-shaped GQD, with the p-band polarized along the long axis of the GQD, the β_1-band polarized perpendicularly to the long axis and the β_2-band mainly along the long axis.

If we now come back to Figure 5.24(a), we can appreciate an increase of the intensity of peak **a** as the size of the GQD increases, indicating an increase of the oscillator strength of the transition. Such behavior could also be observed for other graphenoid systems we studied, such as fjord-edge GNRs [40]. In Figure 5.27(a), I compare the ratio between

[14]As shown in the chapter on experimental methods, the PL spectrum of castor oil prevents its use for the measurement of anisotropy for $C_{78}tBu_6$ and $C_{114}tBu_{10}$ GQDs.

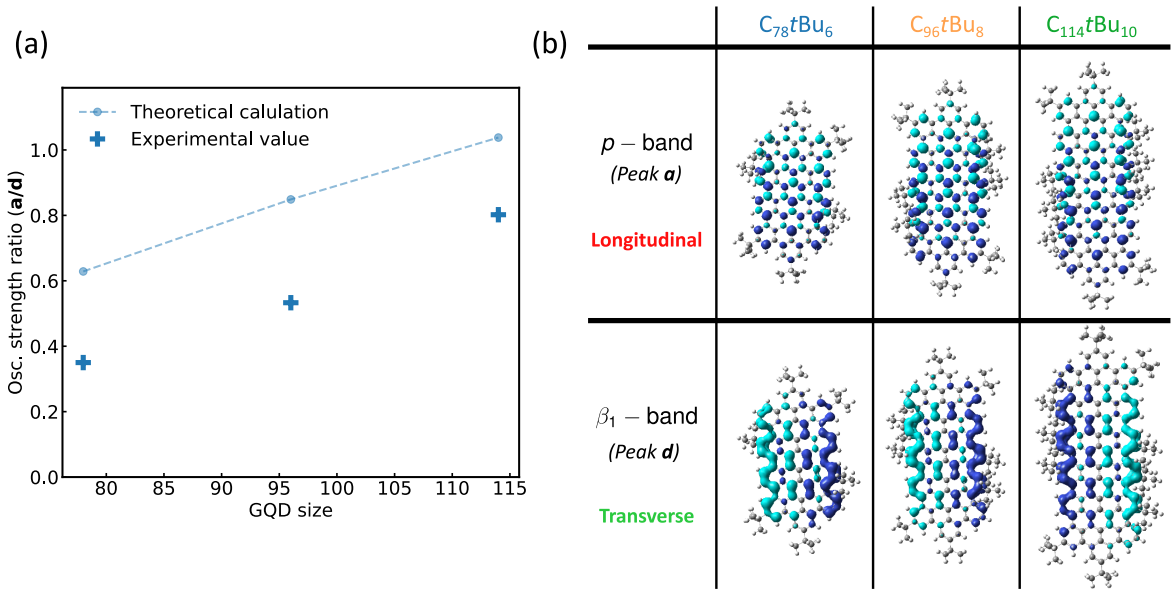

Figure 5.27: (a) Evolution of the oscillator strength ratio between transition **a** (p-band) and transition **d** (β_1-band) with GQD size. (b) Transition electronic densities for p- and β_1-bands for all three sizes.

the intensity of peak **a** and peak **d** with the ratio of the theoretical oscillator strength of these two transitions. The general dependence with size is well respected, we would need a more precise estimation of the experimental oscillator strength if we want to quantitatively compare with theory.

In order to explain this increase in oscillator strength, we can look at the calculated charge density distribution associated with the two transitions, represented in Figure 5.27(b). Concerning the p-band, since the electronic density extends along the long axis of the GQD (longitudinal orientation of the dipole moment), and the transition dipole moment evolves proportionally with the spatial extension of the dipolar distribution, it will be sensitive to an increase of the length of the GQD. Indeed, as it can be seen in the representation given in Figure 5.27(b), the electronic charge density is distributed along the longitudinal direction of the GQDs. The transition dipole moment of the p-band will therefore increase with the length of the GQD, thus validating the increase of the oscillator strength with the GQD size. On the other hand, concerning the transverse-polarized transitions, such as the β_1-band, we can see that it will not be strongly affected by an elongation of the GQD, since the extension of the dipolar moment, which is transverse to the long-axis of the GQD, is limited to the width of the GQD, which is kept the same for the different GQDs studied.

Conclusion

The synthesis of rod-shaped GQDs enabled us to move a step closer to linking the structure of the GQD to its optical properties. In particular, the high solubility of these GQDs enabled us to easily gain access to the intrinsic properties of the GQDs without the difficulty met during the study of $C_{96}C_{12}$ due to the presence of other objects in the sample, in particular aggregates.

By focusing on the $C_{96}tBu_8$ GQD, we managed to describe and attribute the spectral measurements to the various electronic transitions of the GQD. Indeed, theoretical calculations are perfectly reproduced by the experimental measurements. In particular, changing from the D_{3h} symmetry for $C_{96}C_{12}$ to D_{2h} for $C_{96}tBu_8$ resulted in a splitting of the β-bands and an inversion between α- and p-bands, leading to a bright lowest excited singlet state. Moreover, the addition of *tert*-butyl side-chains proved to be efficient in preventing stacking between $C_{96}tBu_8$ GQDs, which leads to an effective observation and manipulation of GQDs at the single-object level, with an homogeneous distribution of optical properties.

By changing the size of the GQD, we verified that the optical properties are satisfyingly protected by the D_{2h} symmetry of the rod-shaped GQDs. The effect of size is seen in the absolute energy of the transitions, which shifts over a range of 100 nm, as a result of the modification of the number of delocalized π electrons, but also in the transition dipole moments, which are sensitive to the spatial extension of the electronic wavefunction on the GQD. Counter-intuitively, the smaller $C_{78}tBu_6$ GQD exhibited signs of excimer formation, while both $C_{96}tBu_8$ and $C_{114}tBu_{10}$ are efficiently dispersed, which can be explained by the lack of efficient steric effects on the smaller GQD, highlighting the importance of these considerations when selecting side-chains.

A large part of the results discussed in this chapter are summarized in an article in preparation at the time of the elaboration of this manuscript [142].

In order to fully characterize and explore the potential of $C_{96}tBu_8$ GQDs, single-molecule measurements at low temperature represent the next experimental objective, in order to explore the line-narrowing of spectral features and evaluate the spectral purity of the ZPL emission of this GQD and the electron-phonon coupling.

Another investigation route could be to continue playing on the structure of the GQD. New GQDs sharing the same geometry as the one presented in this chapter, but with additional *tert*-butyl groups in the periphery of the GQD are underway. As demonstrated when comparing the tendency to aggregate of $C_{96}tBu_8$ compared to $C_{96}C_{12}$, the side-chains represent an essential tool to increase the solubility of the GQD. This would be in particular interesting for the $C_{78}tBu_6$ GQD, which could benefit from extra *tert*-butyl side-chains to inhibit the formation of dimers or excimers.

Finally, the peak we associated with the possible presence of stable conformers of the $C_{96}tBu_8$ GQD remains to be confirmed. Indeed, we have not been able to find any signature in the PL spectra denoting the presence of these conformers given the observed homogeneity in solution. Further studies concerning this issue, along with additional discussions with theoreticians, may be interesting in order to safely conclude on the

attribution of this peak.

General conclusion

Graphene quantum dots are promising objects for a large range of applications, from bio-imaging to quantum technologies. The high tunability of their properties resulting from the precise control of their geometry using bottom-up synthesis lets us contemplate the possibility to perform reverse-engineering, which would allow us to shape the GQD according to the needed property. However, this requires a precise understanding of the dependence between geometry and electronic properties. Studies focusing on the intrinsic properties of these objects remained scarce in the literature, and have thus motivated the work reported in this thesis. To that extent, I have focused on the study of various GQDs with the objective to fully understand the spectroscopic results obtained experimentally. This thorough characterization required also a precise study of all the other fluorescent objects which may contaminate the observations and prevent the correct manipulation of GQDs, in particular at the single-object level.

Investigating the origin of impurities is a fundamental study to perform before studying GQDs at the single-object level. Indeed, as demonstrated by the number of research articles concerning the characterization of impurities observed in samples using single-molecule methods, the issue of sample contamination has not yet been resolved and the clear origin of the contamination remains to be determined. Moreover, understanding the source of these fluorescent contaminants and being able to unambiguously identify them is crucial for the processability of GQDs. During my thesis, I have been able to characterize at both room and low temperature the impurities found in polystyrene, prepared in 1,2,4-trichlorobenzene, deposited on glass substrates and to link their origin to a joint contribution of activated surface defects of the glass substrate and contaminants in the organic solvent. Studying different preparation methods showed that increasing the thickness of the polymer layer decreased the collected signal from the fluorescent impurities, which proved to efficiently reduce their influence on measurements by using a criterion to select objects of interests based on an intensity threshold. This preliminary work allowed us to confidently move on to the study of GQDs at the single object level.

The single-molecule characterization of the triangular $C_{96}C_{12}$ GQD performed before my arrival in the group had already proven the high potential of GQDs for quantum applications needing stable and bright emitters. By continuing this work during my thesis, we managed to fully understand observations in photoluminescence experiments. In particular, the study performed on this GQD in solution revealed the presence of various fluorescent objects in the samples. The emission spectra in solution showed spectral features expected for the $C_{96}C_{12}$ GQDs, along with higher-energy emission features resulting,

to some extent, from the formation of aggregates. This investigation was the occasion to confront the experimental observations with theoretical calculations, which led to a thorough identification of the emission lines of GQDs. Interestingly, the bright emission of the $C_{96}C_{12}$ GQD can be explained by taking into consideration the deformation of the aromatic core through vibration of the system, thus breaking the D_{3h} symmetry of the GQD, which otherwise forbids emission from the lowest-lying excited singlet states. The signature of the formation of aggregates were also verified using calculations. This work was necessary in order to provide a global vision on the composition of GQD samples, a key step to enable the processability of GQDs.

The knowledge acquired on the composition of samples, coupled with the better understanding of the contamination in the samples enabled the confident exploration of the photophysics of $C_{96}C_{12}$ GQD at the single-object level. At room temperature, we characterized the dispersion of the spectral features of single GQDs and managed to differentiate fluorescent objects effectively corresponding to single GQDs from other emitters. We observed the line-narrowing of the emission lines of the GQD at low temperature, with the appearance of vibronic features which could satisfyingly be associated with characteristic vibrational modes of the GQD.

The comprehensive understanding of the properties of $C_{96}C_{12}$ GQD encouraged us to move to new classes of GQDs, namely the rod-shaped GQDs. As elaborated in the last chapter of this thesis, this new class of GQDs have been studied both in solution and at the single-object level, and have exhibited promising results. In particular, measurements in solution have shown a high degree of purity in the synthesis batches and the absence of aggregation for the rod-shaped $C_{96}tBu_8$ GQD. Using theoretical calculations, the various peaks observed in solution could be attributed to electronic transitions and vibrationals replicas. The low tendency of the $C_{96}tBu_8$ GQD to form aggregates is a good asset for its manipulation at the single-object level, and we have confirmed this using single-molecule spectroscopy. Although impurities were still present, the selection criterion elaborated for $C_{96}C_{12}$ GQDs remained efficient in reducing their impact on experimental measurements. The high homogeneity of the properties of single $C_{96}tBu_8$ GQDs, in strong contrast to observations for $C_{96}C_{12}$ samples, is a clear indication of the effective individualization of the objects in the sample.

By exploring different sizes of rod-shaped GQDs, the same degree of purity as for $C_{96}tBu_8$ could be achieved in solution, predicting an equally-efficient homogeneity of properties at the single-object level. Nonetheless, a notable difference is the signature of excimer formation for the $C_{78}tBu_6$ GQD, which can be attributed to the low number of bulky side-chains preventing the interaction between GQDs. This new class of GQDs have thus demonstrated the possiblity to tune the electronic band gap on a 100 nm range while keeping the same general electronic properties, resulting from the shared D_{2h} symmetry.

The comparison of the results for the $C_{96}tBu_8$ with the ones for the triangular $C_{96}C_{12}$ have also improved our understanding of the design of GQDs and have underlined the effect of three key factors. First of all, the D_{2h} symmetry of the $C_{96}tBu_8$ naturally leads to a bright lowest excited singlet state, where symmetry-breaking processes are needed in order to account for the brightness of the triangular $C_{96}C_{12}$. A second aspect is the influence of the side-chains. No aggregates can be observed for $C_{96}tBu_8$ in comparison

to its triangular counterpart, and this may be well explained by the presence of bulky *tert*-butyl groups which prove to be more efficient than the long $C_{12}H_{25}$ alkyl chains in preventing the formation of GQD stacks. And finally, one auspicious factor is the possiblity to purify the synthesis batches and minimize the presence of synthesis by-products in the raw powder material used to prepare samples.

By taking into account the knowledge gained on the design of GQDs, we could create new structures which would be suitable for single-object studies, *i.e.* which do not present any tendency to form aggregates.

Moreover, recently, a large variety of new graphenoid objects have emerged. By engineering defects in the aromatic structure of GQDs or creating specific geometries, one can play with the magnetic properties of GQDs [139]. In particular, the possiblity to probe the unpaired spin of the resulting open-shell GQD may lead to interesting physics if probed at the single-object level. Since no group has since studied these open-shell objects at the single-object level, it would be interesting to perform such experiments on open-shell GQDs which exhibit doublet state emission, and probe the effect for instance of magnetic fields on their emission properties.

Up until now, we have limited our studies to the investigation of the intrinsic properties of the GQD. Given the promising properties of the rod-shaped GQDs and the possibility of manipulating them at the single-object level, testing new matrices and substrates may pave the way for a broadened perspective of possible implementations of the rod-shaped GQDs.

One engaging investigation lead is to embed GQDs in new structures. Up until now, GQDs have only been embedded in polymer matrices, polystyrene in our group. Embedding them in different matrices may enhance their properties, either in order to efficiently isolate the GQD, as it was performed with Sh'polskii matrices, or in order to tune the properties of the GQD (for example in order to enhance the dipole moment for strong Stark effect). The priority should be to find matrices which could improve the line-narrowing process of the GQD at low temperature. As mentioned in the first chapter of this thesis, GQDs may be promising candidates for applications which have up until now used small fluorescent organic molecules for single-photon emitters. Testing the spectral purity is now the next step to prove the relevancy of GQDs for such applications. While technical improvements on our experimental setup need to be achieved, we know that, given the literature, specific crystalline matrices are needed to reach the fundamental limit achievable. We have recently contemplated the possibility of using octadecane, which has a convenient melting temperature in ambiant conditions around 30°C, or grow anthracene cristals doped with rod-shaped GQDs. First growth tests have already been performed by chemist collaborators, but spectroscopic measurements remain to be carried out.

Recently, an objective has also been to couple GQDs to other 2D materials to create van der Waals heterostructures. A large variety of interesting effects may result from such coupling. For instance, one can hope to improve the stability of GQDs. As demonstrated recently, depositing terrylene on hexagonal boron nitride (hBN) may lead to an enhanced photostability [222]. An interesting test would be to deposit GQDs on hBN in order to test the possibility of increasing their stability. Moreover, encapsulating GQDs

in layers of hBN may also be a way to create an inert environment for the GQD and improve the line-narrowing at low temperature. With more ambition, one may also envision the coupling to create interlayer excitons between the GQD and the 2D material. The limited spatial extension of the GQD may be an asset for the localization of interlayer excitons formed with the second material. The possibility to manipulate GQDs at the single-object level, as observed for the rod-shaped GQDs, can thus be interesting for the elaboration of excitonic few-body states by playing on the interaction of neighboring interlayer excitons placed on neighboring GQDs, as demonstrated recently in the case of uncontrolled trapping sites in $MoSe_2/WSe_2$ heterostructures [223]. Before probing the interaction of interlayer excitons, the confirmation of interlayer exciton formation must first be tried, notably using photoluminescence experiments. Our current setup should be operational to perform such measurements. Moreover, the recent development of a micro-photoluminescence excitation setup based on a supercontinuum laser gives us the necessary tools to fully characterize the expected coupling.

References

[1] Novoselov, K. S. *et al.* Electric Field Effect in Atomically Thin Carbon Films. *Science* **306**, 666–669 (2004). [Cited on pages 9 and 15.]

[2] Novoselov, K. S. *et al.* Room-temperature quantum hall effect in graphene. *Science* **315**, 1379 (2007). [Cited on page 9.]

[3] Katsnelson, M. I., Novoselov, K. S. & Geim, A. K. Chiral tunnelling and the Klein paradox in graphene. *Nature Physics* **2**, 620–625 (2006). [Cited on page 9.]

[4] Beenakker, C. W. J. Colloquium: Andreev reflection and Klein tunneling in graphene. *Reviews of Modern Physics* **80**, 1337–1354 (2008). [Cited on page 9.]

[5] Novoselov, K. S. *et al.* A roadmap for graphene. *Nature* **490**, 192–200 (2012). [Cited on page 9.]

[6] Nair, R. R. *et al.* Fine Structure Constant Defines Visual Transparency of Graphene. *Science* **320**, 1308–1308 (2008). [Cited on page 9.]

[7] Geim, A. K. & MacDonald, A. H. Graphene: Exploring carbon flatland. *Physics Today* **60**, 35–41 (2007). [Cited on pages 9 and 15.]

[8] Zhang, Y. *et al.* Direct observation of a widely tunable bandgap in bilayer graphene. *Nature* **459**, 820–823 (2009). [Cited on pages 9 and 16.]

[9] Han, M. Y., Özyilmaz, B., Zhang, Y. & Kim, P. Energy Band-Gap Engineering of Graphene Nanoribbons. *Physical Review Letters* **98**, 206805 (2007). [Cited on pages 9 and 22.]

[10] Zhao, S. *et al.* Single photon emission from graphene quantum dots at room temperature. *Nature Communications* **9**, 3470 (2018). [Cited on pages 9, 39, 44, 45, 81, 102, 105, 114, 115, 129, and 147.]

[11] Toninelli, C. *et al.* Single organic molecules for photonic quantum technologies. *Nature Materials* **20**, 1615–1628 (2021). [Cited on pages 10, 29, and 35.]

[12] Castro Neto, A. H., Guinea, F., Peres, N. M. R., Novoselov, K. S. & Geim, A. K. The electronic properties of graphene. *Reviews of Modern Physics* **81**, 109–162 (2009). [Cited on page 14.]

[13] Novoselov, K. S. *et al.* Two-dimensional gas of massless Dirac fermions in graphene. *Nature* **438**, 197–200 (2005). [Cited on page 15.]

[14] Bolotin, K. I., Ghahari, F., Shulman, M. D., Stormer, H. L. & Kim, P. Observation of the fractional quantum Hall effect in graphene. *Nature* **462**, 196–199 (2009). [Cited on page 15.]

[15] Stoller, M. D., Park, S., Zhu, Y., An, J. & Ruoff, R. S. Graphene-Based Ultracapacitors. *Nano Letters* **8**, 3498–3502 (2008). [Cited on page 15.]

[16] Xia, F., Mueller, T., Lin, Y.-m., Valdes-Garcia, A. & Avouris, P. Ultrafast graphene photodetector. *Nature Nanotechnology* **4**, 839–843 (2009). [Cited on page 15.]

[17] Mueller, T., Xia, F. & Avouris, P. Graphene photodetectors for high-speed optical communications. *Nature Photonics* **4**, 297–301 (2010). [Cited on page 15.]

[18] Cao, L., Meziani, M. J., Sahu, S. & Sun, Y.-P. Photoluminescence Properties of Graphene versus Other Carbon Nanomaterials. *Accounts of Chemical Research* **46**, 171–180 (2013). [Cited on page 16.]

[19] Geim, A. K. & Novoselov, K. S. The rise of graphene. *Nature Materials* **6**, 183–191 (2007). [Cited on page 16.]

[20] Berger, C. *et al.* Electronic Confinement and Coherence in Patterned Epitaxial Graphene. *Science* **312**, 1191–1196 (2006). [Cited on page 16.]

[21] Stampfer, C. *et al.* Tunable Coulomb blockade in nanostructured graphene. *Applied Physics Letters* **92**, 012102 (2008). [Cited on pages 16 and 22.]

[22] Rozhkov, A. V. & Nori, F. Exact wave functions for an electron on a graphene triangular quantum dot. *Physical Review B* **81**, 155401 (2010). [Cited on pages 17 and 18.]

[23] Solà, M. Forty years of Clar's aromatic π-sextet rule. *Frontiers in Chemistry* **1**, 4–11 (2013). [Cited on pages 17, 18, 101, and 164.]

[24] Fujii, S. & Enoki, T. Nanographene and Graphene Edges: Electronic Structure and Nanofabrication. *Accounts of Chemical Research* **46**, 2202–2210 (2013). [Cited on page 18.]

[25] Potasz, P., Güçlü, A. D. & Hawrylak, P. Zero-energy states in triangular and trapezoidal graphene structures. *Physical Review B* **81**, 033403 (2010). [Cited on page 18.]

[26] Ozfidan, I., Korkusinski, M. & Hawrylak, P. Electronic properties and electron-electron interactions in graphene quantum dots. *physica status solidi (RRL) - Rapid Research Letters* **10**, 13–23 (2016). [Cited on pages 18 and 20.]

[27] McGuire, J. A. Growth and optical properties of colloidal graphene quantum dots. *physica status solidi (RRL) - Rapid Research Letters* **10**, 91–101 (2016). [Cited on page 18.]

[28] Zarenia, M., Chaves, A., Farias, G. A. & Peeters, F. M. Energy levels of triangular and hexagonal graphene quantum dots: A comparative study between the tight-binding and Dirac equation approach. *Physical Review B* **84**, 245403 (2011). [Cited on page 18.]

[29] Akola, J., Heiskanen, H. P. & Manninen, M. Edge-dependent selection rules in magic triangular graphene flakes. *Physical Review B* **77**, 193410 (2008). [Cited on page 19.]

[30] Zhang, Z. Z., Chang, K. & Peeters, F. M. Tuning of energy levels and optical properties of graphene quantum dots. *Physical Review B* **77**, 235411 (2008). [Cited on page 19.]

[31] Ozfidan, I., Güçlü, A. D., Korkusinski, M. & Hawrylak, P. Theory of optical properties of graphene quantum dots. *physica status solidi (RRL) - Rapid Research Letters* **10**, 102–110 (2016). [Cited on pages 19 and 21.]

[32] Li, Y., Shu, H., Wang, S. & Wang, J. Electronic and Optical Properties of Graphene Quantum Dots: The Role of Many-Body Effects. *The Journal of Physical Chemistry C* **119**, 4983–4989 (2015). [Cited on pages 19 and 20.]

[33] Ji, Z., Dervishi, E., Doorn, S. K. & Sykora, M. Size-Dependent Electronic Properties of Uniform Ensembles of Strongly Confined Graphene Quantum Dots. *The Journal of Physical Chemistry Letters* **10**, 953–959 (2019). [Cited on pages 19 and 41.]

[34] Cocchi, C., Prezzi, D., Ruini, A., Caldas, M. J. & Molinari, E. Electronics and Optics of Graphene Nanoflakes: Edge Functionalization and Structural Distortions. *The Journal of Physical Chemistry C* **116**, 17328–17335 (2012). [Cited on pages 19, 20, 21, and 173.]

[35] Ozfidan, I., Korkusinski, M., Güçlü, A. D., McGuire, J. A. & Hawrylak, P. Microscopic theory of the optical properties of colloidal graphene quantum dots. *Physical Review B* **89**, 085310 (2014). [Cited on page 19.]

[36] Schumacher, S. Photophysics of graphene quantum dots: Insights from electronic structure calculations. *Physical Review B* **83**, 081417 (2011). [Cited on pages 19, 20, 101, and 110.]

[37] Yamamoto, T., Noguchi, T. & Watanabe, K. Edge-state signature in optical absorption of nanographenes: Tight-binding method and time-dependent density functional theory calculations. *Physical Review B* **74**, 121409 (2006). [Cited on page 20.]

[38] Riesen, H., Wiebeler, C. & Schumacher, S. Optical Spectroscopy of Graphene Quantum Dots: The Case of C132. *The Journal of Physical Chemistry A* **118**, 5189–5195 (2014). [Cited on pages 20, 114, and 172.]

[39] Schumacher, S. *et al.* Effect of exciton self-trapping and molecular conformation on photophysical properties of oligofluorenes. *The Journal of Chemical Physics* **131**, 154906 (2009). [Cited on page 20.]

[40] Yao, X. *et al.* Synthesis of Nonplanar Graphene Nanoribbon with Fjord Edges. *Journal of the American Chemical Society* **143**, 5654–5658 (2021). [Cited on pages 20, 23, 24, 36, 176, and 194.]

[41] Yang, L., Park, C.-H., Son, Y.-W., Cohen, M. L. & Louie, S. G. Quasiparticle Energies and Band Gaps in Graphene Nanoribbons. *Physical Review Letters* **99**, 186801 (2007). [Cited on page 20.]

[42] Denk, R. *et al.* Exciton-dominated optical response of ultra-narrow graphene nanoribbons. *Nature Communications* **5**, 4253 (2014). [Cited on page 20.]

[43] Ritter, K. A. & Lyding, J. W. The influence of edge structure on the electronic properties of graphene quantum dots and nanoribbons. *Nature Materials* **8**, 235–242 (2009). [Cited on page 20.]

[44] Cocchi, C., Prezzi, D., Ruini, A., Caldas, M. J. & Molinari, E. Anisotropy and size effects on the optical spectra of polycyclic aromatic hydrocarbons. *Journal of Physical Chemistry A* **118**, 6507–6513 (2014). [Cited on pages 20, 101, 114, 172, and 176.]

[45] Bischoff, D. *et al.* The importance of edges in reactive ion etched graphene nanodevices. *physica status solidi (RRL) - Rapid Research Letters* **10**, 68–74 (2016). [Cited on page 21.]

[46] Eda, G. *et al.* Blue Photoluminescence from Chemically Derived Graphene Oxide. *Advanced Materials* **22**, 505–509 (2010). [Cited on page 21.]

[47] Bacon, M., Bradley, S. J. & Nann, T. Graphene Quantum Dots. *Particle & Particle Systems Characterization* **31**, 415–428 (2014). [Cited on page 21.]

[48] Tian, P., Tang, L., Teng, K. & Lau, S. Graphene quantum dots from chemistry to applications. *Materials Today Chemistry* **10**, 221–258 (2018). [Cited on pages 21 and 38.]

[49] Pan, D., Zhang, J., Li, Z. & Wu, M. Hydrothermal Route for Cutting Graphene Sheets into Blue-Luminescent Graphene Quantum Dots. *Advanced Materials* **22**, 734–738 (2010). [Cited on pages 22 and 24.]

[50] Peng, J. *et al.* Graphene Quantum Dots Derived from Carbon Fibers. *Nano Letters* **12**, 844–849 (2012). [Cited on pages 22, 134, and 135.]

[51] Ye, R. *et al.* Coal as an abundant source of graphene quantum dots. *Nature Communications* **4**, 2943 (2013). [Cited on page 22.]

[52] Xu, Q. *et al.* Single-Particle Spectroscopic Measurements of Fluorescent Graphene Quantum Dots. *ACS Nano* **7**, 10654–10661 (2013). [Cited on pages 22, 134, and 135.]

[53] Iyer, V. S., Wehmeier, M., Brand, J. D., Keegstra, M. A. & Müllen, K. From Hexa-perihexabenzocoronene to "Superacenes". *Angewandte Chemie International Edition in English* **36**, 1604–1607 (1997). [Cited on page 23.]

[54] Morgenroth, F. & Müllen, K. Dendritic and hyperbranched polyphenylenes via a simple Diels-Alder route. *Tetrahedron* **53**, 15349–15366 (1997). [Cited on page 23.]

[55] Morgenroth, F., Reuther, E. & Müllen, K. Polyphenylene Dendrimers: From Three-Dimensional to Two-Dimensional Structures. *Angewandte Chemie International Edition in English* **36**, 631–634 (1997). [Cited on page 23.]

[56] Yan, X., Cui, X. & Li, L.-s. Synthesis of Large, Stable Colloidal Graphene Quantum Dots with Tunable Size. *Journal of the American Chemical Society* **132**, 5944–5945 (2010). [Cited on page 23.]

[57] Narita, A., Wang, X.-Y., Feng, X. & Müllen, K. New advances in nanographene chemistry. *Chemical Society Reviews* **44**, 6616–6643 (2015). [Cited on page 23.]

[58] Paternò, G. M. *et al.* Synthesis of Dibenzo[*hi,st*]ovalene and Its Amplified Spontaneous Emission in a Polystyrene Matrix. *Angewandte Chemie International Edition* **56**, 6753–6757 (2017). [Cited on pages 23, 37, and 38.]

[59] Qiu, Z. *et al.* Negatively Curved Nanographene with Heptagonal and [5]Helicene Units. *Journal of the American Chemical Society* **142**, 14814–14819 (2020). [Cited on pages 23, 24, and 36.]

[60] Rieger, R. & Müllen, K. Forever young: polycyclic aromatic hydrocarbons as model cases for structural and optical studies. *Journal of Physical Organic Chemistry* **23**, n/a–n/a (2010). [Cited on pages 23, 24, 102, 110, and 172.]

[61] Ito, S. *et al.* Synthesis and Self-Assembly of Functionalized Hexa-perihexabenzocoronenes. *Chemistry* **6**, 4327–4342 (2000). [Cited on page 23.]

[62] Kastler, M., Pisula, W., Wasserfallen, D., Pakula, T. & Müllen, K. Influence of Alkyl Substituents on the Solution- and Surface-Organization of Hexa-*peri*-hexabenzocoronenes. *Journal of the American Chemical Society* **127**, 4286–4296 (2005). [Cited on pages 23, 24, and 35.]

[63] Tan, Y.-Z. *et al.* Atomically precise edge chlorination of nanographenes and its application in graphene nanoribbons. *Nature Communications* **4**, 2646 (2013). [Cited on pages 23 and 24.]

[64] Müllen, K. Evolution of Graphene Molecules: Structural and Functional Complexity as Driving Forces behind Nanoscience. *ACS Nano* **8**, 6531–6541 (2014). [Cited on page 23.]

[65] Wang, L. *et al.* Gram-scale synthesis of single-crystalline graphene quantum dots with superior optical properties. *Nature Communications* **5**, 5357 (2014). [Cited on page 23.]

[66] Gómez, I. J. *et al.* Exploring the Emission Pathways in Nitrogen-Doped Graphene Quantum Dots for Bioimaging. *The Journal of Physical Chemistry C* **125**, 21044–21054 (2021). [Cited on page 23.]

[67] Yuan, F. *et al.* Engineering triangular carbon quantum dots with unprecedented narrow bandwidth emission for multicolored LEDs. *Nature Communications* **9**, 2249 (2018). [Cited on pages 23, 37, and 38.]

[68] Atkins, P. & Friedman, R. *Molecular Quantum Mechanics* (Oxford University Press Inc., 2011). [Cited on page 26.]

[69] Hilborn, R. C. Einstein coefficients, cross sections, f values, dipole moments, and all that. *American Journal of Physics* **50**, 982–986 (1982). [Cited on page 26.]

[70] Orrit, M. Single-Molecule Detection and Spectroscopy. In Andrews, D. L. (ed.) *Photonics*, vol. 4, chap. 2, 59–100 (Wiley, 2015), first edn. [Cited on pages 26, 27, 139, and 145.]

[71] Kozankiewicz, B. & Orrit, M. Single-molecule photophysics, from cryogenic to ambient conditions. *Chem. Soc. Rev.* **43**, 1029–1043 (2014). [Cited on pages 27, 30, 35, 84, 85, 140, and 147.]

[72] Navarro, P., Tian, Y., van Stee, M. & Orrit, M. Stable Single-Molecule Lines of Terrylene in Polycrystalline para -Dichlorobenzene at 1.5 K. *ChemPhysChem* **15**, 3032–3039 (2014). [Cited on pages 28, 35, 146, 147, and 150.]

[73] Rowe, J. M. *et al.* Systematic investigation of the excited-state properties of anthracene-dicarboxylic acids. *Journal of Photochemistry and Photobiology A: Chemistry* **337**, 207–215 (2017). [Cited on page 28.]

[74] Moerner, W. E. & Orrit, M. Illuminating Single Molecules in Condensed Matter. *Science* **283**, 1670–1676 (1999). [Cited on page 29.]

[75] Moerner, W. E. & Kador, L. Optical detection and spectroscopy of single molecules in a solid. *Physical Review Letters* **62**, 2535–2538 (1989). [Cited on page 29.]

[76] Orrit, M. & Bernard, J. Single pentacene molecules detected by fluorescence excitation in a *p*-terphenyl crystal. *Physical Review Letters* **65**, 2716–2719 (1990). [Cited on page 29.]

[77] Tamarat, P., Maali, A., Lounis, B. & Orrit, M. Ten Years of Single-Molecule Spectroscopy. *The Journal of Physical Chemistry A* **104**, 1–16 (2000). [Cited on pages 29, 147, 152, and 161.]

[78] Matsushita, M. *et al.* Single molecules as nanoprobes. A study of the Shpol'skii effect. *The Journal of Chemical Physics* **117**, 3383–3390 (2002). [Cited on page 30.]

[79] Tinnefeld, P. & Sauer, M. Branching Out of Single-Molecule Fluorescence Spectroscopy: Challenges for Chemistry and Influence on Biology. *Angewandte Chemie International Edition* **44**, 2642–2671 (2005). [Cited on page 30.]

[80] Deniz, A. A., Mukhopadhyay, S. & Lemke, E. A. Single-molecule biophysics: at the interface of biology, physics and chemistry. *Journal of The Royal Society Interface* **5**, 15–45 (2008). [Cited on page 30.]

[81] Moradi, A., Ristanović, Z., Orrit, M., Deperasińska, I. & Kozankiewicz, B. Matrix-induced Linear Stark Effect of Single Dibenzoterrylene Molecules in 2,3-Dibromonaphthalene Crystal. *ChemPhysChem* **20**, 55–61 (2019). [Cited on pages 30, 31, and 131.]

[82] Tian, Y., Navarro, P. & Orrit, M. Single Molecule as a Local Acoustic Detector for Mechanical Oscillators. *Physical Review Letters* **113**, 135505 (2014). [Cited on page 30.]

[83] Brunel, C., Tamarat, P., Lounis, B., Woehl, J. C. & Orrit, M. Stark Effect on Single Molecules of Dibenzanthanthrene in a Naphthalene Crystal and in a *n*-Hexadecane Shpol'skii Matrix. *The Journal of Physical Chemistry A* **103**, 2429–2434 (1999). [Cited on page 31.]

[84] Schädler, K. G. *et al.* Electrical Control of Lifetime-Limited Quantum Emitters Using 2D Materials. *Nano Letters* **19**, 3789–3795 (2019). [Cited on page 31.]

[85] Colautti, M. *et al.* Laser-Induced Frequency Tuning of Fourier-Limited Single-Molecule Emitters. *ACS Nano* **14**, 13584–13592 (2020). [Cited on page 31.]

[86] Wang, D. *et al.* Turning a molecule into a coherent two-level quantum system. *Nature Physics* **15**, 483–489 (2019). [Cited on page 31.]

[87] Colautti, M. *et al.* A 3D Polymeric Platform for Photonic Quantum Technologies. *Advanced Quantum Technologies* **3**, 2000004 (2020). [Cited on pages 32 and 33.]

[88] Lettow, R. *et al.* Quantum Interference of Tunably Indistinguishable Photons from Remote Organic Molecules. *Physical Review Letters* **104**, 123605 (2010). [Cited on pages 31 and 32.]

[89] Pscherer, A. *et al.* Single-Molecule Vacuum Rabi Splitting: Four-Wave Mixing and Optical Switching at the Single-Photon Level. *Physical Review Letters* **127**, 133603 (2021). [Cited on pages 32, 33, and 34.]

[90] Brunel, C., Lounis, B., Tamarat, P. & Orrit, M. Triggered Source of Single Photons based on Controlled Single Molecule Fluorescence. *Physical Review Letters* **83**, 2722–2725 (1999). [Cited on page 31.]

[91] Lounis, B. & Moerner, W. E. Single photons on demand from a single molecule at room temperature. *Nature* **407**, 491–493 (2000). [Cited on page 31.]

[92] Kiraz, A. *et al.* Indistinguishable Photons from a Single Molecule. *Physical Review Letters* **94**, 223602 (2005). [Cited on page 31.]

[93] Rezai, M., Wrachtrup, J. & Gerhardt, I. Coherence Properties of Molecular Single Photons for Quantum Networks. *Physical Review X* **8**, 031026 (2018). [Cited on page 31.]

[94] Lombardi, P. *et al.* Triggered emission of indistinguishable photons from an organic dye molecule. *Applied Physics Letters* **118**, 204002 (2021). [Cited on page 31.]

[95] Rezai, M., Wrachtrup, J. & Gerhardt, I. Polarization-entangled photon pairs from a single molecule. *Optica* **6**, 34 (2019). [Cited on page 33.]

[96] Plakhotnik, T., Walser, D., Pirotta, M., Renn, A. & Wild, U. P. Nonlinear Spectroscopy on a Single Quantum System: Two-Photon Absorption of a Single Molecule. *Science* **271**, 1703–1705 (1996). [Cited on page 33.]

[97] Hwang, J. *et al.* A single-molecule optical transistor. *Nature* **460**, 76–80 (2009). [Cited on page 33.]

[98] Maser, A., Gmeiner, B., Utikal, T., Götzinger, S. & Sandoghdar, V. Few-photon coherent nonlinear optics with a single molecule. *Nature Photonics* **10**, 450–453 (2016). [Cited on page 33.]

[99] Kühn, S., Håkanson, U., Rogobete, L. & Sandoghdar, V. Enhancement of Single-Molecule Fluorescence Using a Gold Nanoparticle as an Optical Nanoantenna. *Physical Review Letters* **97**, 017402 (2006). [Cited on pages 33 and 34.]

[100] Ciancico, C. *et al.* Narrow Line Width Quantum Emitters in an Electron-Beam-Shaped Polymer. *ACS Photonics* **6**, 3120–3125 (2019). [Cited on pages 33 and 34.]

[101] Khatua, S. *et al.* Resonant Plasmonic Enhancement of Single-Molecule Fluorescence by Individual Gold Nanorods. *ACS Nano* **8**, 4440–4449 (2014). [Cited on page 33.]

[102] Kinkhabwala, A. *et al.* Large single-molecule fluorescence enhancements produced by a bowtie nanoantenna. *Nature Photonics* **3**, 654–657 (2009). [Cited on page 33.]

[103] Chu, X.-L., Götzinger, S. & Sandoghdar, V. A single molecule as a high-fidelity photon gun for producing intensity-squeezed light. *Nature Photonics* **11**, 58–62 (2017). [Cited on page 33.]

[104] Faez, S., Türschmann, P., Haakh, H. R., Götzinger, S. & Sandoghdar, V. Coherent Interaction of Light and Single Molecules in a Dielectric Nanoguide. *Physical Review Letters* **113**, 213601 (2014). [Cited on page 33.]

[105] Türschmann, P. *et al.* Chip-Based All-Optical Control of Single Molecules Coherently Coupled to a Nanoguide. *Nano Letters* **17**, 4941–4945 (2017). [Cited on page 33.]

[106] Lombardi, P. *et al.* Photostable Molecules on Chip: Integrated Sources of Nonclassical Light. *ACS Photonics* **5**, 126–132 (2018). [Cited on page 33.]

[107] Rattenbacher, D. *et al.* Coherent coupling of single molecules to on-chip ring resonators. *New Journal of Physics* **21**, 062002 (2019). [Cited on page 33.]

[108] Grandi, S. *et al.* Hybrid plasmonic waveguide coupling of photons from a single molecule. *APL Photonics* **4**, 086101 (2019). [Cited on page 33.]

[109] Sandoghdar, V. Nano-Optics in 2020 ± 20. *Nano Letters* **20**, 4721–4723 (2020). [Cited on page 33.]

[110] Adhikari, S. & Orrit, M. Progress and perspectives in single-molecule optical spectroscopy. *The Journal of Chemical Physics* **156**, 160903 (2022). [Cited on page 35.]

[111] Orlov, S. V., Naumov, A. V., Vainer, Y. G. & Kador, L. Spectrally resolved analysis of fluorescence blinking of single dye molecules in polymers at low temperatures. *The Journal of Chemical Physics* **137**, 194903 (2012). [Cited on page 35.]

[112] Sobolev, Y. I., Naumov, A. V., Vainer, Y. G. & Kador, L. Low temperature spectral dynamics of single molecules in ultrathin polymer films. *The Journal of Chemical Physics* **140**, 204907 (2014). [Cited on page 35.]

[113] Smit, R., Ristanović, Z., Kozankiewicz, B. & Orrit, M. Reverse Intersystem Crossing of Single Deuterated Perylene Molecules in a Dibenzothiophene Matrix. *ChemPhysChem* **23**, 1–9 (2022). [Cited on page 35.]

[114] Verhart, N. R., Müller, M. & Orrit, M. Spectroscopy of Single Dibenzoterrylene Molecules in *para*-Dichlorobenzene. *ChemPhysChem* **17**, 1524–1529 (2016). [Cited on page 35.]

[115] Yan, X., Cui, X., Li, B. & Li, L.-s. Large, Solution-Processable Graphene Quantum Dots as Light Absorbers for Photovoltaics. *Nano Letters* **10**, 1869–1873 (2010). [Cited on pages 35 and 38.]

[116] Bonal, V. *et al.* Solution-processed nanographene distributed feedback lasers. *Nature Communications* **10**, 1–10 (2019). [Cited on pages 35, 37, and 38.]

[117] Wasserfallen, D. *et al.* Suppressing aggregation in a large polycyclic aromatic hydrocarbon. *Journal of the American Chemical Society* **128**, 1334–1339 (2006). [Cited on pages 36, 109, 169, and 176.]

[118] Liu, Z. *et al.* Solution-Processed Graphene-Nanographene van der Waals Heterostructures for Photodetectors with Efficient and Ultralong Charge Separation. *Journal of the American Chemical Society* **143**, 17109–17116 (2021). [Cited on pages 36, 38, 102, and 109.]

[119] Zhao, B. & Tan, Z. Fluorescent Carbon Dots: Fantastic Electroluminescent Materials for Light-Emitting Diodes. *Advanced Science* **8**, 2001977 (2021). [Cited on pages 37 and 38.]

[120] Fan, Z., Li, S., Yuan, F. & Fan, L. Fluorescent graphene quantum dots for biosensing and bioimaging. *RSC Advances* **5**, 19773–19789 (2015). [Cited on page 38.]

[121] Han, P. *et al.* Size-dependent electron transfer from atomically defined nanographenes to metal oxide nanoparticles. *Nanoscale* **12**, 16046–16052 (2020). [Cited on page 38.]

[122] Fantuzzi, P. *et al.* Color Sensitive Response of Graphene/Graphene Quantum Dot Phototransistors. *The Journal of Physical Chemistry C* **123**, 26490–26497 (2019). [Cited on page 38.]

[123] Muñoz-Mármol, R. *et al.* Near-Infrared Lasing in Four-Zigzag Edged Nanographenes by 1D versus 2D Electronic π-Conjugation. *Advanced Functional Materials* **31**, 2105073 (2021). [Cited on page 38.]

[124] Paternò, G. M. *et al.* Excited states engineering enables efficient near-infrared lasing in nanographenes. *Materials Horizons* **9**, 393–402 (2022). [Cited on page 38.]

[125] Zhou, S., Xu, H., Gan, W. & Yuan, Q. Graphene quantum dots: recent progress in preparation and fluorescence sensing applications. *RSC Advances* **6**, 110775–110788 (2016). [Cited on page 38.]

[126] Semeniuk, M. *et al.* Future Perspectives and Review on Organic Carbon Dots in Electronic Applications. *ACS Nano* **13**, 6224–6255 (2019). [Cited on pages 38 and 41.]

[127] Yan, Y. *et al.* Recent Advances on Graphene Quantum Dots: From Chemistry and Physics to Applications. *Advanced Materials* **31**, 1808283 (2019). [Cited on page 38.]

[128] Paternò, G. M. *et al.* Large Polycyclic Aromatic Hydrocarbons as Graphene Quantum Dots: from Synthesis to Spectroscopy and Photonics. *Advanced Optical Materials* **9**, 2100508 (2021). [Cited on pages 38 and 169.]

[129] Liu, Z. *et al.* Small Size, Big Impact: Recent Progress in Bottom-Up Synthesized Nanographenes for Optoelectronic and Energy Applications. *Advanced Science* **9**, 2106055 (2022). [Cited on page 38.]

[130] Ponomarenko, L. A. *et al.* Chaotic Dirac Billiard in Graphene Quantum Dots. *Science* **320**, 356–358 (2008). [Cited on page 38.]

[131] Droth, M. & Burkard, G. Spintronics with graphene quantum dots. *physica status solidi (RRL) - Rapid Research Letters* **10**, 75–90 (2016). [Cited on page 39.]

[132] Lombardi, F. *et al.* Quantum units from the topological engineering of molecular graphenoids. *Science* **366**, 1107–1110 (2019). [Cited on page 39.]

[133] Mishra, S. *et al.* Topological frustration induces unconventional magnetism in a nanographene. *Nature Nanotechnology* **15**, 22–28 (2020). [Cited on pages 39 and 40.]

[134] Mishra, S. *et al.* Synthesis and Characterization of π-Extended Triangulene. *Journal of the American Chemical Society* **141**, 10621–10625 (2019). [Cited on page 40.]

[135] Mishra, S. *et al.* Topological Defect-Induced Magnetism in a Nanographene. *Journal of the American Chemical Society* **142**, 1147–1152 (2020). [Cited on page 40.]

[136] Guo, H. *et al.* High stability and luminescence efficiency in donor-acceptor neutral radicals not following the Aufbau principle. *Nature Materials* **18**, 977–984 (2019). [Cited on page 40.]

[137] Abdurahman, A. *et al.* Understanding the luminescent nature of organic radicals for efficient doublet emitters and pure-red light-emitting diodes. *Nature Materials* **19**, 1224–1229 (2020). [Cited on page 40.]

[138] Hudson, J. M., Hele, T. J. H. & Evans, E. W. Efficient light-emitting diodes from organic radicals with doublet emission. *Journal of Applied Physics* **129**, 180901 (2021). [Cited on page 40.]

[139] Zheng, Y. *et al.* Designer spin order in diradical nanographenes. *Nature Communications* **11**, 6076 (2020). [Cited on pages 40 and 201.]

[140] Yoon, H. *et al.* Toward highly efficient luminescence in graphene quantum dots for optoelectronic applications. *Chemical Physics Reviews* **2**, 031303 (2021). [Cited on page 41.]

[141] Tomović, Ž., Watson, M. D. & Müllen, K. Superphenalene-Based Columnar Liquid Crystals. *Angewandte Chemie - International Edition* **43**, 755–758 (2004). [Cited on pages 44, 100, 117, and 118.]

[142] Medina-Lopez, D. *et al.* Highly Individualized Rod-shaped, Graphene Quantum Dots in Solution. *in preparation* (2023). [Cited on pages 44, 45, 46, and 196.]

[143] Singhal, N., Kumar, M., Kanaujia, P. K. & Virdi, J. S. MALDI-TOF mass spectrometry: an emerging technology for microbial identification and diagnosis. *Frontiers in Microbiology* **6** (2015). [Cited on page 47.]

[144] Hughes, J. M. *et al.* High Quality Dispersions of Hexabenzocoronene in Organic Solvents. *Journal of the American Chemical Society* **134**, 12168–12179 (2012). [Cited on pages 48, 101, and 134.]

[145] Zhao, S. *Propriétés optiques de nanorubans et boites quantiques de graphène*. Ph.D. thesis, Université Paris-Saclay (2018). [Cited on pages 48, 79, 100, 128, and 131.]

[146] Lakowicz, J. R. *Principles of Fluorescence Spectroscopy* (Springer, 2006). [Cited on pages 50, 60, and 109.]

[147] Born, M. & Wolf, E. *Principles of Optics* (Cambridge University Press, 1999), seventh edn. [Cited on page 56.]

[148] Grynberg, G., Aspect, A., Fabre, C. & Cohen-Tannoudji, C. *Introduction to Quantum Optics* (Cambridge University Press, Cambridge, 2010). [Cited on page 57.]

[149] Bruhat, G. *Optique* (Masson & Cie, 1954), 4e edn. [Cited on page 63.]

[150] Beveratos, A. *Réalisation expérimentale d'une source de photons uniques par fluorescence de centres colorés individuels dans le diamant ; application à la cryptographie quantique*. Ph.D. thesis, Université Paris-Saud - Paris XI (2002). [Cited on page 67.]

[151] Novotny, L. & Hecht, B. *Principle of Nano Optics* (Cambridge University Press, 2012), second edn. [Cited on page 68.]

[152] Huang, C.-H., Wen, Y.-H. & Liu, Y.-W. Measuring the second order correlation function and the coherence time using random phase modulation. *Optics Express* **24**, 4278 (2016). [Cited on page 69.]

[153] Reynaud, S. La fluorescence de résonance : Etude par la méthode de l'atome habillé. *Annales de Physique* **8**, 315–370 (1983). [Cited on page 69.]

[154] Brouri, R., Beveratos, A., Poizat, J.-P. & Grangier, P. Photon antibunching in the fluorescence of individual color centers in diamond. *Optics Letters* **25**, 1294 (2000). [Cited on page 70.]

[155] Gaertner, A. A., Yoon, H. W. & Germer, T. A. Dispersive Methods. In *Experimental Methods in the Physical Sciences*, vol. 46, 67–95 (Elsevier Inc., 2014), first edn. [Cited on page 73.]

[156] Rabouw, F. T. *et al.* Non-blinking single-photon emitters in silica. *Scientific Reports* **6**, 1–7 (2016). [Cited on pages 79, 80, 82, and 89.]

[157] Neumann, A., Lindlau, J., Thoms, S., Basché, T. & Högele, A. Accidental Contamination of Substrates and Polymer Films by Organic Quantum Emitters. *Nano Letters* **19**, 3207–3213 (2019). [Cited on pages 79, 80, 84, 86, 87, 88, and 95.]

[158] Trinh, C. T., Lee, J. & Lee, K.-G. Fluorescent impurity emitter in toluene and its photon emission properties. *Scientific Reports* **8**, 8273 (2018). [Cited on pages 79, 80, 82, 84, and 88.]

[159] Fleury, L. *et al.* Single Molecule Spectra of an Impurity Found in N-Hexadecane and Polyethylene. *Molecular Crystals and Liquid Crystals Science and Technology. Section A. Molecular Crystals and Liquid Crystals* **283**, 81–87 (1996). [Cited on pages 80, 86, 87, and 90.]

[160] Wang, X. *et al.* Non-blinking semiconductor nanocrystals. *Nature* **459**, 686–689 (2009). [Cited on page 81.]

[161] Martínez, L. J. *et al.* Efficient single photon emission from a high-purity hexagonal boron nitride crystal. *Physical Review B* **94**, 121405 (2016). [Cited on page 82.]

[162] Myers, A. B., Tchenio, P., Zgierski, M. Z. & Moerner, W. E. Vibronic Spectroscopy of Individual Molecules in Solids. *The Journal of Physical Chemistry* **98**, 10377–10390 (1994). [Cited on pages 86, 107, and 140.]

[163] Davis, J. L., Dong, B., Sun, C. & Zhang, H. F. Method to identify and minimize artifacts induced by fluorescent impurities in single-molecule localization microscopy. *Journal of Biomedical Optics* **23**, 1 (2018). [Cited on pages 88 and 98.]

[164] Ronceray, N. *et al.* Liquid-activated quantum emission from native hBN defects for nanofluidic sensing. *arXiv:2204.06287* (2022). [Cited on pages 88, 95, and 98.]

[165] Feist, F. A., Tommaseo, G. & Basché, T. Single-molecule spectroscopy of MEH-PPV polymer molecules in different host matrices'. *Journal of Physical Chemistry C* **113**, 11484–11490 (2009). [Cited on page 89.]

[166] Chen, Q. *et al.* Dibenzo[hi , st]ovalene as Highly Luminescent Nanographene: Efficient Synthesis via Photochemical Cyclodehydroiodination, Optoelectronic Properties, and Single-Molecule Spectroscopy. *Journal of the American Chemical Society* **141**, 16439–16449 (2019). [Cited on page 89.]

[167] White, S. J. U. *et al.* Electrical control of quantum emitters in a Van der Waals heterostructure. *Light: Science & Applications* **11**, 186 (2022). [Cited on page 98.]

[168] Hail, C. U. *et al.* Nanoprinting organic molecules at the quantum level. *Nature Communications* **10**, 1–8 (2019). [Cited on page 98.]

[169] Clar, E. *Polycyclic Hydrocarbons*, vol. 2 (Springer-Verlag, 1964). [Cited on page 101.]

[170] Rätsep, M., Linnanto, J. & Freiberg, A. Mirror symmetry and vibrational structure in optical spectra of chlorophyll a. *The Journal of Chemical Physics* **130**, 194501 (2009). [Cited on page 107.]

[171] Kundu, S., Roy, P. P., Fleming, G. R. & Makri, N. Franck-Condon and Herzberg-Teller Signatures in Molecular Absorption and Emission Spectra. *The Journal of Physical Chemistry B* **126**, 2899–2911 (2022). [Cited on page 107.]

[172] Alcala, J. R. The effect of harmonic conformational trajectories on protein fluorescence and lifetime distributions. *The Journal of Chemical Physics* **101**, 4578–4584 (1994). [Cited on page 109.]

[173] Oña-Ruales, J. O. & Ruiz-Morales, Y. The Predictive Power of the Annellation Theory: The Case of the C 26 H 16 Cata-Condensed Benzenoid Polycyclic Aromatic Hydrocarbons. *The Journal of Physical Chemistry A* **119**, 10451–10461 (2015). [Cited on page 110.]

[174] Terenziani, F., Sissa, C. & Painelli, A. Symmetry Breaking in Octupolar Chromophores: Solvatochromism and Electroabsorption. *The Journal of Physical Chemistry B* **112**, 5079–5087 (2008). [Cited on page 112.]

[175] Dereka, B. *et al.* Solvent tuning of photochemistry upon excited-state symmetry breaking. *Nature Communications* **11**, 1925 (2020). [Cited on page 112.]

[176] Rösch, U., Yao, S., Wortmann, R. & Würthner, F. Fluorescent H-aggregates of merocyanine dyes. *Angewandte Chemie - International Edition* **45**, 7026–7030 (2006). [Cited on page 120.]

[177] Kasha, M. Molecular Excitons in Small Aggregates. In *Spectroscopy of the Excited State*, 1, 337–363 (Plenum Press, 1976). [Cited on page 120.]

[178] Fleming, A. J. *et al.* Optical spectroscopy of isolated and aggregate hexabenzocoronene derivatives: A study of self-assembling molecular nanowires. *Journal of Physical Chemistry B* **107**, 37–43 (2003). [Cited on page 120.]

[179] Zhao, X. J. *et al.* Molecular bilayer graphene. *Nature Communications* **10**, 1–7 (2019). [Cited on page 121.]

[180] Fennel, F., Gershberg, J., Stolte, M. & Würthner, F. Fluorescence quantum yields of dye aggregates: A showcase example based on self-assembled perylene bisimide dimers. *Physical Chemistry Chemical Physics* **20**, 7612–7620 (2018). [Cited on page 123.]

[181] Fleury, L., Tamarat, P., Lounis, B., Bernard, J. & Orrit, M. Fluorescence spectra of single pentacene molecules in p-terphenyl at 1.7 K. *Chemical Physics Letters* **236**, 87–95 (1995). [Cited on page 131.]

[182] Ghosh, S., Oleksiievets, N., Enderlein, J. & Chizhik, A. I. Emission States Variation of Single Graphene Quantum Dots. *The Journal of Physical Chemistry Letters* **11**, 7356–7362 (2020). [Cited on page 136.]

[183] Nonn, T. & Plakhotnik, T. Fluorescence excitation spectroscopy of vibronic transitions in single molecules. *Chemical Physics Letters* **336**, 97–104 (2001). [Cited on page 140.]

[184] Zirkelbach, J. *et al.* High-resolution vibronic spectroscopy of a single molecule embedded in a crystal. *The Journal of Chemical Physics* **156**, 104301 (2022). [Cited on page 140.]

[185] Dresselhaus, M. S. & Eklund, P. C. Phonons in carbon nanotubes. *Advances in Physics* **49**, 705–814 (2000). [Cited on page 141.]

[186] Zhou, J. & Dong, J. Vibrational property and Raman spectrum of carbon nanoribbon. *Applied Physics Letters* **91**, 173108 (2007). [Cited on page 141.]

[187] Zhou, J. & Dong, J. Radial breathing-like mode of wide carbon nanoribbon. *Physics Letters A* **372**, 7183–7186 (2008). [Cited on page 141.]

[188] Gillen, R., Mohr, M. & Maultzsch, J. Symmetry properties of vibrational modes in graphene nanoribbons. *Physical Review B* **81**, 205426 (2010). [Cited on page 141.]

[189] Overbeck, J. *et al.* A Universal Length-Dependent Vibrational Mode in Graphene Nanoribbons. *ACS Nano* **13**, 13083–13091 (2019). [Cited on pages 141 and 142.]

[190] Liu, D., Daniels, C., Meunier, V., Every, A. G. & Tománek, D. In-plane breathing and shear modes in low-dimensional nanostructures. *Carbon* **157**, 364–370 (2020). [Cited on pages 141 and 142.]

[191] Liu, D., Every, A. G. & Tománek, D. Continuum approach for long-wavelength acoustic phonons in quasi-two-dimensional structures. *Physical Review B* **94**, 165432 (2016). [Cited on page 142.]

[192] Ambrose, W. P., Basché, T. & Moerner, W. E. Detection and spectroscopy of single pentacene molecules in a p-terphenyl crystal by means of fluorescence excitation. *The Journal of Chemical Physics* **95**, 7150–7163 (1991). [Cited on pages 145, 146, and 147.]

[193] Kozankiewicz, B., Bernard, J. & Orrit, M. Single molecule lines and spectral hole burning of terrylene in different matrices. *The Journal of Chemical Physics* **101**, 9377–9383 (1994). [Cited on pages 145, 148, and 161.]

[194] Vainer, Y. G., Naumov, A. V. & Kador, L. Local vibrations in disordered solids studied via single-molecule spectroscopy: Comparison with neutron, nuclear, Raman scattering, and photon echo data. *Physical Review B* **77**, 224202 (2008). [Cited on page 147.]

[195] de Vries, H. & Wiersma, D. A. Photophysical and photochemical molecular hole burning theory. *The Journal of Chemical Physics* **72**, 1851–1863 (1980). [Cited on page 147.]

[196] Moerner, W. E. & Fromm, D. P. Methods of single-molecule fluorescence spectroscopy and microscopy. *Review of Scientific Instruments* **74**, 3597–3619 (2003). [Cited on page 147.]

[197] Boiron, A.-M., Tamarat, P., Lounis, B., Brown, R. & Orrit, M. Are the spectral trails of single molecules consistent with the standard two-level system model of glasses at low temperatures? *Chemical Physics* **247**, 119–132 (1999). [Cited on pages 148 and 151.]

[198] Gauglitz, G. & Moore, D. S. (eds.) *Handbook of Spectroscopy* (Wiley-VCH Verlag, 2014), second edn. [Cited on page 150.]

[199] Orrit, M., Bernard, J., Brown, R. & Lounis, B. II Optical Spectroscopy of Single Molecules in Solids. In Wolf, E. (ed.) *Progress in Optics*, vol. 35, 61–144 (1996). [Cited on page 150.]

[200] Ambrose, W. P. & Moerner, W. E. Fluorescence spectroscopy and spectral diffusion of single impurity molecules in a crystal. *Nature* **349**, 225–227 (1991). [Cited on page 151.]

[201] Orrit, M. Frequency jitter of a nano-emitter. *Nature Photonics* **4**, 667–668 (2010). [Cited on pages 151 and 159.]

[202] Zumbusch, A., Fleury, L., Brown, R., Bernard, J. & Orrit, M. Probing individual two-level systems in a polymer by correlation of single molecule fluorescence. *Physical Review Letters* **70**, 3584–3587 (1993). [Cited on pages 151 and 159.]

[203] Reigue, A., Hostein, R. & Voliotis, V. Resonance fluorescence of a single semiconductor quantum dot: the impact of a fluctuating electrostatic environment. *Semiconductor Science and Technology* **34**, 113001 (2019). [Cited on page 152.]

[204] Vernotte, F. Variance Measurements. In *Joint conference of the IEEE International Frequency Control Symposium and European Frequency and Time Forum* (2011). [Cited on pages 154 and 155.]

[205] Lansdorp, B. M. & Saleh, O. A. Power spectrum and Allan variance methods for calibrating single-molecule video-tracking instruments. *Review of Scientific Instruments* **83**, 025115 (2012). [Cited on page 154.]

[206] Allan, D. Time and Frequency (Time-Domain) Characterization, Estimation, and Prediction of Precision Clocks and Oscillators. *IEEE Transactions on Ultrasonics, Ferroelectrics and Frequency Control* **34**, 647–654 (1987). [Cited on page 154.]

[207] Uhrich, P. Stabilité des Oscillateurs ultra-stables. In *Journées X-ENS-UPS de Physique*, 1–41 (2007). [Cited on page 155.]

[208] Noé, J. C. *et al.* Environmental Electrometry with Luminescent Carbon Nanotubes. *Nano Letters* **18**, 4136–4140 (2018). [Cited on page 157.]

[209] Sallen, G. *et al.* Subnanosecond spectral diffusion measurement using photon correlation. *Nature Photonics* **4**, 696–699 (2010). [Cited on page 159.]

[210] Vural, H. *et al.* Characterization of spectral diffusion by slow-light photon-correlation spectroscopy. *Physical Review B* **101**, 161401 (2020). [Cited on page 159.]

[211] Tian, Y., Navarro, P., Kozankiewicz, B. & Orrit, M. Spectral diffusion of single dibenzoterrylene molecules in 2,3-dimethylanthracene. *ChemPhysChem* **13**, 3510–3515 (2012). [Cited on page 159.]

[212] Tran, T. T., Bradac, C., Solntsev, A. S., Toth, M. & Aharonovich, I. Suppression of spectral diffusion by anti-Stokes excitation of quantum emitters in hexagonal boron nitride. *Applied Physics Letters* **115**, 071102 (2019). [Cited on page 159.]

[213] Liu, T. *et al.* Vibronic effect and influence of aggregation on the photophysics of graphene quantum dots. *Nanoscale* **14**, 3826–3833 (2022). [Cited on page 160.]

[214] Liu, T. *et al.* Vibronic fingerprints in the luminescence of graphene quantum dots at cryogenic temperature. *The Journal of Chemical Physics* **156**, 104302 (2022). [Cited on page 160.]

[215] Basko, D. M., Duchemin, I. & Blase, X. Optical properties of graphene quantum dots: the role of chiral symmetry. *2D Materials* **7**, 025041 (2020). [Cited on pages 172 and 173.]

[216] Clar, E. & Zander, M. Aromatische Kohlenwasser-stoffe, LXXII. Mitteil. : Die Zusammenhänge zwischen chemischer Reaktivität, Phosphorescenz und *para*-Absorptionsbanden und die "Wasserstoffähnlichkeit" des oberen Niveaus der *p*-Banden in den Absorptionsspektren aromatischer Kohlenwasserstoffe. *Chemische Berichte* **89**, 749–762 (1956). [Cited on page 173.]

[217] Zeng, T., Hoffmann, R. & Ananth, N. The low-lying electronic states of pentacene and their roles in singlet fission. *Journal of the American Chemical Society* **136**, 5755–5764 (2014). [Cited on page 173.]

[218] Valeur, B. & Berberan-Santos, M. N. *Molecular Fluorescence* (Wiley-VCH Verlag, 2012), second edn. [Cited on page 182.]

[219] Ameloot, M., VandeVen, M., Acuña, A. U. & Valeur, B. Fluorescence anisotropy measurements in solution: Methods and reference materials (IUPAC Technical Report). *Pure and Applied Chemistry* **85**, 589–608 (2013). [Cited on page 182.]

[220] Neuteboom, E. E., Meskers, S. C. J., Meijer, E. W. & Janssen, R. A. J. Photoluminescence of Self-organized Perylene Bisimide Polymers. *Macromolecular Chemistry and Physics* **205**, 217–222 (2004). [Cited on page 193.]

[221] Son, M., Park, K. H., Shao, C., Würthner, F. & Kim, D. Spectroscopic Demonstration of Exciton Dynamics and Excimer Formation in a Sterically Controlled Perylene Bisimide Dimer Aggregate. *The Journal of Physical Chemistry Letters* **5**, 3601–3607 (2014). [Cited on page 193.]

[222] Han, S. *et al.* Photostable fluorescent molecules on layered hexagonal boron nitride: Ideal single-photon sources at room temperature. *The Journal of Chemical Physics* **155**, 244301 (2021). [Cited on page 201.]

[223] Li, W., Lu, X., Dubey, S., Devenica, L. & Srivastava, A. Dipolar interactions between localized interlayer excitons in van der Waals heterostructures. *Nature Materials* **19**, 624–629 (2020). [Cited on page 202.]

Résumé de la thèse

Les boîtes quantiques de graphène (abrégé GQD en anglais) sont des nano-objets composés d'une centaine d'atomes de carbone. Ces atomes peuvent être disposés selon diverses géométries conduisant à un large éventail de propriétés. Leur taille intermédiaire entre petites molécules et solides en fait une plateforme idéale pour tester les prédictions théoriques, à la fois de la chimie quantique et de la physique de la matière condensée. Cependant, bénéficier pleinement des potentialités offertes par l'accordabilité des propriétés des GQDs nécessite de pouvoir rigoureusement relier leur géométrie aux propriétés électroniques qui en découlent. Dans cette optique, une étude approfondie des propriétés intrinsèques de ces objets a été réalisée dans le cadre de cette thèse. Ce travail a été mené en couplant des études spectroscopiques en solution (où les propriétés d'ensemble sont sondées) et à l'échelle de l'objet individuel (où l'on peut s'affranchir des effets d'ensemble pour mesurer des effets locaux) à des simulations théoriques, qui permettent de relier les observations optiques aux états électroniques de l'objet.

Afin de poursuivre les résultats déjà obtenus dans l'équipe concernant une boîte quantique de graphène à symétrie triangulaire (C96C12), diverses mesures spectroscopiques en solution ont été réalisées, et ont mené à la mise en lumière de phénomènes d'agrégation en solution. L'étude en solution a pu ainsi mener à une meilleure compréhension de la composition des échantillons de GQDs, une étape clef afin de mieux comprendre les observations faites sur objets uniques. Parallèlement, des mesures statistiques à l'échelle de la boîte quantique individuelle ont été menées à température ambiante, suivi d'une exploration de signatures spectroscopiques à basse température (7K). Ces études ont notamment permis d'expliquer l'observation de fluorescence, pourtant théoriquement négligeable compte tenu de la symétrie de l'objet, par la prise en compte de déformations mécaniques liées aux vibrations de la boîte quantique, dont certains modes caractéristiques sont observables à basse température.

L'étude de la C96C12 à l'échelle de l'objet unique a notamment nécessité l'élaboration de critères expérimentaux afin d'éviter toute pollution des mesures par des impuretés environnantes. Cela a pu aboutir à une étude des impuretés fluorescentes observables dans les expériences de spectroscopie d'objets uniques, en particulier à la mesure de leur signature spectrale à basse température, ainsi qu'à l'étude de l'origine de la contamination. Ces résultats non directement liés aux boîtes quantiques, mais qui représentent un apport nécessaire à leur utilisation à l'échelle de l'objet unique.

Enfin, l'effet de la symétrie sur les propriétés électroniques a été approfondi par l'étude de boîtes quantiques présentant une symétrie allongée et non plus triangulaire.

Elle a permis d'observer expérimentalement l'influence de la symétrie sur les transitions optiques observables en solution, reproduisant parfaitement les prédictions théoriques. Ces nouvelles boîtes quantiques apportent notamment une homogénéité accrue dans les propriétés sondées au sein d'un échantillon (dont témoigne la finesse des bandes d'absorptions en solution et la faible dispersion des propriétés à l'échelle de l'objet unique), qualité essentielle en terme de reproductibilité lors de leur utilisation. L'effet de la taille a également pu être examiné et permet de faire varier l'énergie des transitions sur une large gamme de longueur d'onde. L'étude de ces GQD allongées a ainsi permis de proposer une nouvelle classe de GQD prometteuse pour les applications.

Cette thèse a ainsi permis d'approfondir l'étude de ces objets, là où leur caractérisation se limite trop souvent à une étude sommaire en solution. Grâce à une compréhension accrue des propriétés des boîtes quantiques, cette thèse contribue à ouvrir la voie à l'utilisation des GQDs dans différentes applications, de l'optoélectronique au développement de capteurs, et à leur couplage avec différents matériaux, permettant encore d'étendre leur domaine d'applications.